Fluid/Structure Impact with Air Cavity Effect

by

Bingyue Song

A dissertation submitted for the degree of

Doctor of Philosophy

Department of mechanical Engineering

University College London

Torrington Place, London WC1E 7JE, UK

January 2015

Declaration

I, Bingyue Song, confirm that the work presented in this thesis is my own. Where information has been derived from other sources, I confirm that this has been indicated in the thesis.

Signature: Bingyue Song Date: 29/05/2015

Abstract

Violent wave attacking offshore and coastal structures is a complex phenomenon frequently involving air entrapment. A study on fluid/structure impact with air cavity effect is carried out in the framework of velocity potential theory. The purpose is twofold. One is to develop methodologies to tackle the technical difficulties involved. The other is to achieve a better insight into the impact dynamics and the subsequent structure/water/air interaction process, as well as the associated air cavity effect and its acting mechanism.

The study starts with axisymmetric problems. Impact by a liquid column on a rigid plate is studied analytically and numerically. The initial singularity at the body-free surface intersection is analysed in detail. The feature of the resulting long thin jet is revealed: providing field solution over larger wetted area without influencing the main impact dynamics. This is favourable in the study of some problems (e.g. steady state solution or local impact over a tiny region), and thus a decoupled shallow water approximation scheme is developed for the computation with long jet. Impact with air cavity of various parameters is studied systematically.

Wave impact with air entrapment in practical engineering situations is then focused. A domain decomposition method together with a dual-system technique is developed to provide fully nonlinear simulation on the early impact stage by a plunging wave crest, tackling the large variation in scales involved. Local pressure peak is found to be generated by the sharp turn of the wave surface along the wall. The trapped cavity, governed by an adiabatic law, is found to cause oscillating loading on the wall. The local free jet drawn from the upper cavity surface in each re-contraction stage reveals its distortion and fragmentation mechanism. The initial dimensionless potential energy of the air cavity is found to largely influence its maximum pressure, and the scaling law revealed could be applied to the prediction of impact pressure in practical situations from a laboratory experiment.

Acknowledgement

I would like to express my sincere gratitude to my supervisor Prof. Guo Xiong Wu for his earnest, rigorous and high-standard guidance for my study on hydrodynamics, as well as his great patience in the revision of this thesis. I am deeply impressed by his sincere attitude in research, which will keep influencing me in future. I would also like to thank Ms Ema Muk-Pavic, Dr Kelvin Drake and Dr Rebecca Shipley for the helpful discussions and suggestions.

Arriving at London by myself nearly 4 years ago, I feel so delighted and grateful for every friend I have met and every experience I have had. The PhD study is not merely a research topic. To finish the long journey, continuous collaboration and communication with others are must needed. It is not possible for me to accomplish the study without the wonderful supports from my dear colleagues and friends: Mr Qicheng Meng, Mr Chongwei Zhang, Ms Anne-Charlotte Gaillard, Ms Yajie Li, Ms Jianjian Dong, Dr Zeeshan Riaz, Mr Cheng-che Lin, Mr John Calleya, Mr Pietro Boselli, Mr Daniel Baeriswyl, Mr Jeremy Nahon, Mr Stephan Van Duijvenbode, Ms Lydia Metcalf, Mr Felix Mak, Mr Keith Lau, Mr Peng Wang, Dr Guodong Xu and Dr Baoyu Ni...The kind friendliness and cheerfulness from you all make me enter the research office with a happy smile every day. It means more than I can express, which I will treasure forever. I also appreciate the help from my previous colleagues at Harbin Engineering University, Prof. Aman Zhang, Dr Shili Sun and Dr Shiping Wang and Prof. Xiongliang Yao.

I owe special thanks to the UCLU Women Football Club. As a new player when first joined in 2011, I barely knew how to play nor how to speak fluent English. Our coach Kav and the girls have shown me great patience, support and love throughout my 3 years there, on top of their professionalism and dedication. This is a quite special and valuable experience in my life.

In addition to the precious overseas study opportunity, I feel especially lucky and grateful to have the chance of getting to know about the London Baha'i communities. Those inspirational discussions have made me a better and happier person with calmer and broader mind, for which I am most grateful. I also appreciate very much for the international student club and Frisbee team organised by All Souls Church.

I would like to thank my family for the unconditional support and love as always and my fiancé, Mr Xing Li, who has always been a source of tranquility, encouragement and inspiration to me. I hope I could be the same to you.

This study is sponsored by Lloyd's Register Educational Trust (LRET, which is now Lloyd's Register Foundation, LRF. Lloyd's Register Foundation helps to protect life and property by supporting engineering-related education, public engagement and the application of research.) and China Scholarship Council (CSC), without which the wonderful overseas study experience at UCL would never have been realised. I am also very grateful for the financial support from the CISN hardship fund during my 4th year CRS study.

Deep thanks are given to the examiners of this work, Prof. Longbin Tao from Newcastle University and Prof. Giles Thomas from UCL. They have provided very careful examination of the thesis, along with discussions and suggestions with deep insight and broad views during the viva. These helped a lot in the improvement of the thesis and my understanding of the knowledge.

Nomenclature

➢ Abbreviations

BEM	Boundary element method
C, *S* system	The Cartesian, stretched coordinate system
2D	Two dimensional
3D	Three dimensional
FEM	Finite element method
SWL	The still water level
min	The minimum value
max	The maximum value

➢ Subscripts

f, b, c, ∞, w, a	The free surface, body surface, control surface, infinity, the wave surface and air cavity surface
jet	The thin jet region
main	The main fluid region (exclusive of the thin jet region)
$0_-, 0_+$	The time right before and after the impact

➢ Roman letters

a_n, b_n, c_n, d_n $(n = 0, ..., 4)$	The weight factors for the numerical calculation of the complete elliptic integral
a_i, b_i, c_i, d_i, e_i $(i = 0, ..., N)$	Coefficients in the energy smoothing method
A, *B*	The cavity bottom point before and after fluid immersion, with

	r_B, u_B the r coordinate and radial velocity of point B
$A_n = -\frac{2Ud}{\mu_n^2}\frac{1}{J_1(\mu_n)}$	Coefficient in the Bessel series for the analytical solution of the initial velocity potential for impact by a cylinder liquid column
$A(p)$	Solid angle at the control/field point p
B_{kj}, C_{kj}, D_{kj}, E_{kj}	Coefficients in the algebraic expression for the discrete boundary integral equation (the subscript denotes the contribution from the j-th node over the k-th one, and $B_{kj} = B_1(k, j) + B_2(k, j-1)$)
H, I	Coefficients for the calculation of B_{kj}, C_{kj}, D_{kj}, E_{kj}
$c_{1,2}$	The two threshold coefficients limiting the minimum and maximum grid size of the air cavity ($c_1 < 1, c_2 \geq 1$)
c	Waterline/wetted width
d	Initial radius of the impacting axisymmetric liquid column
e	Euler's number (in Chapter 3), approximately equal to 2.71828; or a variable for the calculation of integral equation in Chapter 2
E_a	The potential energy of the air cavity, defined as $PV/(\gamma-1)$, with E_{a0} as its initial value.
E_c	The energy of a curve (for the energy smoothing method)
E_G	The gravitational potential energy of the water flow
E_{total}	The total energy related to the fluid ($E_a + P_0V + E_G + K = E_{total}$=constant)
f	Free surface elevation/wave profile
f_b	The vertical coordinate on the body surface at the intersection point with the free surface

$f_j(\vec{x})$	Shape function of linear interpolation
F	The force on the plane per unit length
$F(r,z)$, $H(r,z)$	Auxiliary functions satisfying the Laplace equation
F_c	An objective function including the energy of the curve and the difference before and after smoothing
g	Acceleration due to gravity
G	Green's function
$\vec{G}(\vec{x},t)$	A function defined in a domain
h	Still water depth at the wall; or a variable for the calculation of integral equation in Chapter 2
h_d	Water trough depth at the wall
$h_{\max}$	The maximum vertical span (perpendicular to the impact direction) of the air cavity
H_F	The maximum height of the incident wave
$J_n(x)$	The *n*-th order Bessel function
J	The integral point on the thin jet region S_{jet}
k, j	Subscripts corresponding to the control point p and integral point q
$k_{1,2}$	Control factors with regards to the time step
K	The kinetic energy of the water flow, with K_0 the initial value
$K(m), E(m)$	The complete elliptic integral of the first and the second kind

K_{th}	The thickness ratio of an air cavity ($K_{th} = l_{\max} / (0.5 h_{\max})$)
l	Element size; (l_i size of the *i*-th element on the free surface; l_0 the basic element size; l_a elements size on the air cavity; $l_{\min}$ the minimum element length)
$l_{\max}$	The maximum horizontal span (along the impact direction) of the air cavity
L	The length of the computation domain $\varepsilon \in [0, L]$ in the stretched coordinate system, or *S* system
m	The mass of the plane per unit length in Chapter 1; or a variable in for calculation of integral equation in Chapter 2
$\vec{n} = (n_x, n_y, n_z)$	The normal unit vector of the fluid boundary pointing out of the fluid domain
n_1, n_2	The intersection point of the free surface with the body and the control surface (n_0 specifies that of the cavity surface and the body surface)
N	The number of elements on the fluid boundary (N_f the element number on the free surface; N_a that on the air cavity; N_w that on the outer wave surface next to the cavity)
P	Pressure
$P_{a,}\ P_0$	The atmospheric pressure and its nondimensional value ($P_0 = P_a / \rho U^2$ in Chapters 3 & 4, and $P_0 = P_a / \rho g h$ in Chapter 5). They are also the initial air pressure of the entrapped cavity.
$P_{\max}$	The maximum pressure inside the air cavity at the end of its first compression stage
p, q	The control/field point and the integral/source point

Q_i, P_i	A set of nodes before and after smoothing (with q_i and p_i denoting a coordinate of them)
$\vec{r}$	The position vector of (x, y, z), (x, y) or (r, z)
(r, θ, z)	Cylindrical coordinate system (or $o-r\theta z$)
r_0	The r coordinate of the initial centre of spherical air cavity (r_0, z_0)
R	Initial radius of the entrapped spherical air cavity
R_b	Initial radius of the 2D air circle in contact with the body surface
$R(t)$	The radius of a deforming cavity in a circular shape
s	The stretching ratio; $s_0 = s(t_0)$ is the stretching ratio at the initial time step $t = t_0$
$S_{(f,b,c,\infty,w,a)}$	Fluid boundary (of free surface, body surface, control surface, the far end, the wave surface and the cavity surface)
$S_{outside}$	A closed fluid boundary including the outer free surface and the impacting body surface.
S_{main}, S_{jet}	Boundaries of the main fluid domain and the thin jet region
S'_{jet}	Fluid boundary along one side of the jet surface, or a control surface amid its two sides.
t	Time
t_0	The short instant during which the wave crest is assumed to 'impact into' the wall
U	Constant relative impact velocity, or the horizontal velocity
u_0	The uniform velocity of the incoming flow at infinity

u_n	The normal component of the velocity of a point on the fluid boundary, and is positive pointing outward according to the definition of $\vec{n}$
v	The velocity magnitude (v_i the velocity of the *i*-th node)
V, V_0	Volume of the air cavity (specified as V_a in the deduction on he energy transfer relation in 4.4) and its initial value
$V_{\min}$	The minimum volume of the compressed air cavity
$V_{outside}$	The total volume of the fluid and entrapped air cavity,
$w(z)$	The complex velocity potential
w_i	The weight factors for Gaussian integrations
$W(t)$, W_0, W	Vertical entry velocity as a function of time, at the initial time and as a constant (in Chapter 1)
W	The work done by the air (including the inner air cavity and the outside atmosphere) toward the liquid flow
W_a	The work done by the entrapped air cavity to the surrounding liquid
(x, y)	2D Cartesian coordinate system (or $o-xy$)
x_0	The distance between the initial wave centre and the wall
x_i	The abscissas factors for Gaussian integrations
Y	A function defined based on linear distribution within an element
$z = x + iy$	The complex variable in *z*-plane
z_0	The *z* coordinate of the initial centre of spherical air cavity (r_0, z_0)

- **Greek letters**

β	Deadrise angle
χ	Auxiliary function
δ	The increment value
$\delta E_G = E_G - E_{G0}$	The increment in the gravitational potential energy of the water flow (at the end of the initial compression stage of the air cavity)
$\delta K = K - K_0$	The increment in the kinetic energy of the water flow (at the end of the initial compression stage of the air cavity)
$-(\delta K + \delta E_G)$	the change (or the loss) in the mechanical energy of the surrounding liquid (nondimensional)
δt	The time marching step (δt_1 without air cavity; δt_2 time step considering the effect of the air cavity)
δ_{AB}	The critical angle between the merging fluid boundary *AB* and the central axis
$\delta_{mn} = \begin{cases} 0, m \neq n \\ 1, m = n \end{cases}$	Kronecker delta function
(ε, η)	A local coordinate system in 2.2.1, or the stretched coordinate system in the rest part (or $o-\varepsilon\eta$; $\varepsilon = x/s, \eta = y/s$)
ϕ	Velocity potential (in the Cartesian coordinate system, ϕ_{ana} and ϕ_{num} mean the analytical and numerical results respectively)
$\phi_t = \frac{\partial \phi}{\partial t}$	The partial derivative of ϕ with respect to time *t*. ($\phi_r = \frac{\partial \phi}{\partial r}, \phi_z = \frac{\partial \phi}{\partial z}$ and so on.)
φ	Velocity potential (in the stretched coordinate system)

γ	Specific heat ratio of the air (taken as 1.4)
κ	The smoothness factor in the energy smooth method, set as $\kappa = Cl_{\min}^3 (C = 5 \sim 10)$
λ	Increasing ratio of element size away from the impact surface $(1 < \lambda < 1.01)$
$\lambda_n = \frac{\mu_n}{d}$	Coefficient in the Bessel series for the analytical solution of the initial velocity potential for impact by a cylinder liquid column
$\mu_m^{(v)}$	The m-th zero of vth-order Bessel function $J_v(x)$
μ_n	The n-th root of $J_0(x) = 0$ (could also be written as $\mu_n^{(0)}$)
ν	The kinematic viscosity of the water
θ	Azimuth in the cylindrical coordinate system
θ_0	The threshold value of the jet tip angle
ρ	Density of the water
σ_0	The initial solid angle corresponding to a segment on a circular cavity
$\vec{\tau}$	the tangential unit vector
ς_i	The difference factor in the energy smooth method (set as a unit value)
$\varsigma(r,t)$	Free surface profile of the impacting liquid column
∞	The infinite
Ω	Fluid domain
Δh	Water elevation (above the still water level) at infinity

∇	Gradient operator
∇^2	Laplace equation operator
Π	The pressure impulse

Contents

A list of tables

A list of figures

Chapter 1

1.1 Introduction

With 71% of the Earth's surface being covered by oceans, engineers and naval architects have built numerous types of maritime structures to perform various functions near shore and at sea. Examples include breakwaters and jetties for shore protection, quaywalls and seawalls for ports, harbours and sea-farming, ships for transport, Marine Renewable Energy (MRE) devices, platforms and rigs for resource exploitation. Quite different from structures on land, maritime structures are subjected to hostile actions from strong winds, tidal currents, waves and even tsunami. Among all the environmental conditions, fluid/structure impact is one of the most frequent and fiercest, and thus a very important loading process which needs to be considered in the structure design and construction. Ship launching or seaplane alighting into water, green water on deck, ship slamming and wave impact on offshore and coastal structures are some typical examples. Severe hazard can be posed by violent attack from the seawater, especially during a storm. Great damage or complete destruction can be caused to marine structures, threatening the safety of life and property at sea. In fact, in maritime catastrophes, apart from collisions with reefs, icebergs and other vessels, savage attack from rough waves and water slaps at heavy sea has become one of the main threats to the loss of life and property (see 'List of maritime disasters', Wikipedia). Enormous damage caused by sea storms has been reported almost every year in UK (see Figure 1.1).

(a) (b)

(c) (d)

Figure 1.1. Wave attack during storms. (a) waves hitting the Devon town of Dawlish in 2004 (http://www.telegraph.co.uk/topics/weather/10404746/Storm-warning-hurricane-strength-wind-alerts-extended-to-Midlands.html); (b) Intense waves battered the railway track in Dawlish causing it to collapse in storm 'Charlie' in 2014 (http://travel.aol.co.uk/2014/02/07/uk-weather-storm-charlie-rain-floods-hit-britain/); (c) Hercules' giant waves breaking at Mullaghmore off the Irish coast in 2014 (http://www.independent.co.uk/news/uk/home-news/arrival-of-us-storm-hercules-brings-in-worlds-big-wave-surfers-as-uk-adds-up-cost-of-gales-to-coast-9043711.html0); (d) water shipping on deck at heavy sea (http://coseenow.net/ross-sea/2011/02/one-minute-forty-seconds-in-the-engine-room/).

The author herself, growing up in a traditional fishing village in east China, witnessed the fierceness of the sea storm annually. The brick-wall of a gas station on the beach was always smashed into big holes at the toe, though different designs of support structure were tried each time during the reconstruction; an old fisherman was tragically pulled into the sea some 20 years ago, when trying to tow his dinghy onshore amid storm; a middle-aged diver hired to fix a smashed bottom of a farming seawall never came back last year, only found to be stuck in the breach later; not to mention the tremendous splash of several meters high up the quaywall and the thundering boom generated.

One would wonder where the catastrophic damage comes from, or how the fluid/structure impact at sea generates such high loads. The question itself magnifies the significance of a comprehensive understanding on the impact dynamics and the necessity to identify critical situations, which are essential in the design of reliable offshore and coastal structures and are a main research topic of the present work. Researchers in marine engineering and naval architecture have been undertaking studies on fluid/structure impact since early last century, initially in the need of predicting the water loads on a seaplane during its landing process (Von Karman 1929). It was soon noticed that, apart from the direct impact by the liquid, air cavity trapped during plunging wave impact on a wall is in high correlation with more severe loading conditions (e.g. Bagnold 1939). This has been further observed and

investigated in a lot more laboratory and field experiments, which will be reviewed later. Actually, for most practical fluid/structure impacts in the marine context, an air cavity/pocket is likely to be present near the impact surface due to the fact that (i) the front surface of the liquid seldom matches completely with that of the structure upon impact; (ii) the strong nonlinearity of the free surface can lead to large distorted motion, and an air cavity will be trapped following the initial impact stage. Current work will focus on fluid/structure impact with the entrapment of a single air cavity. Not only the direct impact between water and structure will be studied, but also the characteristics of the body/water/air interaction and the acting mechanism of the air cavity will be looked into.

By now extensive studies have been carried out for various problems of fluid/structure impact, due to water entry, wave-body interaction, wave impact, and sloshing, etc. Strong nonlinearity of the free surface during the impact has posed great impediment in the theoretical study. This is further complicated by the complexity of the process of the free surface motion, including wave breaking, the entrapment of air, water separation from the structure, the formation of jet or a thin film of water, and splashing, etc. Developing methodologies to simulate fluid/structure impact with air cavity effect and techniques to tackle some difficult numerical challenges is also an important aspect of the current work.

Numerical schemes are proposed for the calculation of fluid/structure impact with a long and thin jet, based on a decoupled shallow water theory approximation and a dipole distribution approximation respectively. The former is successfully applied to the problems studied in this work. The shallow water approximation for the thin jet region is extended to axisymmetric cases from the previous work on 2D cases. For axisymmetric impact situations with air cavity, numerical techniques are developed to simulate the impingement and possible fluid immersion of the radial cavity jet along the structure surface. For the problem of overturning wave impact on a wall entrapping an air cavity, originality is claimed for a new domain decomposition method developed based on a coupled dual-system technique, with a stretched coordinate system for the local impact region and the Cartesian coordinate system for the main fluid domain. It resolves the numerical difficulty caused by impact starting from one point by an arbitrary wave crest, and enables a study of higher accuracy for both the direct impact and the following structure/water/air interaction

process. Those methods and techniques developed have broad application in the study of general fluid/structure impact problems.

1.2 Literature Review

A literature review will be given below, outlining the main progress in the theoretical study on the direct impact between water and structure, and the previous work considering the air cavity effect. Given the broadness of the subject, the discussion on direct fluid/structure impact shall be confined to abrupt impact over a short time with large relative velocity where the liquid, whose motion is characterized by strong nonlinearity, is rationally assumed to be inviscid and incompressible.

1.2.1 Fluid/structure impact (without air cavity)

In the marine context, previous studies conducted without consideration of the effect of air entrapment during fluid/structure impact involve in most cases the presence of at least one convex/pointed shape in the impinging front surfaces. A typical model in theoretical study is the water entry of bodies with wedge, quasi-wedge or round shaped bottom. Such two dimensional (2D) models can be applied to the study of ship/seaplane launching, bow-flare and bottom slamming, etc. In particular, the development of methods such as strip theory (Salvesen et al. 1970) and 2D+t theory (Fontaine & Tulin 2001) efficiently extends their application into the practical prediction of wave generation and wave-induced loads of high-speed planing vessels. Thus the accuracy of the 2D results has great significance for engineering applications, for which continuous effort has been made. Impact on a structure by a liquid column staring from one contact point/line, and the 'flip-through' phenomenon occurring when an incident wave approaches a wall in shallow water generating high pressure without direct impact are also discussed in this section.

(i) Wedge entry into initially calm water

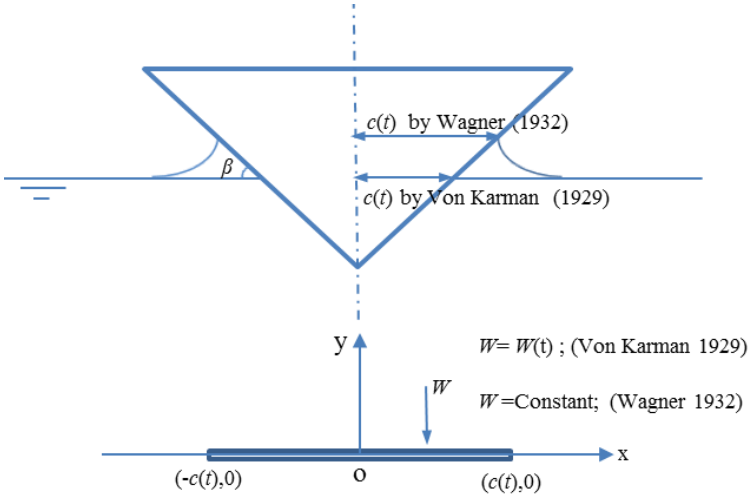

Figure 1.2 Wedge entry models by Von Karman (1929) and Wagner (1932)

The classical problem of wedge entry into initially calm water was first theoretically studied by Von Karman (1929), for the prediction of impact load on a landing seaplane. The seaplane was idealized as a horizontal cylinder with a wedge shaped under surface with deadrise angle β (i.e. the angle between the body surface and the undisturbed free surface), entering the calm water with a velocity changing from W_0 to $W(t)$ (see Figure 1.2). The free surface elevation was neglected, and thus the x coordinate of the interaction point of the body with the free surface $c(t)$ is related to the entry speed through $W(t)=\frac{dc}{dt}\tan\beta$. The virtual inertia/added mass of the body was approximated by an equivalent flat plate of the same waterline width $2c$ moving in unbounded water (of density ρ), which is $\frac{1}{2}\rho\pi c^2$. Thus the force by Newton's second law $F=m\frac{dW}{dt}$ (m the mass of the plane per unit length) can be obtained from the momentum conservation law $mW_0=mW(t)+\frac{1}{2}\rho\pi c^2 W(t)$, as

$$F=\frac{\rho W_0^2\pi c\cot\beta}{(1+\rho\pi c^2/2m)^3} \tag{1.1}$$

where W_0 is the initial speed of the body at t=0 and $c\big|_{t=0}=0$. Therefore the approximated average pressure is

$$P=F/2c=\frac{\rho W_0^2}{2}\frac{\pi\cot\beta}{(1+\rho\pi c^2/2m)^3} \tag{1.2}$$

The maximum pressure is supposed to happen when the vertex first touches the water (i.e. $c=0$), as

$$P_{\max}=\frac{\rho W_0^2}{2}\pi\cot\beta \tag{1.3}$$

This method provides early quantitative analysis on impact load for practical problems, while the neglect of free surface elevation can cause the underestimation of the size of the wetted surface and the impact load for small deadrise angles. Wagner (1932) refined Von Karman's (1929) model and modified the wetted width c by taking into account the free surface elevation irrespective of the spay area. The impact flow was approximated by that of an expanding flat plate moving in a direction perpendicular to its surface with the entering velocity W. The complex potential w can be solved analytically from a conformal mapping method (see Newman 1977, p.122), as

$$w(z)=iW\sqrt{(z^2-c^2)} \tag{1.4}$$

where $z=x+iy$ is the complex variable and the velocity potential is $\phi=\mathrm{Re}(w)$. The coordinate system related to the plate is defined in Figure 1.2. The linear free surface boundary condition is $f_t=\phi_y$. This gives the free surface elevation

$$f=\int_0^t\phi_y dt=\int_0^t\frac{Wx}{\sqrt{x^2-c^2}}dt \tag{1.5}$$

It is equal to the vertical coordinate on the body surface at the intersection point, which is $f_b(x)=x\tan\beta$ for the wedge. Let

$$f_b(x)=\int_0^x\frac{x}{\sqrt{x^2-c(t)^2}}W\frac{dt}{dc}dc \tag{1.6}$$

where W is a constant value. The expanding velocity of the flat plate/wet surface can then be obtained as $\frac{dc}{dt}=\frac{\pi}{2}W\cot\beta$, and the free surface elevation becomes $f=\frac{2}{\pi}x\tan\beta\arcsin(\frac{c}{x})$. The pressure distribution can then be obtained from the Bernoulli equation, as

$$P(x)=\frac{1}{2}\rho W^2\left[-\frac{\pi\cot\beta}{\sqrt{1-x^2/c^2}}-\frac{2\dot{W}}{W^2}\sqrt{c^2-x^2}-\frac{x^2/c^2}{1-x^2/c^2}\right] \tag{1.7}$$

In early cases where this theory has been used, the product term in the Bernoulli equation was ignored to solve the fully linearized problem (e.g. Maceie 1962). The integration of pressure from $-c$ to c then gives the force on the body. Wagner's (1932) model was proved to give good prediction of peak impact pressure of a wedge with small deadrise angles between around 3^o and 15^o in the experiment by Takemoto (1984). The disagreement of the impact pressure between the experimental data and the theoretical value for small deadrise angles is related to the limitation of flat plate approximation, as well as the possible air-cushioning effect for small deadrise angles. Later Wagner's method, frequently referred to as the expanding flat plate approximation, was widely applied in the framework of matched asymptotic expansions for general body geometries of $\eta_b(x)$ with small deadrise angles (or blunt bodies), where different solutions of $\frac{dt}{dc}$ were gained accordingly (e.g. Cointe & Armand 1987, Korobkin & Pukhnachov 1988, Howison et al. 1991).

For wedge entry at a constant vertical velocity W, when the gravity effect can be neglected in the early stage due to high-speed and short-period impact, the 2D irrotational flow is self-similar as there is no length scale. Its hydrodynamic characteristics depend only on the dimensionless parameters x/Wt and y/Wt, and not on x, y, t individually. Based on Wagner's (1932) function, Dobrovol'skaya (1969) employed a self-similar method to solve this problem with fully nonlinear free surface boundary conditions. The complex potential problem was reduced to a nonlinear singular integral equation, which was solved by a method of successive approximations. With the development of numerical methods in the free surface flow problem, for the same entry problem, Zhao & Faltinsen (1993) solved the nonlinear equation numerically with a boundary element method and a time-marching scheme. By now this method has become one of the main techniques for solving potential flow in fluid dynamics. Constant line segments were adopted in their numerical calculation. A jet flow was defined after impact and cut perpendicularly to resolve the difficulty near the three-phase intersection. Kihara (2004) further modified the jet-cutting model by introducing a new intersection point according to a threshold

value of the inclination angle between the free surface and the body. This allows for a better description of the jet flow including its overturning up to re-entry into the underlying free surface. Sun & Faltinsen (2007) employed these techniques in a 2D+t theory to study the steady performance of a planing vessel at a moderate speed. Wagner's (1932) approximation was used for the initial solution upon impact. The gravity effect was considered and a plunging jet separated from the prism-shaped body was simulated.

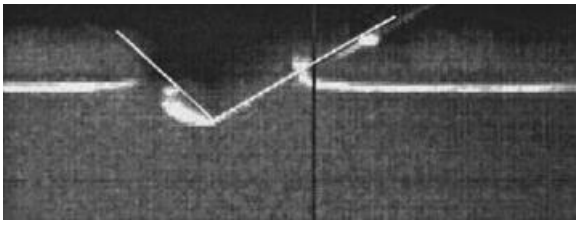

Figure 1.3. Snapshot of flow ventilation in oblique impact of asymmetric wedge (Judge et al. 2004)

Built upon the extensive work on symmetric entry, the vertical or oblique entry of an asymmetric body has also been studied widely. Toyama (1993) extended Wagner's model into the vertical entry problem of asymmetric bodies at a constant speed. With the vertical coordinates of the intersection points, f_b, different on the two sides of the wedge surface, two continuum equations (similar to Eq. (1.6)) were established and combined to give the solution. The accuracy of this model is confined by the applicability of the flat plate approximation. Semenov & Iafrati (2006) studied the same problem semi-analytically with a self-similar method, which was proved of good accuracy later in the fully nonlinear numerical simulation by Xu et al. (2008). The oblique water entry of an asymmetric wedge was studied experimentally by Judge et al. (2004). A flow detachment phenomenon or "ventilation" was observed near the wedge vertex when the geometric or kinematic asymmetry (the latter defined by the ratio between the horizontal and vertical velocities) increases to a certain degree. An air pocket was found to be formed at the side with bigger deadrise angle, or the 'stern' side. A snapshot from the experiment is shown in Figure 1.3. Later in the fully nonlinear numerical study on the oblique entry of an asymmetric wedge (Xu et al. 2008), a negative pressure was found near the wedge vertex, revealing the possibility that air may be sucked during the initial impact stage. Moore et al. (2013) gave similar conclusions in their analytical study on the oblique

impact of a wedge and a parabola with Wagner's (1932) method. However, the observed "ventilation" phenomenon is yet too complex to be included in rigorous analytical or numerical study.

Water entry in real situations mostly occurs through free fall motion. The main difficulty lies in the coupling of body motion and fluid flow, both of which are unknown. Wu et al. (2004) introduced an auxiliary function to decouple the mutual dependence between the body acceleration and the fluid motion, and successfully solved this problem. Another key technique is the stretched coordinate system, which successfully tackled the rapidly changing physical parameters near the wedge vertex during the initial impact process and is further employed in many related studies for fluid/structure impact starting from one contact point. An analytical solution for the local thin jet area was applied based on a shallow water approximation for the 2D flow, which improved the accuracy while keeping the efficiency.

(ii) Impact by liquid wedge/droplet starting with a single contact point

Local impact by a liquid column of various shapes on a structure was frequently studied as a simplified model for wave impact on marine structures (e.g. sea defences, ship deck, the wet deck of a catamaran, platform and columns), as well as landing of lifeboats onto steep waves. In those models, the direct impact between water and the structure was focused, without considering the effect of the entrapped air cavity in some situations of plunging wave impact or the entrained air in a broken wave.

The theoretical study on fluid impact problems can also be traced back to early last century, when the erosion of propellers was observed and found to be caused by high velocity jet impact in cavitation (Cook 1928). With the development of self-similar method, Cumberbatch (1960) solved the problem of impact by a liquid wedge on a solid wall approximately. Zhang et al. (1996) extended the self-similar solution to an asymmetric liquid wedge impacting a wall vertically with a constant velocity. The fully nonlinear boundary conditions on the free surface were imposed, however an approximation for the free surface profile based on an exponential function was used. It was found not sufficiently accurate by Duan et al. (2009), who solved the same problem numerically without any approximation on the free surface by the employment of the stretched coordinate system (Wu et al. 2004). With the same

technique Wu (2007a, 2007b) successfully simulated the impact by a 2D curved liquid droplet on a rigid plate and on a solid wedge with fully nonlinear free surface conditions. Duan et al. (2009) studied the oblique liquid wedge strike on a wedge-shaped structure, as an idealized model for wave crest impact on a sea defence. Two of the above mentioned liquid impact models are shown Figure 1.4. These models were all based on the assumption of constant and uniform impact velocity, as well as known far-field values, yet the numerical techniques developed laid a good foundation for the study on wave impact in more general and practical engineering situations.

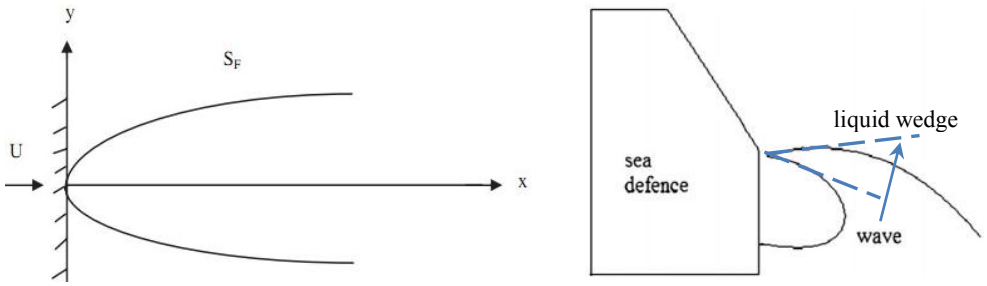

Figure 1.4 Sketches of two liquid impact models: (a) impact by a water droplet on a rigid plate (Wu 2007a); (b) oblique liquid wedge impact on a solid wedge (Duan et al. 2009).

(iii) 'flip-through' of steep waves approaching a wall in shoaling water and the pressure-impulse theory

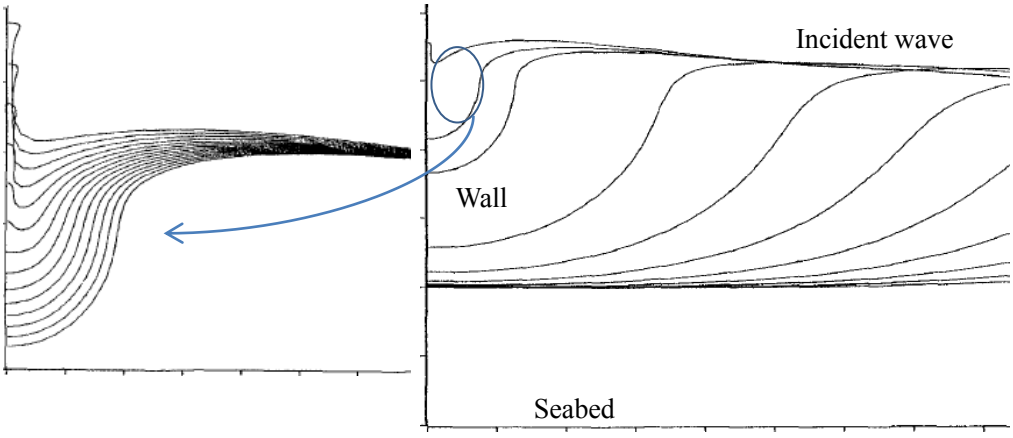

Figure 1.5 Free surface evolution in a flip-through computed by Cooker & Peregrine (1990c)

Apart from the conventional direct impact, there is another intense fluid/structure interaction type. According to the numerical simulation by Cooker & Peregrine

(1990c), when an overturning wave approaches a vertical wall in shoaling water under certain conditions, the direct impact by the wave front can fail to happen as the intersection point of the free surface with the wall moves up with very large speed and acceleration, and a very thin jet is formed on the wall. The peak pressure lies just below the up-turning free surface on the wall, which was around $50-60\rho gh$ (h the still water depth) for the severest conditions computed. An example of the numerical simulation is shown in Figure 1.5. To distinguish from the traditional direct impact, such type of wall/wave interaction was named 'flip-through' by Cooker & Peregrine (1990c).

Typical phenomenon of 'flip-through' was further identified and investigated in many experimental studies, characterized by a concave free face focusing towards one point on the wall with the wave crest moving forward and the trough rapidly rising along the wall with upward accelerations up to 100-1000g (exceeding 1500g measured by Lugni et al. (2006) in a sloshing tank of 0.1m wide and 1m long with water height 0.125m). In a wave flume of 0.3m wide and 20m long (still water depth $h=0.05\text{m}$ at the wall and 0.38m at the wave paddle), Hattori et al. (1994) measured the peak pressure of a flip-through around $9.3\rho gH_F$ at the still water level (SWL), where H_F is the maximum height of the incident wave above the wave trough depth h_d at the wall before impact. This is roughly equal to $40\,\rho gh_d$.

Experiments on wave impacts by Bagnold (1939) and Nagai (1960) have shown that the severest impacts occurred when an incident wave hit the wall with a nearly vertical face/wave front and subsequently reached a great height. Cooker & Peregrine (1990c) attributed this to a violent flip-through motion. Yet the experiment by Hattori et al. (1994) has shown that the highest peak pressure in their experiments occurred when a nearly vertical wave collided with the vertical wall with small amount of air trapped. Here it should be noted that discussions on the severest wave impact situation in most the experimental studies were based on observations from different conditions of wave collision (wave shapes, air entrapment, etc.) in a given experimental set-up, rather than a strict parametric study. As a result, different and even controversial conclusions could be derived from different experiments. For instance, flip-through was not noted by Hull & Müller (2002). Their experiment was conducted in a wave tank of 0.35m wide and 17m long, with still water depth at the

wall $h = 0.1\text{m}$ and 1m at the wave paddle, which is much deeper than that in Hattori et al. (1994). Consequently, only normal slosh up of the water along the wall was observed, generating a single pressure peak at a point near the SWL rather than the fast rising pressure peak below the shooting jet as in a flip-through.

Given the short-lived impulsive pressure generated in a flip-through and a direct impact between fluid/structure at large speed (e.g. the case of a vertical wave front striking on a wall), based on the pressure impulse defined by Batchelor (1967, p. 471) $\Pi = \int_{t_{0_-}}^{t_{0_+}} P dt$, Cooker & Peregrine (1990a, 1990b, 1995) developed a simple analytical model to solve the pressure impulse over the instant flip-through or impact process. Applying a time integral on the *NS* equation over the short impact period from t_{0_-} to t_{0_+}, one can obtain $\vec{u}_{0_+} - \vec{u}_{0_-} = -\frac{\nabla \Pi}{\rho}$ since the nonlinear term and the viscosity term become zero after the integration when $t_{0_+} - t_{0_-} = 0$. By substituting it in the continuity equation for the incompressible liquid, Π can be found to satisfy the Laplace equation. An idealized wave model was established in a semi-infinite rectangular shape, where the fluid next to the wall was divided into two regions: the upper impact region with a constant approaching velocity corresponding to the vertical height of the striking wave, and the lower part in contact with the wall. The boundary conditions for Π can then be obtained, which can be solved analytically. The peak pressure was approximated by $P_{\max} = \frac{2\Pi}{t_{0_+} - t_{0_-}}$. Wu (1991) extended this model to further consider the effect of fluid compressibility. A pressure impulse was defined as a function of time as $\Pi(t) = \int_0^t P dt, (t_{0_-} < t < t_{0_+})$, for which analytical solution was deduced from the obtained wave equation. Thus the peak pressure as well as the impact pressure history can be calculated through its differentiation with respect to time.

1.2.2 Fluid/structure impact with air cavity effect

When more complete overturning of the wave happens, direct impact by a plunging wave could happen entrapping an air cavity on the impact surface. Such impact entrapping an air cavity could also happen when water exceeds the freeboard of a ship or the maximum height of a coastal structure. A discussion on different wave

impact models based on previous experimental studies will be made first, focusing on the effect of the entrapped air cavity and the theoretical models developed.

In addition to the single air cavity entrapped by an overturning wave, air could be entrained in the water as a large number of small bubbles (or bubbly flow), normally following violent wave breaking events. The effect of body surface geometry is another cause to the enclosing of an air cavity. Apart from air-cushioning effect for blunt body entry (e.g. for wedge with deadrise angle below 3^{o}), fluid impact on a structure with the geometry of a hollow or depression on the impact side, such as the water entry of a catamaran, will also cause air entrapment. Previous studies on them are also reviewed briefly in this section.

- **Experimental studies on breaking wave impact and the classification**

An early and typical study on breaking wave impact was undertaken by Bagnold (1939). Different breaking wave modes were categorized, and the one of interest here is the 'full break on the wall'. Three possible situations are given in Figure 1.6 according to the timing of the wave crest collapse and its impact on the wall: (a) wave crest strikes the wall with a thin air cavity well above the SWL, reckoned to be the severest impact condition observed. Phenomenon similar to the 'flip-through' (Cooker & Peregrine 1990c) was also observed, when the intersection of the free surface on the wall shoots upward fast before the wave crest arrives at the wall and no impact or air entrapment occurred, followed by much smaller noise; though it was not named back then; (b) plunging wave crest strikes the wall before it falls entrapping air cavity larger and lower than that in case (a). A low booming sound along with the formation of much spray was recorded for this case; (c) wave breaks before reaching the wall.

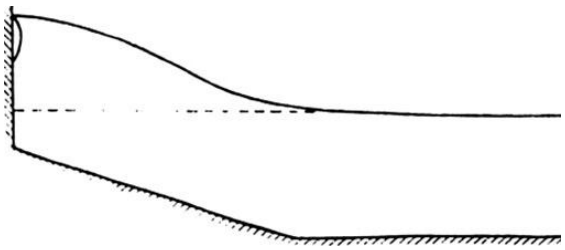

(a) wave crest strikes with thin air cavity above the rising waterline: the condition for the severest impact pressure and noise recorded

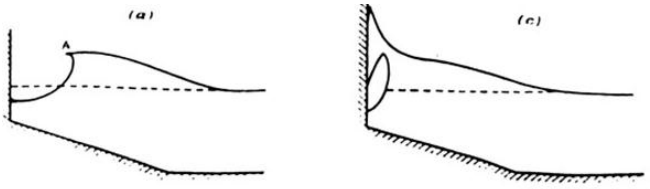

(b) wave crest strikes the wall later before it falls with air cavity enclosed lower

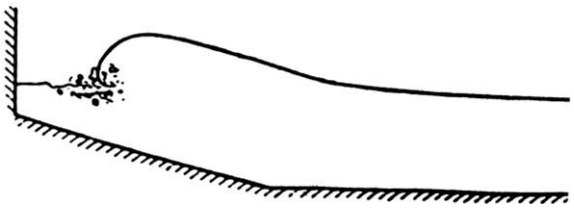

(c) wave breaks before reaching the wall

Figure 1.6 Models of wave breaking against a wall (Bagnold 1939)

After decades of experimental and theoretical studies on breaking wave impact, based on simultaneously recorded pressure distribution and wave evolution, Hattori et al. (1994) further characterized the impact by a shallow water breaking wave on a vertical wall into four modes: (i) flip-through (without/with air entrapment); (ii) collision by nearly vertical wave front with small amount of air trapped due to the curvature in the shape of wave front; (iii) impact by a plunging wave with a thin air cavity; (iv) impact by fully developed plunging wave with a thick air cavity.

It should be noted that flip-through with air entrapment was also recorded in case (i). It happens when the wave crest touches the wall before the fast rising jet arrives at the impact point, and is distinguished from the overturning wave impact with air cavity in cases (iii) & (iv) by the fast rising jet as that in a flip-through. As a result, air cavity of relatively small vertical span will be formed well above the SWL near the outer wave surface. Much larger pressure peak ($28\,\rho g H_F$, i.e.$77\,\rho g h_d$) lasting shorter than that in a pure flip-though ($9.3\rho g H_F$, i.e.$40\,\rho g h_d$) was recorded. The criteria for flip-through without air entrapment were summerised based on experimental recordings. Consequently, the case (a) in Bagnold (1939) (see Figure 1.6(a)), could be inferred from its description to be similar to the case of flip-through with air entrapment here, changing towards case (ii).

The nearly vertical wave front striking in case (ii) could be regarded as a transition between a flip-through inducing fast rising jet in case (i) and a plunging wave crest trapping visible air cavity in cases (iii) and (iv). Here the thickness of the cavity in

(iii) and (iv) could be defined by the ratio between the maximum horizontal span ($l_{\max}$) and half the maximum vertical span ($0.5h_{\max}$) of the cavity K_{th} (>1 for thick cavities and <1 for thin ones), as illustrated in the snapshots shown in Figure 1.7. If the wave crest develops so fully that it touches the free surface ahead before approaching the wall, then a flow of turbulent bore generating small air bubbles will be formed, which is similar to the case (c) in Figure 1.6.

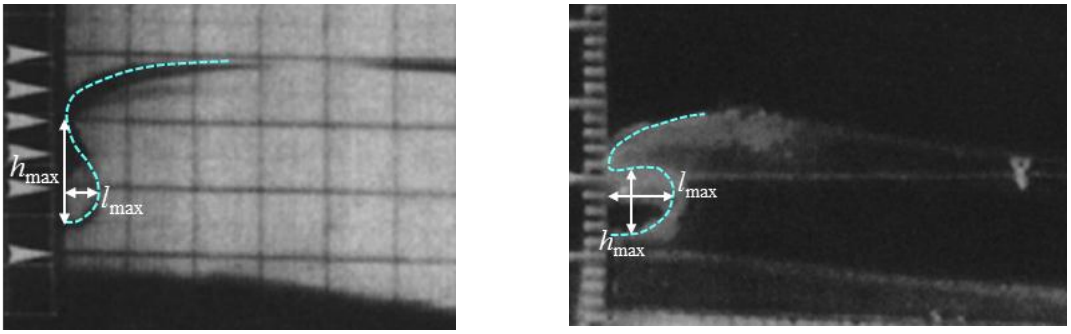

(a) $K_{th} = l_{\max} / (0.5h_{\max}) < 1$ (b) $K_{th} = l_{\max} / (0.5h_{\max}) > 1$

Figure 1.7. Snapshots of breaking wave impact on a wall with (a) a thin and (b) a thick air cavity (Hattori et al. 1994)

Though different conclusions have been made on the severest impact situations in different experimental set-ups as mentioned above, the small amount of air trapped (sometimes too little to form a visible air cavity) by the curvature in the wave front shape was found to play a crucial role in the generation of much severer impact situations than other conditions in many experiments (Bagnold 1939, Nagai 1960, Oumeraci et al. 1993, Hattori et al. 1994, Lugni 2006, etc.). While in Hull & Müller (2002), the maximum loading pressure was found to occur for plunging breaker entrapping a large air cavity on the wall around SWL. Given the absence of strong 'flip-through' in their experiments as mentioned in section 1.2.1 and the relatively slim plunging wave crest (large in curvature and small in width) generated, we can infer that the different observation is due to the different experimental set-up (esp. the water depth). In spite of the controversy, the notable outcome of the entrapment of air cavity was found to be the fast pressure oscillation accompanied, with bigger pressure peak and higher frequency for thinner/smaller air cavities and lower peak and longer period for thicker/bigger ones. However, the oscillation amplitude of pressure could damp much faster for a thinner air cavity. The adiabatic process of the

air pocket was suggested to play an important role, while the detailed characteristic and acting mechanism demand further theoretical study.

- **Theoretical models for wave impact with entrapped air cavity**

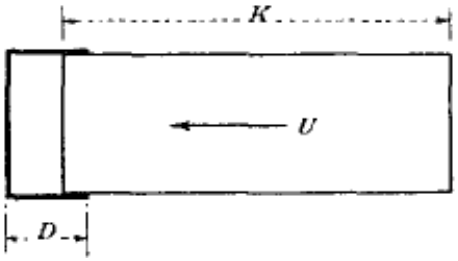

(a) Piston model (Bagnold 1939)

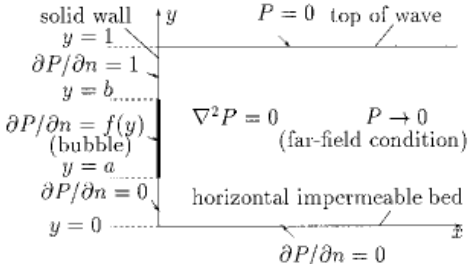

(b) Pressure-impulse model (Wood et al. 2000)

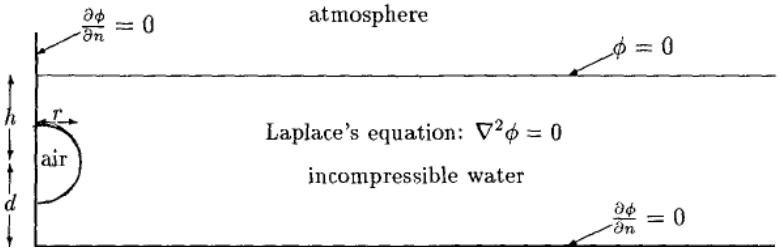

(c) Free oscillation model (Topliss et al. 1992)

Figure 1.8 Some analytical models for wave impact with entrapped air cavity

Based on the large volume of experimental observations, various simplified 2D analytical models have been established by researchers to qualitatively analyse the air cavity effect in a fluid/structure impact, as shown in Figure 1.8. For the impulsive pressure generated by breaking wave with a thin air cavity as shown in Figure 1.6(a), a simplified piston model was set up by Bagnold (1939) (see Figure 1.8(a)). The oncoming impact fluid was represented by a solid rectangular with virtual inertia (i.e. added mass) estimated from experimental data, which was supposed to compress the air adiabatically as a heavy free one-dimensional piston. Then the maximum pressure could be estimated by Newton's second law. At the same time, the total value of pressure impulse on the wall was found to stay independent of impact types, which is not difficult to be verified from the momentum law. Breaking wave impact with a larger air pocket enclosed on the impact surface under the waterline, as shown in Figure 1.6(b), which was found to involve a relatively longer period of pressure oscillation, was not able to be analysed for the lack of mathematical model then.

Wood et al. (2000) extended the pressure-impulse theory of Cooker & Peregrine (1990 a & b, 1992, 1995) on the direct wave impact to include a rebounding trapped air cavity in the simplified 2D model, as shown in Figure 1.8(b). The velocity of the impact wave was still assumed to be uniform, while the expansion of the compressed air cavity was approximated by an additional 'bounce back' condition, represented by a reversed-direction speed for a position corresponding to the vertical span of the air cavity on the wall. Then the pressure impulse can be solved analytically in the rectangular model. A considerable increase in the peak pressure impulse was gained near the cavity compared to that without air rebounding condition. Nevertheless, it should be noted that, the assumption of pressure-impulse theory only applies to impact over very short duration over which the integration of the nonlinear term in Euler equation can be ignored. This might explain the reason why the model was found applicable only for some cases where the depth of the trapped cavity was less than half the impact water height. Beyond it a larger air cavity is more likely to be trapped by a more developed overturning wave which takes longer time to rebound/expand.

The frequency of free oscillation of a 2D air cavity in a semi-circular shape, trapped between a vertical wall and incompressible rectangular flow along the seabed, was solved analytically by Topliss et al. (1992) (see Figure 1.8(c)). The main flow and the free surface elevation were ignored. The Laplace equation was solved analytically with a method of images. The results revealed higher frequency for air pockets smaller in size and closer to the free surface, and were found to agree particularly well with experimentally recorded pressure oscillation frequency for relatively large air cavities, which is more similar to free oscillation in reality.

Those theoretical models shed light on some aspects of the acting mechanism of the entrapped air cavity in a wave impact. To enable an analytical solution, the free surface elevation (the wave shape), the deformation and pressure change of the trapped bubble, and the initial forcing from a real impact situation were not considered. In addition, the employment of those models normally requires information that is not directly available from an experiment. A more advanced and accurate theoretical method is the numerical simulation on the impact process. Boundary Element Method (BEM) applied in the context of fully nonlinear potential theory has shown very high accuracy and efficiency in the description of free surface

transformation problems (e.g. Dommermuth et al. 1988; Grilli et al. 1994; Grilli et al. 1997), including wave propagation, steepening and overturning. However, these numerical simulations were usually interrupted when the overturning wave hit the main body of the liquid or a structure in its path. One of the difficulties for simulation beyond this point is that to accurately describe the local impact, extremely small elements comparable to the tiny impact zone at the initial stage are needed. To use elements of this size in the entire domain would be wholly impractical. At such moment, either other numerical methods with lower resolution in interface tracking and more computationally intensive (e.g. volume of fluid (VOF)) were adopted/coupled (e.g. Grilli et al. 2001, Lachaume et al. 2003, Rafiee et al. 2013), or certain approximations were implemented to enable the BEM simulation to carry on.

To simulate the interaction with air cavity following an overturning wave impact, Tanizawa & Yue (1992) assumed that when the wave front arrived at the wall, the solid surface was 'invisible' to the liquid. The flow would pass the wall undisturbed for another time step. The simulation for impact then started after that and the area between the two intersection points of the wall with the undisturbed wave was taken as the wetted surface. Therefore the transient process of direct fluid/structure impact was not actually considered. Yet the scaling effect caused by the entrapped air cavity was found, revealing the irrationality of previous experimental studies discussing the air cavity effect in a breaking wave impact without considering the effect of the physical scale. Zhang et al. (1996) improved this model by approximating the initial stages of the wave crest impact through an oblique liquid wedge striking with constant speed perpendicular to the wall. This enabled a similarity solution for the local flow over a short period, during which the free surface was assumed to continue without the wall. Their solution for the wedge impact was then matched with the plunging wave surface after time Δt at a distance Δx away from the wall. The simulation was then carried on with BEM for the post-direct impact process with trapped air cavity. This method provides a rational approximation to the initial direct impact stage, though with certain limitations: (i) The approximation of wave crest by a wedge may be applicable only for some cases of slender plunging wave crest with larger curvature in the front. In more general cases, a wave can impact against the structure with a blunt and round head, especially for plungers not fully

developed, which was reckoned to be related to the severest impact situations. (ii) Only with careful choices of Δx and Δt can a smooth transition of velocities and free surface profile be maintained between the local liquid wedge and the main flow, and a difference in the velocity potential was observed at the matching points. The numerical results of pressure were found to be overall larger than the experimental ones, though with similar distribution. This variance was attributed to the spray and air leakage from the vertical wall during the wave impact in real conditions. And to include these effects, the heat ratio γ was treated as a spring coefficient of a smaller value (around 0.5), which is non-physical strictly.

- **Theoretical studies on the entrained air effect**

While the single air cavity trapped by the wave front enhances the impact pressure significantly, the aerated water with small bubbles entrained in water followed by a broken wave (see in Figure 1.6(c)), was found to generate weakened slosh-up motion when propagating against a wall. It is known that the compressibility of small bubbles mixed in the water can reduce the sound speed significantly, and can lead to pressure oscillation in some cases. Ignoring viscosity and gravity effects, Topliss et al. (1992) analytically solved the free oscillation frequency of a compressible bubbly water flow in front of a wall followed by a main incompressible water flow. The approximate sound speed in the aerated region was estimated from an empirical equation. Higher frequency was revealed for narrower bubbly flow region. In the study of a filling flow generated by water impinging into a confined space composed of two horizontal plates, Peregrine & Kalliadasis (1996) employed a simple model to solve the steady state of this problem with the conservation of mass and the momentum flux. Based on this model, Peregrine & Thais (1996) extended the same study to the case where the filling flow is an air-water mixture. A volume fraction of air was added to count for this compressible flow with homogeneously distributed bubbles. The mass and momentum conservation equations were generalized by including the density term. The pressure was then obtained from the Bernoulli equation for the steady inviscid compressible flow. Results from this approximated model enabled the estimation of pressure reduction by the compressibility effect caused by the entrained air. Yet the estimation of the air fraction coefficient is difficult in practical applications. For wave impact with highly aerated flow created by previous violent wave breaking events, Bredmose et al. (2009) employed the

compressible aerated-flow model of Peregrine & Thai (1996) to simulate an overturning wave impact on a wall entrapping another main air cavity. Classical potential flow for incompressible water was adopted to gain different profiles of wave impact on the wall, and then uniform entrained air of 5% aeration was artificially superposed to a water domain in the vicinity of the wall. A finite-volume method with a Riemann solver based on conservation laws for mass, momentum and energy was used for the compressible flow, so that both the trapped air pocket and the pressure shock wave propagating through the aerated water are able to be simulated numerically. Results from the aerated-flow model confirmed the strong sensitivity of the impact pressures to the incident wave conditions, and at the same time revealed more characteristics of impact with entrained air, for instance, the high pressure generated near the toe of the structure by the reflection of pressure waves from the bottom.

- **Body geometry effect**

For air cavity trapped due to the surface geometry effect of a body, Korobkin (1996) considered the entry problem of a blunt body with a shallow depression at its bottom, by extending the water impact theory by Wagner (1932) with regards to a closed air cavity boundary. It could be applied to the entry of a catamaran into still water. Khabakhpasheva & Korobkin (2011) employed the same method in the study of liquid impact onto a corrugated panel with a constant velocity. The method provided an approximate analytical solution for impact with air cavity effect of this type, though with considerable assumptions. Faltinsen et al. (2004) simulated the bottom slamming of restrained barge type floating airport by fully nonlinear potential flow model and BEM. Wagner's (1932) method was used for the initial impact between the flat bottom and the slightly inclined free surface. A thin air cavity was found to be formed during bottom slamming near the front edge, and was taken into account with an adiabatic law. Oscillating loading was caused by the entrapped air cavity, and the experimental pressures were revealed to be not Froude-scaled due to the air cavity effect.

1.2.3 Summary

From the brief overview, we can see that study on fluid/structure impact problems has evolved through some main stages. Early studies are basic analysis based on

fundamental principles such as the conservation laws of mass, momentum and energy, and free surface elevation was ignored. Then more rational analytical studies were performed based on the velocity potential theory with considerable simplifications. Linearized free surface conditions were adopted, and thus phenomena related to the nonlinearity of free surface could not be included, for instance, the spray and free surface jet formed in the impact. Later nonlinear free surface condition was employed combined with a self-similar method in some cases where the gravity effect was ignored, and approximations had to be made in the solving process. After that, the development of numerical computations enabled the calculation of fully nonlinear free surface flow problems during impact. BEM shows great success in simulating wave transforming and water impact problems. Many techniques have been developed so far to tackle numerical difficulties in fluid/structure impact, for instance, the thin jet, flow separation, the rapidly changed parameters starting from one contact point, and the decoupling of the body motion and the impact force, etc.

Air cavity entrapped in a fluid/structure impact, though found to have a significant effect in the large group of experiments on breaking wave impact with ever improving recording technology (1930s~now), was not fully understood due to the lack of effective and comprehensive theoretical studies. Owing to the complication in the physical process, the air cavity, if considered in early analytical models, was simply regarded as a spring with certain restoring force or a line with assumed rebounding velocity, etc. Evolution of the shape and pressure change of the cavity during the impact process was not considered. With the progress in the numerical study of fluid/structure impact problems, water impact with trapped air cavity was able to be simulated with certain local approximations. In particular the scaling effect caused by the entrapment of an air cavity in an overturning wave impact was not revealed until the numerical study by Tanizawa & Yue (1992). Numerical models and techniques accommodating both more accurate simulation and broader applications are in need, with which deeper insights into the air cavity effect in free surface impact problems can be gained.

1.3 Present work and thesis outline

The present work focuses on the effect of a single air cavity/pocket entrapped by a

curled free surface during a fluid/structure impact in the marine context. The theoretical study is conducted within the regime of potential flow, considering the high velocity of the impact and the short duration involved. A boundary element method (BEM) is employed to enable a time-domain solution for fluid/structure impact and wave evolution. The detailed mathematical methods and numerical procedures are described in Chapter 2, including the 2D and axisymmetric cases. New schemes for calculating impact with long and thin jet are proposed. A basic case of impact by an axisymmetric water column on a solid structure is studied analytically and numerically in Chapter 3, validating the numerical model. The initial singularity at the body-free surface intersection is analysed in detail. The thin jet approximation with shallow water theory is extended to the axisymmetric case. With the decoupled thin jet calculation scheme developed, the steady state solution of the impact is studied numerically together with analytical deduction. After that, air cavities of various sizes and positions are added in front of the impact flow to compare with the case without air cavity, enabling a preliminary investigation into the characteristics of trapped air and its influence on the impact dynamics in Chapter 4.

Then numerical techniques for the simulation of more general and practical cases of water wave impact with air cavity effect are developed. A numerical method enabling a more accurate simulation of overturning wave impact on a structure entrapping an air cavity is introduced in Chapter 5. The key technique is the employment of a domain decomposition method based on a dual-system technique. A local stretched coordinate system is employed for the exact free surface shape and velocity in the local impact region, which couples with the main wave plunging in the Cartesian system. With the numerical method developed, breaking wave impact on a wall with different wave front shapes entrapping various air cavity sizes is simulated. The characteristics and acting mechanisms of the air cavity are analysed in depth. The scaling effect caused by the entrapped air cavity is looked into. A scaling law is proposed based on analysis on the energy transfer relation together with the numerical results, which could be applied in the prediction of the maximum pressure from a laboratory experiment carried out in a different scale.

The concluding remarks are given in Chapter 6, highlighting the main conclusions and contributions of the present study, and its potential applications to more general

fluid/structure impact problems in marine engineering, as well as the problem remained and the future perspectives.

Chapter 2 Mathematical model and numerical procedure

The physical problem studied in this thesis involves not only the wave evolution prior to the impact and the transient process of fluid/structure impact, but also the post initial impact process with/without air cavity effect. Only solid body is considered and the air cavity entrapped in the impact is assumed to be an ideal gas. A velocity potential theory combined with a boundary element method (BEM) is introduced in this chapter to solve the fluid flow.

The fully nonlinear potential flow theory combined with BEM has been proved to give excellent predictions for free surface evolution problems by comparison with experimental results, for example by Dommermuth et al. (1988) in a laboratory wave channel of 25m long, 0.7m wide and water depth of 0.6m. Here we shall give formulations of BEM, respectively for the 2D and axisymmetric cases. The stretched coordinate system employed for impact starting from a single contact point is then presented (based on a 2D case). State of the art numerical treatment techniques for an excellent and robust simulation are introduced in the end, which tackle phenomena generated by the strong nonlinearity in impact problems. In particular, two new thin jet treatment schemes are proposed, keeping the integrity of the thin jet in the simulation of impact problems without loss in accuracy or efficiency.

2.1 Mathematical model --- a velocity potential theory

2.1.1 Assumptions

In marine hydrodynamic problems, since the kinematic viscosity of the water ν is around $10^{-6}\,m^2/s$, the water flow is usually at large Reynolds number, which can easily go above 10^6 with characteristic velocities and lengths in approximate orders of 1-100m/s and 1-100m, respectively. Thus the viscous force is negligible in magnitude compared with the inertia force in the bulk of water (see in Batchelor 1967, p. 212), unless in circumstances where the flow separation from a boundary layer plays an important role, for instance, the calculation of ship resistance. In fluid/structure impact problems, the impact of interest usually has high speed and the period of impact is very short, thus the viscosity of the fluid can be ignored since the spatial gradients of velocity are negligible compared with the time derivative

(Batchelor 1967, p. 471). With the speed of sound in seawater around 1500m/s, the Mach number is small for the impact problem. Our intention here is to study the global impact including the spatial and temporal effect of the cavity rather than the initial 'acoustic stage', and hence the fluid can be assumed to be incompressible.

Based on the above assumptions of inviscid and incompressible ideal fluid, supposing the flow to be irrotational, a velocity potential ϕ can be introduced to describe the flow.

2.1.2 **Governing equations**

A general hydrodynamic problem is formulated in terms of a velocity potential $\phi(x, y, z, t)$ in a Cartesian coordinate system, where z is assumed to point upwards. For fluid/structure impact with air cavity, the surface of the water open to the air will be referred to as the wave surface or outer free surface to distinguish from the cavity surface, with the term free surface covering both of them.

From the continuity equation for incompressible and irrotational fluid, the Laplace equation provides the governing equation for the velocity potential ϕ

$$\nabla^2 \phi = 0 \tag{2.1}$$

For an impermeable body surface, the normal velocity of the fluid particle $\frac{\partial \phi}{\partial n}$ is equal to the normal velocity of the body surface at the same location, thus its boundary condition is

$$\frac{\partial \phi}{\partial n} = \vec{u} \cdot \vec{n} \tag{2.2}$$

in which $\vec{u}$ is the velocity of the body surface, and $\vec{n} = (n_x, n_y, n_z)$ is the normal unit vector of the body pointing out of the fluid domain.

In cases where the fluid stays still before the disturbance (e.g. body entry/impact into calm water), the free surface boundary condition at the initial time t=0 can be obtained following the argument in Batchelor (1967, p. 473). Assuming that the hydrodynamic pressure on the free surface equals the atmospheric pressure ($P = P_a$), we have from the Bernoulli equation

$$\frac{1}{2}\nabla\phi\cdot\nabla\phi+\phi_t+gz=0$$

Integrating this equation over the instant initial impulse stage from t_{0_-} to t_{0_+}, given that the spatial gradients and gz are far smaller than the temporal derivative, we can ignore the product term after the integration and obtain

$$\phi=0\text{, on the still free surface at } t=0 \tag{2.3}$$

Other expressions of ϕ can also be exerted on the initial free surface according to the model in concern.

For undisturbed fluid at infinity

$$\frac{\partial\phi}{\partial n}=0 \tag{2.4}$$

Eqs. (2.1)-(2.4) constitute a closed boundary value problem at t=0, in which the unknown values, including the velocity potential ϕ on the body surface and the normal velocity ϕ_n on the free surface, can be solved.

As the impact goes on, the potential on the free surface needs to be updated by the Bernoulli equation

$$\phi_t+\frac{1}{2}\nabla\phi\cdot\nabla\phi+\frac{P}{\rho}+gz=\frac{P_a}{\rho} \tag{2.5}$$

where $\phi_t=\frac{\partial\phi}{\partial t}$, P denotes the pressure with P_a the atmospheric value, and ρ is the density of the water. Note that a spatially independent term $C(t)$ has been omitted from Eq. (2.5) since the flow is decided only by the gradient of ϕ, rather than by itself.

If we substitute the substantial derivative of the fluid particle $\frac{d}{dt}=\frac{\partial}{\partial t}+\nabla\phi\cdot\nabla\phi$ into the above equation, it becomes

$$\frac{d\phi}{dt}=\frac{1}{2}\nabla\phi\cdot\nabla\phi-\frac{P-P_a}{\rho}-gz \tag{2.6}$$

With $P=P_a$ on the outer free surface, we have its dynamic condition

$$\frac{d\phi}{dt} = \frac{1}{2}\nabla\phi \cdot \nabla\phi - gz \tag{2.7}$$

For cases where an air cavity is trapped near the impact surface, assume that it undergoes an adiabatic process during the fast impact process, and the surface tension effect is ignored given that the single air cavity trapped in fluid/structure impact is not in microsize. Therefore the pressure on the air cavity surface (i.e. the inner free surface) is equal to that inside the cavity

$$P = P_0(\frac{V_0}{V})^{\gamma} \tag{2.8}$$

where V is the cavity volume with V_0 being its initial value when the air cavity is just formed, P_0 is the pressure inside the cavity when it is first trapped and can be supposed to be equal to the atmospheric pressure P_a in general cases of wave impact (unless in artificially modulated wave tank), and γ is the specific heat ratio of the air, which is 1.4 (see Oertel 2004). Substituting it into Eq. (2.6), the dynamic condition on the cavity surface becomes

$$\frac{d\phi}{dt} = \frac{1}{2}\nabla\phi \cdot \nabla\phi - \frac{P_a}{\rho}\left[(\frac{V_0}{V})^{\gamma} - 1\right] - gz \tag{2.9}$$

The kinematic condition of the free surface ($\vec{r} = (x, y, z)$) is

$$\frac{d\vec{r}}{dt} = \nabla\phi \tag{2.10}$$

which accounts for deformation of the free surface in the Lagrangian framework.

It can be seen that with the given initial conditions for the free surface potential and its shape, the subsequent velocity potential as well as the deformation of the free surface can be updated at any time with a time marching scheme based on Eqs. (2.7), (2.9) and (2.10), after solving the governing equations at each time step. This constitutes the basic idea for the numerical procedure.

2.1.3 **A boundary value problem for ϕ_t**

Pressure distribution along the body surface is one of the main concerns in the study of fluid/structure impact. An accurate prediction is essential for the analysis of structural deflection and stress, providing reference for the safety design (e.g. Hua et

al. (2000)). The Bernoulli equation provides the formula for pressure calculation. An early method is to perform backward difference of ϕ with respect to time at consecutive time steps (for a fixed position in Eq.(2.5), and a tracked fluid particle in Eq.(2.6)). However, pressure obtained in this way is subjected to numerical errors involved in the differential approximation as well as the motion of tracked fluid particles. Note that ϕ_t is another harmonic function which satisfies Laplace equation, and thus it can be treated as another boundary value problem (Wu & Eatock Taylor 1996, 2003). In the fluid domain, we have

$$\nabla^2 \phi_t = 0 \tag{2.11}$$

On the outer free surface $P = P_a$, the Bernoulli equation gives

$$\phi_t = -\frac{1}{2}\nabla\phi \cdot \nabla\phi - gz \tag{2.12}$$

On the cavity surface

$$\phi_t = -\frac{1}{2}\nabla\phi \cdot \nabla\phi - \frac{P_a}{\rho}\left[(\frac{V_0}{V})^{\gamma} - 1\right] - gz \tag{2.13}$$

On the body surface, we have the boundary condition for a body moving with a constant velocity $\vec{u}$ (Wu, 1998)

$$\frac{\partial \phi_t}{\partial n} = -\vec{u} \cdot \frac{\partial \nabla\phi}{\partial n} \tag{2.14}$$

We have $\phi_t = 0$ for the undisturbed fluid at infinity.

To avoid the numerical difficulty in the calculation of the second order differentiation in Eq. (2.14), we shall employ the idea in Wu & Hu (2004). Divide ϕ_t into two terms as $\phi_t = -\vec{u} \cdot \nabla\phi + \chi$, then we have χ satisfying $\nabla^2 \chi = 0$ and its boundary conditions can be written as

$$\chi = -\frac{1}{2}\nabla\phi \cdot \nabla\phi + \vec{u} \cdot \nabla\phi - gz \quad \text{on the outer free surface} \tag{2.15}$$

$$\frac{\partial \chi}{\partial n} = 0 \quad \text{on the body surface} \tag{2.16}$$

$$\chi = 0 \quad \text{at infinity} \tag{2.17}$$

$$\chi = -\frac{1}{2}\nabla\phi\cdot\nabla\phi + \vec{u}\cdot\nabla\phi - \frac{P_a}{\rho}\left[(\frac{V_0}{V})^{\gamma} - 1\right] - gz \quad \text{on the cavity surface} \tag{2.18}$$

We can then solve χ first and get ϕ_t straightforwardly without any second-order derivative calculations. The pressure can then be calculated from

$$\frac{P - P_a}{\rho} = -\frac{1}{2}\nabla\phi\nabla\phi - \chi + \vec{u}\cdot\nabla\phi \tag{2.19}$$

If the study is only in concern of the direct impact between the fluid and a structure, which happens at a relative high speed U and lasts for a very short time period T, then the effect of the gravity can be ignored given that $U/T >> g$, and the term $-gz$ can be omitted in the governing equations in 2.1.2 and 2.1.3.

2.2 Numerical procedure---boundary integral equation

Boundary element method (BEM) based on the boundary integral equation is widely used to solve the mixed boundary value problem formulated in 2.1, since it can reduce the dimension of the problem by one. Combining Laplace equation with Green's identity, we can transform the differential equation in the fluid domain Ω (Eq. (2.1)) into an integral equation over the boundary surfaces S

$$A(p)\phi(p) = \int_{\partial\Omega}\left[G(p,q)\frac{\partial\phi(q)}{\partial n_q} - \frac{\partial G(p,q)}{\partial n_q}\phi(q)\right]dS \tag{2.20}$$

where $A(p)$ is the solid angle at the control/field point p, $\vec{n}_q$ is the unit outward normal to the fluid boundary at the integral/source point q, G is the Green's function which satisfies the Laplace equation in the fluid domain apart from when $q = p$.

2.2.1 Boundary element method for 2D case

We shall first specify the boundary integral equation for 2D problems. The Green's function in Eq. (2.20) takes the following form in $o-xy$

$$G = \ln\frac{1}{r_{pq}} \tag{2.21}$$

where $\vec{r} = (x, y)$, and $r_{pq} = \sqrt{(x_p - x_q)^2 + (y_p - y_q)^2}$ is the distance between p and q. This gives

$$\frac{\partial G}{\partial n}=\frac{\partial G}{\partial r}\left(\frac{\partial r}{\partial n}\right)=\frac{\partial G}{\partial r}\frac{\vec{r}_{pq}.\vec{n}}{|r_{pq}|}=-\frac{\vec{r}_{pq}.\vec{n}}{r_{pq}^2} \tag{2.22}$$

The solid angle $A(p)$ in the two dimensional system takes the value

$$A(p)=\begin{cases}0, p\notin\Omega\\ \pi, p\in S\\ 2\pi, p\in\Omega\cap p\notin S\end{cases}$$

where the second term is given on the basis of a smooth boundary surface.

Divide the boundary of the fluid domain into N straight-line segments $\vec{r}_{j+1}-\vec{r}_j, 1\le j\le N$, and adopt a linear distribution of ϕ and $\frac{\partial\phi}{\partial n}$ in each segment. Within each segment we have

$$\phi=\sum_{j=1}^{N+1}\phi_j f_j(\vec{r})\ ,\ \frac{\partial\phi}{\partial n_q}=\sum_{j=1}^{N+1}\frac{\partial\phi_j}{\partial n_q}f_j(\vec{r}) \tag{2.23}$$

where ϕ_j and $\frac{\partial\phi_j}{\partial n_q}$ are defined at the j_{th} node $\vec{r}_j$, and

$$f_j(\vec{r})=\begin{cases}\left|\vec{r}-\vec{r}_{j+1}\right|/\left|\vec{r}_j-\vec{r}_{j+1}\right|, \vec{r}\in(\vec{r}_j,\vec{r}_{j+1}), 1\le j\le N\\ \left|\vec{r}-\vec{r}_{j-1}\right|/\left|\vec{r}_j-\vec{r}_{j-1}\right|, \vec{r}\in(\vec{r}_{j-1},\vec{r}_j), 2\le j\le N+1\\ 0, \vec{r}\notin(\vec{r}_{j-1},\vec{r}_{j+1}), 2\le j\le N\end{cases}$$

is the shape function.

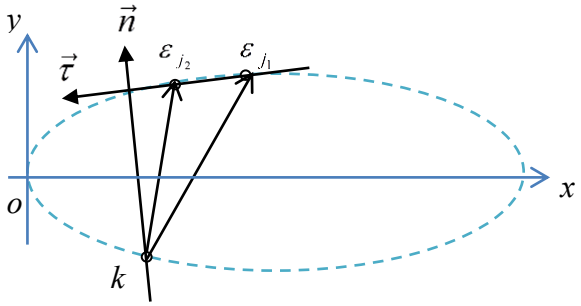

Figure 2.1 Definition of the local coordinate for a 2D problem

Let subscript k and j correspond to the control point p and the integral/source point q, respectively. Denoting by $\vec{\tau}_j$ and $\vec{n}_j$ the tangential and normal unit of the j_{th}

element denoted by $\vec{r}_{j_2} - \vec{r}_{j_1}$, we shall define some local coordinates

$$\varepsilon_{j_1} = \vec{r}_{kj_1}\vec{\tau}_j \ , \ \varepsilon_{j_2} = \vec{r}_{kj_2}\vec{\tau}_j \text{ and } \eta_{kj} = \vec{r}_{kj_1}\vec{n}_j = \vec{r}_{kj_1}\vec{n}_j \tag{2.24}$$

Then within the j_{th} element the linear distribution can be expressed as

$$Y(\varepsilon) = \left[\frac{\varepsilon_{j_2} - \varepsilon}{l_j}, \frac{\varepsilon - \varepsilon_{j_1}}{l_j}\right]\begin{bmatrix} Y_{j_1} \\ Y_{j_2} \end{bmatrix} \tag{2.25}$$

where Y can either be ϕ or $\frac{\partial \phi}{\partial n}$, and $l_j = \varepsilon_{j_2} - \varepsilon_{j_1}$ is the length of the element.

Substituting Eqs. (2.21), (2.22), (2.24) and (2.25) into the boundary integral equation of Eq. (2.20), and letting the field point p approach each node on the boundary, we can deduce the discretized boundary integral equation in an algebraic form

$$\sum_{j=1}^{N+1}[B_{kj}\frac{\partial \phi_j}{\partial n} - C_{kj}\phi_j] = 0, (k = 1, 2, ..., N+1) \tag{2.26}$$

where (Lu et al. 2000)

$$B_{kj} = B_1(k, j) + B_2(k, j-1), C_{kj} = C_1(k, j) + C_2(k, j-1), k \neq j$$

$$B_1(k, j) = -\frac{\varepsilon_{j_2}}{2l_j}I_{21} + \frac{1}{4l_j}I_{22}, B_2(k, j) = \frac{\varepsilon_{j_1}}{2l_j}I_{21} - \frac{1}{4l_j}I_{22},$$

$$C_1(k, j) = \frac{\eta_{kj}}{2l_j}I_{12} - \frac{\varepsilon_{j_2}}{l_j}I_{11}, C_2(k, j) = \frac{\varepsilon_{j_1}}{l_j}I_{11} - \frac{\eta_{kj}}{2l_j}I_{12},$$

and

$$\begin{aligned}
I_{11} &= \arctan(\frac{\varepsilon_{j_2}}{\eta_{kj}}) - \arctan(\frac{\varepsilon_{j_1}}{\eta_{kj}}), \\
I_{12} &= \ln(\varepsilon_{j_2}^2 + \eta_{kj}^2) - \ln(\varepsilon_{j_1}^2 + \eta_{kj}^2), \\
I_{21} &= \varepsilon_{j_2}\ln(\varepsilon_{j_2}^2 + \eta_{kj}^2) - \varepsilon_{j_1}\ln(\varepsilon_{j_1}^2 + \eta_{kj}^2) - 2l_j + 2\eta_{kj}I_{11}, \\
I_{22} &= (\varepsilon_{j_2}^2 + \eta_{kj}^2)\ln(\varepsilon_{j_2}^2 + \eta_{kj}^2) - (\varepsilon_{j_1}^2 + \eta_{kj}^2)\ln(\varepsilon_{j_1}^2 + \eta_{kj}^2) - (\varepsilon_{j_2}^2 - \varepsilon_{j_1}^2).
\end{aligned}$$

To obtain the solid angle at the control point p (i.e. C_{kk}), we shall follow the procedure in Eatock Taylor et al. (2008). Using Eq. (2.20) and taking ϕ as a constant for the whole fluid domain, we have

$$A(p) = -\oint_{\partial\Omega} \frac{\partial G(p,q)}{\partial n_q} dS_q \tag{2.27}$$

This gives

$$A(p) = -\sum_{j=1,\, j\neq k}^{N+1} C_{kj}, k = 1,..,N+1 \tag{2.28}$$

in the numerical form.

Note that Eq. (2.27) is performed over all the boundaries of the fluid domain. Therefore, for problems such as flow around a body in an unbounded fluid domain, the contribution from infinity ought to be included. With Eq. (2.22) we have

$$A(p) = -\oint_{S_b} \frac{\partial G(p,q)}{\partial n_q} dS_q + \oint_{S_\infty} \frac{\vec{r}\cdot\vec{n}_\infty}{r^2} dS_\infty$$

where $\vec{n}_\infty$ denotes the normal vector of the infinite boundary. It can be seen that the second term then equals the solid angle provided by the closed infinite boundary, which is 2π for a two dimensional problem. Thus for a body in an unbounded fluid domain, Eq. (2.28) becomes $A(p) = -\sum_{j=1,\, j\neq k}^{N+1} C_{kj} + 2\pi$.

In the discretized boundary integral equation of Eq. (2.26), either the potential ϕ or its normal derivative $\frac{\partial \phi}{\partial n}$ on each part of the boundaries is known from the corresponding boundary conditions (e.g. Eqs. (2.2) to (2.4)), and they are moved to the right hand side of the equation. Assuming a model with fluid boundaries composed of the body surface S_b (with n_1 segments), the free surface S_f (with n_2 segments) and the control surface at the far filed S_c (with n_3 segments), the remaining unknowns can then be obtained by solving the following matrix equation

$$\begin{bmatrix} -C_{bb}, B_{bf}, B_{bc} \\ -C_{fb}, B_{ff}, B_{fc} \\ -C_{cb}, B_{cf}, B_{cc} \end{bmatrix} \begin{bmatrix} \phi_b \\ \frac{\partial \phi_f}{\partial n} \\ \frac{\partial \phi_c}{\partial n} \end{bmatrix} = \begin{bmatrix} -B_{bb}, C_{bf}, C_{bc} \\ -B_{fb}, C_{ff}, C_{fc} \\ -B_{cb}, C_{cf}, C_{cc} \end{bmatrix} \begin{bmatrix} \frac{\partial \phi_b}{\partial n} \\ \phi_f \\ \phi_c \end{bmatrix} \tag{2.29}$$

The velocity of each discrete node on the boundary can then be calculated through a second-order difference for ϕ together with $\frac{\partial \phi}{\partial n}$. With given initial boundary conditions, successive motions of the liquid and dynamic features of the impact can be captured with a time marching method. The solution within the fluid domain can then be calculated explicitly with the solved boundary values, based on the boundary integral equation (2.20) for internal points.

2.2.2 **Boundary element method for axisymmetric case**

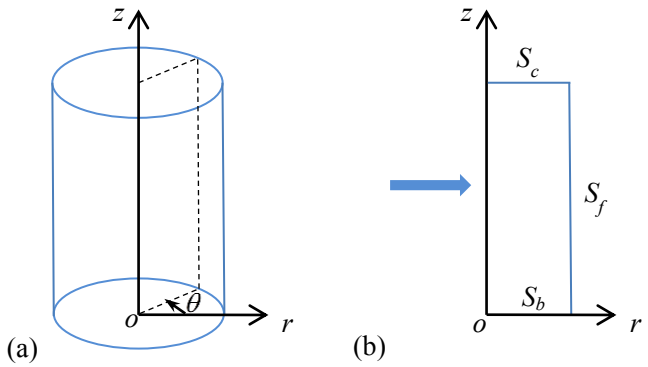

Figure 2.2 Sketch of coordinate systems for axisymmetric case

For hydrodynamic problems which are axisymmetric both geometrically and kinematically, the three dimensional boundary integral equation can be performed on a two dimensional boundary after an integral over the axisymmetric axis. Here we shall give detailed formulations of the boundary element method for axisymmetric problems, by highlighting the difference in BEM with those presented in the last section for 2*D* cases.

Define a cylindrical coordinate system $o-r\theta z$ in which z is the axis about which the problem is axisymmetric (e.g. Figure 2.2(a)). In the boundary integral equation of Eq. (2.20), the Green's function in the three dimensional Cartesian system takes the form

$$G = \frac{1}{r_{pq}} \tag{2.30}$$

where r_{pq} is the distance between the control point p and the integral point q. Then

$$\frac{\partial G}{\partial n}=\frac{\partial G}{\partial r}\left(\frac{\partial r}{\partial n}\right)=\frac{\partial G}{\partial r}\frac{\vec{r}_{pq}.\vec{n}}{\left|r_{pq}\right|}=-\frac{\vec{r}_{pq}\cdot\vec{n}}{\left|r_{pq}\right|^{3}} \tag{2.31}$$

For three dimensional problems, the solid angle $A(p)$ becomes

$$A(p)=\begin{cases}0, p\notin\Omega\\ 2\pi, p\in S\\ 4\pi, p\in\Omega\cap p\notin S\end{cases}$$

Since the problem is axisymmetric about *z*-axis, we can deal with the circumferential integration with regard to θ from 0 to 2π separately, and Eq. (2.20) becomes

$$\mathrm{A}(p)\phi(p)=\int_{l_q} r_q\left[H\frac{\partial\phi(q)}{\partial n_q}-\phi(q)\frac{\partial H}{\partial n_q}\right]dl \tag{2.32}$$

where $H=\int_0^{2\pi}\frac{1}{r_{pq}}d\theta=\int_0^{2\pi}\left[r_p^2+r_q^2-2r_pr_q\cos\theta+(z_p-z_q)^2\right]^{-\frac{1}{2}}d\theta$;

$$\frac{\partial H}{\partial n_q}=\int_0^{2\pi}\frac{\partial}{\partial n_q}\left(\frac{1}{r_{pq}}\right)d\theta=-\int_0^{2\pi}\frac{(r_q-r_p\cos\theta)n_r+(z_q-z_p)n_z}{r_{pq}^3}d\theta;$$

and (r_q,z_q), (r_p,z_p) are the coordinates of the field point q and the integral point p in the cylindrical system at any given azimuth θ (as shown in Figure 2.2(b)), which are to be denoted by *j* and *k*, respectively.

After performing the integration with respect to θ, the above equations become (Schiffman & Spencer 1951)

$$H=\frac{4K(m)}{\left[(r_j+r_k)^2+(z_j-z_k)^2\right]^{\frac{1}{2}}} \tag{2.33}$$

$$\frac{\partial H}{\partial n_q}=-\left[r_jn_r+(z_j-z_k)n_z-r_kn_r\frac{e}{h}\right]I+\frac{r_kn_r}{h}H \tag{2.34}$$

where

$$m=\frac{(r_j-r_k)^2+(z_j-z_k)^2}{(r_j+r_k)^2+(z_j-z_k)^2};$$

$$I=\frac{4E(m)}{\left[(r_j+r_k)^2+(z_j-z_k)^2\right]^{\frac{1}{2}}\left[(r_j-r_k)^2+(z_j-z_k)^2\right]};$$

$e=r_j^{\,2}+r_k^2+(z_j-z_k)^2$, $h=2r_jr_k$;

$K(m)=\int_0^{\frac{\pi}{2}}\frac{d\theta}{\sqrt{1-m\sin^2\theta}}$ and $E(m)=\int_0^{\frac{\pi}{2}}\sqrt{1-m\sin^2\theta}d\theta$ are the complete elliptic integral of the first and the second kind respectively, which can be calculated numerically by (see to Abramowitz & Stegun 1965)

$$\begin{aligned}K(m)&\doteq\sum_{n=0}^{4}a_nm^n+\sum_{n=0}^{4}b_nm^n\ln(1/m);\\ E(m)&\doteq\sum_{n=0}^{4}c_nm^n+\sum_{n=0}^{4}d_nm^n\ln(1/m)\end{aligned}\qquad(2.35)$$

where $a_{n(n=0,..,4)}=(1.38629,0.09666,0.03590,0.03742,0.01451)$,

$b_{n(n=0,..,4)}=(0.5,0.12498,0.06880,0.03328,0.00441)$,

$c_{n(n=0,...,4)}=(1,0.44325,0.06260,0.04757,0.01736)$,

$d_{n(n=0,..,4)}=(0,0.24998,0.09200,0.04069,0.00526)$

are the weights of the 4th degree polynomial approximations by Hastings (1955).

After discretizing the boundary in Figure 2.2(b) into N straight-line segments and substituting the shape function of linear distribution in Eq. (2.23) (here $\vec{r}=(r,z)$) into (2.32), we shall also get the discrete boundary integral equation in a similar algebraic expression

$$\sum_{j=1}^{N+1}[D_{kj}\frac{\partial\phi_j}{\partial n}-E_{kj}\phi_j]=0,(k=1,2,...,N+1)\qquad(2.36)$$

where

$$D_{kj}=\left(\int_{\vec{r}_{j-1}}^{\vec{r}_j}+\int_{\vec{r}_j}^{\vec{r}_{j+1}}\right)r_jf_j(\vec{r})Hdl_j\qquad(2.37)$$

$$E_{kj,k\neq j}=-\left(\int_{\vec{r}_{j-1}}^{\vec{r}_j}+\int_{\vec{r}_j}^{\vec{r}_{j+1}}\right)r_jf_j(\vec{r})\frac{\partial H}{\partial n_j}dl_j\qquad(2.38)$$

The integrals for D_{kj} and E_{kj} have to be evaluated numerically, for which Gauss's Formula with arbitrary interval is used

$$\int_a^b f(y)dy = \frac{b-a}{2}\sum_{i=1}^{n} w_i f(y_i) \tag{2.39}$$

where $y_i = (\frac{b-a}{2})x_i + \frac{b+a}{2}$.

The abscissas and weight factors for 10-point Gauss method are as follows (Abramowitz & Stegun 1972)

$x = \mp(0.14887,\ 0.43339,\ 0.67940,\ 0.86506,\ 0.97390)$;

$w = (0.29552,\ 0.26926,\ 0.21908,\ 0.14945,\ 0.06667)$.

When $k = j$, we shall come across a logarithmic singularity, which can be solved by Gaussian Integrations with a logarithmic singularity (Abramowitz & Stegun 1972),

$$\int_0^1 \ln x f(x)dx = \sum_{i=1}^{n} w_i f(x_i) \tag{2.40}$$

where $x = (0.041448,\ 0.245275,\ 0.556165,\ 0.848982)$;

$w = (0.383464,\ 0.386875,\ 0.190435,\ 0.039225)$ for n=4.

Alternatively, the singularity calculation can be eliminated through an analytical transformation

$$\begin{aligned} \int_0^a f(x)\ln x dx &= \int_0^a [f(x) - f(0)]\ln x dx + \int_0^a f(0)\ln x dx \\ &= \int_0^a [f(x) - f(0)]\ln x dx + f(0)(a\ln a - a) \end{aligned} \tag{2.41}$$

since $\lim_{x\to 0} x^y \ln x = 0, (y > 0)$. This is the approach we have employed in the numerical codes.

Similar to Eq. (2.28), the solid angle at the control point $E_{kk} = A(p)$ can also be obtained for a closed boundary by

$$A(p) = -\sum_{j=1, j\neq k}^{N+1} E_{kj}, k = 1,.., N+1 \tag{2.42}$$

For three dimensional problems where an enclosed infinite fluid boundary is

involved, if we substitute Eq. (2.31) into Eq. (2.27),

$$A(p) = -\oint_{S_b} \frac{\partial G(p,q)}{\partial n_q} dS_q + \oint_{S_\infty} \frac{\vec{r} \cdot \vec{n}_\infty}{r^3} dS_\infty = -\sum_{j=1, j\neq k}^{N+1} E_{kj} + 4\pi$$

will be obtained.

The unknowns on the fluid boundary can be solved from the matrix equation similar to Eq. (2.29), and the fluid motion can be updated combining the dynamic conditions with a time marching method. As for the pressure calculation, based on the mathematical model in section 2.1.3, the above boundary element method can also be adopted to solve the boundary value problem for ϕ_t. At each time step, its boundary conditions can be obtained from the numerical results related to ϕ. The pressure can subsequently be solved by Eq. (2.19).

2.2.3 **The time marching step**

When the solution is found, the time marching step for the case of fluid/structure impact without air cavity can be determined by limiting the displacement of the nodes, or

$$\delta t_1 = k_1 \min(\frac{l_i}{v_i})_{i=1,2,\ldots,N_f+1}, 0 < k_1 < 1 \tag{2.43}$$

where l_i denotes the length of element i on the free surface, v_i the corresponding velocity, and N_f the total element number on the free surface. k_1 is a control factor to ensure the element nodes not to cross each other when time step advances and is chosen between 0.1~0.3 in the simulations below.

When the air cavity is trapped during the impact process, it may go through a series of contraction and expansion processes. The velocity of nodes will become nearly zero when it reaches its maximum or minimum volume. At those time instants, the time step obtained by limiting the displacement of the nodes might be too big. To take into account the possible large acceleration, the time step is also restrained by (Gibson & Blake 1982, Best 1993)

$$\delta t_2 = k_2 \Big/ \max\left(\left| \frac{d\phi_j}{dt} \right|_{j=1,\ldots,N_a+1} \right); \ \delta t = \min(\delta t_1, \delta t_2)$$

where N_a denotes the number of elements on the cavity, and $\left|\frac{d\phi_j}{dt}\right|_{j=1,...,N_a+1}$ can be obtained from the dynamic condition of the cavity surface (Eq. (2.9)) at each time step. The control factor, k_2, is a value yet to be decided. Here it is chosen as the mean value of $\delta\phi$ ($=\frac{d\phi}{dt}\cdot\delta t$) obtained on the proximate wave surface during a preliminary time step obtained from Eq. (2.43). The expressions for δt_1 and δt_2 are then combined to determine the time step in the simulation of impact with air cavity

$$\delta t = \min\left(\frac{mean\left(\left|\frac{d\phi_i}{dt}\right|_{i=1,...,N_w+1}\right)}{\max\left(\left|\frac{d\phi_j}{dt}\right|_{j=1,...,N_a+1}\right)}\cdot\delta t_{1w}, \delta t_1\right) \tag{2.44}$$

where $i=1,...,N_w+1$ denotes nodes on the wave surface proximate to the air cavity, which in this case is the impacting front water region and could be decided by a domain of several times of the cavity length from the structure surface; $\left|\frac{d\phi_i}{dt}\right|_{i=1,...,N_w+1}$ is obtained from Eq. (2.7); δt_{1w} is obtained correspondingly by performing Eq. (2.43) over $i=1,...,N_w+1$, while the second term δt_1 covers all the nodes on the free surfaces .

2.3 Stretched coordinate system for impact starting from one point

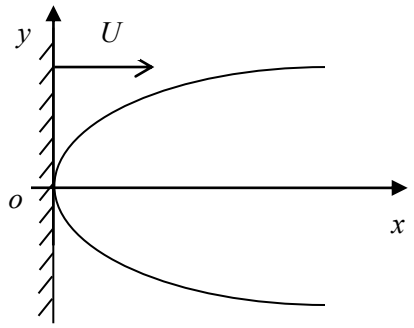

Figure 2.3 Sketch of a 2D liquid droplet impact

Fluid/structure impact with a flat impacting front is rare in reality, and the impact usually starts from a single contact point. At the initial stage of the impact, the significant effect of the impact on the fluid flow will be confined to a very small region near the contact point. Consequently the physical parameters within this

region (e.g. velocity and pressure) can change rapidly. To accurately capture the changing, extremely small elements corresponding to the tiny impact region need to be used. This is clearly not viable for the entire domain based on the normal Cartesian system. An ideal approach is to employ a stretched coordinate system, defined based on the ratio of the Cartesian system to a distance increasing with time, for instance, the distance of the relative motion or the size of the wetted surface (Wu et al. 2004, Wu 2006). Thus the size of elements utilized in the stretched coordinate system remains roughly in the same order. Here we shall give the basic idea of stretched coordinate system based on the case of impact by a two dimensional water droplet on a wall at a constant velocity U, as illustrated in Figure 2.3.

At the local impact point, a stretched coordinate system $o-\varepsilon\eta$ is introduced. Together with the local velocity potential $\varphi(\varepsilon,\eta,t)$, they are defined as

$$\phi(x,y,t)=Us\varphi(\varepsilon,\eta,t) \tag{2.45}$$

$$\varepsilon=x/s(t),\eta=y/s(t) \tag{2.46}$$

where s is the stretching ratio, and U can be set equal to the absolute value of the horizontal velocity of the contact point at the moment of impact.

In the water entry problem of wedges studied by Wu et al. (2004) and Wu (2006), s was chosen as the distance travelled into the water by the body, which is equivalent to $s=Ut$ in the present case. However, for impact by a curved water surface on a wall, as discussed by Wu (2007a), such choice would lead to an extremely large initial wetted surface at the impact point, and thus the size of the wetted surface was chosen instead

$$s=y(Ut) \tag{2.47}$$

where y represents the vertical coordinate of the free surface symmetric about y=0.

$\varphi(\varepsilon,\eta,t)$ also satisfies Laplace equation in the stretched coordinate system

$$\nabla^2\varphi=0 \tag{2.48}$$

The boundary condition on the solid surface can be obtained through

$$\frac{\partial\varphi(\varepsilon,\eta)}{\partial n}=U^{-1}\frac{\partial\phi(x,y)}{\partial n} \tag{2.49}$$

The kinetic and dynamic conditions on the free surface in the stretched coordinate system become

$$\frac{d(s\varepsilon)}{dt} = U\frac{\partial\varphi}{\partial\varepsilon},\quad \frac{d(s\eta)}{dt} = U\frac{\partial\varphi}{\partial\eta} \tag{2.50}$$

$$\frac{dUs\varphi(\varepsilon,\eta,t)}{dt} = \frac{1}{2}U^2\nabla\varphi.\nabla\varphi - gs\eta \tag{2.51}$$

Similar to Eq. (2.43), the time step adopted during the employment of the stretched coordinate system can be determined by

$$\delta t = k_1 \min(s\, l_i \Big/ \sqrt{\left[\frac{d(s\varepsilon_i)}{dt}\right]^2 + \left[\frac{d(s\eta_i)}{dt}\right]^2} = k_1 \frac{s}{U}\min(l_i \Big/ \sqrt{\left(\frac{\partial\varphi}{\partial\varepsilon}\right)^2 + \left(\frac{\partial\varphi}{\partial\eta}\right)^2}) \tag{2.52}$$

where l_i is the element size in the stretched coordinate system, and $T_s = \frac{s}{U}$ could be interpreted as the stretching ratio for time.

ϕ_t at this stage can also be calculated with the help of the stretched coordinate system. If we write $\chi(\varepsilon,\eta,t) = \phi_t(x,y,t)$, then χ satisfies the Laplace equation. Its boundary conditions can be obtained from Eqs. (2.12) and (2.14)

$$\chi = -\frac{1}{2}U^2(\varphi_\varepsilon^2 + \varphi_\eta^2) - gs\eta \tag{2.53}$$

on the free surface, and

$$\frac{\partial\chi}{\partial n} = 0 \tag{2.54}$$

on the wall.

2.4 Numerical treatments

2.4.1 Incompatibility of boundary conditions at the intersection

Note that at the intersection of the free surface and the solid wall, the normal derivatives of the velocity potential are not continuous, with $\phi_n\big|_{S_b}$ on the body surface and $\phi_n\big|_{S_f}$ on the free surface being different, while the velocity potential ϕ is continuous and known from the free surface. Therefore the intersection point

contains two known values $\phi_n|_{S_b}$ and ϕ, and one unknown $\phi_n|_{S_f}$ which needs to be solved. To deal with the incompatibility of boundary conditions at the intersection point, we shall employ the idea similar to that of Lin et al. (1984) who specified both the stream function and the velocity potential at the intersection point in the Cauchy integral equation for 2D problems. Both the body surface and free surface conditions will be imposed at the intersection point.

Denote the node number of the intersection point by n_1, with $1\sim n_1$ standing for the nodes on the body surface and $n_1\sim n_2$ for the nodes on the free surface. The integral coefficient of the intersection point with regard to the normal velocity (e.g. B_{kn_1} in Eq. (2.26)) will then be divided into two terms accordingly

$$B_{kn_1}\frac{\partial\phi_{n_1}}{\partial n}=B_{kn_1\_b}\left.\frac{\partial\phi_{n_1}}{\partial n}\right|_{S_b}+B_{kn_1\_f}\left.\frac{\partial\phi_{n_1}}{\partial n}\right|_{S_f} \tag{2.55}$$

where $B_{kn_1\_b}=B_2(k,n_1-1)$ and $B_{kn_1\_f}=B_1(k,n_1)$, following those defined in Eq. (2.26) for the 2D case.

The intersection of free surface and the far-end control surface can be treated in the same way, of which the node number is n_2. Substituting the above equation into the discretized boundary integral equation (2.26), and moving the unknown terms to the left-hand side of the equation and the known ones to the right, the new algebraic equations take the form

$$\begin{aligned}&\sum_{j=1}^{n_1-1}-C_{kj}\phi_j+B_{kn_1\_f}\left.\frac{\partial\phi_{n_1}}{\partial n}\right|_{S_f}+\sum_{j=n_1+1}^{n_2}B_{kj}\frac{\partial\phi_j}{\partial n}+B_{kn_2\_c}\left.\frac{\partial\phi_{n_3}}{\partial n}\right|_{S_c}-\sum_{j=n_2+1}^{n}C_{kj}\phi_j\\&=-\sum_{j=1}^{n_1-1}B_{kj}\frac{\partial\phi_j}{\partial n}-B_{kn_1\_b}\left.\frac{\partial\phi_{n_1}}{\partial n}\right|_{S_b}+\sum_{j=n_1}^{n_2}C_{kj}\phi_j-B_{kn_2\_c}\left.\frac{\partial\phi_{n_1}}{\partial n}\right|_{S_c}-\sum_{j=n_2+1}^{n}B_{kj}\frac{\partial\phi_j}{\partial n}\end{aligned} \tag{2.56}$$

Thus the numerical difficulty caused by the incompatible conditions at the intersection is avoided. The treatment for the axisymmetric case follows the same scheme, with $D_{kn_1\_b}=\int_{\vec{r}_{n_1-1}}^{\vec{r}_{n_1}}r_q f_{n_1-1}(\vec{r})Hdl_q$ and $D_{kn_1\_f}=\int_{\vec{r}_{n_1}}^{\vec{r}_{n_1+1}}r_q f_{n_1}(\vec{r})Hdl_q$ from Eq. (2.37). However, singularity may still exist in the initial solution for the velocity, which is to be discussed in the theoretical study of impact by an axisymmetric liquid column in

2.4.2 Thin jet treatment schemes

Violent fluid/structure impact with a free surface usually involves a dramatic feature: the formation of a long and thin jet stretching along the body surface. In numerical simulations, a singularity may exist in the velocity of the intersection point at early stages of some cases, producing a fast stretching long jet of nearly zero thickness near the jet tip. It may have little physical influence on the main fluid domain, but the proper treatment is essential for the accuracy of the whole solution. The close distance between the two sides of a jet can generate ill-conditioned matrix in BEM, leading to numerical errors and instabilities along the thin jet (e.g. pressure undulation, penetration of nodes into the body surface), and subsequently the failure of the simulation. To resolve the numerical difficulties associated, several treatment schemes have been developed.

An early one is a direct cut-off of the thin jet in a direction normal to the body surface in the simulation of wedge entry by Zhao & Faltinsen (1993). Thus the computation of the long thin jet is avoided without affecting the overall simulation. The results of pressure, however, exhibit some deviation from the atmospherical value near the cut edge. In addition, due to the lack of information in the jet tip area, the simulation will not be able to continue in situations where the jet tip starts to 'pull back' or plunge (e.g. under the effect of gravity or body geometry). Kihara (2004) later modified the cut model by introducing a new intersection point of the free surface and the body according to their contact angle obtained in the similarity solution of Dobro-vol'skaya (1969) for the wedge entry. In this way the intersection point can be kept while effectively limiting the length and thickness of the jet.

Another scheme is to keep the integrity of the jet by introducing a local analytical solution based on shallow water approximation for the thin jet region (Wu et al. 2004). The unknowns along its two sides were solved directly under the assumption of a linear potential distribution (only applicable for 2D problems), and then substituted into the boundary integral equation for the calculation of the remaining main fluid domain. Thus the size of the calculation matrix (e.g. Eq. (2.26) for the 2D case, and Eq. (2.36) for the axisymmetric case) is significantly reduced, enhancing the calculation efficiency. The accuracy of pressure calculation is also improved.

Nevertheless, there are situations where the thin jet stretches so long that the numerical integrals along its two sides (though with approximate solutions) become increasingly time consuming (in Eq. (2.57)).

In the current study of fluid/structure impact, we shall employ different jet treatment schemes for different circumstances. For instance, the impact by a wave front usually starts from a single contact point, for which a stretched coordinate system needs to be employed to seek the local solution characterized by rapidly changing parameters. For the sake of accuracy, the integrity of the long thin jets formed upon impact is essential for the transfer of the simulation into the physical system. Two approximate jet treatment schemes will be proposed in this work, where the thin jets can be kept in the simulation with improved efficiency and accuracy.

(1) Decoupled thin jet calculation based on the shallow water approximation

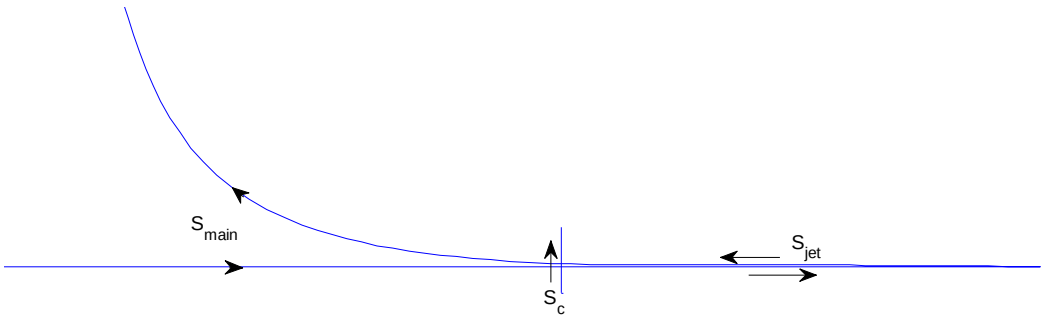

Figure 2.4 Division of the fluid boundaries into S_{main} and S_{jet}, connected by S_c

Here we shall first propose a thin jet treatment scheme based on the shallow water theory. The thin jet region will still be calculated by a shllow water approximation, while in stead of substituting the values on the two sides of the entire long jet into the intergral equation, they will be replaced by that over a control surface from where the thin jet starts. At each time step, the defined thin jet region and the remaining fluid domain will then be calculated respectively.

When a thin jet has developed along the body surface, divide the whole fluid boundaries into two parts: the two sides of the thin jet S_{jet} (determined by a threshold value of the fluid thickness or the inclination angle with the wall), and the remaining main fluid boundaries S_{main}. Denote a field point in the main fluid domain constituted by S_{main} as p, the integral point on S_{main} as q, and that on S_{jet} as J. The

boundary integral equation of Eq. (2.20) can then be rewritten as

$$A(p)\phi(p) = \int_{S_{main}} \left[G\frac{\partial \phi_q}{\partial n} - \frac{\partial G}{\partial n_q}\phi_q \right] dS_q + \int_{S_{jet}} \left[G\frac{\partial \phi_J}{\partial n} - \frac{\partial G}{\partial n_J}\phi_J \right] dS_J \tag{2.57}$$

Define the intersection boundary of S_{main} and S_{jet} vertical to the wall, whose normal direction is from the main fluid domain towards the jet region, as S_c shown in Figure 2.4. For a control point p on S_{main}, performing the boundary integral equation over $S_{main} + S_c$, the main fluid domain could be solved from

$$A(p)\phi(p) = \int_{S_{main}} \left[\frac{\partial G}{\partial n_q}\phi_q - G\frac{\partial \phi_q}{\partial n} \right] dS_q + \int_{S_c} \left[\frac{\partial G}{\partial n_c}\phi_c - G\frac{\partial \phi_c}{\partial n} \right] dS_c \tag{2.58}$$

As a cut-off boundary to the thin jet region, S_c could be represented by a single segment with linear distribution of ϕ_c and $\frac{\partial \phi_c}{\partial n}$, where its normal velocity $\frac{\partial \phi_c}{\partial n}$ can be represented by the radial velocity along the body surface of its intersection point with the free surface. Unknowns at the intersection points can either be solved from the above boundary integral equation or from the shallow water approximation for the thin jet region, which only vary little.

At the same time, the unknowns on the two sides of S_{jet} (ϕ_J on the wall and $\frac{\partial \phi_J}{\partial n}$ on the free surface) can be solved with a simplified distribution of the velocity potential across the thin fluid layer within each element. For 2D cases, the shallow water approximation of linearized distribution $\phi = A + Bx + Cy$ could be applied, detailed formulation of which could be referred to Wu (2007b), whereas that for the axisymmetric case was not yet developed. For the axisymmetric case an approximate distribution satisfying the Laplace equation could take the form $\phi = A + B\ln r + Cz$. Detailed deduction will be given in the case study of axisymmetric impact problem in 3.4.4. After the local solution for the thin jet area is gained, the free surface of the thin jet can be updated by its kinematic and dynamic conditions

$$\frac{d\vec{r}_J}{dt} = \nabla \phi_J \tag{2.59}$$

$$\frac{d\phi_J}{dt} = \frac{1}{2}\nabla\phi_J \cdot \nabla\phi_J \tag{2.60}$$

(2) A dipole distribution approximation

Denote a node on the free surface of the thin jet by $\vec{r}_k$, and assume the line passing it in the normal direction of the wall intersects at the wall at point $\vec{r}_J$. Suppose that the thin jet has been formed into a considerable length, and nodes on its free surface are in close proximity to the wall. Considering the small inclination angle between the thin jet and the body surface, we can assume approximately

$$\frac{\partial\phi_k}{\partial n} \doteq -\frac{\partial\phi_J}{\partial n} \ , \ \phi_k = \phi_J - h_J \frac{\partial\phi_J}{\partial n} \tag{2.61}$$

where $h_J = \left|\vec{r}_k - \vec{r}_J\right|$ is the thickness of the thin jet at $\vec{r}_k$, which is taken below a small value and approaches to zero near the jet tip.

Substituting the above relations for the thin jet into the boundary integral equation of Eq. (2.57), with Eqs. (2.21) and (2.30), we have for the 2D and 3D (including axisymmetric) cases respectively

$$A(p)\phi(p) = \int_{S_{main}} \left[\ln r_{pq} \frac{\partial\phi(q)}{\partial n} - \phi(q) \frac{\partial}{\partial n_q}(\ln r_{pq}) \right] dS_q - \int_{S'_{jet}} (-h_J \frac{\partial\phi_J}{\partial n}) \frac{\partial}{\partial n_J}(\ln r_{pJ}) dS_J \tag{2.62}$$

$$A(p)\phi(p) = \int_{S_{main}} \left[\frac{1}{r_{pq}} \frac{\partial\phi(q)}{\partial n} - \phi(q) \frac{\partial}{\partial n_q}(\frac{1}{r_{pq}}) \right] dS_q - \int_{S'_{jet}} (-h_J \frac{\partial\phi_J}{\partial n}) \frac{\partial}{\partial n_J}(\frac{1}{r_{pJ}}) dS_J \tag{2.63}$$

where S'_{jet} is along one side of the jet surface, or a control surface amid its two sides. Thus the contribution from the thin jet part, as shown in the last term of the above equations, can be regarded as a dipole distribution with strength $-h_J \frac{\partial\phi_J}{\partial n}$ along S'_{jet}.

Method (1) of the decoupled shallow water approximation is to be employed in the present study where long jets have been formed and need to be kept; while the method of introducing a new liquid-body intersection point by Kihara (2004) will be used when the jet length needs to be limited, for instance those developed inside a deforming air cavity.

2.4.3 Numerical stabilizing techniques

i. Remeshing

Within the Lagrangian framework, nodes on the free surface move with their material velocities and can stretch or cluster over a substantial simulation time. To ensure the numerical accuracy, the free surface needs to be regridded/remeshed every several time steps. A traditional idea is to interpolate new nodes on the original boundary surface to redistribute it evenly. Wang & Wu (2006) and Sun (2007) used a cubic spline approximation on the free surface and interpolated new nodes according to equal arc length. In consideration of the computation efficiency, here we shall employ a linear interpolation to re-discretize the linear elements. First the total length of free surface will be calculated from summation of all the element length. With a given grid size range, the number of new segments N are determined. The last step is to search the position of each new node based on a linear interpolation on all the elements. The value of ϕ and $\frac{\partial \phi}{\partial n}$ of the new nodes can be determined by Eq. (2.23). An example of the outcome of the regridding method is shown in Figure 2.5.

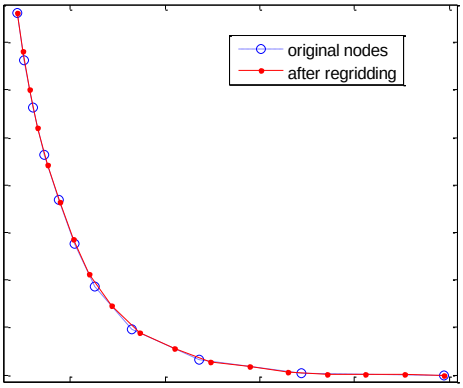

Figure 2.5. Nodes on the free surface: before and after regridding

There may be a significant change of cavity size during its contraction and expansion. Imagine the case where the cavity is in a circular shape with $R(t)$ denoting its radius. Assume that the initial solid angle of a segment on the circle is around σ_0, then it is reasonable to apply a grid size varying with $\sigma_0 R(t)$ to accurately capture the local curvature, especially when the cavity contracts considerably. Therefore, we shall remesh the air cavity according to grid sizes l_a related to the change of its volume

$$l_a = \begin{cases} \max(l_0 \sqrt[n]{\frac{V}{V_0}}, c_1 l_0), c_1 < 1 (\text{contraction stage}) \\ \min(l_0 \sqrt[n]{\frac{V}{V_0}}, c_2 l_0), c_2 \geq 1 (\text{expansion stage}) \end{cases} \tag{2.64}$$

Where n=2 for 2D problems and n=3 for 3D problems; $c_1 < 1$ and $c_2 \geq 1$ are two threshold coefficients limiting the minimum and maximum value of grid size, and l_0 is the basic element size applied initially on the air cavity.

ii. Smoothing

A smoothing technique needs to be adopted in order to avoid the saw-tooth behaviour of nodes on the free surface in the progress of simulation. A traditional one is the five-point smoothing method. Formulas of different orders have been employed by Longuet-Higgins & Cokelet (1976), Maruo & Song (1994) and Sun (2007), etc. Nevertheless, this method is theoretically based on nodes equally spaced in a certain direction. Here we shall employ an energy method for smoothing presented by Zhu (2000), which is applicable for both regularly and irregularly spaced nodes and has been used by Wang & Wu (2006) in the simulation of wave/body interactions with a finite element method (FEM). Supposing a set of discrete nodes $Q_i (i = 0, ..., N)$ on the curve becomes P_i after smoothing, and q_i and p_i denote a coordinate of Q_i and P_i, respectively. Then the energy of a curve after smoothing is defined by

$$E_c = \sum_{i=1}^{N} \frac{1}{l_i + l_{i+1}} \left(\frac{p_{i+1} - p_i}{l_{i+1}} - \frac{p_i - p_{i-1}}{l_i} \right)^2 \tag{2.65}$$

where $l_i = |Q_i - Q_{i-1}|$ is the distance between Q_{i-1} and Q_i. In addition to achieving high smoothness of the new curve, the new nodes on it after smoothing have to be bounded close to the original ones. Therefore an objective function including the energy of the curve and the difference between P_i and Q_i is defined as

$$F_c = \kappa E_c + \sum_{i=0}^{n} \varsigma_i (p_i - q_i)^2 \tag{2.66}$$

where κ and ς_i are constants related to the smoothness of the curve and the

difference from original nodes, respectively. Their different ratios can yield various smoothed curves. Generally, if we fix the difference factor ς_i, bigger smoothness factor κ will generate smoother curves, whereas smaller κ can generate curves closer to original nodes with less smoothness. One can determine the ratio according to particular cases. The summation of the two terms should be made minimal by setting $\frac{\partial F_c}{\partial p_i} = 0, i = 0, ..., N$. This leads to a matrix equation which provides the result for p_i

$$[A][P] = [Q] \tag{2.67}$$

where A is a sparse matrix of size $(N+1)\times(N+1)$ with bandwidth equal to five:

$$A = \begin{bmatrix} c_0 & d_0 & e_0 & 0 & 0 & 0 & 0 & 0 & ... & 0 \\ b_1 & c_1 & d_1 & e_1 & 0 & 0 & 0 & 0 & ... & 0 \\ a_2 & b_2 & c_2 & d_2 & e_2 & 0 & 0 & 0 & ... & 0 \\ 0 & a_3 & b_3 & c_3 & d_3 & e_3 & 0 & 0 & ... & 0 \\ 0 & ... & ... & ... & ... & ... & ... & ... & ... & ... \\ 0 & ... & 0 & a_i & b_i & c_i & d_i & e_i & ... & 0 \\ 0 & ... & ... & ... & ... & ... & ... & ... & ... & 0 \\ 0 & ... & 0 & 0 & 0 & a_{N-2} & b_{N-2} & c_{N-2} & d_{N-2} & e_{N-2} \\ 0 & ... & 0 & 0 & 0 & 0 & a_{N-1} & b_{N-1} & c_{N-1} & d_{N-1} \\ 0 & ... & 0 & 0 & 0 & 0 & 0 & a_N & b_N & c_N \end{bmatrix}$$

in which

$$a_i = \frac{\kappa}{\varsigma_i l_{i-1} l_i (l_{i-1} + l_i)};\ b_i = -\frac{\kappa}{\varsigma_i l_i^2}\left(\frac{1}{l_{i-1}} + \frac{1}{l_{i+1}}\right);$$

$$c_i = \frac{\kappa}{\varsigma_i}\left[\frac{1}{l_i^2 (l_{i-1} + l_i)} + \frac{1}{l_i l_{i+1}^2} + \frac{1}{l_i^2 l_{i+1}} + \frac{1}{l_{i+1}^2 (l_{i+1} + l_{i+2})}\right] + 1;$$

$$d_i = -\frac{\kappa}{\varsigma_i l_{i+1}^2}\left(\frac{1}{l_i} + \frac{1}{l_{i+2}}\right);\ e_i = \frac{\kappa}{\varsigma_i l_{i+1} l_{i+2} (l_{i+1} + l_{i+2})}.$$

The difference factor ς_i was set to be a unit value and the smoothness factor κ was set as $\kappa = C l_{\min}^3$ in Wang & Wu (2006), where C was chosen to be 5 to 10 by numerical tests. In this study we shall employ similar parameters.

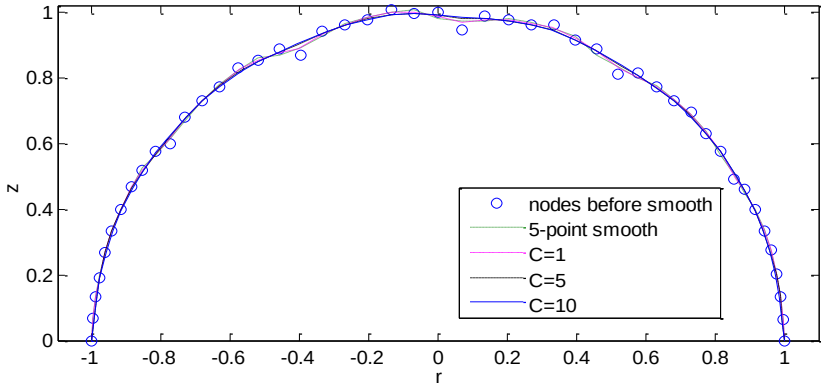

Figure 2.6 Curve smoothing by 5-point smooth and energy smooth with various *C*

Outcomes of nodes smoothing by a 5-point formula in Sun (2007) and the energy method, with *C* from 1 to 10, are shown in Figure 2.6. It can be seen that, energy smooth can better eliminate the saw-tooth behaviour of the original nodes with higher value of *C*, while 5-point smooth method seems to produce a similar outcome as that with a small value of *C*.

Chapter 3 Impact by axisymmetric water column on a rigid plate

In this chapter, the axisymmetric impact by a water column on a rigid plate will be studied without considering the gravity effect. Based on the mathematical and numerical models proposed in Chapter 2 for the axisymmetric problem (see 2.2.2), deeper insight is aimed to be gained for the impact dynamics by the pure liquid column without any air entrapment. Some analytical studies are performed for the initial impact moment as well as the steady state solution, which are investigated combined with the numerical simulation. Numerical difficulties caused by the initial singularity and the long thin jet are tackled. The shallow water approximation for the thin jet calculation will be extended to the axisymmetric case here. The air cavity effect will then be studied preliminarily by including an assumed air cavity near the impact front in the next chapter.

3.1 The computational model

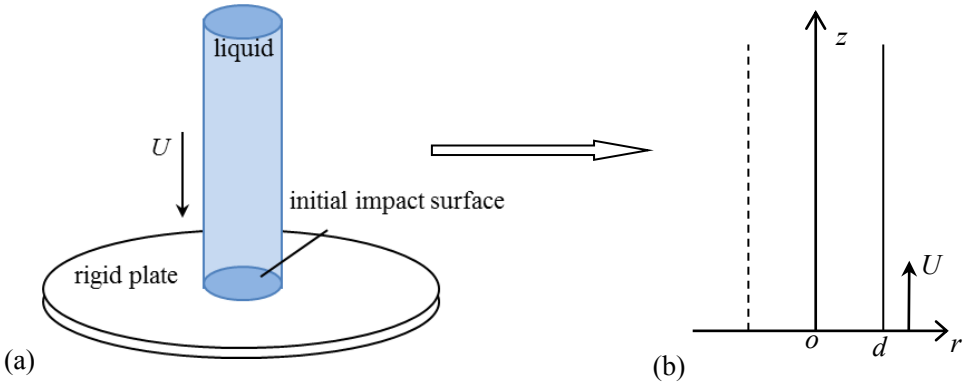

Figure 3.1 (a) sketch of the problem; (b) the computational model: projection of initial impact at a given azimuth $0 \le \theta \le 2\pi$

Consider the case where a cylindrical liquid column with radius d hits on a rigid plate with a constant velocity U without considering the effect of gravity. The main interest of this problem is the initial period of the impact at relatively large velocity; as a result, the effect of the gravity is negligible following the argument in at the end of section 2.1. For the post-initial impact stage, when the impact flow approaches to the steady state, the gravity effect is ignored given the thin fluid layer generated. From Newton's principle, this problem is dynamically equivalent to the case where the water column is at rest and the rigid plate moves against it suddenly at the same

velocity. A cylindrical coordinate system $o-r\theta z$ is established, in which the origin o is located at the impact centre and fixed on the moving plate, and the z-axis is along the axisymmetric axis of the liquid column. The 3D problem can then be solved in a plane coordinate system $o-rz$ as the flow is independent of θ, as shown in Figure 3.1.

3.2 Some analytical solutions for the initial impulse stage

3.2.1 The initial velocity potential

At the initial impulse stage, when the liquid column just impacts the solid plate and no deformation happens yet, this problem could be solved analytically. For this axisymmetric problem ($\frac{\partial \phi}{\partial \theta}=0$), the Laplace equation in the cylindrical coordinate system (see Figure 3.1(b)) can be written as

$$\frac{1}{r}\frac{\partial}{\partial r}(r\frac{\partial \phi}{\partial r})+\frac{\partial^2 \phi}{\partial z^2}=0 \tag{3.1}$$

Following the mathematical model given in 2.1, here the boundary conditions are

$$\frac{\partial \phi}{\partial n}=-U,\ \text{at}\ z=0 \tag{3.2}$$

$$\phi=0,\ \text{at}\ r=d\ \text{when}\ t=0 \tag{3.3}$$

$$\frac{\partial \phi}{\partial n}=0,\ \text{at}\ z\to\infty \tag{3.4}$$

In addition, we also have $\frac{\partial \phi}{\partial n}=0$ along the z-axis (r=0) due to the axisymmetry. Using the method of separation of variables, the solution of Eq. (3.1) can be found to take the form of Bessel series, as

$$\phi=\sum_{n=0}^{\infty}A_n e^{-\lambda_n z}J_0(\lambda_n r) \tag{3.5}$$

where $J_0(x)$ is the zeroth order Bessel function (Abramowitz & Stegun 1972), and A_n and λ_n are unknown coefficients that need to be solved.

From the boundary condition on the free surface in Eq. (2.3), we have for this case

$$\lambda_n = \frac{\mu_n}{d}$$

where μ_n denotes the n^{th} root of $J_0(x) = 0$.

The orthogonality of Bessel functions in this case is (Abramowitz & Stugun 1972)

$$\int_0^d rJ_v(\frac{\mu_m^{(v)}}{d}r)J_v(\frac{\mu_n^{(v)}}{d}r)dr = \frac{d^2}{2}J_{v-1}^2(\mu_m^{(v)})\delta_{mn} = \frac{d^2}{2}J_{v+1}^2(\mu_m^{(v)})\delta_{mn} \tag{3.6}$$

where $\mu_m^{(v)}$ is the mth zero of vth-order Bessel function $J_v(x)$, and

$$\delta_{mn} = \begin{cases} 0, m \neq n \\ 1, m = n \end{cases}$$

is the Kronecker delta function.

Applying it to the boundary condition of the body surface in Eq. (3.2) between $0 < r < d$, we have

$$\int_0^d -A_n \frac{\mu_n}{d} rJ_0{}^2(\frac{\mu_n}{d}r)dr = \int_0^d UrJ_0(\frac{\mu_n}{d}r)dr \tag{3.7}$$

The left hand side of the equation can be solved by Eq. (3.6), and the right hand can be solved by a derivative identity (Abramowitz & Stugun 1972)

$$\frac{d}{dx}\left[x^n J_n(x)\right] = x^n J_{n-1}(x)$$

A_n can then be obtained as

$$A_n = -\frac{2Ud}{\mu_n^2}\frac{1}{J_1(\mu_n)}$$

where $J_1(x)$ is the first order Bessel function.

Therefore the analytical result of the velocity potential at t=0 is

$$\phi(r,z) = -2Ud\sum_{n=0}^{\infty}\frac{1}{\mu_n{}^2 J_1(\mu_n)}e^{-\mu_n\frac{z}{d}}J_0(\mu_n\frac{r}{d}) \tag{3.8}$$

This equation provides a way for validation of the numerical simulation (see section 3.4.1), as well as the value of initial boundary conditions for ϕ_t in the following analytical deductions of the initial pressure.

3.2.2 **Pressure distribution immediately after the impulse**

From the Bernoulli equation, the pressure impulse over an instant impact period from $t=0_-$ to $t=0_+$ could be found to be $\Pi=\int_{0_-}^{0_+} p dt=\int_{0_-}^{0_+}-\rho\phi_t dt=-\rho\phi$ (Batchelor 1967, p.471). It shows that the variation of Π follows that of the initial potential, from 0 at the free surface $r=d$ to a maximum value at the impact centre $r=0$ along the wall (see Table 1 or Figure 3.2). Nevertheless, the impact pressure immediately after the impulse stage at $t=0_+$ was surprisingly found to be a constant value as $P=\rho U^2$ in a similar 2D problem of impact by rectangular fluid on a plate (Wu 2001). The pressure at the intersection point of the fluid and the wall was found to be discontinuous, changing abruptly from $P=\rho U^2$ to the zero ambient pressure. We may speculate whether there are similar features in the present axisymmetric 3D problem.

At the stage just after $t=0_+$, the potential itself is the same as that given in Eq. (3.8), whereas the temporal derivative ϕ_t is no longer infinite as it was between $t=0_-$ and $t=0_+$, and needs to be found. As the method proposed in 2.1.3, ϕ_t also satisfies the Laplace equation in the cylindrical coordinate system

$$\nabla^2\phi_t=\frac{1}{r}\frac{\partial}{\partial r}\left(r\frac{\partial\phi_t}{\partial r}\right)+\frac{\partial^2\phi_t}{\partial z^2}=0 \tag{3.9}$$

With the method of separation of variables, this solution takes the same form of Bessel series as that for the initial ϕ (see Eq. (3.8)).

Substituting the solution of ϕ in Eq. (3.8) into the boundary conditions of ϕ_t on the free surface and the body surface with the effect of gravity ignored. With Cauchy product, Eqs. (2.12) and (2.14) become

$$\phi_t\big|_{r=d}=-2U^2\sum_{n_1=0}^{\infty}\sum_{n_2=0}^{\infty}\frac{1}{\mu_{n_1}\mu_{n_2}}e^{-(\mu_{n_1}+\mu_{n_2})\frac{z}{d}} \tag{3.10}$$

$$\left.\frac{\partial\phi_t}{\partial z}\right|_{z=0}=-U\frac{\partial^2\phi}{\partial z^2}=\frac{2U^2}{d}\sum_{n=0}^{\infty}\frac{J_0(\mu_n\frac{r}{d})}{J_1(\mu_n)} \tag{3.11}$$

where the term of Bessel function has been eliminated in Eq. (3.10) with

$J_0'(x) = -J_1(x)$.

To simplify the calculation with the scheme introduced in 2.1.3, we have from $\phi_t = -U\phi_z + \chi(r,z)$ that

$$\frac{1}{r}\frac{\partial}{\partial r}(r\frac{\partial \chi}{\partial r}) + \frac{\partial^2 \chi}{\partial z^2} = 0 \tag{3.12}$$

The boundary conditions of χ can then be written as

$$\chi\big|_{r=d} = -2U^2 \sum_{n_1=0}^{\infty}\sum_{n_2=0}^{\infty} \frac{1}{\mu_{n_1}\mu_{n_2}} e^{-(\mu_{n_1}+\mu_{n_2})\frac{z}{d}} \tag{3.13}$$

$$\left.\frac{\partial \chi}{\partial z}\right|_{z=0} = 0 \tag{3.14}$$

Because of the inhomogeneous condition in Eq. (3.13), we shall divide χ into two parts

$$\chi(r,z) = F(r,z) + H(r,z)$$

where both *F* and *H* satisfy the Laplace equation. Let $F\big|_{r=d} = \chi\big|_{r=d}$, then we have the boundary conditions for *F* and *H*, respectively

$$F\big|_{r=d} = -2U^2 \sum_{n_1=0}^{\infty}\sum_{n_2=0}^{\infty} \frac{1}{\mu_{n_1}\mu_{n_2}} e^{-(\mu_{n_1}+\mu_{n_2})\frac{z}{d}} \tag{3.15}$$

$$H\big|_{r=d} = 0 \tag{3.16}$$

$$\left.\frac{\partial H}{\partial z}\right|_{z=0} = -\left.\frac{\partial F}{\partial z}\right|_{z=0} \tag{3.17}$$

It can be confirmed that

$$F = -2U^2 \sum_{n_1=0}^{\infty}\sum_{n_2=0}^{\infty} \frac{1}{\mu_{n_1}\mu_{n_2} J_0(\mu_{n_1}+\mu_{n_2})} J_0[(\mu_{n_1}+\mu_{n_2})\frac{r}{d}] e^{-(\mu_{n_1}+\mu_{n_2})\frac{z}{d}} \tag{3.18}$$

satisfies both the Laplace equation and the boundary condition in Eq. (3.15).

Then Eq. (3.17) becomes

$$\left.\frac{\partial H}{\partial z}\right|_{z=0} = -\frac{2U^2}{d}\sum_{n_1=0}^{\infty}\sum_{n_2=0}^{\infty}\frac{\mu_{n_1}+\mu_{n_2}}{\mu_{n_1}\mu_{n_2}J_0(\mu_{n_1}+\mu_{n_2})}J_0[(\mu_{n_1}+\mu_{n_2})\frac{r}{d}] \tag{3.19}$$

According to Eq. (3.16), the condition of H on $r=d$ allows us to write its solution in the form of

$$H = \sum_{n=0}^{\infty} a_n J_0(\mu_n \frac{r}{d}) e^{-\mu_n \frac{z}{d}} \tag{3.20}$$

Combining Eqs. (3.19) and (3.20), and applying the orthogonality of the Bessel functions in Eq. (3.6), we have

$$\begin{aligned}&\int_0^d -a_n \frac{\mu_n^{(0)}}{d} r J_0^2(\mu_n^{(0)}\frac{r}{d})dr \\ &= -\int_0^d \frac{2U^2}{d} r J_0(\mu_n^{(0)}\frac{r}{d})\sum_{n_1=0}^{\infty}\sum_{n_2=0}^{\infty}\frac{(\mu_{n_1}^{(0)}+\mu_{n_2}^{(0)})}{\mu_{n_1}^{(0)}\mu_{n_2}^{(0)}J_0(\mu_{n_1}^{(0)}+\mu_{n_2}^{(0)})}J_0[(\mu_{n_1}^{(0)}+\mu_{n_2}^{(0)})\frac{r}{d}]dr\end{aligned} \tag{3.21}$$

The left hand side of the equation can be resolved from Eq. (3.6), leading to

$$a_n = \frac{4U^2}{\mu_n^{(0)} d^2 J_1^2(\mu_n^{(0)})}\int_0^d r J_0(\mu_n^{(0)}\frac{r}{d})\sum_{n_1=0}^{\infty}\sum_{n_2=0}^{\infty}\frac{(\mu_{n_1}^{(0)}+\mu_{n_2}^{(0)})}{\mu_{n_1}^{(0)}\mu_{n_2}^{(0)}J_0(\mu_{n_1}^{(0)}+\mu_{n_2}^{(0)})}J_0[(\mu_{n_1}^{(0)}+\mu_{n_2}^{(0)})\frac{r}{d}]dr$$

This gives

$$\phi_t = -U\phi_z - 2U^2\sum_{n_1=0}^{\infty}\sum_{n_2=0}^{\infty}\frac{J_0[(\mu_{n_1}^{(0)}+\mu_{n_2}^{(0)})\frac{r}{d}]e^{-(\mu_{n_1}^{(0)}+\mu_{n_2}^{(0)})\frac{z}{d}}}{\mu_{n_1}^{(0)}\mu_{n_2}^{(0)}J_0(\mu_{n_1}^{(0)}+\mu_{n_2}^{(0)})} + \sum_{n=0}^{\infty} a_n J_0(\mu_n^{(0)}\frac{r}{d})e^{-\mu_n^{(0)}\frac{z}{d}} \tag{3.22}$$

Although the solution in Eq. (3.22) is in an analytical form, the series has been found failing to converge at z=0. This may be attributed to the initial singularity at the intersection point caused by the incompatibility of the conditions in Eqs. (3.2) and (3.3). Some suitable treatment could be applied to obtain a realistic solution near the intersection, similar to the work by Lin et al. (1985). However, it is beyond the scope of the current study, since the initial singularity will diminish soon after the initial impact stage (as shown later in the numerical study). The deduction is still provided here for reference to further investigation. The initial impact pressure by the axisymmetric water column is then to be discussed later in a numerical way.

3.3 Nondimensionlisation

To generalize the study, the initial radius of the impact liquid column d, the water

density ρ and the impact velocity U, are utilized to nondimensionalise the physical parameters. As a result, d/U, Ud, ρU^2 and $\pi d^2 \rho U^2$ are used as the characteristic scales for the time t, potential ϕ, pressure P and force F respectively. Correspondingly, r and z can be redefined as r/d and z/d. The dimensionless governing equations and boundary conditions listed in 2.1.2 & 2.1.3 will then take the same form after changing ρ, g and U into the unit value.

Unless specially specified, parameters in the following studies on axisymmetric water column impact in Chapters 3 & 4 refer to the nondimensional ones as defined above. In addition, the impact pressure will be given as the value above the atmospheric pressure.

3.4 Numerical simulation

In the numerical simulation, the computation domain is truncated at z=10, where the fluid is supposed far enough not to be influenced by the impact. Varying grid sizes are employed on fluid boundaries, with l_0 for those within $z \le 1$ and increasing gradually at an equal ratio of λ ($\lambda > 1$), until reaching a maximum grid size of $k_{\max} l_0$. Therefore, for the following i^{th} node outside the region of $z \le 1$ in the direction away from the wall, its grid size l_i takes the form

$$l_i = k l_0, k = \min(\lambda^i, k_{\max}) \tag{3.23}$$

where coefficients within $1 < \lambda < 1.01$ and $k_{\max} \in [2,5]$ can be applied according to the case in consideration.

The marching time step in the numerical simulation has been discussed in 2.2.3, and in this case will simply be decided by Eq. (2.43). The optimal value of the grid size l_0 and the coefficient k_1 in Eq. (2.43) will be evaluated below, to provide convergent results with respect to the element size and the time marching step.

3.4.1 Validation

Based on the analytical solution of the initial potential given in Eq. (3.8), the numerical method can be validated by its comparison between the numerical and analytical results at t=0, as shown in Table 3.1.

Table 3.1. Numerical and analytical results of the velocity potential on the body surface at t=0

r	Φ_{ana}	Φ_{num} (l_0=0.1)	*error1*	Φ_{num} (l_0=0.05)	*error2*
0	-0.5348	-0.53 8	0	-0.5349	0.0002
0.05	-0.534			-0.5338	0.0004
0.1	-0.5315	-0.5311	0.0008	-0.5314	0.0002
0.15	-0.5273			-0.5272	0.0002
0.2	-0.5214	-0.521	0.0008	-0.5213	0.0002
0.25	-0.5138			-0.51 6	0.0004
0.3	-0.5043	-0.5039	0.0008	-0.5042	0.0002
0.35	-0.4929			-0.4928	0.0002
0.4	-0.4796	-0.4791	0.001	-0.4795	0.0002
0.45	-0.4641			-0.464	0.0002
0.5	-0.4464	-0.4459	0.0011	-0.4463	0.0002
0.55	-0.4262			-0.426	0.0005
0.6	-0.4033	-0.4027	0.0015	-0.4031	0.0005
0.65	-0.3773			-0.3771	0.0005
0.7	-0.3478	-0.347	0.0023	-0.3476	0.0006
0.75	-0.3142			-0.314	0.0006
0.8	-0.2756	-0.2745	0.004	-0.2753	0.0011
0.85	-0.2306			-0.2302	0.0017
0.9	-0.1768	-0.1746	0.0124	-0.1762	0.0034
0.95	-0.1087			-0.1076	0.0101
1	0	0	0	0	0

It can be seen that the numerical result of initial ϕ agrees very well with the analytical solution. Compared to the analytical result (ϕ_{ana} in Table 3.1), the relative errors of the numerical results (ϕ_{num}) with grid sizes of $l_0 = 0.1$ and $l_0 = 0.05$ both remain in the order of 10^{-4} to 10^{-2}. The distributions of ϕ on the plate surface is plotted in Figure 3.2, based on much finer grid size of $l_0 = 0.01$ in the numerical simulation and the analytical solution, along with the numerical result with $l_0 = 0.05$.

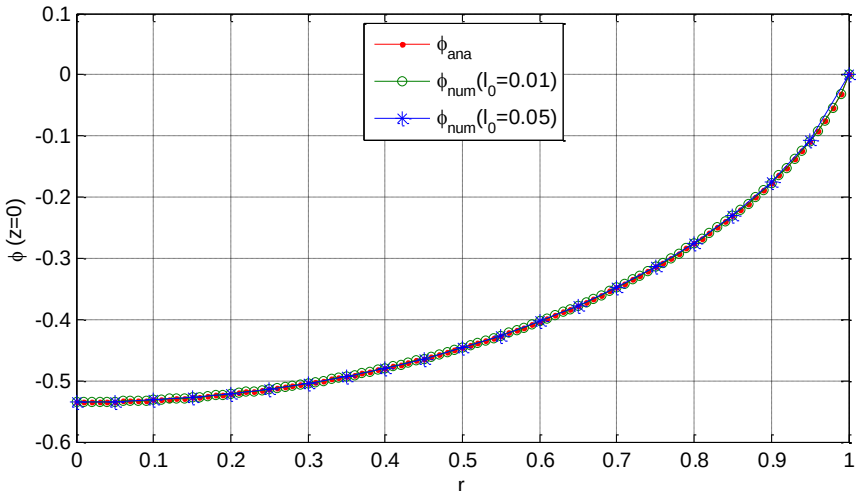

Figure 3.2. Analytical and numerical results of initial ϕ on the plate

3.4.2 **Singularity at the intersection**

For the current case of impact by a body moving suddenly and intersecting the free surface of a water column perpendicularly, from the result of initial ϕ in Eq. (3.8) (plotted in Figure 3.2), we can obtain its radial derivative ϕ_r (i.e. the radial velocity)

$$\phi_r = 2\sum_{n=0}^{\infty} \frac{1}{\mu_n J_1(\mu_n)} J_1(\mu_n r) e^{-\mu_n z} \tag{3.24}$$

At the intersection of the free surface and the wall (1, 0) it then takes the value

$$\phi_r\big|_{(1,0)} = 2U\sum_{n=0}^{\infty} \frac{1}{\mu_n} \tag{3.25}$$

Since $\mu_n > 0$ and $\mu_{n+1} = \mu_n + \pi$ when $n \to \infty$ (Abramowitz & Stugun 1972), the above solution is a divergent infinite series. Therefore we have theoretically $\phi_r \to \infty$ at the intersection point at the initial impact moment.

The variation of ϕ_r at $t = 0$ along the solid plate (at $z = 0$, $0 \le r \le 1$) and the lower part of the free surface (at $r = 1$, over $0 \le z \le 1$) are further plotted in Figures 3.3(a) & (b), respectively, with results obtained analytically from Eq. (3.24) and numerically with the second-order finite difference method.

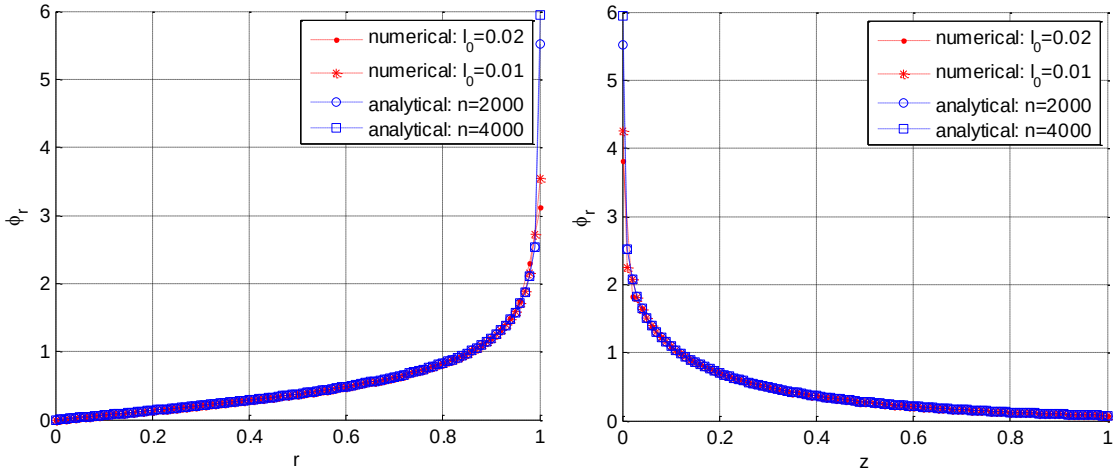

(a) ϕ_r along the solid plate (z=0)

(b) ϕ_r on the free surface (r=1, $0 \le z \le 1$)

Figure 3.3. Initial ϕ_r (radial velocity) distributions near the intersection from (a) the body surface and (b) the free surface. n: number of terms in Eq. (3.24); l_0: the grid size.

It can be seen from Figures 3.3(a) & (b) that, apart from the region near the intersection point, the overall numerical results of ϕ_r agree well with the analytical solution both along the wall and the free surface. In the numerical calculation, the result of the radial velocity at the intersection becomes increasingly larger with smaller grid size, due to the singularity of ϕ_r there. The singularity at the intersection point is caused by the initial incompatible boundary conditions on the wall and the free surface in Eqs. (3.2) and (3.3), though the numerical difficulty associated has been resolved by imposing both the body and free surface conditions there (as discussed in 2.4.1).

Given that the boundary condition for ϕ_t on the free surface is $\phi_t = -\frac{1}{2}(\phi_r^2 + \phi_z^2)$ (see Eq. (2.12)), it can be speculated that the numerical result of initial pressure distribution on the wall right after the impact is likely to be affected by the singularity of ϕ_r near the intersection. The numerical result of initial pressure is shown in Figure 3.4, which can be seen to converge slowly near the intersection with grid refinement. Away from that area, the pressure converges fast with mesh. The analytical deduction of ϕ_t has been discussed in 3.2.2.

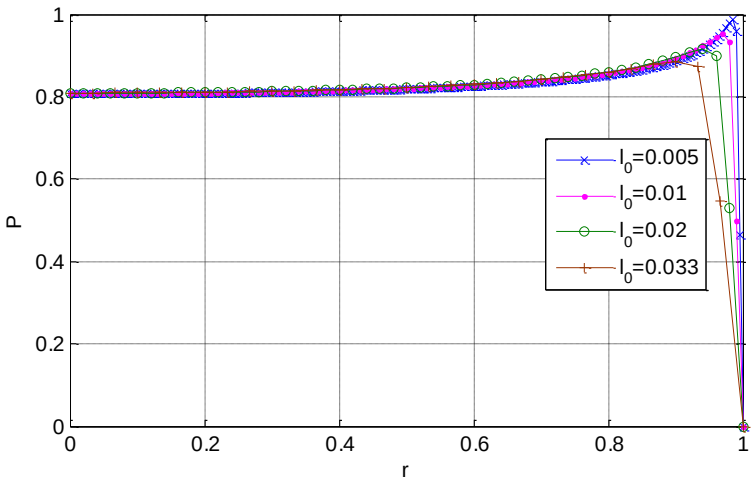

Figure 3.4. Initial impact pressure distribution on the wall with various grid sizes

A conclusion can then be made that, compared to the 2D impact studied by Wu (2001), the pressure is no longer constantly distributed along the wall. Its value seems to be around 0.8 from the impact centre on the plate, gradually increasing to around 1 at the intersection when very fine meshes are employed in the simulation. However, similar to the 2D case (Wu 2001), there is a discontinuity feature for the initial pressure at the intersection, where it drops sharply to zero the ambient pressure on the free surface from a maximum value on the rigid plate. The discontinuity of the initial pressure is also related to the initial incompatible boundary conditions on the wall and the free surface.

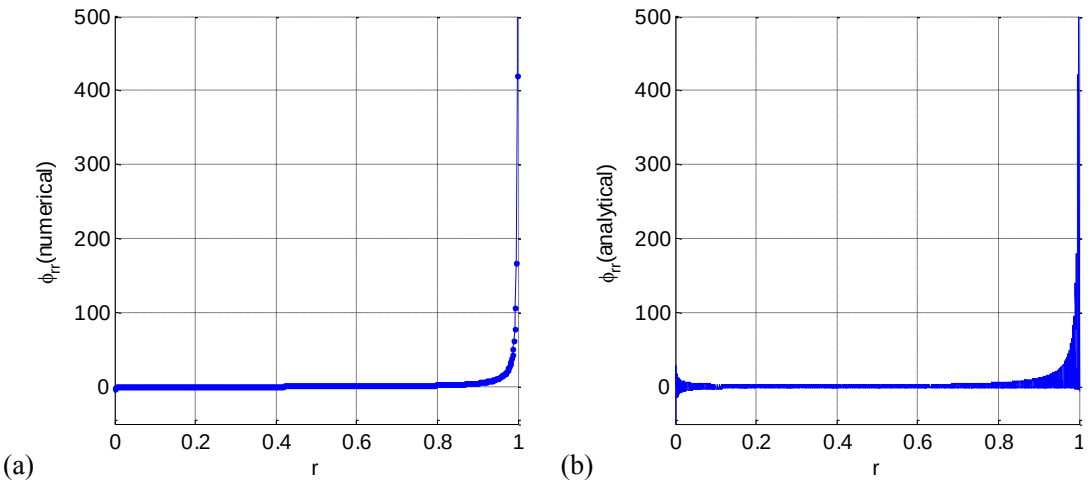

Figure 3.5. ϕ_{rr} along the plate at t=0 from (a) numerical simulation and (b) analytical deduction

We also have obtained numerically $\phi_{rr} \to \infty$ near the intersection at t=0, as can be seen from its distribution on the plate shown in Figure 3.5(a). The numerical result is

also calculated by the second-order finite difference method for ϕ at each node on the body surface, where very small grids with size of $l_0 = 0.002$ have been used. Its analytical expression in the form of Bessel series can be obtained from Eq. (3.8) or Eq. (3.24), with the relation $J_1'(x) = \frac{1}{2}\left[J_0(x) - J_2(x)\right]$

$$\phi_{rr} = \sum_{n=0}^{\infty} \frac{1}{J_1(\mu_n)} \left[J_0(\mu_n r) - J_2(\mu_n r)\right] e^{-\mu_n z} \tag{3.26}$$

However, the result of this equation has strong oscillation along the body surface (z=0), as shown in Figure 3.5(b).

The singularities in the initial ϕ_r and ϕ_{rr} near the intersection caused by the incompatible boundary conditions there will not diminish until a thin fluid layer of free surface jet is formed along the body surface. Before that, numerical results of the intersection point, including ϕ_r and ϕ_{rr}, are increasingly larger in magnitude with smaller grid size, and thus it is expected that a longer thin jet will be generated with smaller grid size in the numerical simulation when the same time step is used.

3.4.3 **Convergence study and the singularity effect**

To evaluate the effect of the initial singularity on the results, as well as for the convergence study with respect to grid size and time step, numerical experiments are carried out with l_0 decreasing from 0.05 to 0.02. The time step is decided by Eq. (2.43), where k_1 is taken as 0.3. The increasing ratio of the grid size is taken as $\lambda = 1.006$ in Eq. (3.23), and the maximum gird size applied in the far end is taken as 0.1 (i.e. $k_{\max} = 0.1/l_0$ in Eq. (3.23)). The development of a long thin jet at t=2.0 and the successive deformations of main free surface profiles are plotted in Figures 3.6(a) and (b), respectively.

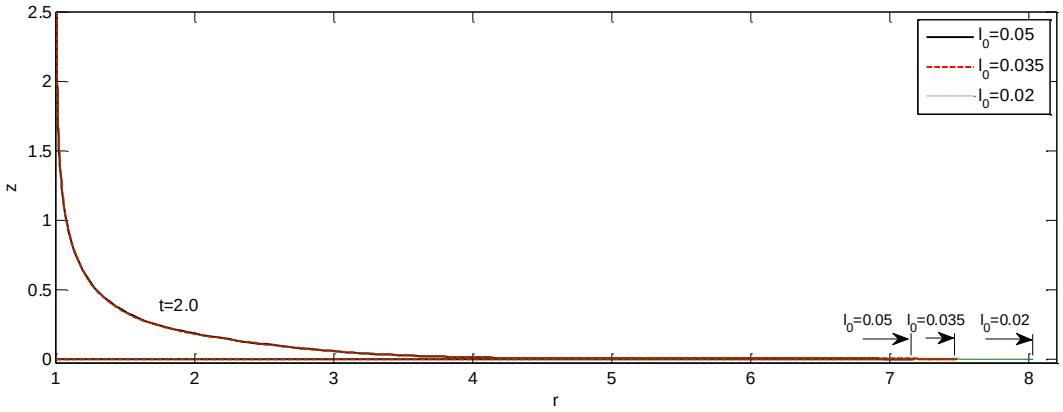

(a) free surface jets with various gird sizes at t=2.0

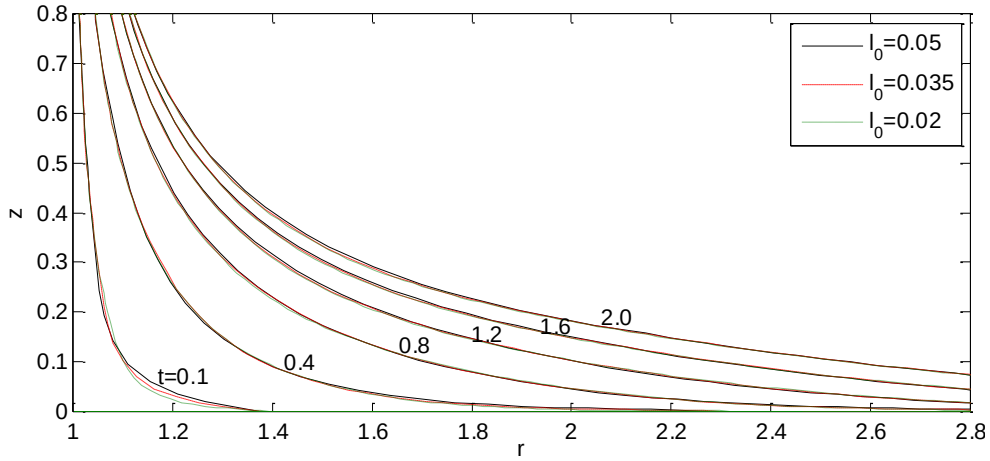

(b) local magnification of lower free surface profiles at different times ($0 < t \le 2.0$)

Figure 3.6. Snapshots of free surface profiles with various gird sizes of $l_0 = 0.05, 0.035$ and 0.02

It can be seen from Figure 3.6(a) that, the length of the free surface jet formed at t=2.0 varies with different grid sizes, and is longer as the jet tip stretches faster with smaller gird size. Nevertheless, from Figure 3.6(b) we can see that, apart from the variation in the length of the thin jet, the main free surface profiles show good convergence with grid size and the corresponding varying time step. Thus it is important to realize that the discrepancy in the jet length, caused by different grid sizes, does not cause divergence in the numerical result at a fixed location in the main fluid domain after certain time. In other words, the numerical results with regards to a fixed position, or the same coordinate, could converge well with grid size and time step.

To further look into the effect of different jet lengths, we shall compare results of the variation of ϕ along the rigid plate (z=0) when two different element sizes of 0.02

and 0.05 are employed in the numerical simulation, as shown in Figure 3.7. It can be seen that $\phi(r,0,t)$ agrees very well at the same r coordinate, despite of the big discrepancy in the jet length caused by the different grid sizes employed. However, the solution can be obtained over increasingly larger wetted surface on the plate when a smaller grid size is employed, for the same time in the numerical simulation. This is owing to the generation of a longer thin jet area. It may also be inferred that numerical computation with finer grids will yield faster the steady state solution at a fixed point.

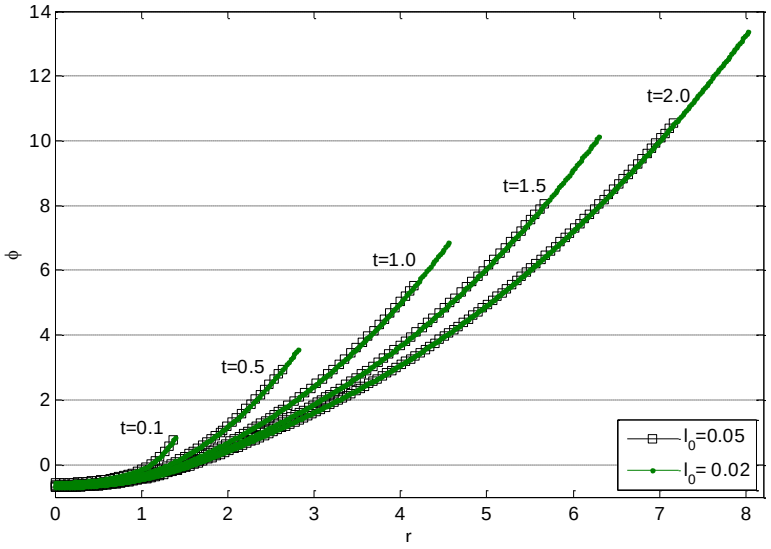

Figure 3.7. Potential variation along the rigid plate from t=0.1 to 2.0, with different jet lengths generated by grid sizes of $l_0 = 0.05$ and 0.02.

The contribution from the thin jet area has been approximated as a dipole distribution with strength $-h_J \dfrac{\partial \phi_J}{\partial n}$ in the boundary integral equation of Eq. (2.63), in which the dimensional form is $h_J U$ in this case. Since the thickness $h_J \to 0$ near the jet tip, the second term on the right hand side of Eq. (2.63) is very small (near 0) when performing the integration there. This explains the reason why the main fluid domain is not very much influenced by the length of free surface jet.

The result of the history of potential distribution on the plate in Figure 3.7 also shows that, after a substantial time, when a thin jet has been formed along the impact surface, singularity caused by the initial incompatible boundary conditions at the intersection has diminished. The radial velocity at the intersection, or the jet tip, becomes finite.

3.4.4 Thin jet approximation for axisymmetric problem

To investigate the impact dynamics continuously until it approaches the steady state, simulation over sufficiently long time needs to be performed. Very long jet will be generated in small thickness, and the inclination angle of the jet tip will approach to 0 when it stretches along the body surface as the impact continues. To look into the steady state solution, it is inappropriate to restrain the jet length according to the threshold value for the inclination angle at the jet tip. Taking consideration of not only the numerical accuracy but also the efficiency in gaining the steady solution for a fixed position as analysed earlier, it is essential to keep the integrity of the thin jet region here. As a result, as proposed in 2.4.2, we shall develop a decoupled local shallow water approximation for the thin jet region for the axisymmetric problem. The velocity potential, satisfying the Laplace equation in the cylindrical coordinate system, is assumed to take the approximate form

$$\phi = A + B\ln r + Cz \tag{3.27}$$

across each element in the thin jet area.

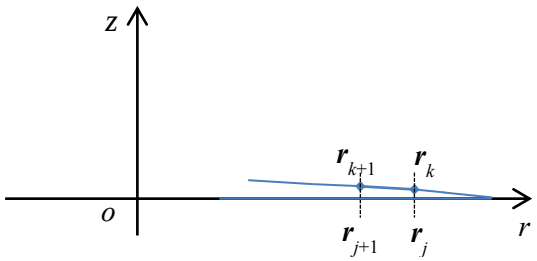

Figure 3.8. Sketch of a segment on the thin jet in the (r,z) plane of the cylindrical coordinate system

Suppose (r_k, z_k) and (r_{k+1}, z_{k+1}) two adjacent nodes in one element on the free surface of the thin jet, denoted by $\vec{r}_k$ and $\vec{r}_{k+1}$, respectively, as shown in Figure 3.8. ϕ_k and ϕ_{k+1} are their velocity potential known from the free surface condition. (r_j, z_j) and (r_{j+1}, z_{j+1}) are the two corresponding intersected points on the body surface from the straight lines perpendicular to it. Substituting the free surface condition into the approximate expression of Eq. (3.27) for the thin jet, we have within the region constituted by $\vec{r}_k$, $\vec{r}_j$ $\vec{r}_{j+1}$ and $\vec{r}_{k+1}$

$$\phi_k = A + B\ln r_k + Cz_k \tag{3.28}$$

$$\phi_{k+1} = A + B\ln r_{k+1} + Cz_{k+1} \tag{3.29}$$

Thus

$$B = \frac{\phi_{k+1} - \phi_k - C(z_{k+1} - z_k)}{\ln r_{k+1} - \ln r_k} \tag{3.30}$$

$$A = \phi_k - Cz_k - \frac{\phi_{k+1} - \phi_k - C(z_{k+1} - z_k)}{\ln r_{k+1} - \ln r_k}\ln r_k \tag{3.31}$$

can be obtained.

The velocity potential within the region, including the corresponding body surface, can then be represented by

$$\phi = \phi_k + \frac{\phi_{k+1} - \phi_k - C(z_{k+1} - z_k)}{\ln r_{k+1} - \ln r_k}(\ln r - \ln r_k) + C(z - z_k) \tag{3.32}$$

where $C = -\dfrac{\partial \phi}{\partial n}$ can be obtained from the boundary condition on the body surface.

The normal velocity on the free surface is then

$$\frac{\partial \phi}{\partial n} = \frac{\partial \phi}{\partial r}n_r + \frac{\partial \phi}{\partial z}n_z \tag{3.33}$$

where $\dfrac{\partial \phi}{\partial r} = \dfrac{B}{r}, \dfrac{\partial \phi}{\partial z} = C$.

Given that B and C are assumed to be constants within each segment on the jet surface, thus Eq. (3.33) can first be applied on the middle point of (r_k, z_k) and (r_{k+1}, z_{k+1}). After that $\dfrac{\partial \phi}{\partial n}$ of the jet node can be obtained from interpolation of values on the adjacent mid-points.

At the same time, the boundary integral equation will be solved over the main fluid domain as in Eq. (2.58), which is decoupled of the long thin jet area and thus is much more numerically efficient. Results obtained for the two regions will be substituted to solve and update the whole fluid domain.

Pressure calculation of the thin jet area on the wall is similar to that in the 2D case

(Wu 2007b). From Bernoulli equation, we can obtain the normal derivative of pressure on the body surface

$$\frac{1}{\rho}\frac{\partial P}{\partial n} = -\frac{\partial \phi_t}{\partial n} - \nabla\phi \cdot \frac{\partial \nabla\phi}{\partial n} \tag{3.34}$$

Given that the boundary condition for ϕ_t is (Wu & Eatock Taylor 1996)

$$\frac{\partial \phi_t}{\partial n} = -\vec{u} \cdot \frac{\partial \nabla\phi}{\partial n} \tag{3.35}$$

where $\vec{u} = (U, W)$ is the constant moving velocity of the body, which equals $\nabla\phi$ on its surface. Substituting Eq. (3.35) into Eq. (3.34), we can get on the body surface

$$\frac{\partial P_j}{\partial n} = 0 \tag{3.36}$$

With the dynamic condition $P_k = 0$ on the free surface, we have $P_j = 0$ on the body surface.

Since the main fluid domain has been decoupled from the thin jet area with a boundary integral equation with regard to ϕ_t similar to Eq. (2.58), ϕ_t on the jet surface attached to the body and $\frac{\partial \phi_t}{\partial n}$ on its free surface do not need to be further solved. The boundary condition of the control surface S_c where the thin jet region starts from, as shown in Figure 2.4, will be approximated by a uniform distribution of $\frac{\partial \phi_t}{\partial n}$ obtained from the value of $\frac{\partial \phi_t}{\partial r}$ on the free surface there. $\frac{\partial \phi_t}{\partial r}$ can be obtained by a difference method for ϕ_t in the r direction, with ϕ_t obtained from Eq. (2.12) (with the gravity term ignored).

3.4.5 **Numerical results**

Dynamics of water column impact without cavity are discussed in this section. The process of free surface elevation as well as the corresponding pressure distribution along the plate is solved numerically. Basic grid size of $l_0 = 0.02$ is employed, with the element distribution the same as prescribed. The successive impact process before t=4.0 is shown in Figure 3.9, where the 3D graphs show the deformation of the water column and the 2D figures illustrate the corresponding local free surface

shape and pressure distribution along the wall at a certain azimuth.

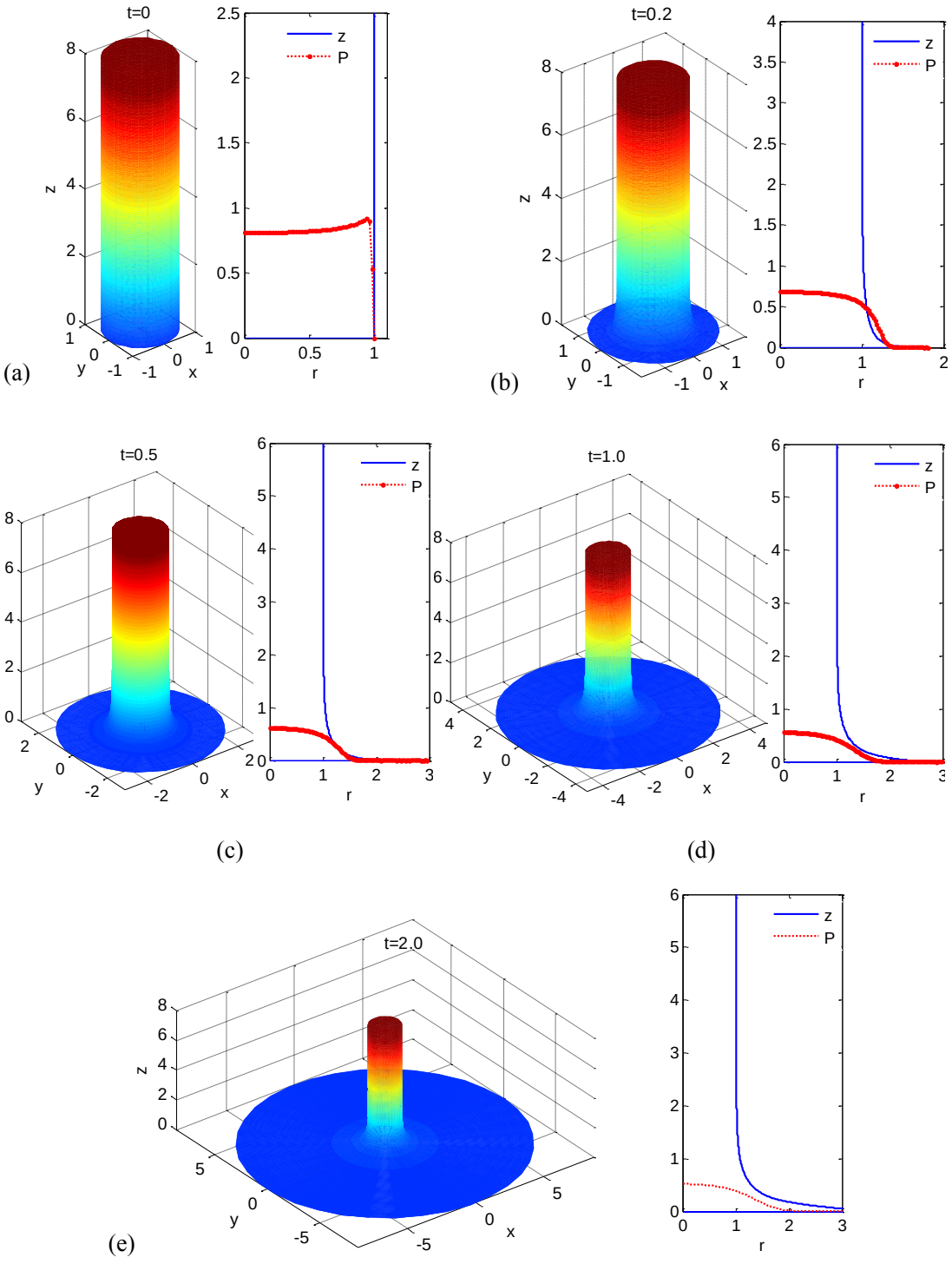

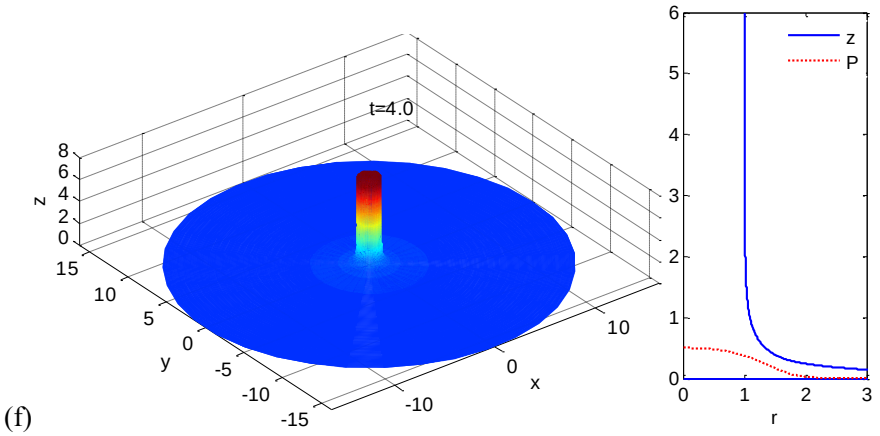

(f)

Figure 3.9. Snapshots of water column impact on the plate: the overall deformation (3D graph in *o-xyz*, where the colour is for a clear display of the free surface shape), and corresponding local free surface profiles and pressure distribution along the plate (2D plot in *o-rz*)

The numerical result of the initial pressure right after the impact at $t = 0_+$, which converges slowly with grid size near the intersection, has been discussed in 3.4.2 (see Figure 3.4). After the initial impulsive stage, a very thin jet begins to form along the wall, as shown in Figure 3.9(b) at t=0.2. At the same time, the discontinuity feature existing in the initial pressure distribution near the water-body intersection point seems to be eliminated with the formation of the thin jet. The pressure falls slowly from its maximum value at the centre to the near-ambient pressure value near the jet root. As the impact continues, the jet becomes longer as it stretches along the plate, during which the overall pressure falls increasingly more slowly until reaching a similar distribution for the same region, as shown in Figures 3.9(c)-(f) from time 0.5 to 4.0.

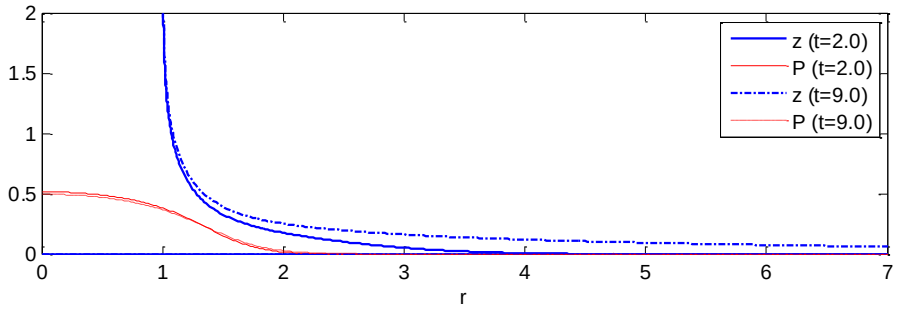

(a)

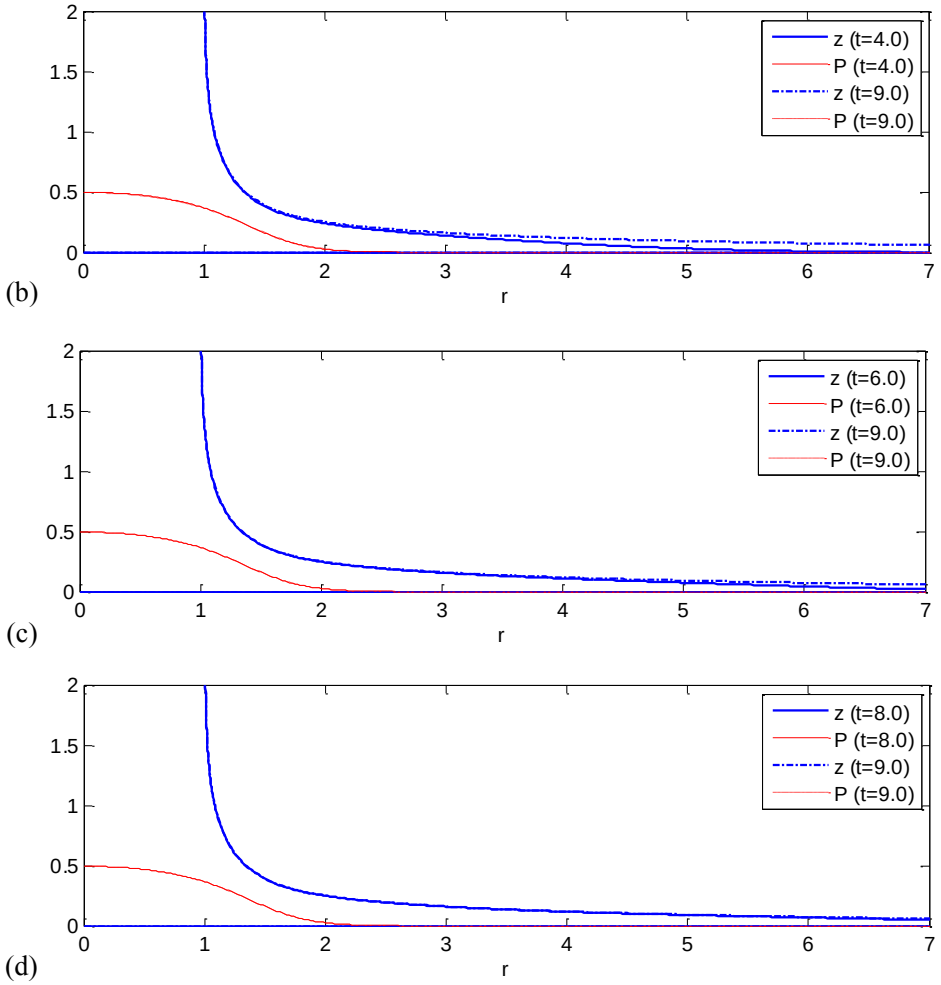

Figure 3.10. Comparisons of local free surface profile and pressure distribution at different time instants (t=2, 4, 6, 8) with those at t=9.

To look into the steady state of the water column impact at constant speed, we shall compare the results of local free surface profiles and pressure distribution at $t = 2, 4, 6$ and 8 with those at t=9, respectively, as shown in Figure 3.10. It can be seen that at time t=2 (Figure 3.10(a)), both the free surface profile and the pressure distribution show evident discrepancy, and no steady state has been achieved over any region; at t=4, the profile of a small region on the local free surface around $1 < r < 1.3$ becomes very similar to that at t=9, as shown in Figure 3.10(b). Yet the overall pressure distribution has small discrepancy. At times t=6 and 8 shown in Figures 3.10(c) & (d), larger regions of free surface profile from around $1 < r < 3$ to $1 < r < 4.5$ agree approximately with that at t=9. The pressure distribution also approaches a steady state over the region (including $r \le 1$) before it drops to the quasi-ambient pressure at around r=2.5. It can be speculated that, although the jet will stretch continuously as the impact continues, increasingly larger area will

approach the steady state starting from the central region. In other words, there exists a steady state of water column impact for any point. It can be obtained by numerical simulation in the time domain, provided that sufficiently long computation time is allowed. The farther the point is away from the impact centre, the longer it takes to achieve the steady state solution. As a result, the analytical result of the steady state should exist theoretically, which needs further investigation. Impact by a water column with small inner angle of 2^{o} was studied by a self-similar method by Sun & Wu (2013), which can be regarded as an approximate solution to the steady state of the impact problem here.

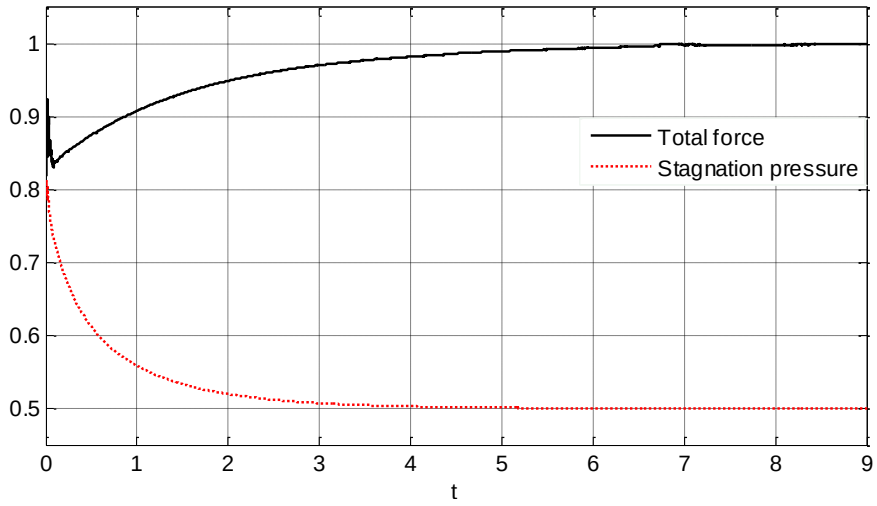

Figure 3.11. History of pressure at the stagnation point and the total force

The history of the pressure at the stagnation point $(0,0)$, as well as the total force on the plate obtained by the integration of the pressure over the wetted surface, is plotted from t=0 to t=9, in Figure 3.11. It can be seen that, after a certain time, pressure at the stagnation point gradually decreases from around 0.8 to 0.5 above the atmospheric pressure, agreeing with the result from the Bernoulli equation for a steady flow (i.e. $\frac{\partial \phi}{\partial t} = 0$). The total force on the plate approaches to 1 at around t=7, which equals the changing rate of the momentum of the impacting flow in the z-axis direction, and thus agrees with the momentum conservation law for a steady flow. This also implies that the main fluid region, excluding the jet area characterized by nearly-zero pressure, has reached the steady state, as analysed in Figure 3.10.

3.4.6 **Analysis on the steady state**

From Bernoulli equation we have on the free surface $z=\varsigma(r,t)$ for the case of a running water column with unit radius impacting on a rigid plate with velocity -1

$$\frac{\partial\phi}{\partial t}+\frac{1}{2}\left[\left(\frac{\partial\phi}{\partial r}\right)^2+\left(\frac{\partial\phi}{\partial z}\right)^2\right]=\frac{1}{2} \tag{3.37}$$

The kinetic condition on the free surface gives

$$\frac{\partial\phi}{\partial r}\varsigma_r-\frac{\partial\phi}{\partial z}=\varsigma_t \tag{3.38}$$

Given the analyses following Figure 3.10, we can assume that the fluid domain located anywhere at $r\le r_1$ will approach a steady state after a sufficiently long impact time (say t_1), while the region beyond continues varying until increasingly larger domain approaches to the steady state. The free surface profile within $1\le r\le r_1$ then takes the steady form $z=\varsigma(r)$, with $\frac{\partial\phi}{\partial t}=0$ in Eq. (3.37) and $\varsigma_t=0$ in Eq. (3.38). Combining Eqs. (3.38) and (3.37) and given that $\frac{\partial\phi}{\partial r}\ge 0$ and $\frac{\partial\phi}{\partial z}\le 0$ in the running flow, we then have on the free surface for the region where the steady state has been reached ($1\le r\le r_1$), that

$$\frac{\partial\phi}{\partial r}=\frac{1}{\sqrt{1+\varsigma_r^2}},\quad \frac{\partial\phi}{\partial z}=-\frac{1}{\sqrt{1+\frac{1}{\varsigma_r^2}}} \tag{3.39}$$

Eq. (3.39) throws light on the velocity distribution along the water surface at the steady state. In the current case of water column impact, the free surface slope is $\varsigma_r\to-\infty$ near r=1, and increases gradually to $\varsigma_r\to 0$ as $r\to\infty$ at the steady state (see Figure 3.10). Therefore, it can be inferred that, for the domain reaching its steady state, $\frac{\partial\phi}{\partial r}$ ought to increase from 0 on the undisturbed free surface at r=1 ($z\to\infty$) and gradually to near 1 if r_1 is big enough to have a small free surface slope there. $\frac{\partial\phi}{\partial z}$ will then varies from -1 for the running water column at the far end ($z\to\infty$) at r=1 towards 0 at $r_1>>1$. On the other hand, considering the initial

singular behaviour of $\frac{\partial \phi}{\partial r}$ near the intersection (see Figure 3.3), we can speculate that before reaching the steady state, the numerical result of $\frac{\partial \phi}{\partial r}$ on the free surface at a particular location at $r \geq 1$ is likely to take a value much bigger than that at the steady state, which will then slowly decrease until reaching the steady state solution.

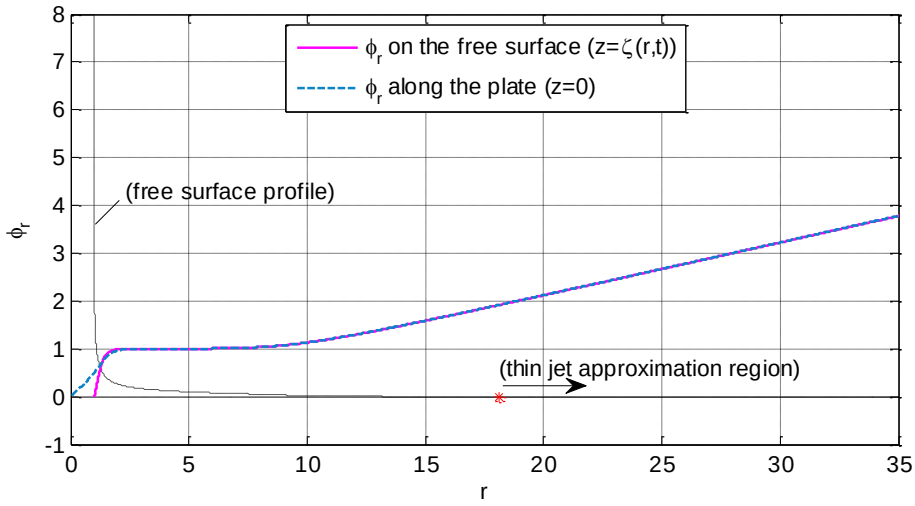

Figure 3.12. Numerical results of radial velocity ϕ_r along the free surface ($z = \varsigma(r,t)$) and the rigid plate ($z = 0$) at t=9; the black dot dash line refers to the free surface profile, and the red asterisk denotes the starting of the thin jet approximation region in the numerical simulation.

The numerical results of the radial distribution of $\frac{\partial \phi}{\partial r}$ at $t = 9$ are plotted respectively on the free surface $z = \varsigma(r,t)$ and along the impact plate at $z = 0$, in Figure 3.12. We can see from the result on the free surface that, the radial velocity $\frac{\partial \phi}{\partial r}$ increases from 0 from r=1 to a value near 1 at around r=4, while beyond that $\frac{\partial \phi}{\partial r}$ exceeds 1 and increases with r. Therefore, combining the results of free surface profiles compared in Figure 3.10(d) between t=8 and t=9, it can be inferred that, only the region approximately within r<4 has reached the steady state by the time t=9. The water surface away at r>4 will continue varying as the numerical simulation carries on until increasingly larger region takes the value of near 1 for $\frac{\partial \phi}{\partial r}$, which implies that the steady state has been reached there.

From the conservation law of mass, across the fluid layer over $0 \sim \varsigma(r,t)$ in the

generated jet region at r, the flow flux is equal to that of the incoming cylinder water flow at the far end, which is in unit radius at unit velocity and thus takes the value π

$$\int_0^{\varsigma} 2\pi r \frac{\partial \phi(r,z)}{\partial r} dz = \pi \tag{3.40}$$

where the distribution of $\frac{\partial \phi}{\partial r}$ is unknown in the z direction. A Taylor expansion approximation for $\frac{\partial \phi}{\partial r}$ could be applied with respect to z across the thin fluid layer around z=0

$$\frac{\partial \phi}{\partial r} = \frac{\partial \phi}{\partial r}\bigg|_{z=0} + \frac{\partial}{\partial z}\left(\frac{\partial \phi}{\partial r}\right)\bigg|_{z=0} z + \frac{\partial^2}{\partial z^2}\left(\frac{\partial \phi}{\partial r}\right)\bigg|_{z=0} z^2 + \ldots \tag{3.41}$$

With the boundary condition of $\frac{\partial \phi}{\partial z}\Big|_{z=0} = 0$ on the rigid plate, we have

$$\frac{\partial^2 \phi}{\partial z \partial r}\bigg|_{z=0} = 0 \tag{3.42}$$

Therefore Eq. (3.41) takes the form

$$\frac{\partial \phi}{\partial r} = \frac{\partial \phi}{\partial r}\bigg|_{z=0} + O(z^2) \tag{3.43}$$

which is only of good accuracy for regions proximate to the rigid plate ($z \to 0$).

With $\frac{\partial \phi}{\partial r}$ known on the free surface $z = \varsigma(r)$ from Eq. (3.39), the application of Eq. (3.43) implies that, for the thin jet area where $\varsigma(r)$ is small, the approximation for $\frac{\partial \phi}{\partial r}$ takes the form

$$\frac{\partial \phi}{\partial r} = \frac{\partial \phi}{\partial r}\bigg|_{z=\varsigma} + O(z^2) \tag{3.44}$$

across the thin fluid layer. This agrees with the numerical results shown in Figure 3.12, from which it can be found that, at a small distance away from the water column root, the distribution curve of $\frac{\partial \phi}{\partial r}$ on the free surface almost overlaps with that on the rigid plate in the jet region. Substituting Eqs. (3.39) and (3.44) into Eq. (3.40), we have for the steady state of the jet region by the first order Taylor

expansion approximation

$$\int_0^{\varsigma(r)} r\left[\frac{1}{\sqrt{1+\varsigma_r^2}}+O(z^2)\right]dz=\frac{1}{2} \tag{3.45}$$

from which a nonlinear differential equation for $z=\varsigma(r)$ could be obtained as

$$\frac{\varsigma}{\sqrt{1+\varsigma_r^2}}-\frac{1}{2r}+O(\varsigma^3)=0 \tag{3.46}$$

where $\lim_{r\to\infty}\varsigma=\varsigma_r=0$. If Eq. (3.46) could be solved, the steady state solution for the thin jet region (say at $r>r_J$) could be obtained from Eq. (3.39). The analytical solution for the steady state of the main impact region demands further study, though a lot of analysis has been made based on the numerical results and theoretical analysis.

3.5 Summary

The axisymmetric problem of a cylinder liquid column impact on a rigid plate at constant relative velocity is studied numerically and analytically in this chapter. The shallow water approximation for the thin jet calculation is successfully extended to the axisymmetric case, and is applied in the decoupled computation for impact with long jet. Some conclusions and insights are gained:

1. The numerical model developed is of very good accuracy, by comparison with the analytical result of the initial potential on the impact surface, and through the agreement of stagnation pressure and total force near the steady state with the Bernoulli equation and momentum conservation law.
2. The impact pressure (above the atmospheric value) immediately after the initial impulse stage at $t=0_+$ is not a constant value as that in the 2D impact case by Wu (2001), and increases from around 0.8 at the impact centre to around 1 at the intersection. It shows a similar discontinuous feature at the intersection point. As the impact continues, the initial pressure peak at the intersection disappears very soon. The maximum pressure stays at the stagnation point (or the impact centre in this case) and falls gradually to 0.5 near the steady state.

3. There is a singularity in the initial radial velocity at the body/water/air intersection (i.e. $\phi_r \to \infty$ from the analytical deduction). It is caused by the initial incompatible boundary conditions there from the free surface and the body surface, and will be eliminated soon after a free surface jet is developed after the initial impact.
4. A longer jet will be generated in the numerical simulation when finer meshes are employed, due to the initial singularity. However, the result at a fixed point converges well with the grid and time step. The feature of a longer thin jet in the numerical simulation is found to provide filed solution over larger wetted surface without influencing the overall result.
5. Expanding region from the impact centre will reach the steady state solution in the time domain. From the analytical deduction on the steady state, the radial velocity ϕ_r should increase from 0 on the undisturbed free surface at $r = 1$ ($z \to \infty$) and gradually to near 1 when r is big enough to have a small free surface slope there. This could be used as a criterion for the steady state in the numerical simulation. Its analytical solution demands further study.

Chapter 4 Axisymmetric water column impact with entrapped air cavity

To investigate preliminarily the effect of an entrapped compressible air cavity on the dynamics of fluid/structure impact, a cavity in spherical shape will be inserted on/near the impact front of the axisymmetric water column in this Chapter. Impact dynamics are computed with numerical techniques developed for the simulation of jet impingement and fluid immersion inside the cavity. The effect of the entrapped air cavity on liquid column impact will be discussed with regard to some key parameters, including the initial air pressure, cavity size, its shape and position, etc.

4.1 Calculation model and numerical set-up

Longitudinal sections of axisymmetric impact models with spherical air cavity entrapped at different locations are shown in Figure 4.1. R refers to the initial radius of the spherical contour of the air cavity. The initial centre of the sphere is at (r_0, z_0), and we have $r_0 = 0$ for the axisymmetric model.

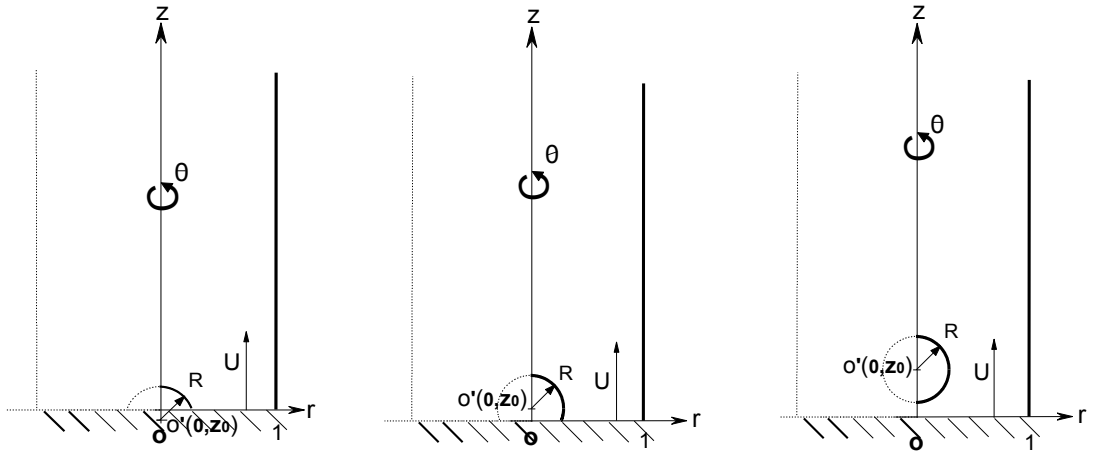

$-R < z_0 < 0$ (thin cavity) $0 < z_0 < R$ (thick cavity) $z_0 > R$

(a, b) cavity on the interface (c) cavity inside the fluid

Figure 4.1. Sketch of axisymmetric water column impact with entrapped air cavity

The definition of the thickness ratio $K_{th} = \dfrac{h_{\max}}{0.5 l_{\max}}$ in Chapter 1 (see Figure 1.7) is extended to the axisymmetric case, with $K_{th} = \dfrac{R + z_0}{\sqrt{R^2 - z_0^2}} = \sqrt{\dfrac{R + z_0}{R - z_0}}$. Consequently,

$-1 < z_0 / R < 0$ denotes a thin air cavity ($0 < K_{th} < 1$); while $0 < z_0 / R < 1$ corresponds to a thick one ($K_{th} > 1$), as shown in Figures 4.1(a) & (b). The air cavity will be fully immersed in water when $z_0 / R > 1$ ($K_{th} = 2$), as shown in Figure 4.1(c). The radius of the 2D air circle in contact with the impact body surface at the initial time will be denoted by R_b, which equals $\sqrt{R^2 - z_0^2}$.

The mathematical and numerical methods for the simulation of impact with air cavity effect have been included in the formulation of 2.1. Assuming a uniform impact velocity over the fluid domain, the initial free surface condition in Eq. (2.3) will also be applied on the cavity surface. Its dynamic condition has been given based on the assumption of ideal and non-condensable gas that undergoes adiabatic contraction and expansion processes (see Eq. (2.8)). The initial dimensionless air pressure in this case, according to the definition in 3.3, is $P_0 = \dfrac{P_a}{\rho U^2}$ for fluid/structure impact in nature. With the atmospheric pressure $P_a = 1.01325 \times 10^5 \,\mathrm{Pa}$ and the density of water $\rho = 1025 \,\mathrm{kg/m^3}$, P_0 is decided solely by the impact velocity. Two initial pressure values of $P_0 = 100$ and 10 are considered in the numerical simulation, corresponding to impact velocities of $U = 0.9934 \,\mathrm{m/s}$ and $3.1441 \,\mathrm{m/s}$ respectively.

Basic grid sizes of $l_0 = 0.015$ and $0.6\, l_0$ are applied respectively for the lower part of the outer free surface and the air cavity surface at the beginning of the simulation. The distribution of elements on the outer free surface is the same as that prescribed at the beginning of section 3.4 (see Eq. (3.23)). Then revised mesh size l_c for the regridding of the cavity, as well as the time marching step, taken into account the deformation of the cavity, are decided by Eqs. (2.64) and (2.44), respectively. c_1 and c_2 are set to be 0.3 and 1.0 in Eq. (2.64).

In the numerical simulation, extra care is needed for the velocity of the middle point on the top surface of the cavity in the *z*-axis direction. External interpolation from one side on the cavity can lead to a non-smooth top surface during its deformation process, due to even a small numerical error. As a result, we shall employ a third-order Lagrangian interpolation method, based on the results of velocity of the four

neighbouring nodes in the z-axis direction, from the two sides of the axisymmetry axis.

4.2 Computation algorithms for the radial cavity jet impingement and fluid immersion

When an air cavity is trapped on the water/body interface at the beginning of the impact, the intersection of the air cavity and the body surface is to flow inwards along the body surface. For the axisymmetric case, the generated radial cavity jet is to meet at the impact centre, where fluid particles will impinge with each other. An algorithm needs to be worked out to continue the numerical simulation.

4.2.1 Velocity calculation at the impingement point

During the process of jet formation along the wall inside the cavity, the jet tip (denoted by node n_0) has been calculated by the algorithm for the intersection point proposed in 2.4.1, where the velocity potential ϕ_{n_0} is unique and known as the value on the cavity surface while the normal velocity has two components consisting of $\left.\frac{\partial \phi_{n_0}}{\partial n}\right|_{S_a}$ on the air cavity and $\left.\frac{\partial \phi_{n_0}}{\partial n}\right|_{S_b}$ on the body surface. In addition, $\left.\frac{\partial \phi_{n_0}}{\partial n}\right|_{S_b}$ has been imposed at the jet tip in the calculation of its velocity, causing it to stick on the wall as stretching along it.

At the time the radial jet impinges, the point on the cavity is expected to be detached from the body surface by a relative velocity along the z-axis generated upon the impingement. After that the cavity-wall intersection point disappears, and the whole cavity will be submerged in water. This could be inferred from the physical phenomenon of the impingement of two liquid jets. Moreover, from the pressure distribution along the body surface at the moment of jet impingement later shown in Figure 4.3(b) (at t=0.0295), we can see that, a relatively large pressure region appears near the impact centre compared with that inside the cavity. Consequently a large pressure gradient appears in the z-direction, surrounding the central impact point. It then leads to the generation of a protruding jet away from the impact surface, which in this case is along the central axis due to the axisymmetry.

To simulate the time instant of the impingement, unknowns at the intersection point

are to be calculated with the same scheme, whereas the node on the cavity is supposed to become independent of, or free from the body surface. Its velocity there will thus be obtained by the interpolation of ϕ and $\frac{\partial \phi}{\partial n}$ on the cavity surface.

4.2.2 Immersion of thick fluid layer after the impingement

After the impingement point becomes detached from the body surface with the algorithm described above, it will move upward at high speed. When the inclination angle at the intersection of the cavity on the body surface is small, for instance those with a thin jet, a protruding vertical jet is expected to form soon after the jet meets (see later the cases studies in section 4.3.2). However, there are cases where the inclination angle is big and the local impinging cavity surface will get merged before a protruding jet is formed. The fluid layer between the air cavity and the body surface is normally thick in such situation, for instance the one shown later in Figure 4.12(a).

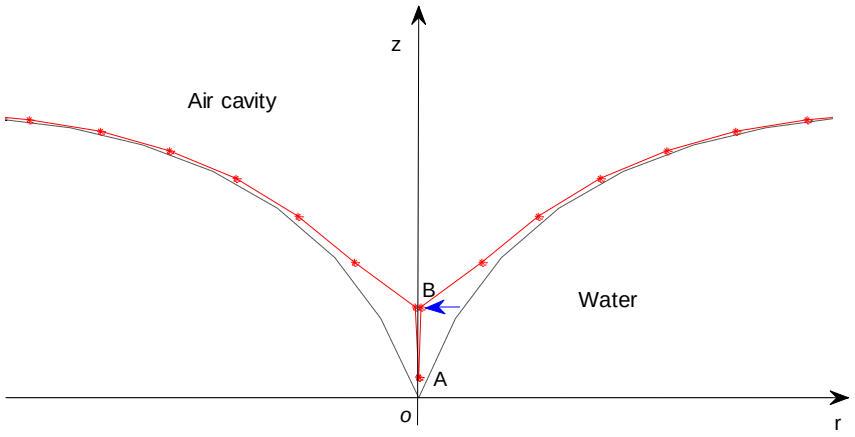

Figure 4.2. Sketch of the immersion of the cavity surface. The solid-dashed line is the cavity surface upon impingement; *AB* is the cavity surface before merging.

As illustrated in Figure 4.2, before the original impingement point *A* is able to shoot upward, its adjacent nodes on the cavity surface, denoted by point *B*, will reach the central axis first. As a result, the cavity boundary between *AB* is to be immersed into the fluid, and a new bottom point is expected to be generated for the cavity. In the numerical simulation, the situation of jet immersion is recognised by setting a critical value for the angle between *AB* and the central axis, δ_{AB}. The merging of point *B* on the central axis is supposed to happen when $\tan\delta_{AB} \le 0.002$ and $r_B \le 0.1 l_0$, by

either artificially setting $r_B = 0$, or carrying on with the simulation for another time step decided by $\delta t = r_B / |u_B|$, where u_B is the radial velocity of B. Node A will be excluded from the cavity surface after that.

Due to axisymmetry, the central axis here has similar impermeable condition as that for a solid boundary in fluid/structure impact. In situations where the initial contact angle between the impacting liquid surface and body surface is very small, for instance, impact by a water droplet or round wave crest, similar phenomenon of liquid boundary merging onto the body surface will happen at the early impact stage. The same treatment method will then be employed for such moment before the formation of an impinging jet along the body surface, for instance in the case of plunging wave impact to be studied in Chapter 5.

4.3 Impact with cavity trapped on the interface ($-1 < z_0 / R < 1$)

The dynamics of axisymmetric water column impact with air cavity in a spherical contour trapped on the interface of the fluid and the rigid plate will first be studied, as the models shown in Figures 4.1(a) & (b).

4.3.1 The initial impact pressure---the effect of entrapped air cavity

We shall first look into the effect of the air cavity on the distribution of initial pressure on the plate right after the impact. It should be noted that, when assuming the initial pressure of the trapped air cavity equal to the ambient value, its magnitude does not have any influence on the initial impact pressure. The result of initial impact pressure by pure liquid column has been discussed in Figure 3.4 (its evolution see Figure 3.9). Here numerical experiments are first carried out for the initial impact instant by water column with different sizes of hemispherical air cavity (i.e. $z_0 = 0$ in Figures 4.1) trapped on the impact surface. The results are shown in Figure 4.3(a), for $R = 0.1, 0.2, 0.4$ and 0.6, respectively.

It can be seen that, upon impact at $t = 0_+$, the pressure distribution along the rigid plate is characterized by two rapidly varying locations falling suddenly to the ambient pressure. One is next to the cavity surface and the other is next to the outer free surface. The entrapment of a hemispherical air cavity can significantly increase the initial impact pressure on the wall, compared with that without air entrapment. In

addition, the smaller the cavity size is, the bigger the pressure is next to the cavity surface. And it is found through numerical experiment that when $R \to 0$ the pressure gradient next to the air cavity approaches to ∞, rather than tending to the result of without air cavity. However, the result of the initial impact pressure at the air cavity/wall/water intersection is likely to be also affected by the singularity caused by the incompatible initial conditions from the free surface and the solid plate, therefore the results near the intersection shown in Figure 4.3 might not reflect the physical reality.

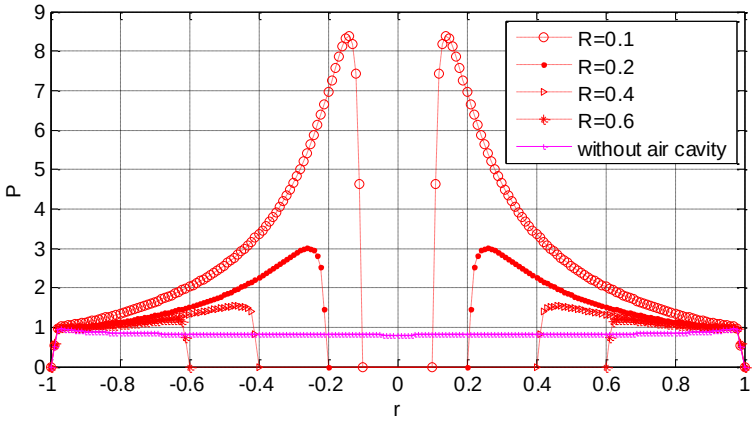

(a) $z_0 = 0$ (hemispheric cavity)

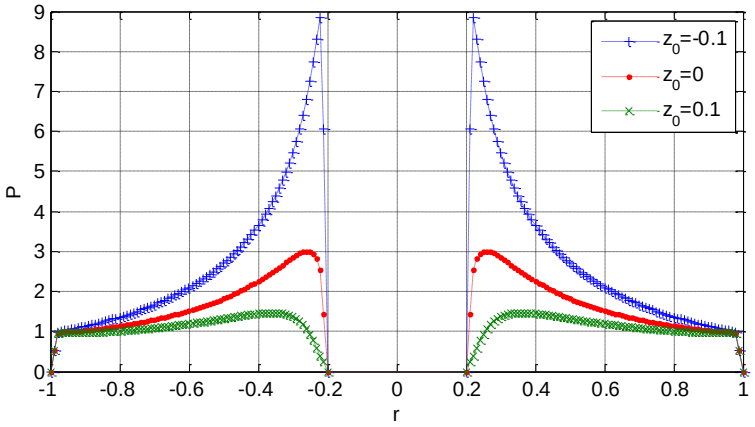

(b) $R_b = 0.2$

Figure 4.3. Initial impact pressure with (a) different air sizes on the body surface ($z_0 = 0$, R_b=0.1-0.6); and (b) different cavity shapes: thin to thick air cavities ($R_b = 0.2$, $z_0 = -0.1, 0$ and 0.1).

Nevertheless, we could perform an analysis on the effect of the air entrapment on the distribution of the pressure impulse on the impact surface during the initial impulsive stage from $t = 0_-$ to 0_+, which is $\Pi = \int_{0_-}^{0_+} P dt$ as defined in Chapter 1 (see also the beginning of section 3.2.2). The Euler equation based on the law of momentum

conservation for inviscid and incompressible fluid reads

$$\frac{\partial \vec{u}}{\partial t} + \vec{u} \cdot \nabla \vec{u} = -\nabla P \tag{4.1}$$

which is written in the dimensionless form following the definitions in section 3.3.

Applying it in the *r*-axis direction and performing a temporal integration over the instant impact period from $t = 0_-$ to 0_+, we have

$$u_{0_+} - u_{0_-} = -\frac{\partial \Pi}{\partial r} \tag{4.2}$$

where u_{0_+} and u_{0_-} refer to the radial velocity of the three-phase (i.e. air, water and rigid plate) intersection point along the impact surface, right before and after the impact, respectively.

At the moment the water column impacts on the rigid plate with the entrapped air, fluid particles near the intersection of the air cavity and the wall are to change direction abruptly and flow inside along the wall, as those on the outer free surface move outward. However, the circumference of the trapped air circle in contact with the wall could be much smaller than that of the water column. If we assume the conservation law of mass is satisfied on the 2D cross-section of the water column on the rigid plate right after the impact, denoting by $u_a^{0_+}$ and $u_f^{0_+}$ respectively the radial velocity of the intersections of the cavity surface and the outer free surface with the plate, we have

$$u_a^{0_+} = \frac{u_f^{0_+}}{R_b} \tag{4.3}$$

where $0 < R_b < 1$ is the radius of the 2D air circle on the rigid plate at the beginning of the impact (when $z_0 = 0$, R_b equals the cavity radius *R*).

For this perpendicular fluid/structure impact, we have $u_a^{0_-} = u_f^{0_-} = 0$ before the impact. Then the combination of Eqs. (4.2) and (4.3) would yield a larger gradient of the pressure impulse, $\frac{\partial \Pi}{\partial r}$, near the intersection of the cavity surface and the plate than that near the outer free surface. Moreover, the smaller R_b is, the bigger $\frac{\partial \Pi}{\partial r}$ is

near the cavity surface. As a result, it can be seen that the distribution of $\frac{\partial \Pi}{\partial r}$ over the initial impulsive stage agrees with that of $\frac{\partial P}{\partial r}$ right after the impact, as shown in Figure 4.3(a).

For the same R_b on the wall, when the centre of the spherical cavity is above the wall (i.e. $z_0 > 0$, as the thick cavity shown in Figure 4.1(b)), the initial cavity surface on the wall inclines towards the impact centre, and it takes smaller pressure gradient for the cavity-wall intersection to flow inward, as can be seen from Figure 4.3(b). On the other hand, a thin air cavity with the same R_b on the wall will yield an initial cavity surface inclined towards the opposite direction, and thus a bigger local pressure gradient is needed for the intersection point to take turn to flow inward.

We can see that both the initial air size R_b on the impact surface and its surface inclination direction on the rigid plate play an important role in the initial impact pressure distribution. Their influence on the following impact dynamics will be examined respectively through case studies in 4.3.2 and 4.3.3; after that the effect of initial air pressure will be looked into in 4.3.4.

4.3.2 Case studies with z_0 =0 and various R (P_0=100)

First the case is considered where an air cavity in a hemispherical shape is trapped on the impact surface ($z_0 = 0$ in Figure 4.1). The initial air pressure is fixed as $P_0 = 100$, while the radius of the hemispherical cavity R, which is also the radius of the air circle on the plate R_b in this case, will be first set to be 0.2, and then bigger as 0.2629 and smaller as 0.1611, respectively, to study the impact dynamics.

i. R=0.2 (V_0=0.0168)

Figure 4.4 shows the numerical results of axisymmetric water column impact with an entrapped hemispherical cavity of initial size $R = R_b = 0.2$ and pressure $P_0 = 100$, in the form of longitudinal sections passing the axisymmetric axis. The local free surface profiles near the impact surface, including the deformation of the cavity surface and the outer column surface, are shown first, followed by the corresponding pressure distribution on the body. The results are illustrated in sequence of the

deformation of the air cavity.

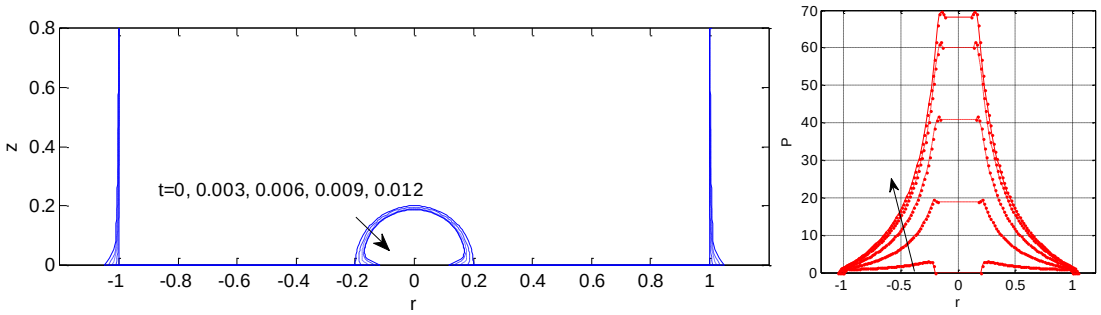

(a) contraction stage ($t \le 0.012$)

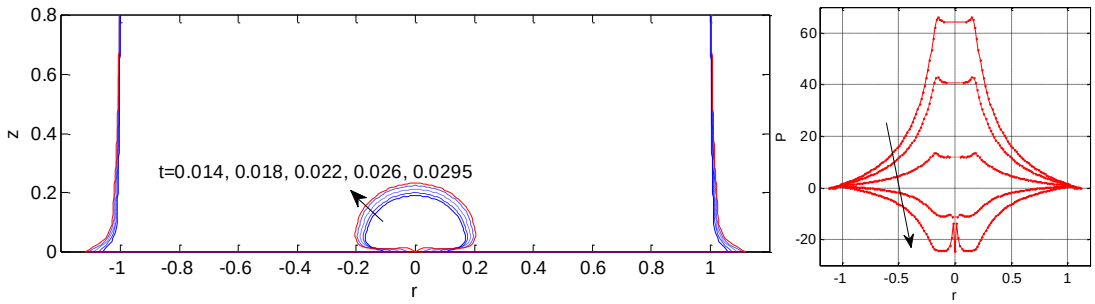

(b) expansion stage i: formation of cavity jet along the wall until impingement ($0.012 \le t \le 0.0295$)

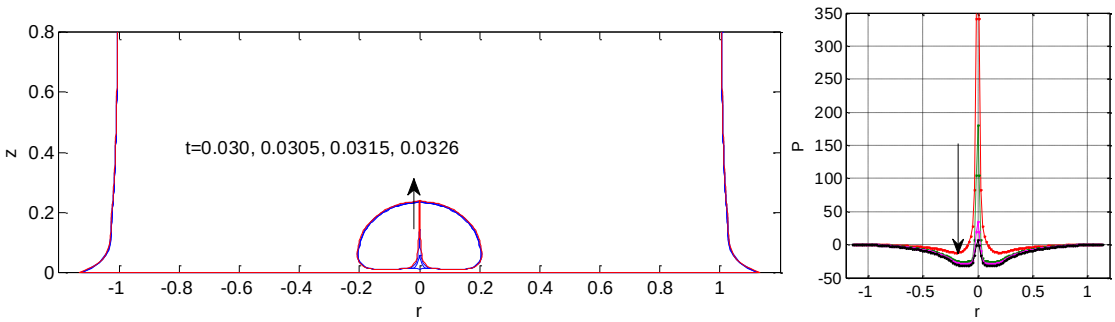

(c) expansion stage ii: formation of the protruding jet spike ($0.0295 \le t \le 0.0326$)

Figure 4.4. Longitudinal sections of axisymmetric liquid column impact with initial hemispherical cavity on the interface: deformation of the free surface near the rigid plate, as well as the corresponding impact pressure, in sequence of the evolution of the cavity ($z_0 = 0$, $R = 0.2$, V_0=0.0168, P_0 =100)

The initial impact pressure on the body surface in this case ranges approximately from 3 next to the cavity surface to 1 near the outer free surface, which has been discussed in Figure 4.3. After the impact starts, the air cavity is compressed by the running liquid. Its pressure inside increases continuously under the adiabatic law, as can be seen in the volume and pressure history plotted in Figure 4.5, and the contraction stage is shown in Figure 4.4(a). The outer free surface keeps its atmospheric pressure there as it flows outward along the plate. Meanwhile, the

overall pressure on the impact surface undergoes fast rising period caused by the contracting air cavity, as the pressure distribution curve shown in Figure 4.4(a). Pressure on the plate has been composed by a central flat region equal to the value inside the cavity and the rest transition region, characterized by a gradual change from a pressure extremum to the ambient value. The pressure extremum point is located near the jet root of the cavity, where the fluid particle is blocked by the wall and has to take a sharp turn to flow inward.

When the air cavity reaches its minimum volume at around t=0.012, its pressure inside reaches the maximum value of 68.15. The large pressure inside then begins to push the surrounding fluid outwards, leading to the expansion of the air cavity, as shown in Figure 4.4(b). The overall pressure on the plate starts to fall fast from the central area next to the air cavity. During this process, the pressure extremum point remains near the jet root of the cavity, despite of the thinner and longer fluid layer developed. This could be explained by an analysis on the flow direction near the impact surface. As the cavity starts to expand under the high pressure inside, the main fluid surrounding the cavity changes its moving direction to outward. However, at the same time, the intersection of the cavity and the body continues to flow towards the impact centre. As a result, a stagnation region is likely to appear near the jet root, leading to a local pressure peak there. The pressure inside the cavity falls below the atmospheric pressure after t=0.0239, causing a negative pressure distribution (relative to the ambient pressure), as shown at t=0.026. The radial jet meets at the impact centre at t=0.0295, and the algorithm described in section 4.2.1 is employed for its velocity calculation to continue the numerical simulation.

The continuing expansion stage of the cavity after the jet impingement is shown in Figure 4.4(c). As expected, a protruding jet starts to form along the central axis away from the impact surface, under the large pressure gradient in the z-axis direction. It moves at a high velocity towards the other side of the cavity surface, at an average speed exceeding 70. At the same time, the cavity continues expanding and the overall negative pressure on the wall keeps decreasing slowly, given that there is only a thin fluid layer between the cavity and the body surface apart from the protruding jet region. A remarkable feature in the pressure distribution appears in the form of a pressure spike, located at the bottom of the protruding jet. It increases to a very high magnitude immediately after the immersion of the cavity into the fluid,

and provides the large acceleration for the early stage of the upward jet. After the protruding jet is well formed as shoots upwards, the magnitude of the pressure peak falls gradually. The simulation stops at t=0.0326 when the protruding jet reaches the top surface of the cavity, after which a ring cavity is expected to be formed but is not included in the current study.

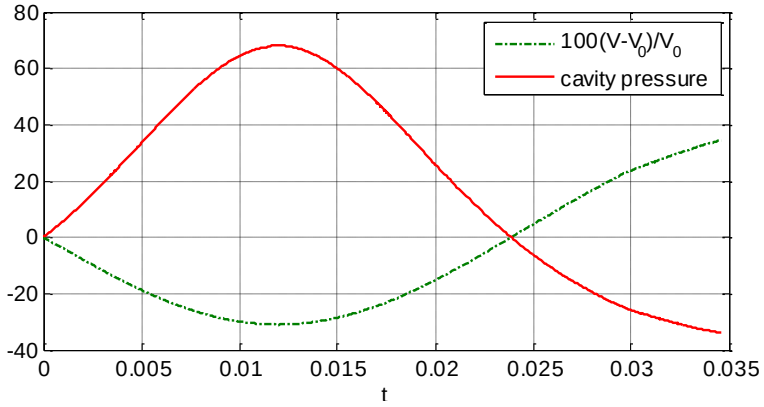

Figure 4.5. Time history of cavity volume $(100(V-V_0)/V_0)$ and its internal pressure $P-P_0$ ($z_0=0$, $R=0.2$, $P_0=100$, $V_0=0.0168$)

ii. R=0.2629 **(**V_0=0.0381**)**

Water column impact under the same initial air pressure of $P_0=100$, with initial hemispherical cavity of radius bigger as R=0.2629 and smaller as R=0.1611 trapped on the interface, are simulated and shown in Figures 4.6 and 4.7, respectively. The corresponding pressure and volume changes

of the cavity during the impact process before the protruding jet reaches its top surface are plotted and compared with that of the case R=0.2 in Figure 4.8.

It can be seen that, the pressure distribution along the wall for impact with trapped hemispherical cavities show similar variations during the contraction and expansion stages of the cavity, in terms of the pressure extremums near the cavity jet root and the pressure spike for the protruding jet. The initial contraction stage takes longer time for bigger cavity, lasting for 0.016, 0.012 and 0.0092 for the case R=0.2629, 0.2 and 0.1611, respectively. It is all during the first expansion stage that the radial jet of the cavity along the body surface meets at the impact centre, at t=0.0455, 0.0295 and 0.0204, respectively. The generated upward vertical jet also touches the top surface of the cavity during the continuing expansion stage, at t=0.0514, 0.0346 and 0.0234,

respectively. Nevertheless, the range of the pressure variation along the plate and inside the cavity is in approximate reverse proportion to the initial cavity radius on the plate. The maximum pressure at the end of the first contraction stage takes decreasing value of 92.62, 68.15 and 45.85 respectively for the three cases. As a result, the overall impact process seems to be more intense (i.e. bigger in pressure peak values and its changing rate, while shorter in the cavity life circle before it is penetrated by the protruding jet), when smaller air cavity is trapped on the impact surface in hemispherical shape. This is in agreement with the initial pressure distribution upon impact for cases with air cavity trapped in hemispherical shape ($z_0 = 0$), as analysed in 4.3.1 (see Figure 4.3(a)).

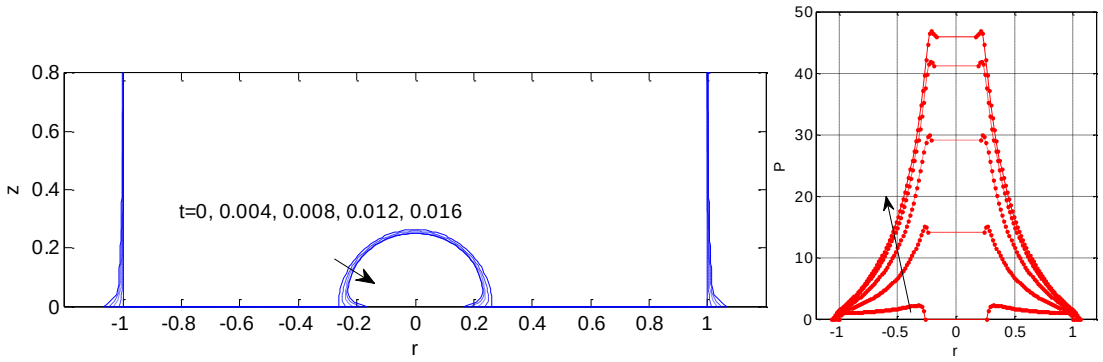

(a) contraction stage ($t \le 0.016$)

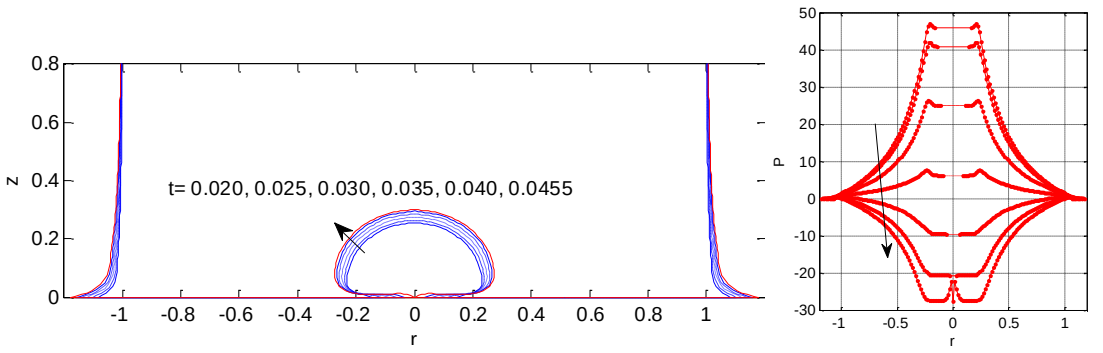

(b) expansion stage I: formation of cavity jet along the wall until impingement ($0.016 \le t \le 0.0455$)

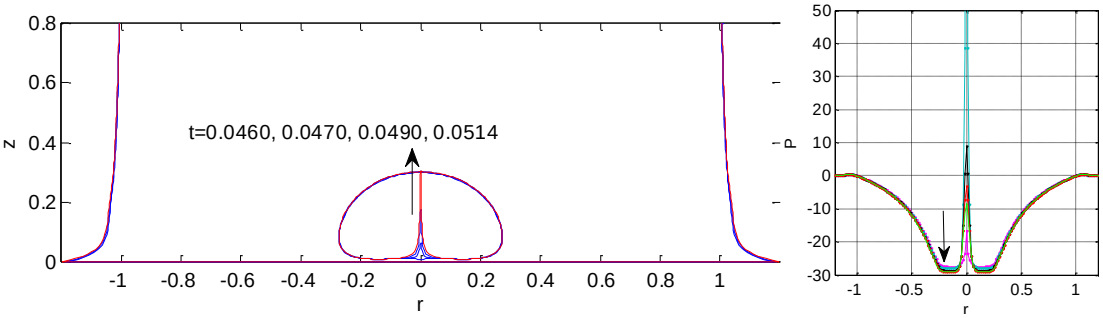

(c) expansion stage II: formation of the protruding jet spike ($0.0455 \le t \le 0.0514$)

Figure 4.6. Longitudinal sections of axisymmetric liquid column impact with initial hemispherical cavity on the interface: deformation of the free surface near the rigid plate, as well as the corresponding impact pressure, in sequence of the evolution of the cavity ($z_0 = 0$, $R = 0.2629$, V_0=0.0381, $P_0 = 100$)

iii. R=0.1611 **(**V_0=0.0088**)**

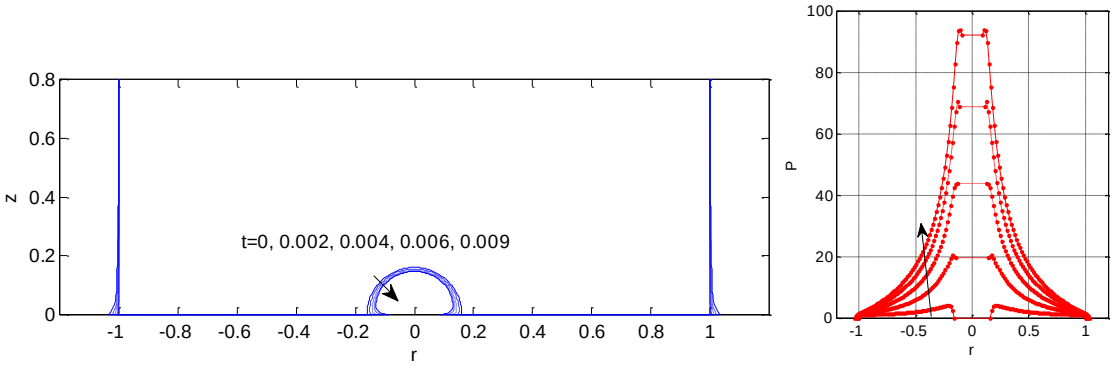

(a) contraction stage ($t \le 0.0092$)

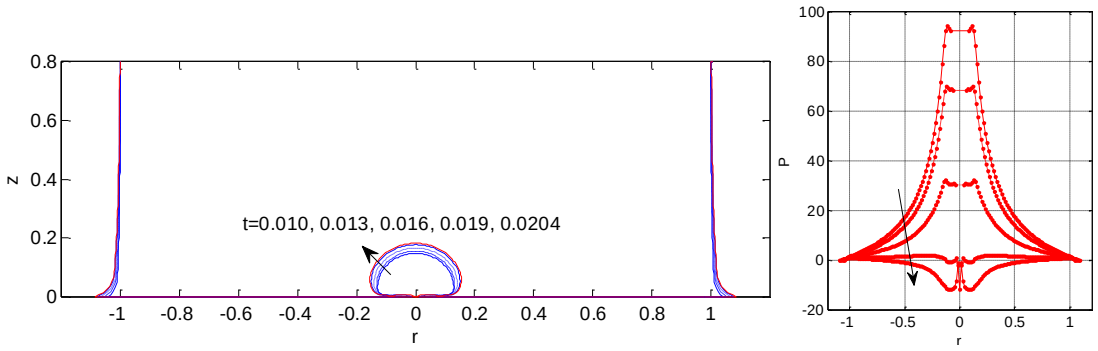

(b) expansion stage I: formation of cavity jet along the wall until impingement ($0.0092 \le t \le 0.0204$)

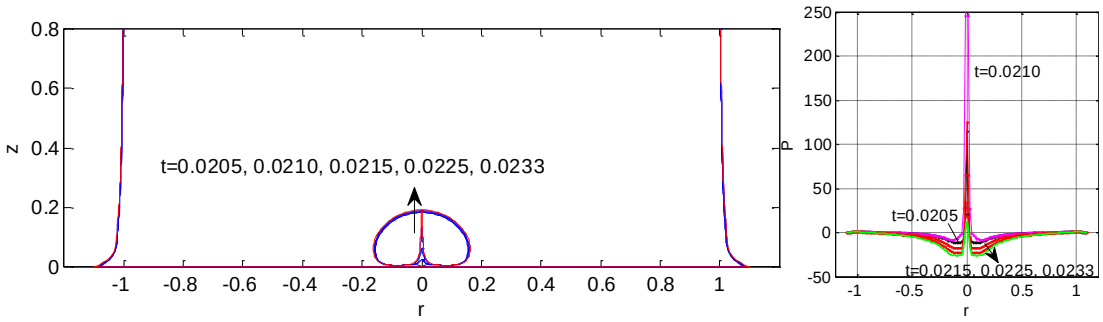

(c) expansion stage II: formation of protruding cavity jet ($0.0204 \le t \le 0.0233$)

Figure 4.7. Longitudinal sections of axisymmetric liquid column impact with initial hemispherical cavity on the interface: deformation of the free surface near the rigid plate, as well as the corresponding impact pressure, in sequence of the evolution of the cavity ($z_0 = 0$, $R = 0.1611$,

V_0=0.0088, $P_0 = 100$)

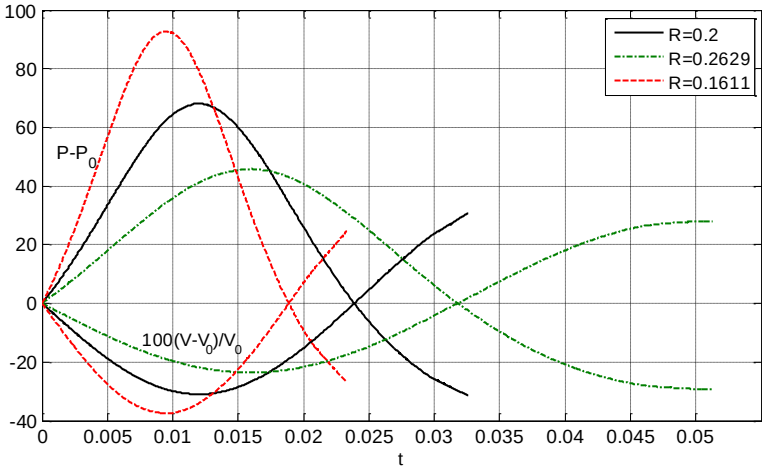

Figure 4.8. Time history of cavity volume ($100(V-V_0)/V_0$) and its pressure inside ($P-P_0$) for impact cases with initial hemispherical cavity radius of R=0.2, 0.2629, 0.1611 respectively, corresponding to volumes of $V_0 = 0.0381, 0.0168, 0.0088$ ($z_0 = 0$, $P_0 = 100$).

4.3.3 Case studies with R_b=0.2 and various z_0 (P_0=100)

Following the pervious case studies on impact with a hemispherical air cavity, we shall proceed to look into the dynamics of impact with air cavities in different shapes (or of different thickness ratio). The initial air pressure and the 2D air circle radius on the body surface stay the same, as $P_0 = 100$ and $R_b = 0.2$, respectively, while the cavity shape is taken as thick ($z_0 = 0.1$ in Figure 4.1) and thin ($z_0 = -0.1$) respectively, to compare with the previous hemispherical case with $z_0 = 0$ studied in 4.3.2 (i).

i. z_0=0.1, R_b=0.2 **(**V_0=0.0381**)**

A thicker air cavity with the centre of its spherical contour located at $z_0 = 0.1$ in Figure 4.1, and thus of radius $R = \sqrt{R_b^2 + z_0^2} = 0.2236$, will be simulated first, which is entrapped on the liquid/solid interface at the beginning of the impact. The initial volume of the cavity is then $V_0 = 0.0381$, the same as that in case R=0.2629 and $z_0 = 0$.

The numerical results of free surface profiles and pressure variation on the plate are shown in Figure 4.9. The corresponding time history of the cavity volume and its pressure inside are shown and compared in Figure 4.10. By the end of the first

contraction stage of the cavity at t=0.0161, the air is compressed to its minimum volume of $0.7804V_0$, and the pressure inside rises to its first maximum value of 41.49 above the ambient pressure, compared to the values of $0.6899V_0$ and 68.15 for the case of $R_b = 0.2, z_0 = 0$ ($V_0 = 0.0168$) discussed in Figure 4.4. The corresponding first contraction stage of the thick air cavity is shown in Figure 4.9(a). Compared with the contraction of a hemispherical cavity, an obvious difference can be observed for the pressure distribution, that there is no pressure extremum near the root of the thick air cavity soon after the initial impact stage. This is because no obvious cavity jet is formed yet as the cavity contracts as a whole. Consequently, the maximum pressure on the plate is the same as that inside the cavity during most of the contraction stage. The pressure distribution on the impact surface is thus characterized by a gradual transition from the cavity pressure to the ambient zero value.

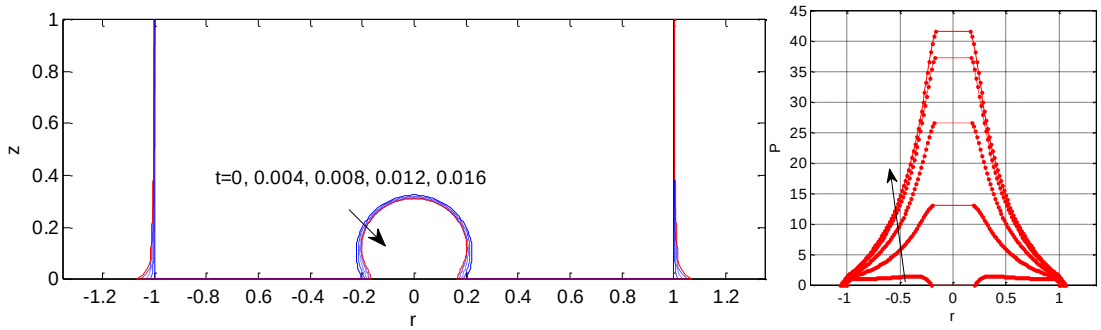

(a) 1st contraction stage ($t \le 0.0161$)

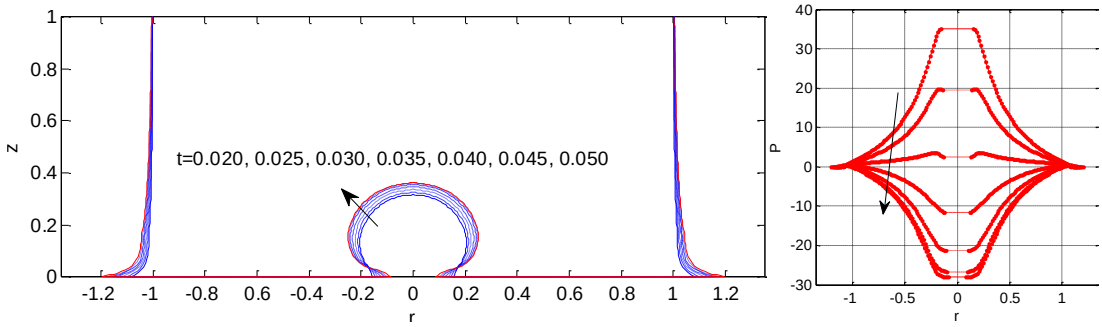

(b) 1st expansion stage: ($0.0161 \le t \le 0.0504$)

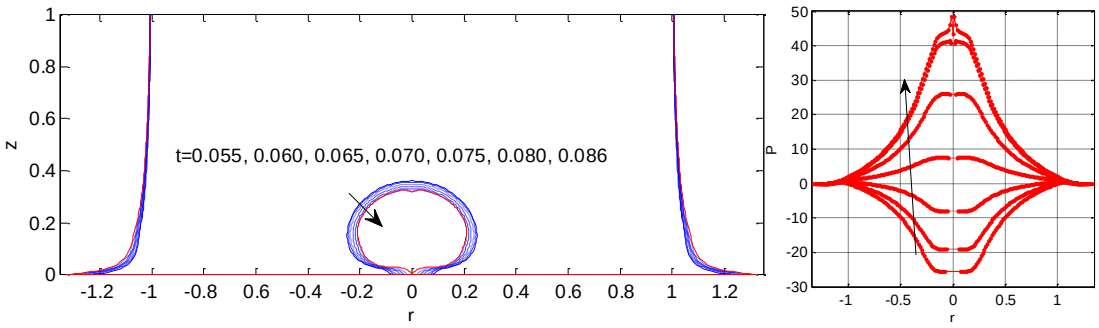

(c) 2nd contraction stage: until impingement of cavity jet at the plate centre ($0.0504 \le t \le 0.0861$)

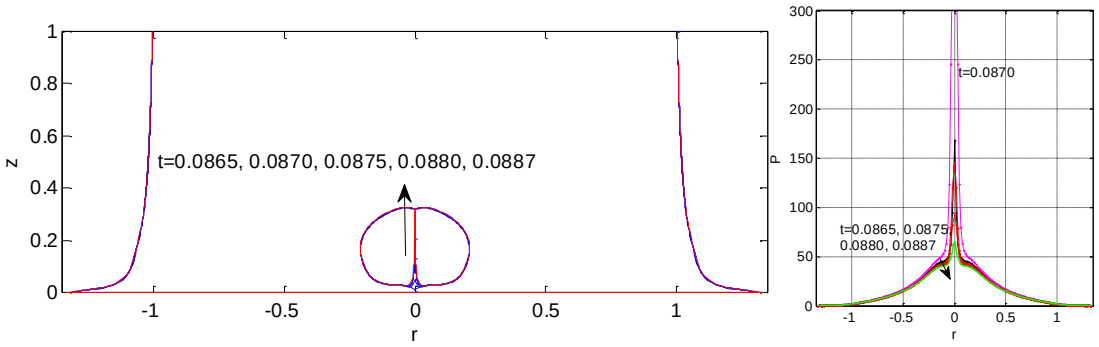

(d) 2nd expansion stage: formation of protruding jet spike ($0.0861 \le t \le 0.0887$)

Figure 4.9. Longitudinal sections of axisymmetric liquid column impact with initial thick cavity trapped on the interface with z_0=0.1 (R_b=0.2, V_0=0.0381, P_0=100): deformation of the free surface near the rigid plate, and the corresponding pressure distribution.

Then the air cavity begins to expand under the acceleration provided by the high pressure inside, leading to the decrease in the cavity pressure as well as the overall pressure on the plate. However, a pressure extremum starts to appear near the jet root of the cavity in early expansion stage, as shown in Figure 4.9(b) fro t=0.025 and 0.030, when the pressure inside the cavity is still above zero. This could also be explained by an analysis on the flow direction near the body surface, similar to what happened in the expansion stages in previous case studies for hemispherical cavities. Despite that the overall cavity is expanding under the high pressure inside, the intersection of the cavity and the body continues to flow inwards, and a cavity jet is formed. There will thus be a stagnation region near the jet root, providing a local pressure gradient for the fluid diversion there. When the cavity continues expanding and its pressure inside falls below zero, the local pressure extremum disappears since the pressure gradient caused by the pressure variance across the cavity surface near the wall becomes in the same direction of and big enough for the jet flow. The

minimum negative pressure on the plate is around -28, happening at the end of the expansion stage of the cavity at t=0.0504, which can be seen from Figure 4.9(b) or Figure 4.10. The overall pressure on the wall increases fast as the cavity contracts again (shown in Figure 4.9(c)), until the radial jet meets at the impact centre at t=0.0861.

A local pressure peak appears on top of the increasing overall pressure at the end of the second contraction stage of the air cavity. Before and at early stages of the formation the upward protruding jet, this local pressure peak at the impact centre first rises very fast as the local fluid particles start to accelerate upward, as the pressure distribution shown in Figure 4.8(d) from t=0.0865 to t=0.0870. When a jet spike has been formed, the pressure peak there starts to decrease as the jet shoots upwards with large velocity, as shown at times after t=0.0875. Meanwhile, the impact pressure next to the peak region still changes according to that of the cavity, since there is only a thin fluid layer between the plate and the cavity. An exception is the short time period during which the concave cavity bottom formed when the cavity is just immersed into the water (see at t=0.0865,) changes gradually into convex shape (see at t=0.0870). During such period, the main pressure on the impact surface shows an overall increment on the plate, due to the large acceleration of fluid particles during the formation of the upward jet.

We can therefore infer that this variation in the pressure peak, at the initial stages of the formation of the protruding jet, is bigger in cases where the radial cavity jet area is overall thicker before the impingement. This is because, when the cavity is just immersed in water, a steeper concave bottom is to take a bigger turn to generate the upward jet, for which larger amount of fluid needs to be accelerated. The jet shoots upward after the impingement in the radial direction, at a mean velocity around 10, until it approaches near the top surface at t=0.0887, as shown in Figure 4.9(d).

We can see that with the same initial cavity pressure ($P_0 = 100$) and air radius on the body surface ($R_b = 0.2$), a bigger cavity volume V_0 for the case of thicker air cavity leads to a pressure variation in smaller range and at a slightly slower changing rate. Moreover, if we compare the current result with that of a hemispherical cavity with the same V_0 (case R=0.2629, $z_0 = 0$ in 4.3.2 (ii)), only a slight decrease in the maximum cavity pressure can be observed, which is caused by the initial cavity

shape (i.e. the effect of the initial inclination angle as discussed in Figure 4.3(b)). The pressure amplitude and changing rate are quite similar for the two cases, as can be seen in Figures 4.8 & 4.10. As a result, for impact with the same initial pressure, the initial volume of the entrapped air cavity has significant influence on the cavity pressure oscillation, while its shape (or surface inclination angle) has relatively smaller effect. Such feature will continue to be looked into in the following case study for a thin air cavity.

ii. z_0=-0.1, R_b=0.2 (V_0=0.0088)

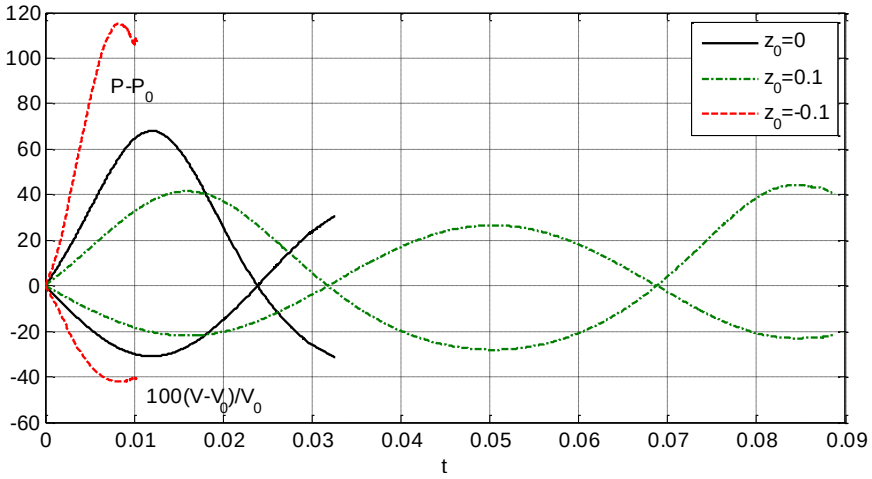

Figure 4.10. Time history of cavity volume ($100(V-V_0)/V_0$) and its pressure inside ($P-P_0$) for impact with thick (z_0=0.1, R=0.2236, and V_0=0.0381), hemispherical (z_0=0, R=0.200, and V_0=0.0168), and thin (z_0=-0.1, R=0.2236, and V_0=0.0088) air cavities. (R_b=0.2, P_0=100)

We then perform numerical simulation on axisymmetric liquid column impact with a thinner air cavity located at $z_0 = -0.1$ in the model shown in Figure 4.1. The same initial size of air circle on the plate $R_b = 0.2$ is kept. Thus the radius of the assumed spherical contour of the air cavity stays as R=0.2236, whereas the actual cavity volume is much smaller as $V_0 = 0.0088$ (which is the same as that in case R=0.1161, $z_0 = 0$ in 4.3.2 (iii)). The numerical results of free surface profiles and corresponding pressure distribution are shown in Figure 4.11, with the corresponding time history of cavity volume and pressure given in Figure 4.10.

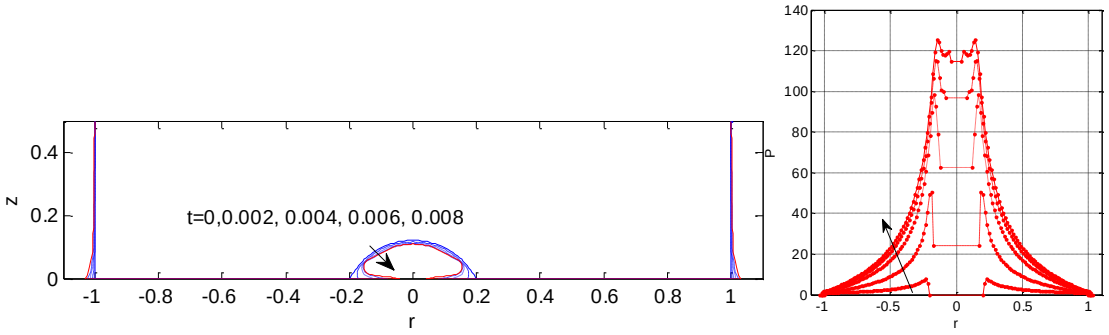

(a) contraction stage ($t \le 0.0082$)

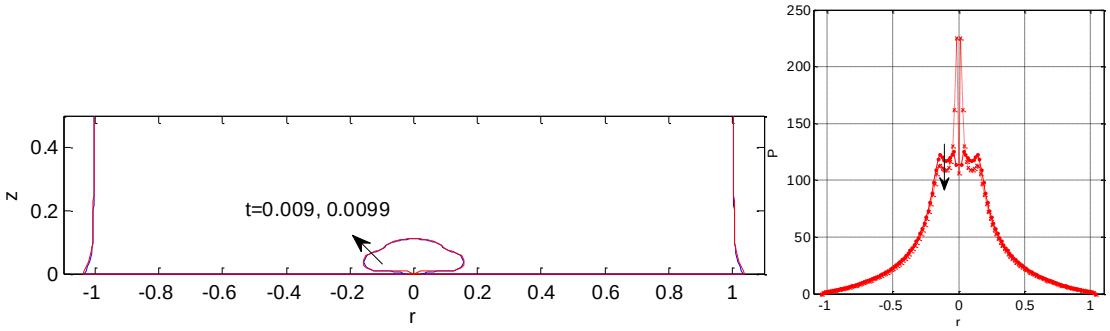

(b) expansion stage I: formation of cavity jet along the wall until impingement ($0.0082 \le t \le 0.0099$)

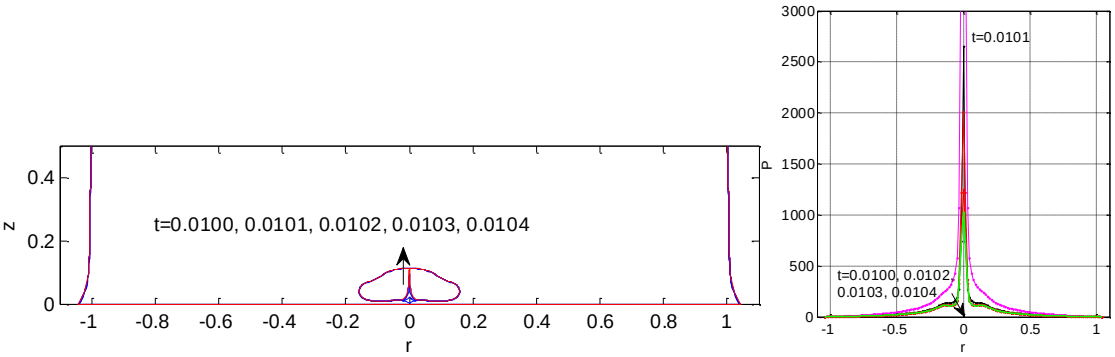

(c) expansion stage II: formation of protruding cavity jet ($0.0099 \le t \le 0.0104$)

Figure 4.11. Longitudinal sections of axisymmetric liquid column impact with initial thinner cavity on the interface when z_0=-0.1 (R=0.2236, V_0=0.0088, P_0=100): deformation of the free surface near the rigid plate, as well as the corresponding pressure distribution.

From the process shown in Figure 4.11(a) when the thin air cavity is compressed by the surrounding fluid, we can see from the pressure distribution that the pressure gradient near the cavity surface increases very fast as the overall pressure rises. Compared with the cavity profiles in the contraction stage of the initial hemispherical cavity with $z_0 = 0$ shown in Figure 4.4(a) and the initial thick air cavity with $z_0 = 0.1$ in Figure 4.9(a), the cavity root in this case has to take a much

steeper turn to flow inward and form a thin jet, a larger local pressure gradient is therefore generated near the cavity root right after the initial impact, as discussed in Figure 4.3(b). After a thin fluid layer has been formed, the local pressure peak decreases in magnitude, as can be seen from the late contraction stage. Moreover, much bigger pressure maximum value (around 115 above P_0) is generated inside the air cavity by the end of its contraction stage at t=0.0082. This could be due to the act of larger pressure gradient generated for the thin air cavity, as well as related to the effect of the smaller initial air volume entrapped. If we compare the current case and the one with hemispherical cavity trapped with the same initial air volume of $V_0 = 0.0088$ (i.e. case R=0.1161, $z_0 = 0$ in 4.3.2 (iii)), from Figures 4.8 & 4.10, it can be seen that the thin cavity here can enhance the maximum cavity pressure a bit, while the pressure oscillation amplitude and speed are similar in the two cases. This verifies again the significant effect of the entrapped air volume on impact pressure for a given P_0.

The radial cavity jet soon meets at the impact centre on the plate at the beginning of the expansion stage at t=0.0099, which is surrounded by a local pressure peak region. This has also been observed in all the previous cases, whereas its amplitude is much bigger in this case, as shown in Figure 4.11(b). This indicates the generation of a faster protruding jet, at a mean speed exceeding 200, as shown in Figure 4.11(c). The outer boundary of the cavity continues expanding, before the fast shooting jet spike touches the top cavity surface at t=0.0104. However, the overall air volume decreases slightly because of the formation of the violent protruding liquid jet in the middle of the cavity. As a result, pressure inside the cavity shows a short unstable increment period near the end, as its history curve shown in Figure 4.10. Meanwhile, pressure spike near the impact centre undergoes first a rising period corresponding to the big acceleration of the jet root, and then a decreasing period after the jet is well formed as shooting up.

4.3.4 The effect of initial air pressure P_0

To study the effect of the initial air pressure on the impact dynamics, the same impact model as the first case studied in 4.3.2 ($z_0 = 0$, $R = 0.2$) will be simulated with a smaller initial air pressure $P_0 = 10$. This indicates a fluid/structure impact happening at higher dimensional velocity, according to the nondimensionlisation

parameters defined in section 3.3.

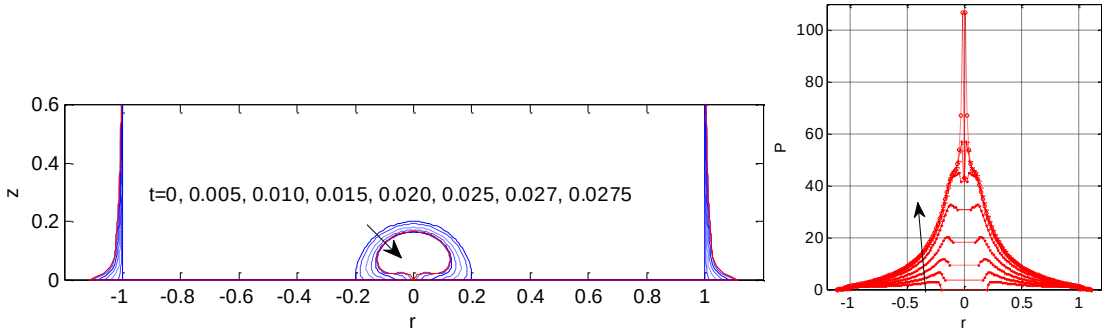

(a) contraction stage I: before the impingement of the radial jet ($t \le 0.0275$)

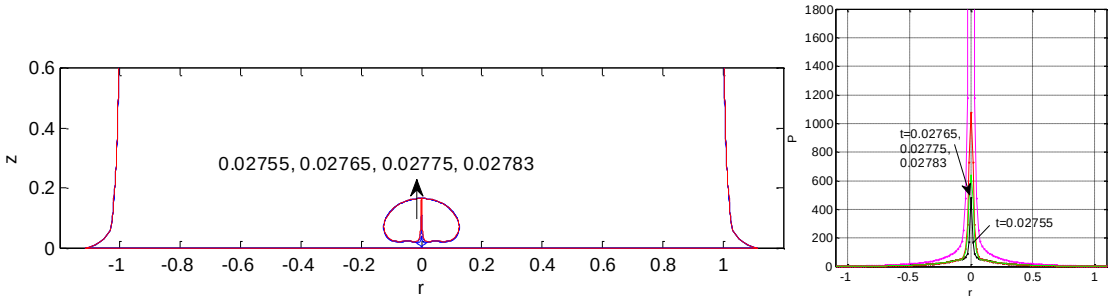

(b) contraction stage II: formation of protruding cavity jet ($0.0275 \le t \le 0.02783$)

Figure 4.12. Longitudinal sections of axisymmetric liquid column impact with initial hemispherical cavity (z_0=0, R=0.2) on the interface, with P_0=0: deformation of the cavity and outer free surface, and the corresponding pressure distribution along the rigid plate.

Numerical results of the impact dynamics before the jet inside the cavity penetrates its top surface are shown in Figure 4.12. The corresponding time history of the cavity volume and its pressure inside are shown in Figure 4.13. Compared to the same impact model but with P_0=100 shown in Figure 4.4, the air cavity here is compressed for a much longer time period by the surrounding liquid, and the minimum volume is much smaller and thus much larger $P_{\max}/P_0$ is generated inside the cavity ($P_{\max}$ the maximum cavity pressure). The radial cavity jet keeps sketching and meets at the impact centre at t=0.02755 near the end of the first contraction stage. The pressure inside the cavity increases to over $5P_0$, as the cavity is compressed to the minimum volume of around $0.3V_0$. Pressure extremum near the jet root of the cavity is obvious during this process, providing the pressure gradiant for the stretching of the cavity jet in spite of the increasing high pressure inside. A big pressure peak is also formed surrounding the impingment point, preparing for the generation of acclerated vertical jet in the z-axis direction.

The process of the jet formation and shooting upward is shown in Figure 4.12(b). Due to the small meeting angle of the radial cavity jet upon impingement, the surface immersion process described in section 4.2.2 happens before the formation of a protruding jet. After that, the vertical jet formed shoots upwards with very large velocity around 500, and penetrates the top cavity surface after a short time duration of 0.0003 at t=0.02783. Pressure on the impact surface first increases significantly from the centre as the fluid at the bottom is about to accelerrate, and then falls fast after the protruting jet is formed and shoots upward, back to a value near that before the impingement.

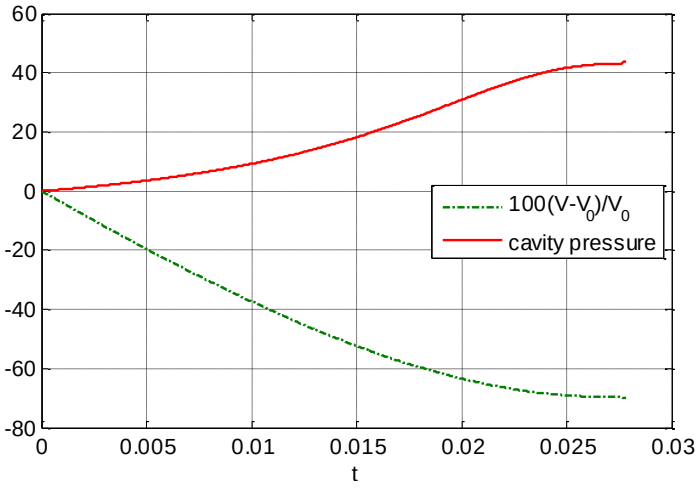

Figure 4.13. Time history of cavity volume and its pressure inside when $P_0 = 10$ ($z_0 = 0$, $R = 0.2$, $V_0 = 0.0168$)

4.4 The energy transfer relation and the first maximum cavity pressure

The first compression stage of the air is of great concern, since it provides a significant increase of overall pressure on the structure under impact by liquid with trapped air cavity in-between, until the first pressure maximum is produced. Here we intend to look into its relation with different initial conditions of the air cavity, by analysing the energy transformation relation between the kinetic energy of the running liquid and the potential energy of the air cavity.

In the process of fluid/structure impact with a deforming air cavity, the work done by the surrounding air (including the inner air cavity and the outside atmosphere) toward the running liquid is

$$W = -\int_0^t \int_{S_a} P u_n dS dt - \int_0^t \int_{S_{outside}} P_0 u_n dS dt = -\int_0^t P \left(\int_{S_a} u_n dS \right) dt - \int_0^t P_0 \left(\int_{S_{outside}} u_n dS \right) dt \quad (4.4)$$

where S_a is the cavity boundary; u_n is the normal component of the velocity of a point on the fluid boundary, and is positive pointing outward according to the definition of $\vec{n}$. The work done by P_0 (the dimensionless ambient air pressure) is obviously on the outer free surface. However, as $u_n = 0$ on the body surface, $S_{outside}$ in the equation can include the body surface to form a closed boundary. This could similarly be applied to air cavity entrapped on the interface of liquid and structure.

The transport theorem gives (e.g. Lamb (1932))

$$\frac{d}{dt}\int_V G dV = \int_V \frac{\partial G}{\partial t} dV + \int_s G u_n dS \quad (4.5)$$

where $\vec{G}(\vec{x},t)$ is a function defined in the volume V. Letting $G = 1$ and V in Eq. (4.5) be the combined volume $V_{outside}$ of the fluid and cavity, and the cavity volume V_a respectively, we have

$$\begin{aligned} \frac{dV_{outside}(t)}{dt} &= \int_{S_{outside}} u_n dS, \\ \frac{dV_a(t)}{dt} &= -\int_{S_a} u_n dS \end{aligned} \quad (4.6)$$

where $S_{outside}$ and S_a are the boundaries of $V_{outside}$ and V_a, respectively. With the law of mass conservation, for this incompressible water flow, we have $V_{outside} - V_a = constant$, and thus $dV_a = dV_{outside}$. Eq. (4.4) then becomes

$$W = \int_{V_0}^{V} \left(P - P_0 \right) dV \quad (4.7)$$

which with the adiabatic law is $W = \frac{P_0 V_0}{\gamma - 1} - \frac{PV}{\gamma - 1} - P_0 (V - V_0)$.

The work done by the entrapped air cavity itself, corresponding to the first term in the brackets of Eq. (4.7), will be discussed separately as

$$W_a = \frac{P_0 V_0}{\gamma - 1} - \frac{PV}{\gamma - 1} \quad (4.8)$$

It can be regarded as the energy change of the air cavity, and thus we can define

$$E_a = \frac{PV}{\gamma - 1} \tag{4.9}$$

as the potential energy of the air cavity, with its initial value as $E_{a0} = \frac{P_0 V_0}{\gamma - 1}$.

With the law of energy conservation, the work done to the water is equal to its increment in the kinetic energy, which in the dimensionless form is

$$K = \frac{1}{2}\int_S \phi u_n dS \tag{4.10}$$

where S is the liquid boundary in calculation.

Substituting $W = K - K_0$ into Eq. (4.7) (with the gravity effect ignored), we can obtain with the adiabatic gas law

$$\left(\frac{V_0}{V}\right)^{\gamma-1} + (\gamma - 1)\frac{V}{V_0} - \gamma = -\frac{\delta K}{E_{a0}} \tag{4.11}$$

where $\delta K = K - K_0$. Applying the above equation to the moment when the air cavity is compressed to its minimum volume $V_{\min}$ and its pressure reaches the maximum value $P_{\max}$, we have

$$\left(\frac{P_{\max}}{P_0}\right)^{\frac{\gamma-1}{\gamma}} + (\gamma - 1)\left(\frac{P_0}{P_{\max}}\right)^{\frac{1}{\gamma}} - \gamma = -\frac{\delta K}{E_{a0}} \tag{4.12}$$

The above equation is in a generalized form of the simplified 1D piston, 2D cylinder and 3D spherical models for the air cavity in Bredmose & Bullock (2008). It is not easy to see the relation straightforwardly from Eq. (4.12), so we plot $\frac{P_{\max}}{P_0}$ (>1) as a function of $-\frac{\delta K}{E_{a0}}$ in Figure 4.14. The minus sign is attributed to the transformation of the kinetic energy of the impacting liquid to the potential energy of the entrapped air cavity during its first compression stage.

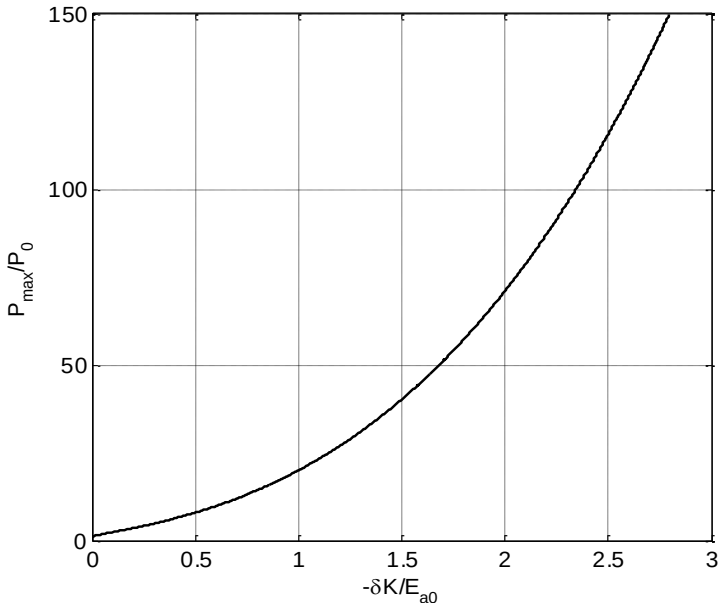

Figure 4.14. Variation of $\frac{P_{\max}}{P_0}$ (>1) as a function of $-\frac{\delta K}{E_{a0}}$ in Eq.(4.12)

Comparing the cases studied in 4.3.2 (i) and 4.3.4, the initial dimensionless air pressure P_0 changes from 100 to 10, with the same hemispherical air cavity trapped on the impact interface, therefore the initial potential energy of the cavity E_{a0} in the latter case is only $\frac{1}{10}$ of that in the former one. At the same time, the change in the kinetic energy of the impacting liquid at the end of the first contraction stage, δK, since it is in the nondimensional form, differs in much smaller range (though it is bigger in the latter case with the cavity compressed harder and for longer time period). As a result, $-\frac{\delta K}{E_{a0}}$ becomes much bigger in Eq.(4.12) for the case of $P_0 = 10$, and thus much larger $\frac{P_{\max}}{P_0}$ is generated than that with $P_0 = 100$, which are respectively around 5.20 and 1.68 according to the numerical simulation. When the initial cavity energy E_{a0} becomes smaller because of smaller initial cavity size V_0, for instance the cases studied in 4.3.2 (i-iii), it can be seen that $\frac{P_{\max}}{P_0}$ also becomes bigger. Thus it can be seen that the magnitude of the initial potential energy of the air cavity plays an important role in the value of $\frac{P_{\max}}{P_0}$ when the air is compressed to its

first minimum volume. Smaller initial potential energy of the air relative to the loss in the kinetic energy of the liquid can produce higher pressure maxima relative to the ambient pressure both inside the air cavity and for the pressure peak in the water above. Such relation and acting mechanism will be further looked into in the study of plunging wave impact in Chapter 5.

4.5 Impact with cavity fully trapped inside the liquid ($z_0 / R > 1$)

When $z_0 / R > 1$ in Figure 4.1, the air cavity will be fully immersed in the impact liquid at the beginning of the impact. Numerical computations will be carried out to look into the effect of such air cavity on the impact dynamics. The distribution of grid size and time marching step will be the same as that utilized in above simulations.

4.5.1 The initial impact pressure

The initial pressure distribution on the rigid plate will be examined first to shed light on the effect of air cavity fully immersed in the impact liquid. Numerical experiments will be performed with air cavity of various sizes and located at different distances away from the impact surface, of which the results are shown in Figure 4.14.

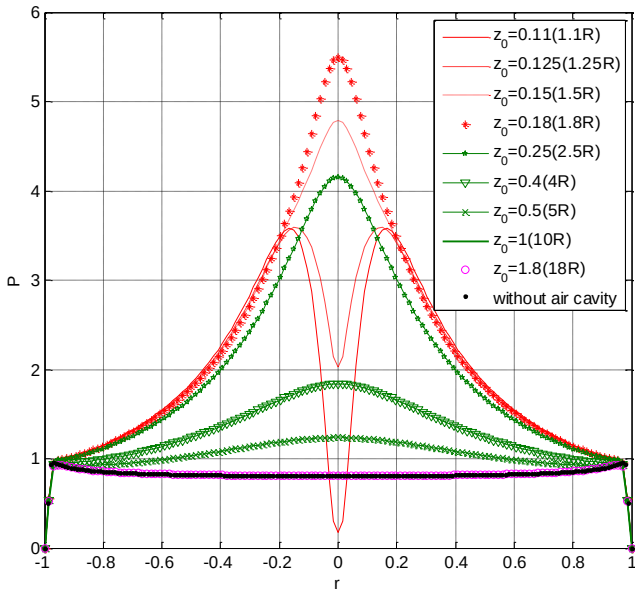

(a) $R = 0.1$

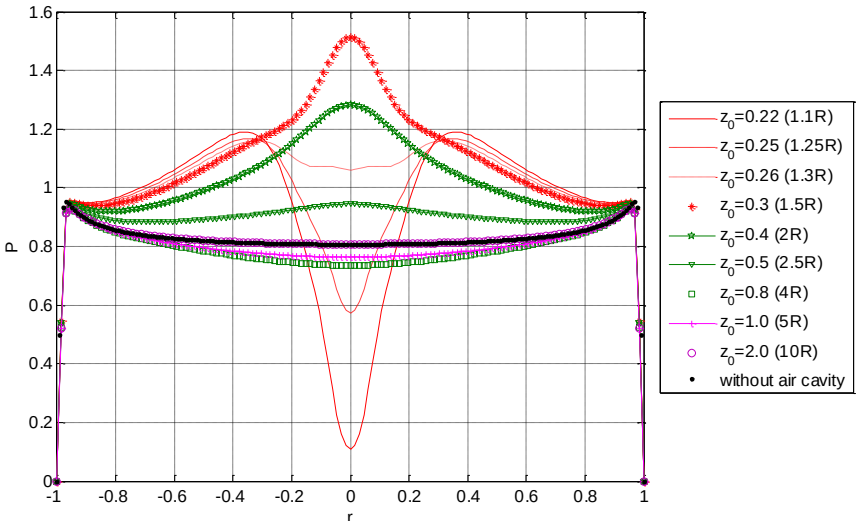

(b) $R = 0.2$

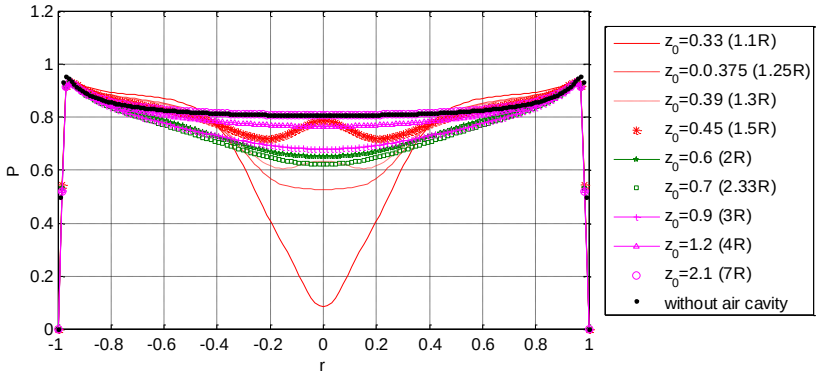

(c) $R = 0.3$

Figure 4.15. Variation of initial pressure distribution on the rigid plate, with spherical air cavity of radius *R*=0.1, 0.2 and 0.3 completely entrapped in the water column located at $z_0 = 1.1R$ and then gradually farther away.

It is surprising to see from Figure 4.14 that the overall pressure on the impact surface does not keep decreasing as the cavity is paced farther away at the beginning of the impact. The impact centre stays as a pressure extremum point. It is a valley value when the initial cavity is placed very close to the rigid plate, for instance in Figures 4.14(a), (b) & (c) for $z_0/R = 1.1$. When *R* is small, there is a pressure peak circle surrounding the impact centre, as shown in Figures 4.14(a) & (b) for the case of *R*=0.1 and 0.2. The pressure peak value is bigger with smaller *R*, similar to the previous case where air cavity is entrapped on the impact surface, until the extremum point disappears as *R* increases, as the result shown in Figure 4.14(c) for *R*=0.3.

When the initial cavity is placed farther away from the impact surface, the pressure extremum value at the impact centre (i.e. the stagnation point) first increases

continuously until a peak value is reached. It happens at $z_0/R = 1.8$, 1.5 and 1.5 ($z_0 = 0.18$, 0.3 and 0.45) respectively for cases of R=0.1, 0.2 and 0.3. The smaller the cavity is, the larger the maximum stagnation pressure is. The overall pressure on the plate starts to decrease when the initial cavity is farther away, to a minimum value even below that when no air is entrapped in the liquid. The locations of air cavity corresponding to the happening of the pressure minimum are around $z_0/R = 10$, 4 and 2.33 ($z_0 = 1$, 0.8 and 0.7), respectively. Beyond it the overall pressure gradually rebounds to the value as if no air cavity is involved in the impact liquid, for instance, when $z_0/R > 18$, 10 and 7 ($z_0 = 1.8$, 2.0 and 2.1) for R=0.1, 0.2 and 0.3 respectively.

Note that the result of initial impact pressure is independent of the initial air pressure value, since it is only at the beginning of the impact, and the adiabatic deformation of the air cavity has not yet started to act on the fluid dynamics. It can be speculated that the big variation of initial pressure caused by different locations of the air cavity is likely to have a significant effect on the following impact process.

4.5.2 **Numerical results**

Numerical simulations are performed in this section for water column impact with spherical cavity of radius R=0.2 located at different distances away from the impact surface, of which the initial pressure distribution has been discussed in Figure 4.14(b). z_0 is assumed to vary from 0.22 (1.1R) to 0.3 (1.5R), and the initial air pressure is set to be $P_0 = 10$ and 100 respectively. The results of $z_0 = 0.22$ and $z_0 = 0.3$ with $P_0 = 10$ are first shown in Figures 4.15 & 4.16 respectively.

i. $z_0 = 0.22$ (1.1R), $P_0 = 10$

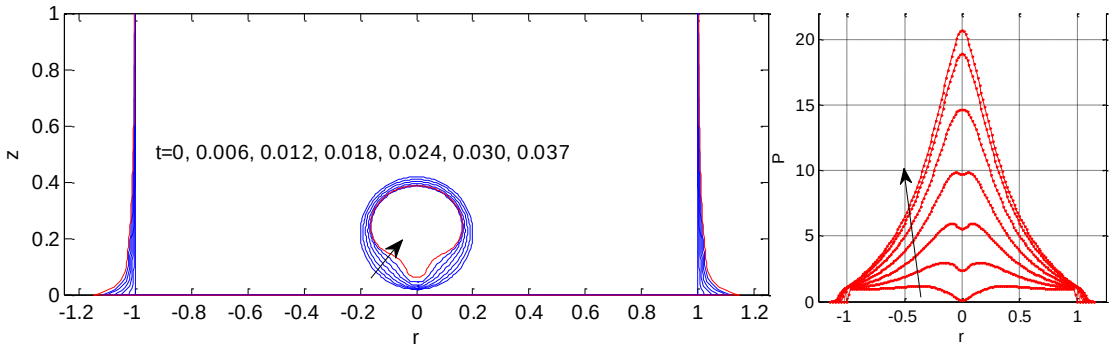

(a) contraction stage ($t \le 0.0367$)

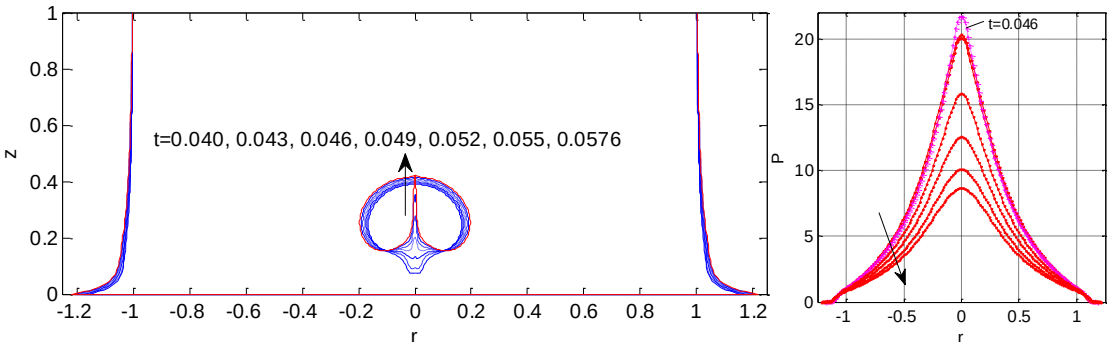

(b) expansion stage: before the penetration of the vertical jet ($0.0367 \le t \le 0.0576$)

Figure 4.16. Longitudinal sections of axisymmetric liquid column impact with spherical cavity trapped inside: deformation of the free surface near the rigid plate, and the corresponding impact pressure distribution, in sequence of the deformation of the cavity ($z_0 = 0.22$, $R = 0.2$, $P_0 = 10$)

From the contraction stages for $z_0 = 0.22$ and 0.3 shown respectively in Figures 4.15(a) and 4.16(a), an obvious distinction in the shape of the cavity bottom could be observed. With the pressure valley distribution around the impact centre at the early stage for impact with a cavity close to the body surface (see Figure 4.14(b) for $z_0 = 0.22\,(1.1R)$), a big pressure gradient is generated focusing towards the central axis in the radial direction. The lower part of the air cavity bottom is therefore squeezed by the surrounding liquid, and the cavity is formed into a bulb shape after the initial compression stage, as t=0.037 shown in Figure 4.15(a). At the same time, the stagnation pressure rises fast to become a central peak point on the impact pressure curve. Whereas when the initial air cavity is initial placed farther away at $z_0 = 0.3(1.5R)$ (as discussed in Figure 4.14), the initial pressure at the impact centre is a peak value and thus there is no inward radial pressure gradient as that for $z_0 = 0.22\,(1.1R)$, but a small outward one in the radial direction and an upward one in the z-axis direction. The cavity bottom is thus flattened slightly as being compressed in Figure 4.16(a).

In the following expansion stage after the air cavity is compressed to its minimum volume, a vertical jet begins to form at the bottom of the bulb shape cavity, as shown in Figure 4.15(b). At the same time the lower part of the cavity is pushed gradually upward to merge with the protruding jet. During this process the stagnation pressure at the plate centre rises first and then drops back when the vertical jet is shooting upward fast (after t=0.046). This is similar to the pressure variation in previous

studies on impact with air cavity trapped on the interface, when radial jet just meets at the impact centre before a fast shooting vertical jet is formed. During the expansion process for $z_0 = 0.3(1.5R)$ shown in Figure 4.16(b), on the other hand, there is no such pressure variation. The overall pressure drops gradually as the cavity expands, and at the same time a vertical jet is formed inside the cavity shooting upwards. This is because, there is no such impediment as the bulb shape cavity in Figure 4.15(a) or concave cavity bottom along the plate in Figure 4.9(b), during the formation of the shooting jet spike.

ii. $z_0 = 0.3\ (1.5R)$, $P_0 = 10$

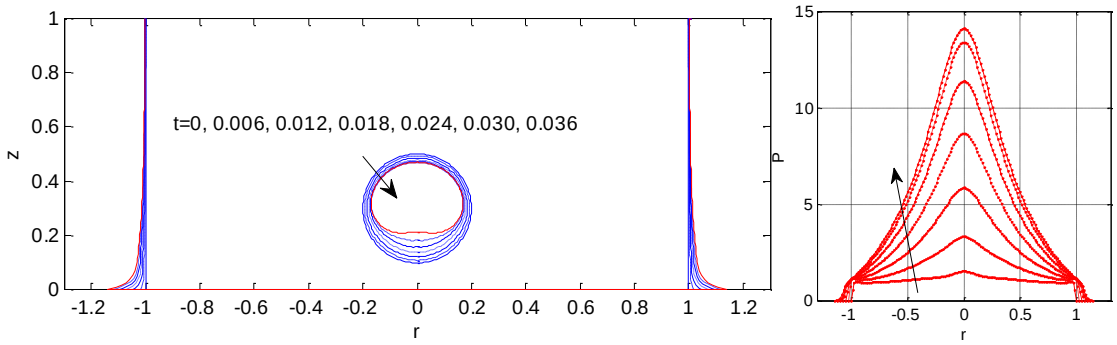

(a) contraction stage ($t \le 0.036$)

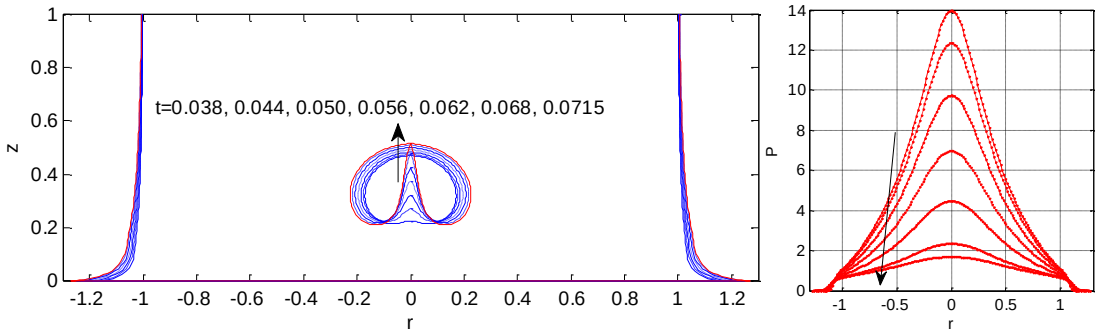

(b) expansion stage: before the penetration of the vertical jet ($0.036 \le t \le 0.0715$)

Figure 4.17. Longitudinal sections of axisymmetric liquid column impact with spherical cavity trapped inside: deformation of the free surface near the rigid plate, and the corresponding impact pressure distribution, in sequence of the deformation of the cavity ($z_0 = 0.3$, $R = 0.2$, $P_0 = 10$).

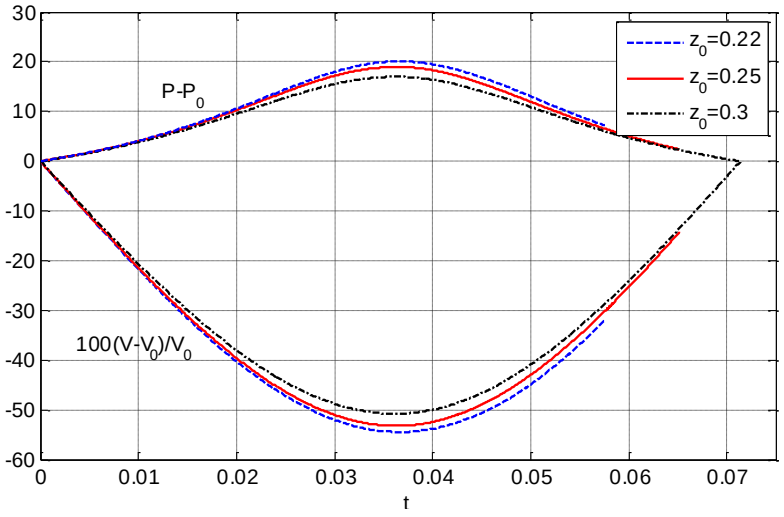

Figure 4.18. Time history of cavity volume and its pressure inside with $z_0 = 0.22$, 0.25 and 0.3 when $P_0 = 10$ ($R = 0.2$, $V_0 = 0.0335$)

The volume and pressure history of the fully immersed cavity during the impact process are plotted and compared in Figure 4.17 for $z_0 = 0.22, 0.25$ and 0.3 (1.1R, 1.25R and 1.5R), before the vertical jet reaches the other side of the cavity surface. It can be seen that the pressure variation range is slightly bigger with cavity closer to the impact surface, which is because the cavity is compressed harder by the surrounding liquid with the corresponding induced pressure filed. However, it can be speculated from the initial pressure distribution laws discussed in Figure 4.14 that, there might be exceptions if the cavity is placed farther away, at a small distance before the location where cavity starts to deform as if free from the solid boundary.

Numerical results of the same impact models as above but with bigger initial air pressure of P_0 = 100 are discussed in Appendix A. The cavity is able to undergo more oscillation periods before the penetration of the vertical jet. The amplitude of volume change is much smaller, and so is that of P/P_0 inside the cavity. The whole impact process thus is weaker, corresponding to the smaller physical (or dimensional) impact velocity.

4.6 Summary

The axisymmetric water column impact with an air cavity in spherical contour trapped near the impact surface is studied in the chapter. The air cavity is found to influence the impact dynamics dramatically, and can cause significant pressure

increase both for the initial impact stage and the following body/water/air interaction process. Numerical techniques are developed for the impingement of the radial cavity jet on the plate, as well as the cavity surface immersion in some situations. Some main conclusions have been gained:

1. For impact with air cavity trapped on the impact surface, there are initial discontinuous pressure distributions near the two body/water/air intersections. Smaller initial air radius on the rigid plate R_b and the surface inclination direction of a thin air cavity can both cause significant increment on the pressure gradient near the intersection of the air cavity and the body surface; and vice versa. For a hemispherical air cavity, the pressure gradient at its intersection with the body surface approaches to ∞ when $R_b \to 0$.
2. The cavity deformation in the body/water/air interaction process causes pressure oscillation on the impact surface. In the numerical simulation, smaller initial air volume V_0 and smaller initial air pressure P_0 (or the dimensionless atmospheric pressure) can lead to bigger ratio between the maximum cavity pressure and the ambient pressure ($P_{\max}/P_0$). While the oscillation process is faster with smaller V_0 or bigger P_0. The cavity shape (i.e. its initial inclination direction on the plate) can also play a role, but not as much as that caused by the variation of P_0 or V_0.
3. When the radial jet impinges at the impact centre, a vertical jet with large speed will be formed. There is a local pressure spike there, which rises fast in the early stage of the jet formation and drops gradually as it shoots up with large speed. The thicker the local impinging fluid layer is, the bigger such pressure variation is. When the cavity jet meets with small angles, fluid immersion can happen before the formation of the vertical jet. The vertical jet will then penetrate the cavity top surface and form a toroidal shape, which is not included in the current study.
4. Through a deduction on the energy transfer relation during the body/water/air interaction process, it is found that the initial potential energy of the air cavity (E_{a0}, defined related to be product of P_0 and V_0) plays an important role in the first maximum cavity pressure relative to the atmospheric value ($P_{\max}/P_0$). With given conditions, smaller E_{a0} can produce higher pressure $P_{\max}/P_0$, agreeing with the numerical results.

5. If an air cavity is initially fully immersed in the impact liquid, as it is placed farther away from body surface, the initial impact pressure at the impact centre first increases from a valley value to a peak value, and then gradually falls to a minimum value below that without air entrapment. As the cavity is placed farther away, the pressure distribution will then rebound to the value as if no air is entrapped. The initial pressure distribution can largely reflect the following cavity deformation characteristics. A bulb shape cavity will be formed when it is initially close to the rigid plate, while the cavity bottom will be only slightly flattened as it is placed a little farther away. A vertical jet is also formed shooting upward from the cavity bottom, causing a sudden pressure increase near the impact centre.

Chapter 5 Breaking wave impact on a wall with air entrapment

Breaking waves attacking structures at heavy sea is one of the typical examples of violent fluid/structure impact in marine engineering involving air entrapment. Dynamics of the entrapped air cavity are suggested to be closely related to the severest impact situations in the large volume of laboratory and field experiments carried out on breaking wave impact on a wall in shallow water (Bagnold 1939, Nagai 1960, Oumeraci et al. 1993, Hattori et al. 1994, Lugni 2006, etc.). Nevertheless, the strong nonlinearity involved has posed great difficulties in the theoretical study. As mentioned in Chapter 1, the simulation of wave evolution with fully nonlinear potential theory and BEM, has to stop or carry on with compromise on the accuracy or efficiency upon the occurrence of wave impact on a structure. A main difficulty lies in the accurate simulation of the local impact starting from one point.

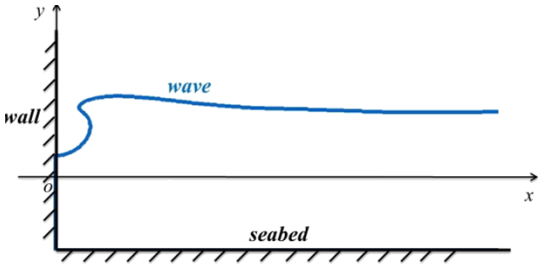

Figure 5.1. Sketch of a wave plunging against a seawall

In this chapter, a numerical technique will be developed, enabling the employment of fully nonlinear velocity potential theory in the simulation of overturning wave impact on the wall. A sketch of the problem is shown in Figure 5.1. A dual coordinate system is to be established to tackle the initial stages of wave crest impact, by applying the stretched coordinate system (as introduced in section 2.3) on the exact free surface conditions in the local impact region and coupling it with the simultaneous overall wave propagation computed in the Cartesian coordinate system. Thus the successive process of wave plunging, overturning (stage 1), and impact on the wall while entrapping an air pocket (stage 2) is able to be simulated with higher accuracy. The effect of the entrapped air cavity in the following wall/water/air interaction process (stage 3) will then be able to be investigated in the physical system. Numerical experiments will be carried out with the method developed,

looking into the characteristics of impact with air cavity and the scaling effect, as well as the possible scaling law.

5.1 The computational model

5.1.1 The initial incident wave model

Among a wide range of incident waves, we shall consider the problem of a long wave propagating near shore and then plunging against a wall. The incoming wave model is the same as that in Cooker & Peregrine (1990c). They focused on the cases in which 'flip-through' would occur, or the water level on the wall would rise up rapidly but no direct impact would be involved. For situations where the direct impact by an overturning wave would happen, their simulation stopped at the moment when the wave touched the wall and therefore the subsequent impact process was not considered.

A 2D Cartesian system $o-xy$ is defined such that the origin is located at the intersection of the wall and the still water surface, with the x-axis in the horizontal direction and y-axis pointing vertically upwards. The initial incident wave, as sketched in Figure 5.2, has an elevation of Δh at infinity above the undisturbed surface.

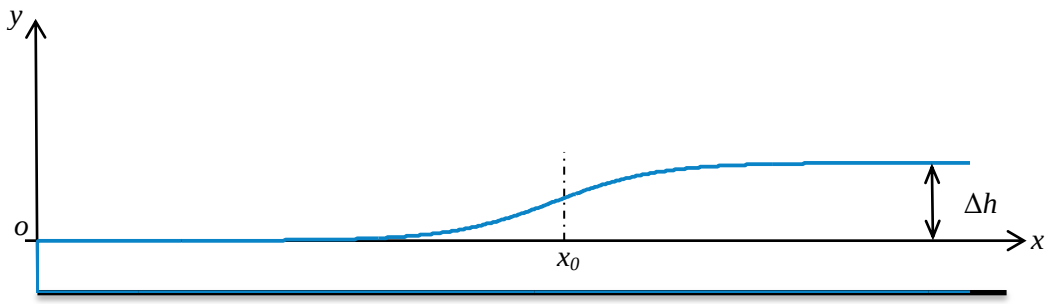

Figure 5.2. The initial incident wave model

- Nondimensionlisation

For this problem of wave surging, plunging and impacting on the vertical wall in shallow water, the effect of gravity is important, and cannot be ignored. We shall then adopt some new parameters for the nondimensionlisation of the current case study, different from those in Chapters 3 & 4. Let the initial still water depth h,

$\sqrt{gh}$, $\sqrt{h/g}$, $h\sqrt{gh}$ and ρgh be the nondimensionalising parameters for length, velocity u, time t, the velocity potential ϕ and pressure P, respectively, where g is the acceleration due to gravity and ρ is the water density. Unless specially specified, parameters in the following study in Chapter 5 refer to the dimensionless ones.

The horizontal velocity of the incoming wave, averaged along the vertical direction, is assumed to take the form (Cooker & Peregrine 1990c)

$$\bar{u}(x) = -\frac{1}{2}u_0\left\{1+\tanh\left[k\left(x-x_0\right)\right]\right\} \tag{5.1}$$

which is a uniform incoming flow with velocity $-u_0$ at infinity at $x\to\infty$, and is still at $x\to-\infty$. Here x_0 will be referred to as the position of the initial wave centre. The corresponding initial wave profile, which is a solution based on Airy's theory (e.g. Mei 1983), can be written as

$$f = -\bar{u} + \frac{1}{4}\bar{u}^2 \tag{5.2}$$

which elevates gradually from the still water surface 0 at $x\to-\infty$ to $\Delta h = u_0 + \frac{1}{4}u_0^2$ at $x\to\infty$.

In the simulation, a rigid wall is suddenly placed at $x=0$, and thus the free surface at the wall has an initial elevation of $f(0) = -\bar{u}(0) + \frac{1}{4}\bar{u}(0)^2$, which is close to 0 when x_0 in Eq. (5.1) is sufficiently large. The initial water depth at the wall is then approximately equal to 1 after the nondimensionlisation.

Based on the Airy's wave theory (e.g. Mei 1983), the incident velocity potential averaged over the depth can be obtained as

$$\bar{\phi}(x) = \int_{x_0}^{x}\bar{u}(x)dx = -\frac{1}{2}u_0\left[x - x_0 + \frac{\ln(\cosh k\left(x-x_0\right)}{k}\right] \tag{5.3}$$

In the numerical simulation, the initial wave shape (see Eq. (5.2)) and the boundary condition at $x\to\infty$ (see Eq. (5.1)) are taken from the Airy's wave model. The initial velocity penitential in Eq. (5.3) is only applied on the free surface, and the fluid flow

is then computed with the fully nonlinear potential flow theory combined with a time marching scheme, as the mathematical model described in 2.1. Note that the choice of the initial wave shape and boundary conditions could be arbitrary (e.g. from an experimental situation). To flexibly generate the impact situations in concern, here the Airy's wave model is applied for the initial conditions of the free surface. Some specific formulations on this case are given below.

5.1.2 **Detailed formulation**

Assuming the free surface at infinity has the atmospheric pressure, with Bernoulli equation, pressure in the flow field can be calculated by

$$P - P_0 = -\phi_t - \frac{1}{2}\nabla\phi\cdot\nabla\phi + \frac{1}{2}u_0^2 + (\Delta h - y) \tag{5.4}$$

where P_0 is the nondimensional atmospheric pressure ($= \frac{P_a}{\rho g h}$), as well as the initial air pressure of the cavity when first trapped by an overturning wave. Then the dynamic condition on the outer wave surface takes the form

$$\frac{d\phi}{dt} = \frac{1}{2}\nabla\phi\nabla\phi + \frac{1}{2}u_0^2 + (\Delta h - y) \tag{5.5}$$

As has been discussed in Eq. (2.5), the constant terms in Eqs. (5.4) and (5.5) can be omitted without influencing the physical results. Here they will be kept.

Correspondingly, the dynamic condition on the cavity surface becomes

$$\frac{d\phi}{dt} = \frac{1}{2}\nabla\phi\nabla\phi + \frac{1}{2}u_0^2 + (\Delta h - y) - P_0\left[\left(\frac{V_0}{V}\right)^{\gamma} - 1\right] \tag{5.6}$$

From the impermeable solid surface condition, we have on the wall and the seabed

$$\frac{\partial\phi}{\partial n} = 0, \text{ at } x = 0 \text{ and } y = -1 \tag{5.7}$$

According to Eq. (5.1), the flow is uniform at infinity, which is

$$\frac{\partial\phi}{\partial n} = -u_0, \text{ at } x \to \infty \tag{5.8}$$

In the numerical simulation, this equation is imposed at a control surface S_c at a large distance away from the the wall. In particular, the x coordinate of S_c can be

estimated from $x_c = x_0 + C/k$, where C can be determined by the equation $\left|\frac{u_0 - \bar{u}(C)}{u_0}\right| < \sigma$. σ is a value chosen sufficiently small to ensure that the boundary condition at S_c has no noticeable effect on the results near the wall, and is taken as 10^{-4} in the simulation.

At t=0, we have on the free surface $y = f$ decided by Eq. (5.2) and $\phi(x, f) = \bar{\phi}(x)$ by Eq. (5.3).

With Eq. (5.8), the potential at the intersection of the fixed control surface S_c and the free surface at the far end can be assumed to be unchanged

$$\phi_t = 0 \tag{5.9}$$

which also serves as the boundary condition for ϕ_t there in the pressure calculation.

The boundary condition for ϕ_t on the outer wave surface, based on the Bernoulli equation as given in Eq. (2.12), in this case then becomes

$$\phi_t = -\frac{1}{2}\nabla\phi\cdot\nabla\phi + \frac{1}{2}u_0^2 + (\Delta h - y) \tag{5.10}$$

On the cavity surface formed after air is entrapped by wave overturning and impacting on the wall, with the adiabatic gas law, the boundary condition for ϕ_t is

$$\phi_t = -\frac{1}{2}\nabla\phi\cdot\nabla\phi + \frac{1}{2}u_0^2 + (\Delta h - y) - P_0\left[\left(\frac{V_0}{V}\right)^{\gamma} - 1\right] \tag{5.11}$$

The solid boundary condition on the wall and bottom can be written as (Wu 1998)

$$\left.\frac{\partial\phi_t}{\partial n}\right|_{S_w + S_b} = 0 \tag{5.12}$$

which can also be applied on the control surface in the far field as the flow there is uniform.

5.2 A dual system for overturning wave impact (stage 2)

We shall name the initial process of wave surging and plunging until impact on the wall as stage 1; the short process of direct impact by the overturning wave crest on

the wall as enclosing an air cavity will be referred to as stage 2; stage 3 represents the post-direct impact process when the wave interacts with the entrapped air cavity as acting on the wall.

Stages 1 & 3 can then be solved with the 2D boundary element method provided in 2.2.1, in the Cartesian coordinate system. However, the direct impact by the overturning wave crest on the wall as entrapping an air cavity starts from one single point. To seek a simulation of good accuracy for this period, the stretched coordinate system as introduced in section 2.3 will be employed for the local solution near the contact point, which is to match the solution at the far field, obtained in the usual Cartesian coordinate system.

5.2.1 Stretched coordinate system for the local wave impact zone

Assume a wave crest overturns and impacts on the wall at the point (x_I, y_I) (here $x_I = 0$), and the time t is reset as 0 hereafter. Establish a local coordinate system $o' - x'y'$ with o' located at the impact point, then $x' = x, y' = y - y_I$, as shown in Figure 5.3.

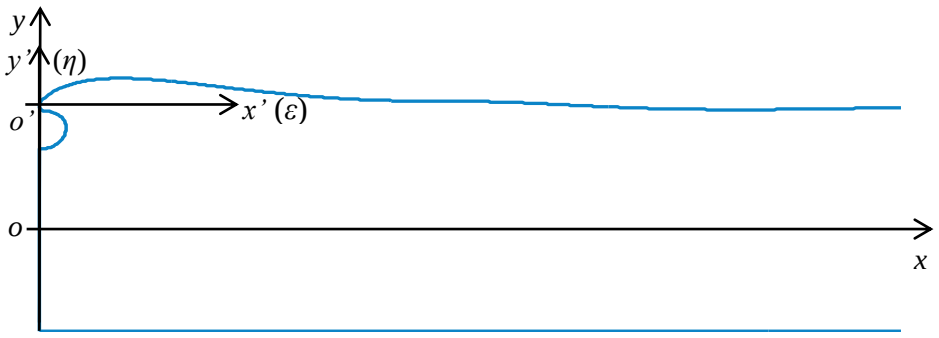

Figure 5.3. Definition of the coordinate systems upon wave impact

At the local impact point, a stretched coordinate system $o' - \varepsilon\eta$ is introduced (abbreviated as S system hereafter, and the Cartesian system abbreviated as C system). With the definition in 2.3, the local velocity potential $\varphi(\varepsilon, \eta, t)$ in this case is

$$\phi(x', y', t) = Us\varphi(\varepsilon, \eta, t) \tag{5.13}$$

$$\varepsilon = x'/s, \eta = y'/s \tag{5.14}$$

where U is set equal to the absolute velocity in the x'-axis direction at $x' = y' = 0$ at the moment of impact. Similar to the practice in Wu (2007a) for the case of symmetric liquid impact (see Eq. (2.47)), the stretching ratio s is set to be half the width of the incident wave crest at time t in the present case

$$s(t) = \frac{1}{2}\left[y_1'(x',t) - y_2'(x',t)\right]\Big|_{x'=0} \tag{5.15}$$

where $y_1'(>0)$ and $y_2'(<0)$ are the vertical coordinates of the free surface on the upper and lower sides of the wave crest. Even after the impact, y_1' and y_2' are obtained in the parallel computation under the assumption that the wave keeps plunging without the wall, as the sketch later shown in Figure 5.4.

To solve the harmonic function of $\varphi(\varepsilon,\eta,t)$, the boundary conditions on the solid surfaces, as well as the kinetic free surface condition, take the same form as those in Eqs. (2.49) and (2.50). The dynamic free surface conditions, corresponding to Eqs. (5.5) and (5.6), are

$$\frac{dUs\varphi(\varepsilon,\eta,t)}{dt} = \frac{1}{2}U^2\nabla\varphi.\nabla\varphi + \frac{1}{2}u_0^2 + (\Delta h - s\eta) \tag{5.16}$$

on the outer free surface, and

$$\frac{dUs\varphi(\varepsilon,\eta,t)}{dt} = \frac{1}{2}U^2\nabla\varphi.\nabla\varphi + \frac{1}{2}u_0^2 + (\Delta h - s\eta) - P_0\left[(\frac{V_0}{V})^\gamma - 1\right] \tag{5.17}$$

on the cavity surface.

During the computation in stage 2, the time step will be chosen based on the stretched coordinate system, as given in Eq. (2.52).

The boundary conditions for $\chi(\varepsilon,\eta,t) = \phi_t(x,y,t)$ in the calculation of the direct impact pressure, as prescribed in section 2.3, then take the form

$$\chi\big|_{S_f} = -\frac{1}{2}U^2(\varphi_\varepsilon^2 + \varphi_\eta^2) + \frac{1}{2}u_0^2 + (\Delta h - s\eta) \tag{5.18}$$

on the outer wave surface

$$\chi\big|_{S_c} = -\frac{1}{2}U^2(\varphi_\varepsilon^2 + \varphi_\eta^2) + \frac{1}{2}u_0^2 + (\Delta h - s\eta) - P_0\left[(\frac{V_0}{V})^\gamma - 1\right] \tag{5.19}$$

on the cavity surface, and

$$\left.\frac{\partial \chi}{\partial n}\right|_{S_w} = 0 \tag{5.20}$$

on the wall.

With the employment of the *S* system, the local impact of wave crest starting from one point could be solved with high accuracy. In previous related studies (Wu 2007a, 2007b, Duan et al. 2008), however, the velocity and potential of incoming flow are known, and thus could be used for the boundary conditions ($\varphi, \frac{\partial \varphi}{\partial n}$) in the far field of the *S* system. For the current problem of overturning wave impact, however, the main wave keeps plunging as its crest impacts on the wall, and its velocity and potential have to be updated constantly. As a result, φ in the *S* system and ϕ in the *C* system, near and away from the contact zone respectively, need to be solved simultaneously. Their solutions are to be matched on their interface, which is also continuously updated with the growing stretching ratio *s*. Detailed computation algorithms thus need to be worked out, to couple the calculation of the local crest impact carried out in the *S* system with the main wave evolution calculated in the physical, or *C* system.

5.2.2 Computation algorithms for combined solutions in the *S* and *C* coordinate systems

With the definition of the stretching ratio *s* in Eq. (5.15), if we fix the computation domain as $\varepsilon \in [0, L]$ in the *S* system, it corresponds to an expanding domain $x \in [0, Ls(t)]$ in the *C* system, as shown by the sketch in Figure 5.4(a). Within the *S* system, solution of φ is found from Window 1. Simultaneous computation in Window 2 is made for ϕ in the *C* system without the wall, and the wave will keep plunging, as shown by the dashed line in Figure 5.4(b). Then the solution at $x = Ls(t)$ in the *C* system from Window 2 will be used as the far field condition for φ at $\varepsilon = L$. This in fact has assumed that the local impact does not have significant effect on the flow at $x = Ls(t)$. It could be justified, as the examples of impact by a 2D rectangular water column (Wu 2001) and the axisymmetric water column solved in section 3.2.1 (see Eq. (3.8)) both show that, the initial disturbance decays

exponentially away from the impact surface.

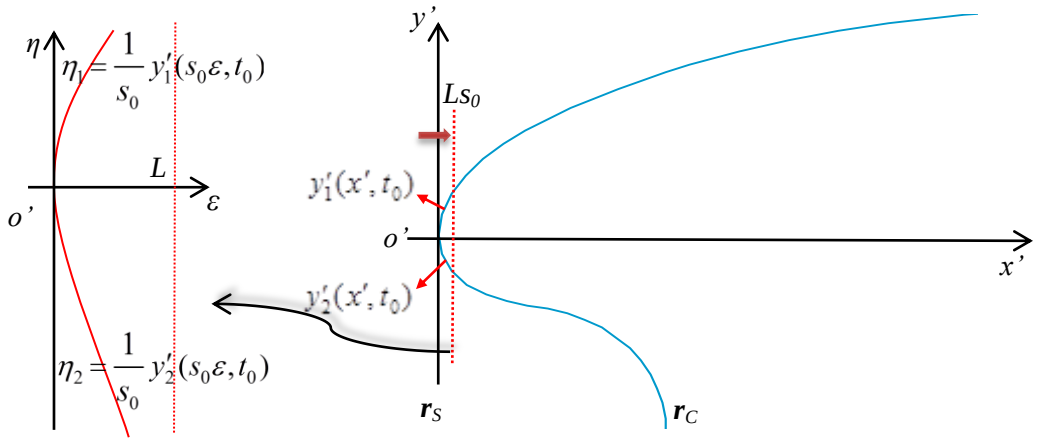

(a) definition of the *S* and *C* coordinate systems right after the impact at $t = t_0$ ($s_0 = s(t_0)$)

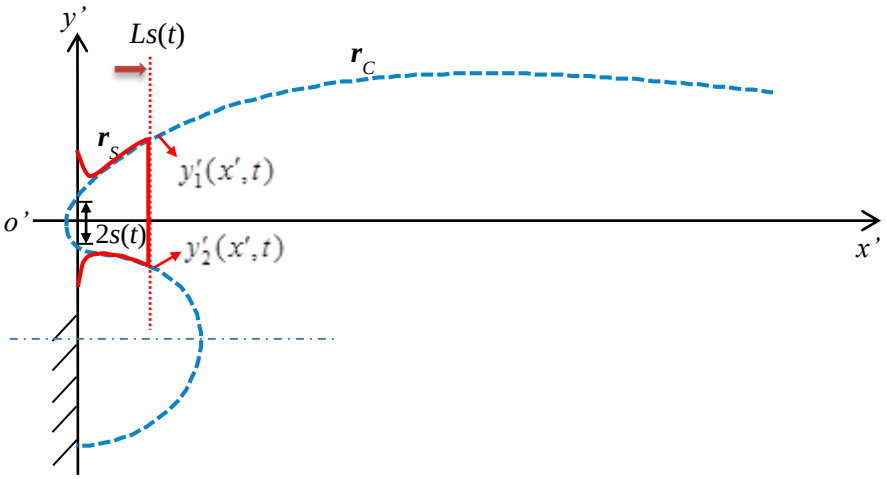

(b) simultaneous computation in the two windows at time *t*

Figure 5.4. Sketch of the coupling of the dual systems (the time is reset from 0 upon impact)

Numerically, $\frac{\partial \varphi(\varepsilon, \eta)}{\partial n}$ at $\varepsilon = L$ in the y*S* system is obtained from a linear interpolation of $\frac{\partial \phi}{\partial x}$ across the upper and lower wave crest surfaces at $x = s(t)L$ in the *C* system. For the pressure calculation, the boundary condition of the control surface $\left.\frac{\partial \chi}{\partial n}\right|_{\varepsilon=L} = s \left.\frac{\partial \phi_t}{\partial x}\right|_{x=sL}$ can similarly be obtained by a linear approximation of $\frac{\partial \phi_t}{\partial x}$ on the upper and lower free surfaces, where ϕ_t is solved simultaneously in the *C* system (Window 2).

The detailed computation algorithms are given below, with the main procedures outlined in the flow chart shown in Figure 5.5:

1. Decide the stretching ratio by Eq. (5.15). Set $t=0$ upon impact. At the first time step, assume that the wave plunges 'into' the wall for a very short time t_0 which could be set as small as desired (in the order of 10^{-5} in the present work). Set the computation domain in the S system $(o-\varepsilon\eta)$ as $\varepsilon\in[0,L]$. It corresponds to the domain between $x'\in[0,sL]$ in $o'-x'y'$ of the C system (see Figure 5.4(a) where $s_0=s(t_0)$).

2. At the initial time $t=t_0$, ϕ and ϕ_n which are defined in the C system but are within $x'\in[0,s(t_0)L]$ will be transferred to $\varphi=\phi/(Us),\varphi_n=\phi_n/U$ in the S system as the initial condition. Piecewise cubic-spline interpolation can be used for the interpolation of the significantly increased number of nodes in the S system; for subsequent time steps at $t>t_0$, the free surface and its potential in the S system corresponding to $x'\in\left[s(t-\delta t)L,s(t)L\right]$ are also transferred from those updated in the C system, and so is the boundary condition at $\varepsilon=L$.

3. In window 1, $\nabla^2\varphi=0$ is solved in the S system for the dynamics of local wave crest impact on the wall, with boundary conditions prescribed above; and at the same time, in window 2, $\nabla^2\phi=0$ is solved in the C system for the whole wave evolution without the effect of the wall.

4. Decide the time marching step δt by Eq. (2.52) ($k_1=0.2$). The free surface and its potential within $x'\in\left[0,s(t)L\right]$ are updated with Eqs. (2.50), (5.16) and (5.17) using results obtained from the S system; those beyond are updated with Eqs. (2.6) and (2.10) in the C system, and $t=t+\delta t$;

5. Repeat the processes from 1 to 4 until the wetted surface on the wall grows sufficiently big (say at least 10 times larger than the element size in the C system), and the whole simulation will then be carried out in the C system alone.

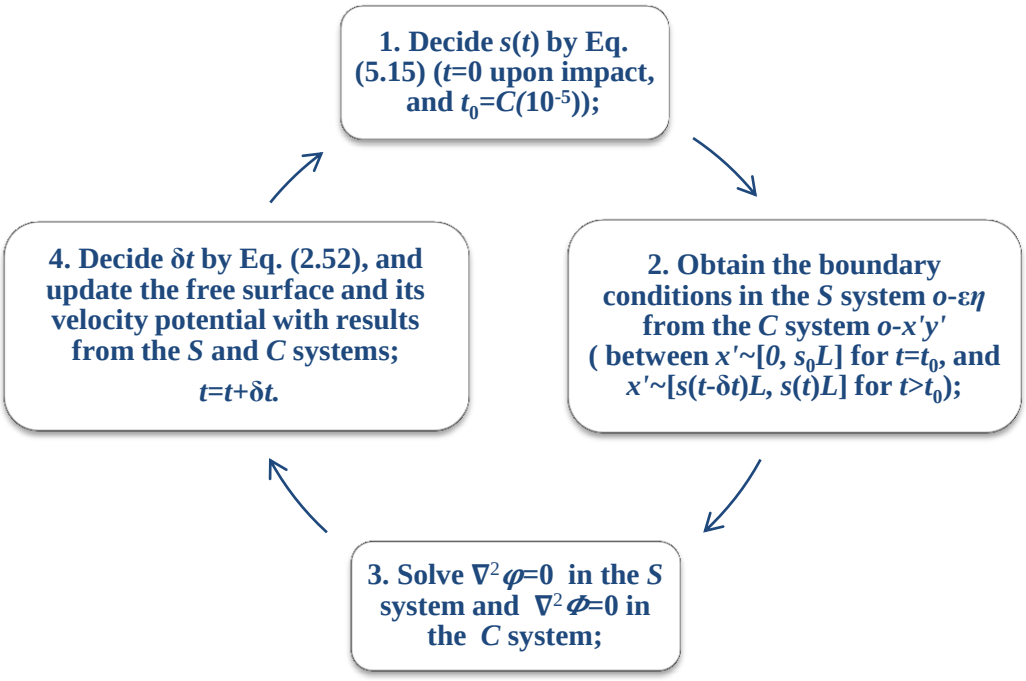

Figure 5.5. Flow chart of the simultaneous computation algorithm in the *S* and *C* system for stage 2

Note that it is not until the process of wave interaction with the entrapped deforming air cavity in stage 3 that the effect of the pressure variation inside the cavity is significant and starts to have major effect on impact dynamics. In consideration of the subtle change in the cavity volume during the instant period of direct impact by the wave crest, and consequently that of the inner air pressure, the analysis in stage 2 will be based on the assumption of ignoring the enclosed air cavity effect. Mathematically, this implies that the cavity pressure in its dynamic conditions with regard to the *S* system as given in Eqs. (5.17) & (5.19) will be approximated by P_0, and the conditions will become the same as those on the outer wave surface as given in Eqs. (5.16) & (5.18).

Even though, there is a scheme to include the effect of the cavity in the calculation conducted in the dual system. Different free surface conditions are caused by the pressure difference on the upper and lower sides of wave surface in the *C* system. One corresponds to the ambient pressure and the other is the cavity pressure. They could be applied through a gradual change of the pressure distribution over the part of wave crest exceeding the wall. This is not strictly physical, while it is effective in keeping the continuity of the velocity and free surface without affecting the impact

dynamics in the *S* system. The volume of the compressed cavity could be evaluated by matching the lower free surfaces obtained from the dual system.

For general case studies, the calculation duration in stage 2 can be flexibly decided according to the evolution of the impact zone, provided that the time period is not long enough to cause a large change in the cavity volume (say not bigger than $0.2V_0$), otherwise the cavity effect could be taken into account with the above scheme.

5.3 Impact jet flow treatment

Two different jet treatment schemes will be employed in this chapter. For the local impact by the overturning wave carried out in the *S* system (stage 2), it is more desirable to keep the integrity of the generated free surface jet after impact, since the numerical study on water column impact in Chapter 3 has shown that a longer jet can provide field solution over a larger wetted surface without influencing the main fluid domain. This is favourable for the transfer of the simulation into the physical system at the beginning of stage 3, since more nodes could be accommodated in the local impact region. As a result, the decoupling method with a local thin jet approximation scheme prescribed in 2.4.2, similar to what has been employed in the simulation of axisymmetric water column impact, will be utilized for the local direct impact in stage 2.

The post-direct impact process in stage 3 is characterized by the interaction between the water and the entrapped air. In the current 2D simulation, the computation terminates when the free surface jets inside the cavity meet each other on the wall. Given the small influence of the free surface jet on the overall fluid dynamics, we shall restrain the length of the cavity jet, so that a longer simulation period could be carried out for a better investigation into the dynamics of wave impact with entrapped air cavity. The jet restraining method of Kihara (2004) by introducing a new intersection point of the free surface and the body according to a threshold value for their contact angle will be employed. This is based on whether (i) the angle of the jet tip has reached a threshold value θ_0 ($\theta_0 = \pi/100$ in this paper), or (ii) the tip of the jet on the wall is about to touch the other side of the cavity surface. If one of these happens, the retraining method will be applied. In this way the length and

thickness of the jet can be effectively limited, and at the same time the calculation accuracy can be well kept, especially for the capture of the local flow features (e.g. the local free surface hump, the pulling up of cavity jet along the wall during the expanding process).

5.4 Numerical simulation

Assume the initial wave has an elevation of $\Delta h = 1.5$ at $x \to \infty$. With Eqs. (5.1) and (5.2), this corresponds to an initial incident flow with $u_0 = 1.1623$ from infinity. Taking $k = 0.5$ and $x_0 = 9$ in Eq. (5.1), Cooker & Peregrine (1990c) numerically observed an overturning wave crest hitting the wall and the simulation stopped there. To validate the current 2D numerical model, initial element sizes of $l_0 = 0.04, 0.03$ and 0.02 are employed respectively in the simulation of the same process of wave plunging with $x_0 = 9$. When the wave starts to overturn, smaller elements of size $0.6l_0$ are employed near the wave front, or the point with its slope nearly vertical. Time marching steps are decided by Eq. (2.43) with $k_1 = 0.2$. Results of the wave evolution are shown and compared with those of Cooker & Peregrine (1990c) in Figure 5.6, where good convergence and agreement can be seen. In consideration of the computation accuracy and efficiency, basic element size of $l_0 = 0.03$ is then employed in the following simulations carried out in the *C* system for the main wave evolution.

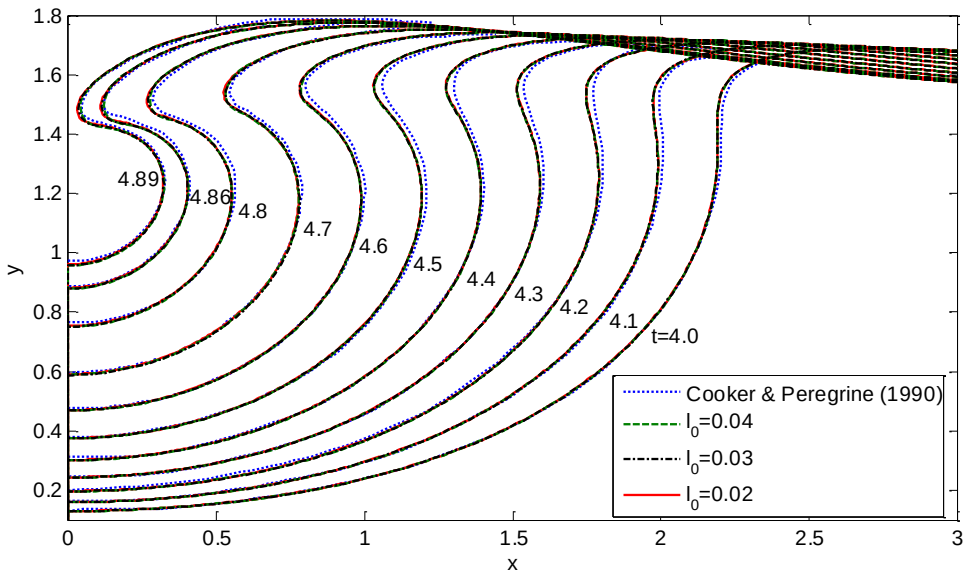

Figure 5.6. Overturning wave profiles with various grid sizes and the comparison with the result

of Cooker & Peregrine (1990c) ($x_0 = 9$)

With the atmospheric pressure P_a and water density ρ the same as those given in 4.1, the dimensionless initial air pressure P_0 is determined by the water depth h for the current problem of plunging wave impact happening in nature. A large number of laboratory experiments (e.g. Bagnold 1939, Nagai 1960, Oumeraci et al. 1993, Hattori et al. 1994, Hull and Müller 2002, Lugni 2006, etc.) have been conducted to study the dynamics of wave impact with entrapped air cavity effect. However, in most of them the order of water depth is around $10^{-1}m$. The length scale is therefore very much different from that in the real case. From the dimensional analysis in the present study, we can see that prior to the enclosing of air cavity by the impact flow, the process of wave surging and propagating has been characterized only by u_0, ρ, g and h. After an air cavity is trapped in the impacting water flow, the initial dimensionless air pressure P_0 starts to exert effect on the impact dynamics. Therefore when P_a in the laboratory is the same as that in the field, there was significant scaling effect in the traditional experiments. The similarity requirements could not be met until more recently that the air pressure is adjustable in specially designed wave tank (e.g. Lugni et al. 2010). To investigate on the scaling effect, the post-direct impact process with air cavity (stage 3) is first simulated with dimensionless initial air pressure $P_0 = 10.087$. It corresponds to an initial water depth of $1m$. Then impact with bigger initial air pressure value of $P_0 = 100.87$ (i.e. h=0.1m) and smaller value of $P_0 = 2.017$ (i.e. h=5m) are simulated respectively. The cases to be considered are summarized in Table 5.1. Convergence study with regard to the S system will be included in stage 2 of the first case study with $x_0 = 10$.

Table 5.1. A summary of cases studied

Case	(1) P_0=10.087 (stage 3)	(2) P_0= 100.87 (stage 3)	(3) P_0=2.017 (stage 3)
a. x_0=10 (in Eq.(5.1))	a-1	a-2	a-3
b. x_0=9 (in Eq.(5.1))	b-1	b-2	b-3

5.4.1 Case a. x_0=10

i. Stage 1: wave propagation and plunging until impact on the wall

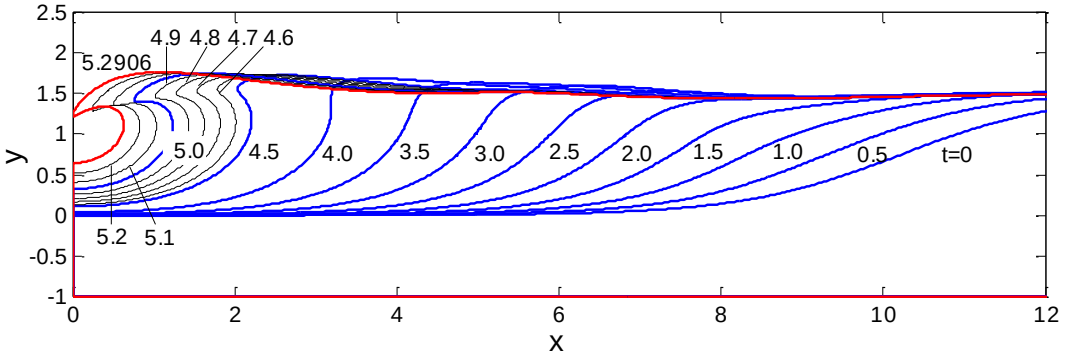

Figure 5.7. The process of wave surging and plunging before impact (stage 1, $x_0 = 10$)

When the initial wave centre is at $x_0 = 10$ away from the wall, the development of wave propagation and plunging until the wave crest touches the wall (stage 1) is shown in Figure 5.7. It can be seen that the wave front becomes nearly vertical when the wave starts to plunge at around $t = 4.0$. Before that the water level at the wall barely lifts. Then a protruding wave crest is formed quickly, and at the same time the water level at the wall starts to move up. The protruding wave hits the wall at $t = 5.2906$, enclosing an air cavity of initial size $V_0 = 0.3438$ on the wall.

The local impact by the wave crest happens with a relative velocity of (-2.625, -0.771), at the point (0, 1.236) on the wall in the $o-xy$ coordinate system. A local coordinate system $o'-x'y'$, as specified in 5.2.1, will then be established there, based on which the following results in stages 2 & 3 will be given. $U = 2.625$ is employed in Eq. (5.13) as the velocity scale for the *S* system in stage 2.

ii. Stage 2: simulation of initial stages of local direct impact on the wall in the dual system

For the initial computation model in the *S* system, to obtain the initial stretching ratio by Eq. (5.15), we assume that the wave crest has moved across the wall for a short instant t_0 and the wave profile is unaffected by the impact (see 5.2.2, step 1). This may seem to be similar to the practice of Tanizawa & Yue (1992). However the difference is that the choice of t_0 can be arbitrarily small here. Strictly speaking, the numerical result does not reflect the real physics at this moment. However, at

$t >> t_0$, the assumption made at an extremely small t_0 will not have significant effect on the result. In fact the study on the vertical water entry of a cone by Sun & Wu (2013) has shown that, when $t/t_0 > 20 \sim 30$, the numerical transient effect due to the initial assumption will diminish. Similar practice is adopted here, where t_0 is set small enough (of order 10^{-5}) to ensure results provided do not have significant effect from the initial assumption.

During stage 2, the dual system is combined to calculate the initial stages of wave impact, and a computation domain of length L is taken in S system, as prescribed in 5.2.2. Two different values of L will be employed first to assess our earlier assumption and proposed computation algorithms with the combined dual system in 5.2.2. Let $t_0 = 10^{-5}$, and this then gives an initial stretching ratio of $s_0 = 0.0017$ from Eq. (5.15) for the S system. It corresponds to an initial local wetted surface of width 0.0034 on the wall and domain lengths of 0.0051($L = 3$) and 0.0068 ($L = 4$) respectively for the current wave model in the C system. With grid size in the S system firstly set as 0.03, the numerical results with $L = 3$ and 4 from t_0 until $t = 0.02$ are shown and compared in Figure 5.8.

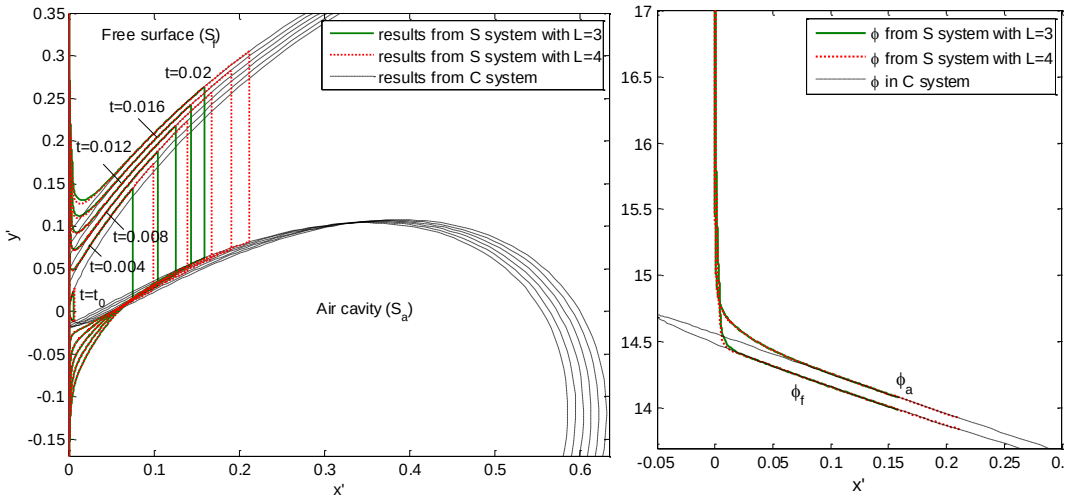

(a) (b)

Figure 5.8. Computation in the dual window (stage 2, $x_0 = 10$) with computation lengths L=3 and 4 in S system: (a) close-up of free surface profiles from t_0 =10^{-5} to 0.02; (b) velocity potentials along the outer free surface ϕ_f and the cavity surface ϕ_a at t=0.02, obtained respectively from S system by $\phi = Us\varphi$ and directly from C system.

It can be seen that, $L = 3$ and 4 yield results of good agreement for the local impact

in the *S* system, in terms of both the evolution of local wave profiles (Figure 5.8(a)) and the velocity potential distribution along the free surfaces at t=0.02 (Figure 5.8(b)). In addition, at the interface/matching region of the two systems, we can see that both $L=3$ and $L=4$ give smooth and continuous transitions for the numerical results. This verifies our earlier assumption that the local impact can be considered to have no major effect on the flow beyond a certain distance away from the impact zone. $L=3$ seems to be sufficiently large to satisfy this assumption, and will be used in the following simulations of stage 2.

To check convergence with mesh at stage 2, grid sizes of 0.03, 0.02 and 0.015 are employed in the *S* system respectively. We can see from Figure 5.9(a) that, the result for free surface profiles shows good convergence with the grid size. It can be noted that the peak of the pressure in Figure 5.9(b) converges more slowly. This is partly due to the fact the pressure changes rapidly near the peak and the slope of the pressure curve is nearly vertical there, which clearly requires very small elements. Apart from the peak region, the results of pressure show good convergence with grid sizes.

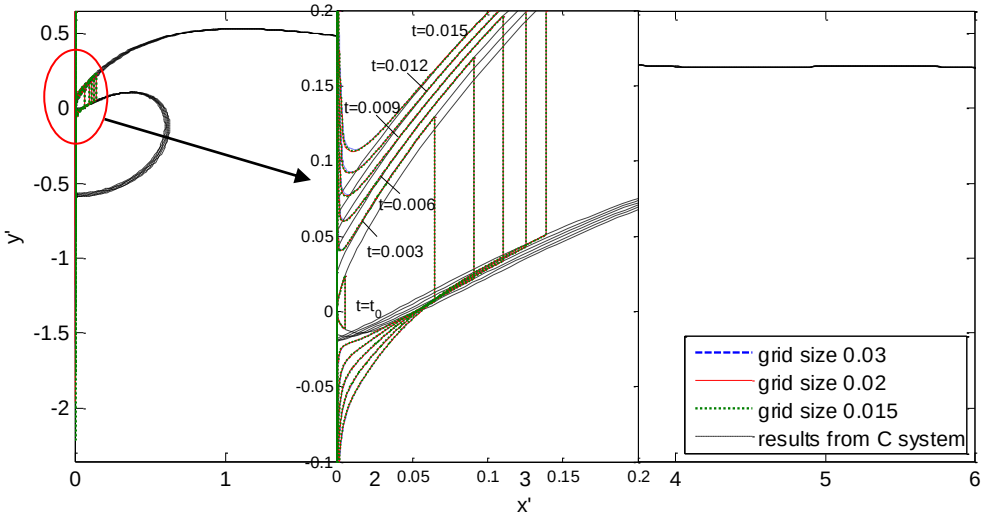

(a)

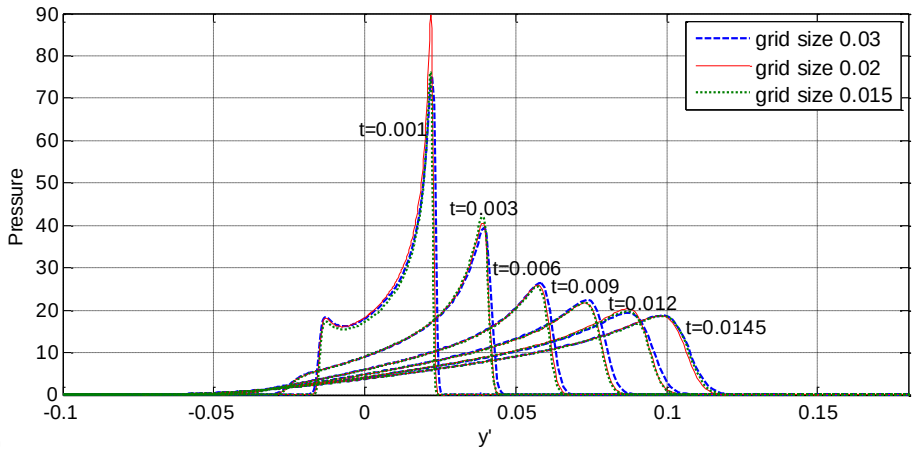

(b)

Figure 5.9. Numerical results of the impact dynamics from the dual windows with different grid sizes in S system ($x_0 = 10$, stage 2): (a) close-up of local free surface profiles; (b) local impact pressure (P-P_0) on the wall

The result in Figure 5.9(b) also shows that the pressure distribution at t=0.001 has two extremum points corresponding to the two jet roots. Beyond these points the pressure drops fast to the ambient value. The upper one (at $y' > 0$) corresponding to the outer wave surface has much bigger magnitude than the lower one (at $y' < 0$) and falls rapidly with time, while the lower one in this case disappears very fast after the initial impact.

- Pressure extremums in fluid/structure impact

The reason for the local pressure peak/extremum points near the free surface jet root might be explained in a way similar to that by Wu & Sun (2014) for the self-similar problem of expanding paraboloid entering water with constant vertical velocity W. They showed that the derivative of the pressure along the body surface can be zero near the jet root, which is close to the intersection point of the body and the undisturbed free surface. This is accompanied by a large local pressure gradient nearby. Physically, near the intersection of the wall and the incident wave surface, the path of the fluid particle is blocked by the wall, and it has to take a shape turn to move along the wall. The blocked region, similar to a stagnation point, corresponds to a local pressure extremum. The sharp turn of the fluid particle means a large acceleration which corresponds to a large pressure gradient. Away from this point, the fluid will move with large speed in a thin jet and the pressure there is close to the ambient value.

The analysis is consistent with what has been observed in many cases, including a liquid wedge impact on the wall (Wu 2007a, Figures 2-4) and vertical entry of a cone (Xu et al. 2011, Figure 3). It can also be found that the pressure extremum near the jet root only exists when the described local intersecting angle is below a certain value, and the smaller the angle is, the larger the local pressure extremum value becomes. This is in agreement with the evolution of the two pressure peaks shown in Figure 5.9(b). We can also perform an analysis on the moment of the momentum flux entering and leaving a control region, constituted by the oncoming flow and the two jets, about the mid-point of the original oncoming flow on the wall. Assuming the moment of the momentum flux from the oncoming flow to be approximately zero, the direction of the whole moment in the control region is apparently clock-wise, due to the larger component of the lower jet flow. Therefore the total force acting on the wave crest will be yielded located on the upper side.

- The critical condition

With the above analysis on the generating mechanism of the pressure extremum associated with the jet root in fluid/structure impact, here we shall attempt to look into the critical condition for its generation, using the example of water entry problems. Wagner's (1932) method of approximating the impact flow by a blunt body as that of an expanding plate of the same wetted width $2c(t)$ moving at the same relative velocity W has been discussed in Chapter 1. The free surface elevation has been taken into account, irrespective of the jet region which is characterized by the approximate ambient air pressure. Thereby the result provides good prediction for pressure distribution by the main impact flow, including the peculiarity of pressure peak near the spay root. Taking the case of wedge entry into calm water as example (see Figure 1.2), the pressure distribution along the impact surface has been solved based on the velocity potential theory, as given in Eq. (1.7). For the case where W is constant, let its derivative equal zero

$$\frac{\partial P}{\partial x} = \frac{\rho W^2 c x}{2(c^2 - x^2)^{\frac{3}{2}}} \left[\pi \cot \beta - \frac{2c}{\sqrt{c^2 - x^2}} \right] = 0 \tag{5.21}$$

Then it can be seen that, other than at $x = 0$, the above equation will have the second root at

$$x = Wt\sqrt{\frac{\pi^2}{4}\cot^2\beta - 1} \tag{5.22}$$

when and only when $\tan\beta < \frac{\pi}{2}$, i.e. $\beta < 0.3195\pi$.

For the problem of wedge entry into calm water, the deadrise angle of the wedge β is always equal to the intersection angle between the body surface and the undisturbed free surface. The obtained critical intersection angle, $\beta < 0.3195\pi$, is in good agreement with the range of the critical deadrise angle for the presence of pressure extremum near the jet root observed in related numerical studies with fully nonlinear potential theory and *BEM*, which was found to be between $\frac{\pi}{4}$ and $\frac{\pi}{3}$ (Wu et al. 2004).

The above analysis can be applied to water entry problem at constant speed by blunt bodies in other geometries, which would give a general result of the location of pressure extremum point near the jet root, at

$$x = c\sqrt{1 - W^2 \Big/ (\frac{dc}{dt})^2} \tag{5.23}$$

only on the condition that $\frac{dc}{dt} > W$, where $W \Big/ \frac{dc}{dt} = A_0 + A_1 c + A_2 c^2 + \ldots$ is decided and could be solved by the body geometry with the method described in Chapter 1, and thus the critical condition for pressure extremum points can be gained related to specific body geometries. The pressure extremum value, if exsits, is $P_{ext} = \frac{1}{2}\rho\left[\left(\frac{dc}{dt}\right)^2 + W^2\right]$.

At t=0.02, the stretching ratio increases to s=0.053 ($31s_0$), which suggests a wetted surface big enough for the whole calculation to be carried on in the physical system, or the C system. The change in the cavity volume during the short impact period in stage 2 is from 0.3438 at t=0 to 0.3010 at t=0.02, and consequently the pressure changes from P_0 to $1.205\,P_0$, which is small enough to ignore its effect during the transit period.

iii. Stage 3: wall, wave/air cavity interaction after the initial direct impact

a-1. P_0=10.087

Through numerical experiments, it is found that for the initial steps of stage 3, small elements comparable to those transferred from the *S* system at the end of stage 2 need to be adopted near the impact zone to ensure accurate result of the impact pressure, especially in the transition region towards the jet. As a result, elements of gradual change in size decided by Eq. (3.23) are employed. The small basic element size near the impact zone is chosen similar to that by the end of stage 2, as l_S (typically in the order of 10^{-3}). On the free surface, l_S is applied from the wall ($x'=0$) to half the width of the cavity ($x'=\frac{1}{2}x'_c$). Beyond that larger element sizes increasing with $\lambda=1.01$ in Eq. (3.23) are applied until they reach the upper limit of 0.03 which was adopted in the simulation of wave plunging. Larger elements are also applied for the thin jet region on the outer wave surface. As the impact further continues, a basic element size of 0.01 for l_S near the impact region provides satisfactory results.

Numerical results of the wall/water/air interaction in the post-direct impact process (stage 3) with initial air pressure of $P_0=10.087$ (i.e. h=1m) are shown in Figure 5.10, in sequence of the deformation of the entrapped air cavity, including the corresponding free surface evolution and pressure variation on the entire wall. The pressure and volume history of the entrapped cavity is given in Figure 5.11.

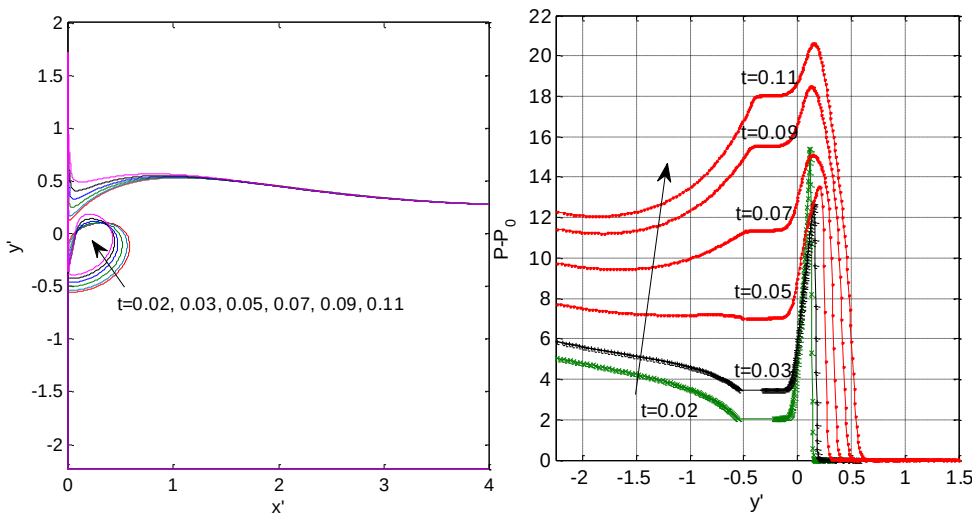

(a) 1st contraction stage (0.0200<*t*<0.1169)

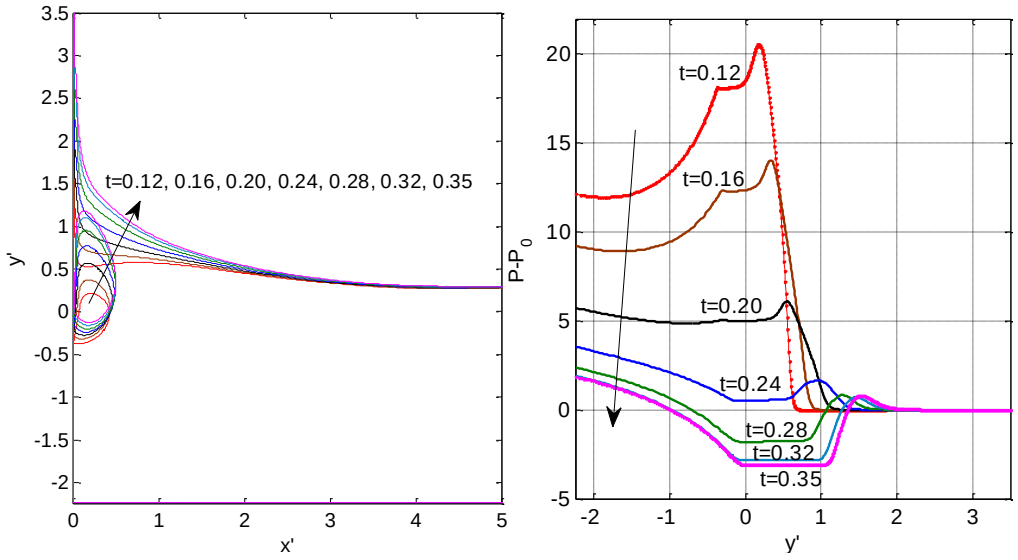

(b) 1st expansion stage (0.1169<*t*<0.3532)

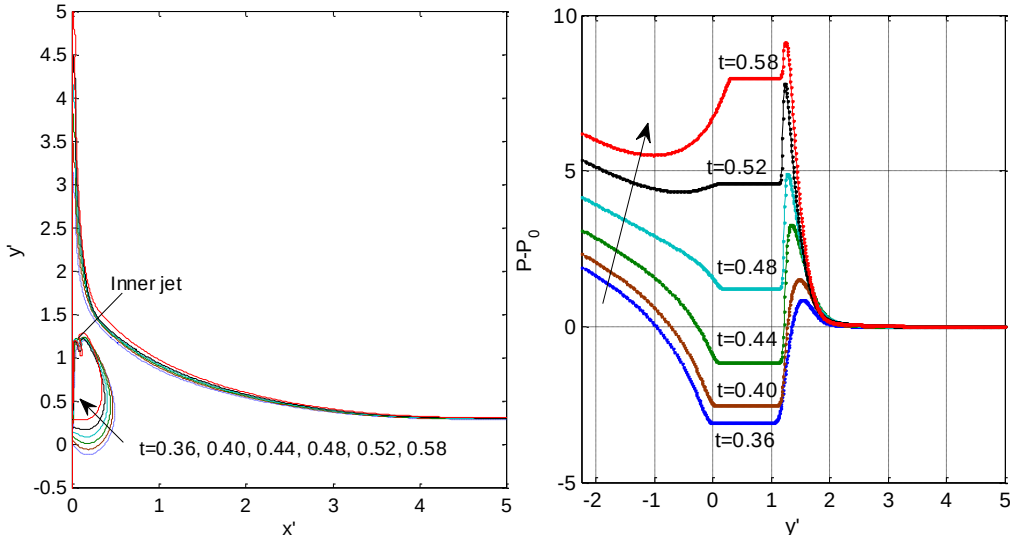

(c) 2nd contraction stage (0.3532<*t*<0.5806)

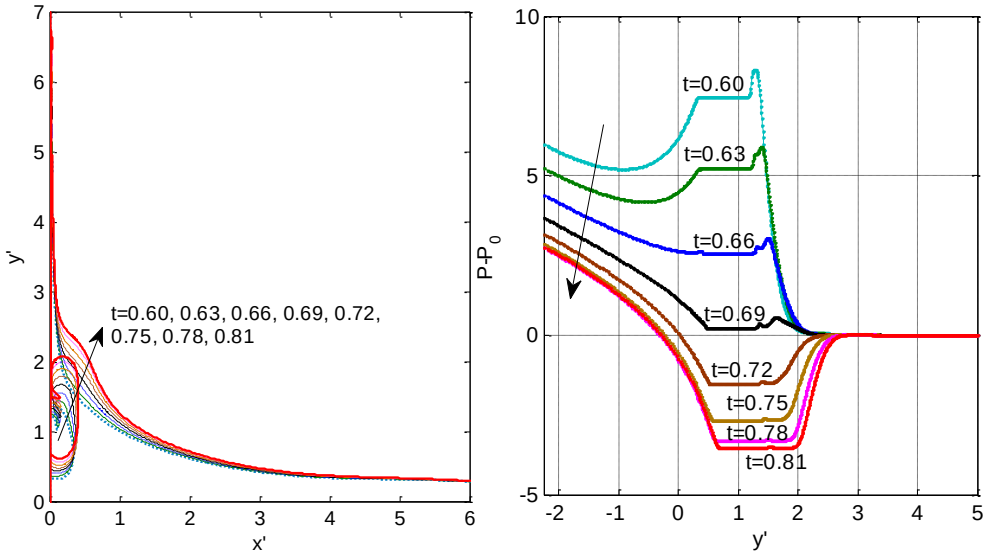

(d) 2nd expansion stage (0.5806<*t*<0.8100)

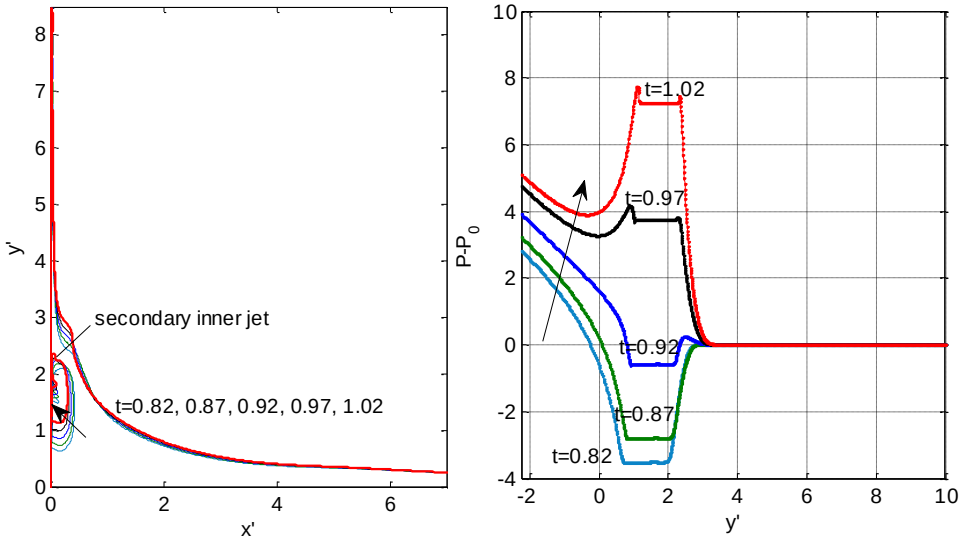

(e) 3rd contraction stage (0.8100<*t*<1.0210)

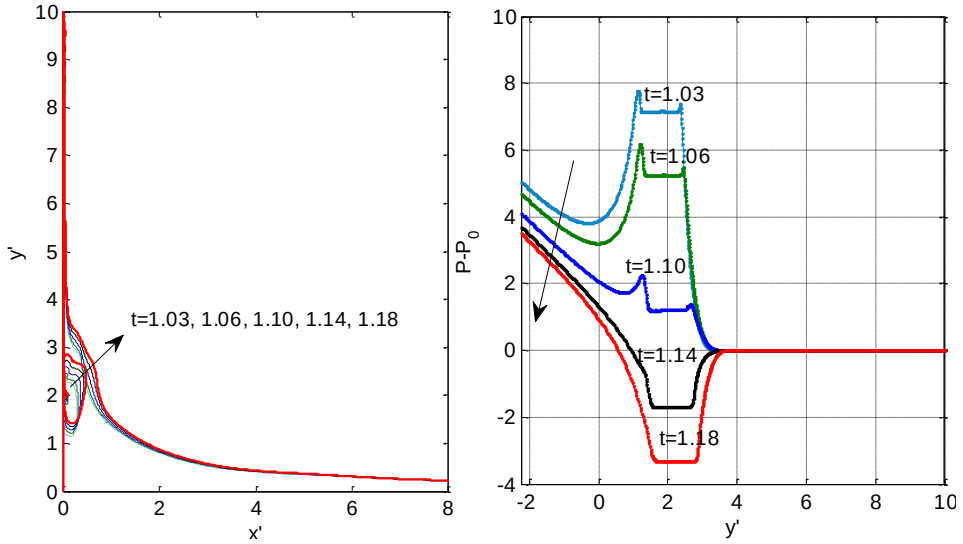

(f) 3rd expansion stage until the inner free jet meets the lower cavity surface (1.0210<*t*<1.1800)

Figure 5.10. Evolution of free surface profiles (left) and pressure distribution on the wall (right) during the wall/wave/air cavity interaction in stage 3 (case *a*-1: x_0=10, P_0=10.087)

From Figure 5.10(a), we can see that the entrapped air cavity first undergoes a contraction stage as being compressed by the impacting water flow. The pressure inside the cavity, as can be seen from Figure 5.11, increases to around 18 above the atmospheric value at the end of the first contraction stage at around *t*=0.117. In the region on the wall next to the cavity, either in direct contact with the air or by a thin fluid layer, the pressure is almost equal to that of the cavity. As a result, there is a small region on the wall with nearly uniform pressure distribution (the middle straight region on the pressure curves), varying with that inside the cavity throughout

the interaction process until the fluid layer in-between is no longer thin or smooth. Above the cavity region, the pressure peak on the wall stays in the wetted area formed by the original impacting wave crest. It first continues decreasing, for a very short time period, as the local inclination angle between the incident outer wave surface (undisturbed by the impact) and the wall increases, similar to that in stage 2 (see Figure 5.9(b)). As soon as the variation of cavity pressure has some noticeable effect, say after around t=0.03, the local pressure peak begins to increase as the cavity pressure increases. The maximum peak pressure on the wetted surface, exceeding the atmospheric value by 20.5 in magnitude, happens at the same time when the air cavity is compressed to its minimum volume at t=0.117. Moreover, the position of the pressure peak moves from the jet root of the wave surface to near that of the compressed upper cavity surface during this stage.

The overall pressure in the lower water body also varies with that of the air cavity, but at an increasingly slower rate at a distance farther away from the lower cavity surface down to the rigid bottom. This could be observed in all the pressure curves of the cases studied.

After the minimum volume of the cavity is reached, it starts to expand driven by the high internal pressure, as shown in Figure 5.10(b). A notable feature in the expansion stage is that the upper wave surface elevates vary fast, and meanwhile the cavity shape becomes elongated along the wall. The reason might be explained through an examination into the pressure variation on the wall during the late period of the previous compression stage in Figure 5.10(a). The pressure peak in the wetted area above the cavity has kept increasing as that inside the compressed air cavity. Meanwhile, the relative pressure in the upper wave surface jet stays zero (relative to the atmospheric pressure). Therefore when the wetted surface above the cavity is small as in the present study, a large pressure gradient is generated on the wall pointing upwards. As soon as the cavity starts to expand, the water above is pushed to shoot upwards under the action of the accumulated large pressure. This might reveal preliminarily the mechanism of the extremely violent upward water spray formed after an overturning wave strikes a wall and entraps an air cavity observed in the experiment (e.g. Bredmose et al. 2009).

The minimum pressure becomes negative relative to the ambient pressure in the region next to the cavity in late the expansion stage (around -3 in the current case of

a-1), and so are the small adjacent regions in the water area above and in the water body below, as can be seen from t=0.28 to 0.35 in Figure 5.10(b). Meanwhile the local pressure peak above stays positive of around 1.5 in the wetted area. Consequently, there is a local pressure gradient near the turning point of the upper cavity surface at the end of the expansion stage, pointing from the pressure peak on the wetted surface into the fluid domain, towards the adjacent cavity surface. This then leads to the generation of an inner jet with free surface on both sides there when the much elongated air cavity starts to contract again, as can be seen from Figure 5.10(c). The position of the root of the inner jet on the wall is found corresponding to the position of the increasing local pressure peak, moving from around $y' = 1.55$ to 1.25 during the second contraction stage.

As the distorted cavity expands upward again, the small pressure peak corresponding to the described inner jet root begins to separate gradually from the pressure peak caused by the sharp turn of the upper cavity surface along the wall, as the early stage of the second expansion shown in Figure 5.10(d) from $t = 0.60$ to 0.69. The former one is in much smaller magnitude than the later one. Nevertheless, the pressure peak in the top water region disappears when the cavity pressure drops below the atmospheric pressure in late stage of the second expansion, owing to the much flattened upper cavity surface, as can be seen from $t = 0.72$ to 0.81. The pressure there then drops fast from the ambient pressure near the top wave surface jet root downwards to the negative cavity pressure. Moreover, the outer wave surface is pushed by the much expanded cavity to form a small hump.

In the subsequent contraction stage as the cavity is compressed for the third time, there is also a tendency of the formation of secondary interior jet near the turning point of the upper cavity surface, as can be seen from Figure 5.10(e).

In the third expansion stage, the cavity further moves up and push the proximate wave surface, during which a local pressure peak appears as the lower cavity surface is to take turn along the wall. The simulation stops as the lower cavity surface meets with the small free jet located in the middle of the upper jet formed earlier during the first re-contraction (or the second contraction) stage, at around t=1.18.

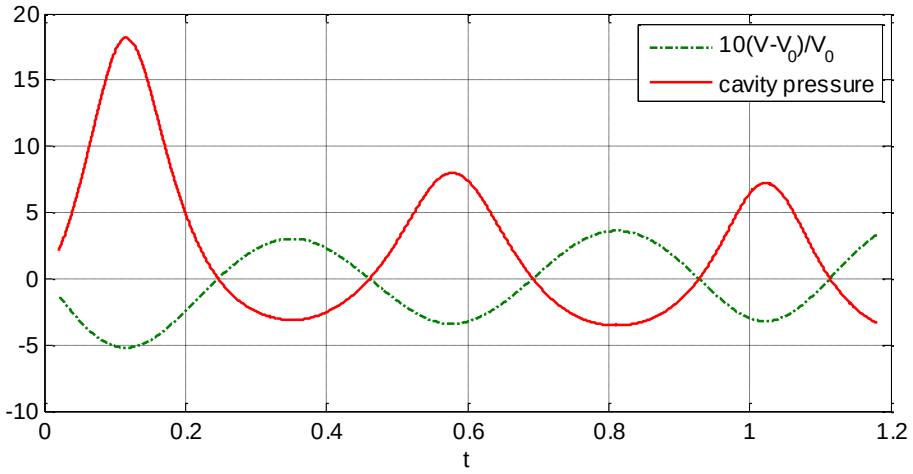

Figure 5.11. Time history of the volume and pressure of the entrapped air cavity (x_0=10, V_0=0.3438, P_0=10.087: case *a*-1)

a-2. P_0=100.8

The post-direct impact process with air cavity (stage 3) is simulated for the same case of $x_0 = 10$ but with much larger initial pressure of $P_0 = 100.87$. This corresponds to an initial still water depth of $h = 0.1\text{m}$ for the current wave model, which is a typical scale for the still water depth in laboratory experiments conducted for breaking wave impact. Numerical results of wall/water/air interaction in stage 3 are given in Figure 5.12, proceeding with the simulation of stages 1 & 2 shown in Figure 5.7 & Figure 5.9. The corresponding history of volume and pressure change of the air cavity is shown in Figure 5.13.

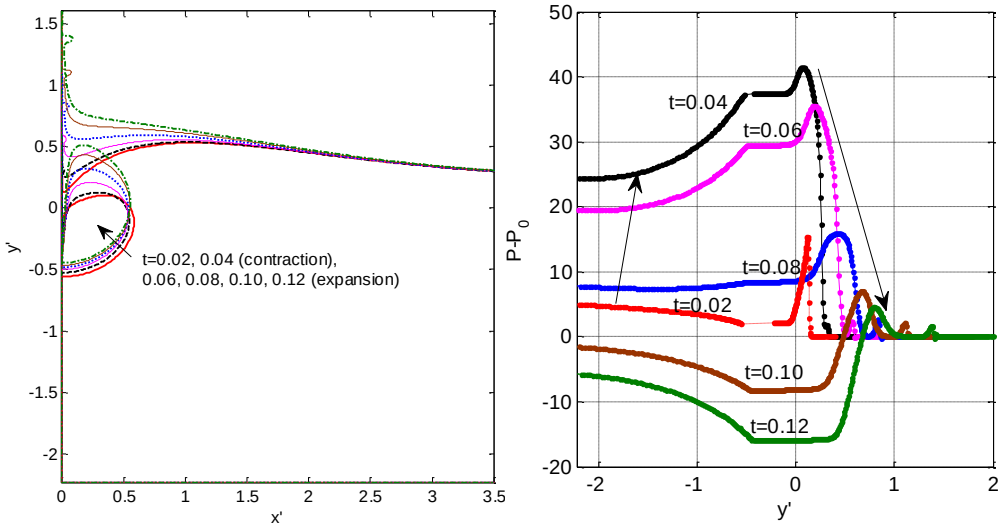

(a) 1st contraction (t<0.0435) and expansion stages (0.04335 <t<0.1272)

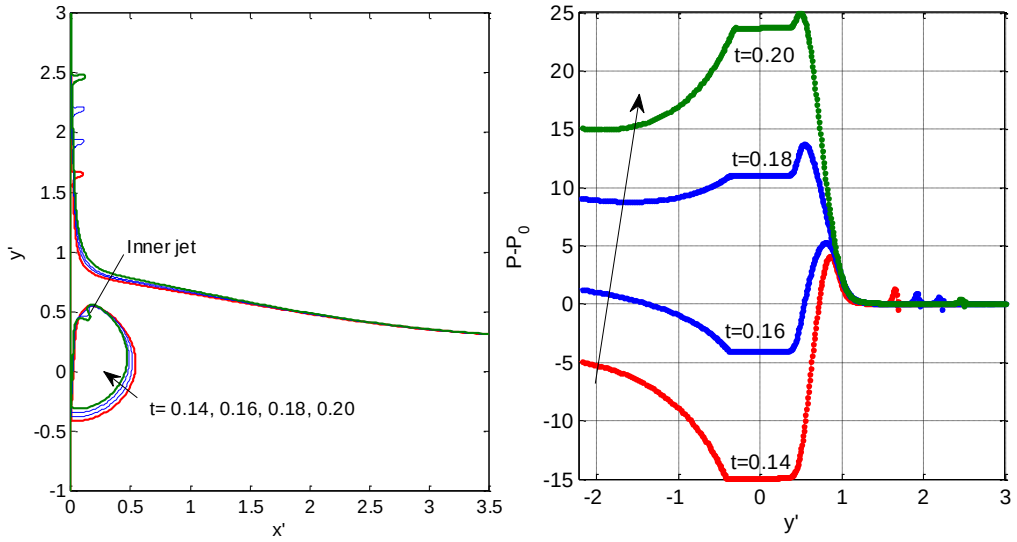

(b) 2nd contraction stage ($0.1272<t<0.2095$)

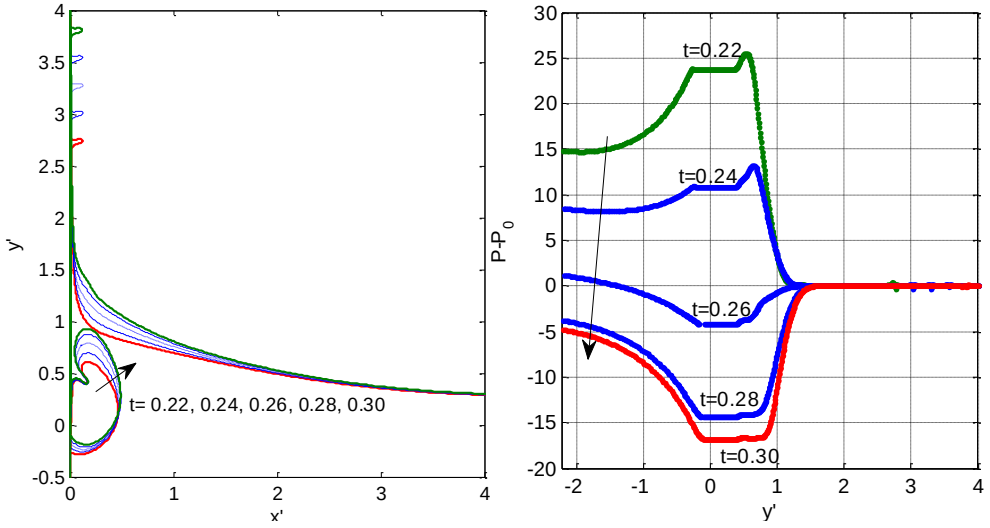

(c) 2nd expansion stage ($0.2095<t<0.2940$)

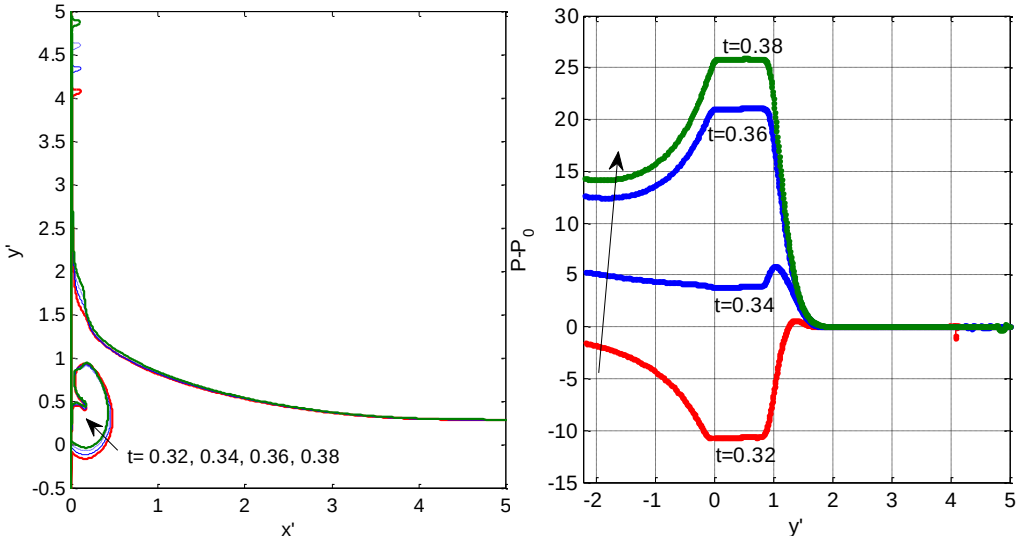

(d) 3rd contraction stage ($0.2940<t<0.375$)

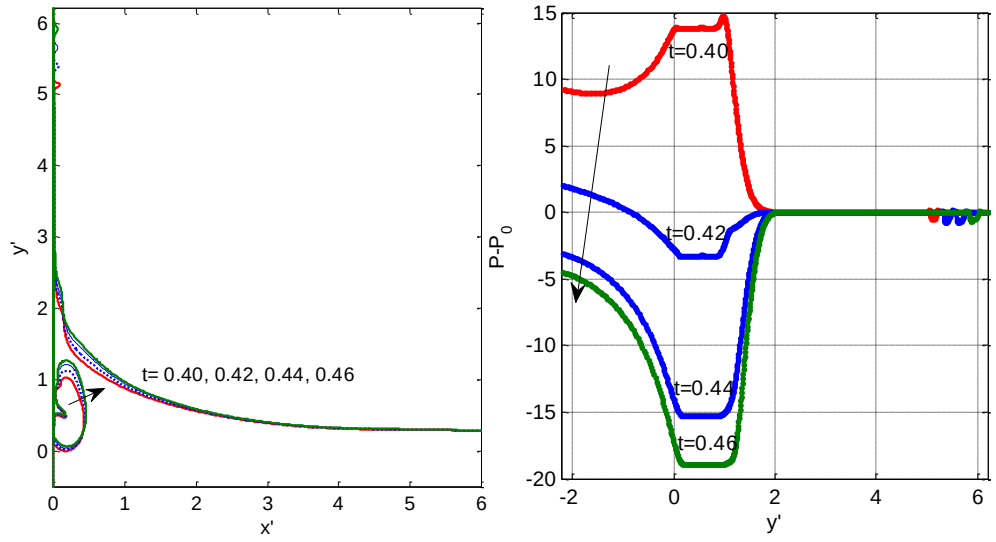

(e) 3rd expansion stage (0. 375<*t*<0.4595)

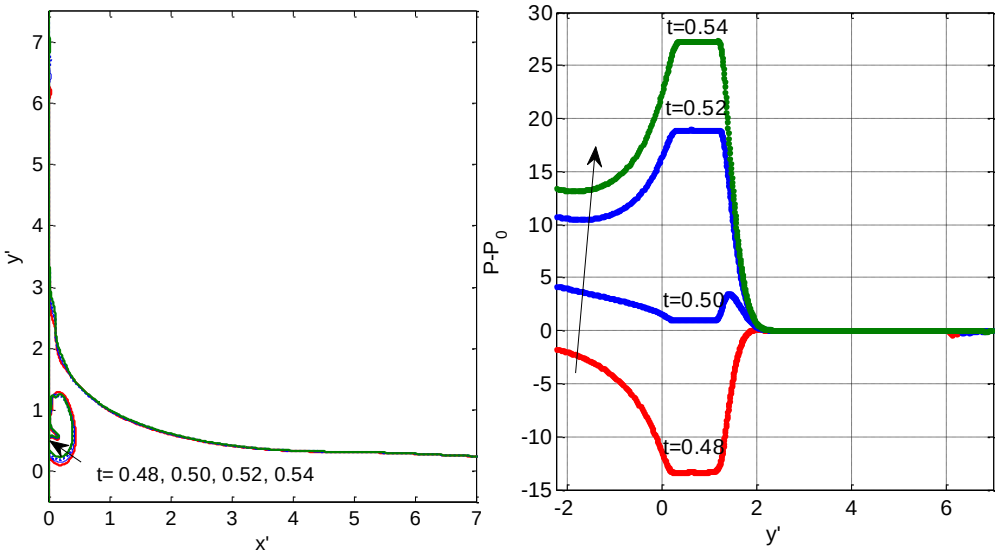

(f) 4th contraction stage (0.4595<*t*<0.5379)

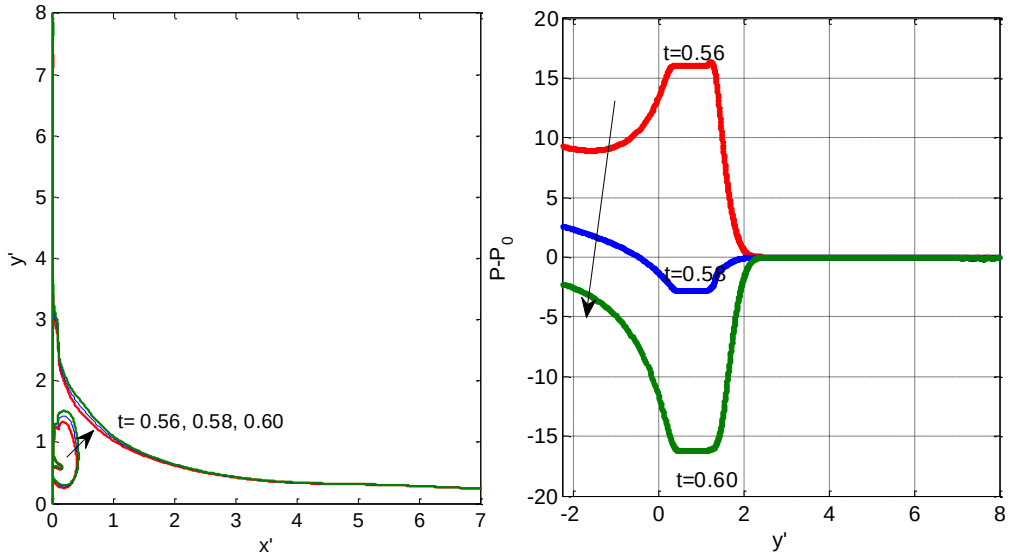

(g) 4th expansion stage until the inner free jet meets the lower cavity surface ($0.5379<t<0.6087$)

Figure 5.12. Evolution of free surface profiles (left) and pressure distribution on the wall (right) during the wall/wave/air cavity interaction in stage 3 (case *a*-2: x_0=10, P_0=100.87)

Compared to the results of $P_0=10.087$ (i.e. $h=1m$) discussed in Figure 5.10, it can be seen from Figure 5.12(a) that, under the initial air pressure of $P_0=100.87$ the entrapped air cavity is compressed less intensely by the impacting wave to a bigger minimum volume. The compression stage lasts for a shorter time period, and the cavity starts to expand soon after around $t=0.04$. The relations between $\frac{V_{\min}}{V_0}$, or $\frac{P_{\max}}{P_0}$, and the energy are the same as those deduced in section 4.3.5 for water column impact with entrapped air cavity (see Eqs.(4.11) & (4.12)), except for changing the right hand side expression of $-\frac{\delta K}{E_{a0}}$ into $-\frac{\delta K+\delta E_G}{E_{a0}}$, where $\delta E_G=E_G-E_{G0}$ is the increment of the gravitational potential energy of the impacting flow. With the same impact wave model, the initial potential energy of the cavity E_{a0} (Eq.(4.9)) with $P_0=100.87$ is 10 times as big as that with $P_0=10.087$. According to the relation plotted in Figure 4.14, assuming that the changes in the nondimensional mechanical energy of the surrounding liquid $-(\delta K+\delta E_G)$ are in similar range during the first contraction stage, a much smaller $\frac{P_{\max}}{P_0}$, or bigger $\frac{V_{\min}}{V_0}$ is then generated for the cavity with the much bigger E_{a0} in the current case. However, the pressure *P* itself varies in bigger amplitude, as can be seen from Figure 5.13.

A particular feature appears at the beginning of the expansion stage as a small hump near the root of the upper wave surface jet (see Figure 5.12(a)). It happens if the local pressure gradient on the wetted surface grows sufficiently large, which is decided by both the pressure peak magnitude and its location relative to the upper free surface. In the present case with $P_0=100.87$, the pressure peak magnitude is bigger (around 40). In addition, the cavity starts to expand so soon that the pressure peak is still located at the very root of the upper free surface jet, and thus an extremely large local pressure gradient is generated there at the end of the

contraction stage. The generated small upper free surface hump later moves away upward with the impinging water. A similar free surface hump could also be observed in the numerical simulation of an intense 'flip-through', where the water was accelerated up the wall below the up-turning concave free surface (Cooker & Peregrine 1990c, Scolan 2010).

When the expanded cavity starts to contract again in the second period after around t=0.12, a local free jet is also drawn near the root of the upper cavity surface jet at around $y' = 0.5$, as can be seen in Figure 5.12(b). The mechanism is similarly related to the local large pressure gradient pointing nearly vertical to the nearby cavity surface from the peak pressure on the wall. It can be seen that the local pressure peak of around 5 on the wall falls rapidly to the cavity pressure of -15 (relative to the ambient pressure) across the fluid layer located around $y' = 0.5 \sim 0.75$. As a result, the local fluid particles are accelerated toward the inner cavity surface when the cavity starts to contract again, and a free jet is evoked there. The second maximum pressure of the air cavity around 23 is much smaller than the first one at t=0.20, as can be seen from Figure 5.12(b) or Figure 5.13.

In the following two expansion and three contraction circles of the air cavity, as shown in Figure 5.12(c)-(g), the expansion stages have also been accompanied by an elevation of outer wave surface and the elongation of the cavity along the wall. It is interesting to see that, at the beginning of each contraction stage, the tendency of the generation of another secondary interior jet appears again on the upper cavity surface, from where it takes the sharp turn downwards the wall, though not as well formed as the first one. The simulation stops for the same reason as that in Figure 5.10, at around t=0.61, when the previously formed inner free jet reaches the lower cavity surface.

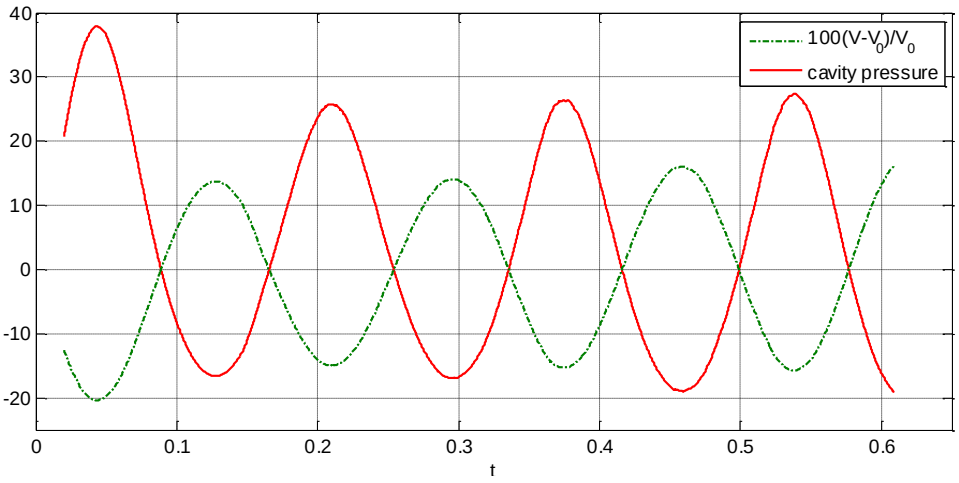

Figure 5.13. Time history of the volume and pressure of the entrapped air cavity (x_0=10, V_0=0.3438, P_0=100.87: case a-2)

a-3. P_0=2.0174

With the same plunging wave model developed with $x_0 = 10$ (see Figure 5.7), stage 3 is simulated again with smaller initial air pressure of $P_0 = 2.0174$ (i.e. $h = 5m$). The numerical results of the impact dynamics are shown in Figure 5.14, and the corresponding history of the pressure and volume change is shown in Figure 5.15.

Following the instant direct impact period of stage 2 shown in Figure 5.9, the pressure peak continues to fall at early stage of the compressed air cavity before it increases with that inside the cavity at around $t = 0.08$. With the much smaller initial air pressure compared to the above two cases, the cavity is compressed more and over longer period by the surrounding impact flow, to a minimum volume of $0.1584V_0$ at t=0.169, as shown in Figure 5.15. The corresponding process is shown in Figure 5.14(a). This produces a maximum cavity pressure of 24.587 above the ambient value, which is over 12 times of the atmospheric pressure. The much bigger value of $\frac{P_{\max}}{P_0}$, can also be attributed to the much smaller initial potential energy of the air cavity E_{a0}, according to the relation plotted in Figure 4.14. Meanwhile, the loss in the nondimensional mechanic energy of the water during the compression stage differs in much smaller range than that of E_{a0} (which should be bigger than the two previous cases as the cavity is compressed harder for $P_0 = 2.0174$).

Similar to the previous expansion stages, with the large pressure gradient formed in

the top water region above the air cavity at the end of the contraction stage, the waterline at the wall shoots significantly upward the wall, as shown in Figure 5.14 (b). A small free surface hump is also formed near the root of the outer wave surface jet and moves fast upward. The cavity is also significantly elongated along the wall as it expands, and we can find through the three cases that the smaller it was compressed to in the first contraction stage, the more elongated it becomes. The pressure on the wall next to the cavity, equal to its pressure inside, falls below the ambient pressure (around -8) when the cavity reaches to its maximum volume at around $t = 0.556$.

While the cavity begins to contract, the upper wave surface almost ceases elevating except for the jet region along the wall. Again, a small free jet is formed protruding from the upper cavity surface near the wall, as the local pressure gradient grows larger near the upper cavity jet root, as shown in Figure 5.14(b). Current simulation will stop if such inner jet touches the nearby cavity surface. In this case it is still very small when the simulation stops at t=0.76.

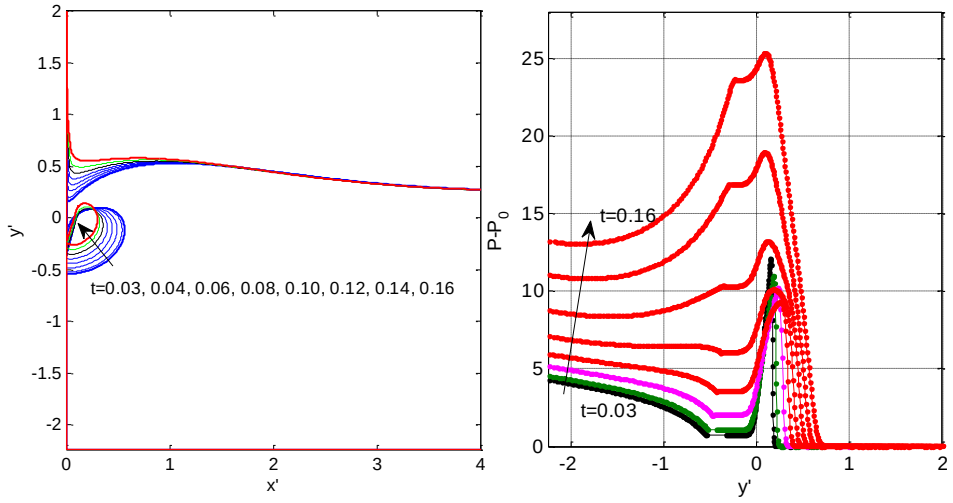

(a) 1st contraction stage ($0 \le t \le 0.169$)

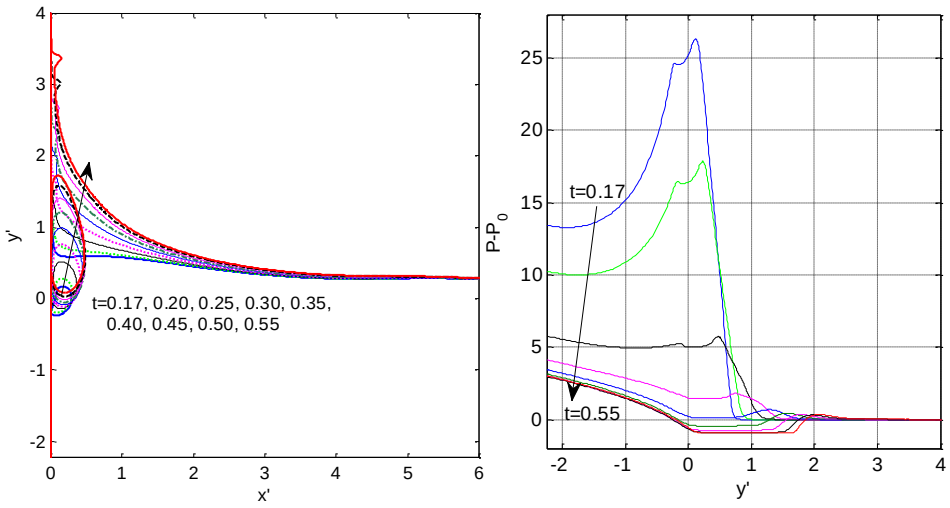

(b) 1st expansion stage ($0.169 \le t \le 0.556$)

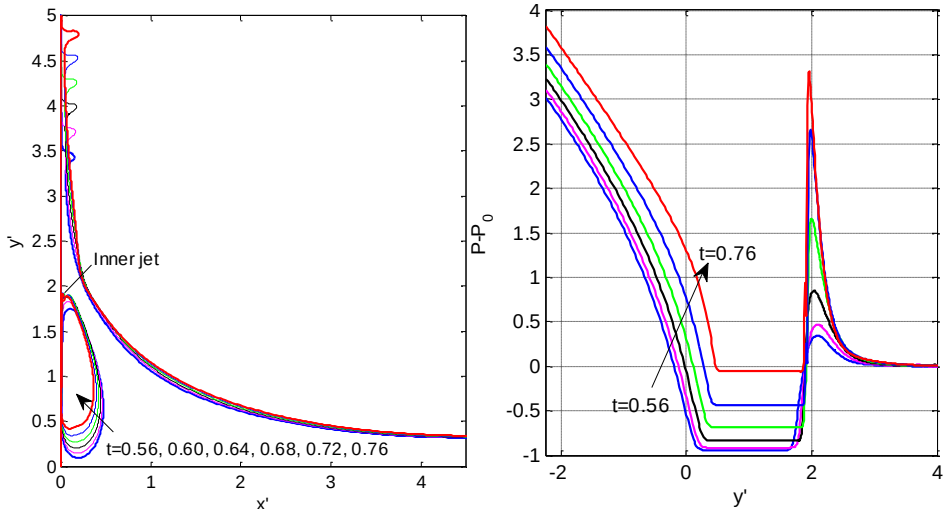

(c) 2nd contraction stage until inner free jet touches the nearby surface ($0.556 \le t \le 0.76$)

Figure 5.14. Evolution of free surface profiles (left) and pressure distribution on the wall (right) during the wall/wave/air cavity interaction in stage 3 (case *a*-3: x_0=10, P_0=2.0174)

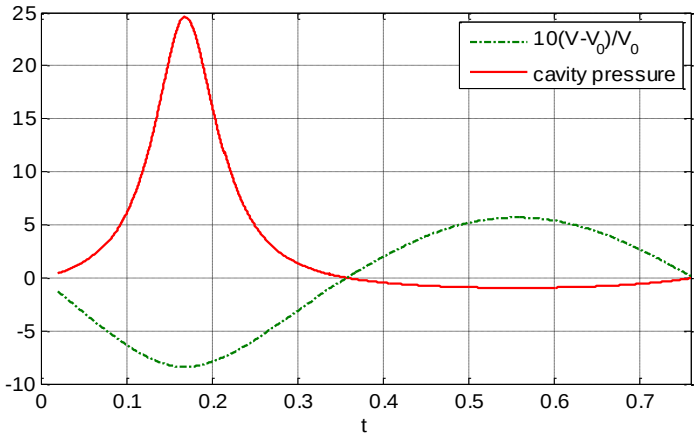

Figure 5.15. Time history of the volume and pressure of the entrapped air cavity (x_0=10 , V_0=0.3438, P_0=2.0174: case a-3)

5.4.2 Case b. x_0=9

With the same initial wave model of $\Delta h = 1.5$ (i.e. $u_0 = 1.1623$) and $k = 0.5$ in Eqs. (5.1) and (5.2), the case where the wall is placed nearer of $x_0 = 9$ away from the initial incident wave centre will be looked into in this section.

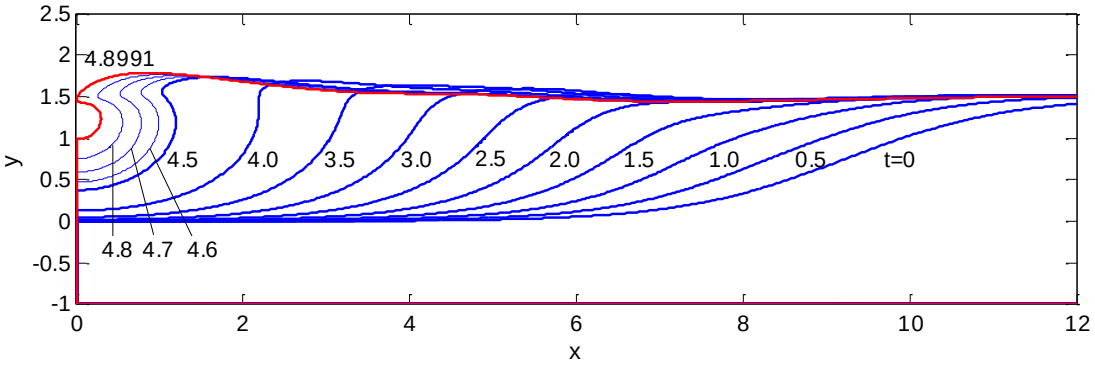

Figure 5.16. Wave surging and overturning until impact on the wall at t=4.8991 (x_0=9, stage 1)

From Figure 5.16, it can be seen that incident wave also first surges without being significantly influenced by the wall. The water line there stays approximately still, but for a shorter period of around $t = 3.0$, compared to that of $t = 4.0$ in the case $x_0 = 10$ (Figure 5.7). The front of the surging wave does not steepen enough to overturn until after around $t = 4.0$, which is similar to the previous case of $x_0 = 10$. However, the water level at the wall elevates much faster in this case as the wave plunges, and the wave crest hits the wall after a shorter time of t=4.8991 at (0, 1.4713) with a velocity of (-2.6509, -0.3695). This leads to the formation of a blunter wave crest (i.e. with smaller front curvature and bigger width) than that in Figure 5.7, as well as a smaller cavity of initial size $V_0 = 0.1052$.

The local coordinate system $o' - x'y'$ is then established at (0, 1.4713) for stages 2 & 3. $U = 2.609$ is employed in Eq. (5.13) for the S system. The initial penetration time upon impact is set to be $t_0 = 5 \times 10^{-5}$, the same computation parameters (computation domain length L in the S system, grid size and time step coefficient, etc.) are employed as the previous case with $x_0 = 10$. Computation in stage 2 is to be illustrated in the physical coordinate system, without details of the dual window as those shown in Figure 5.8(a) and Figure 5.9(a). The close-up of wave profiles and the local impact pressure are given in Figure 5.17, from $t = t_0$ to 0.0103.

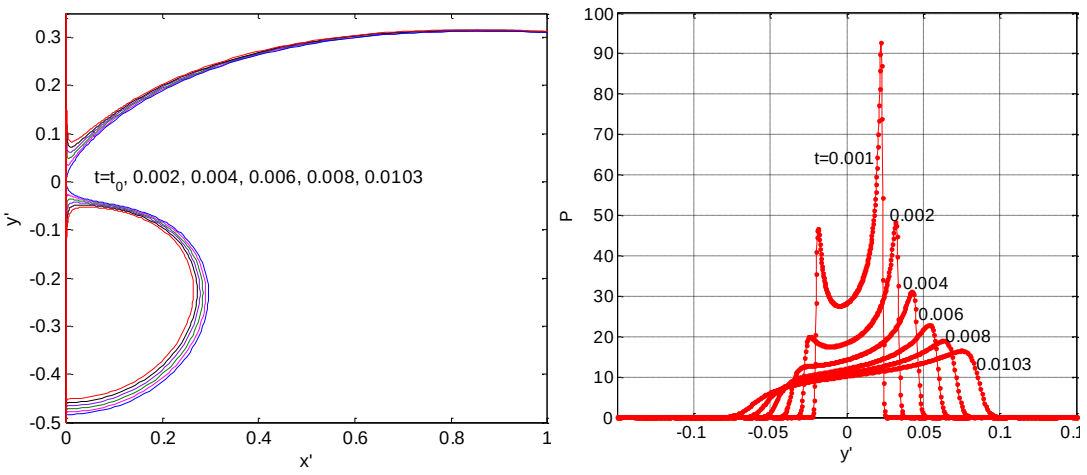

(a) (b)

Figure 5.17. Direct impact by the wave crest with results extracted from the dual system in stage 2 with $x_0 = 9$: (a) close-up of free surface profiles ($t_0 = 5\times10^{-5}$); (b) corresponding local pressure variation on the wall

Compared to the case of $x_0 = 10$ (see Figure 5.9(b)), the wave head in this case touches the wall with smaller initial deadrise angles at $t = t_0$, and thus yields two bigger peak pressure, which can be evidently seen in the pressure curve for t=0.001. Their magnitude decreases as the inclination angles increase gradually as the impact continues. The peak with $y' > 0$ is bigger and lasts for longer period than the one with $y' < 0$. Pressure extremum near the lower free surface jet root lasts for longer time period than that of $x_0 = 10$ before disappearing. Those results all agree with the close relation between the pressure peak near the jet root and the corresponding local inclination angle by the undisturbed free surface on the structure: the smaller the local inclination angle is, the bigger the pressure extremum is; and it will disappear as the angle increases.

After the initial impact stages simulated in stage 2, the wetted surface grows large enough (with the width of the incident wave crest undisturbed by the wall 0.0905 at t=0.0103). The effect of the trapped air cavity is then taken into account in stage 3. Results of cavity deformation with initial air pressure of $P_0 = 10.087$, 100.87 and 2.0174, in terms of its volume change and pressure variation, are shown and compared in Figure 5.18. The corresponding wall/water/air interaction results showing the corresponding wall/wave/air cavity interactions are given in Figure 5.20-Figure 5.21.

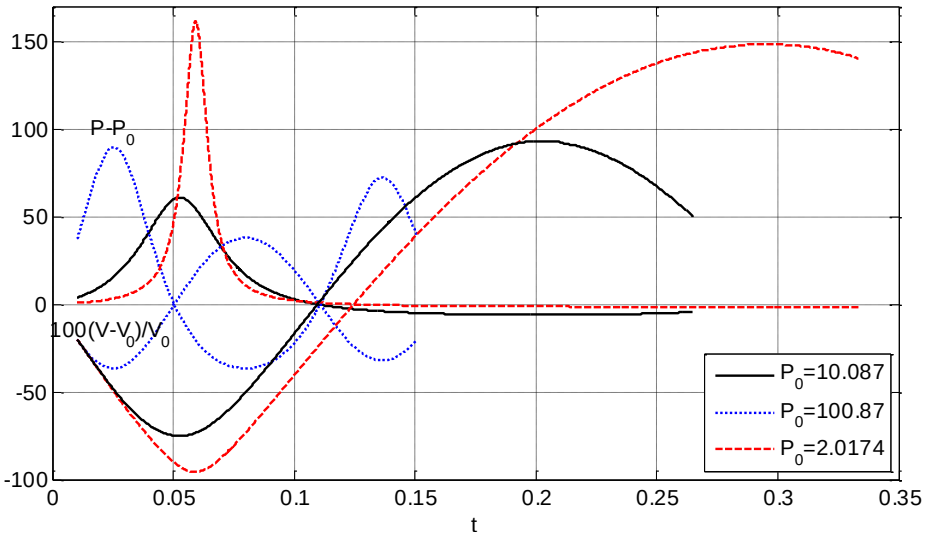

Figure 5.18. Time histories of the volume and pressure of the entrapped air cavity in stage 3 (x_0=9, V_0=0.1052, case b-1,2 & 3)

From Figure 5.18, behaviour similar to that in the case $x_0 = 10$ can be observed. The smaller the initial air pressure is, the more and longer the cavity is compressed. In addition, for each P_0, the cavity volume variation is faster and larger in range for the case $x_0 = 9$ with smaller V_0 than that for $x_0 = 10$, and thus much bigger maximum pressure is generated in the air cavity (around 89.64, 60.98 and 161.7 above the atmospheric pressure respectively for cases b-1, 2 & 3, respectively at t=0.026, 0.053 and 0.059), as well as on the wall. The governing mechanism underneath related to the air cavity effect is to be analysed in detail later in 5.4.3.

b-1. P_0=10.087

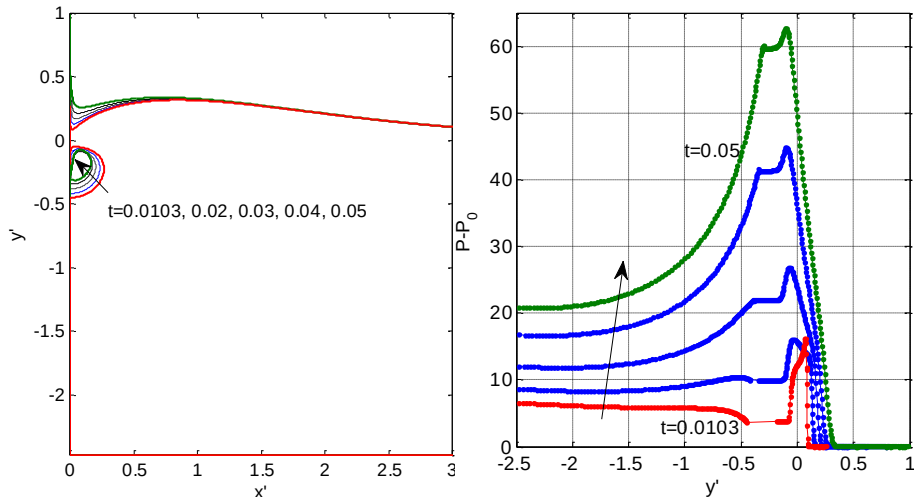

(a) 1st contraction stage (0.0103<t<0.0531)

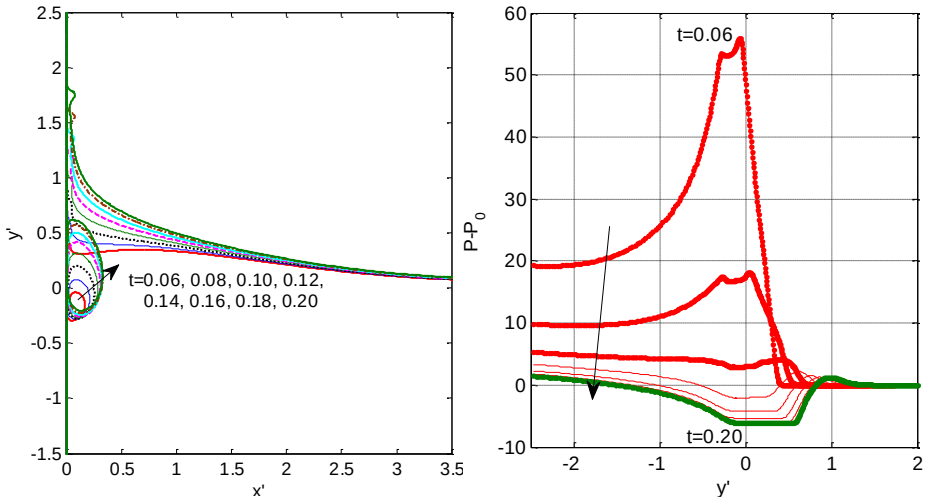

(b) 1st expansion stage ($0.0531<t<0.2045$)

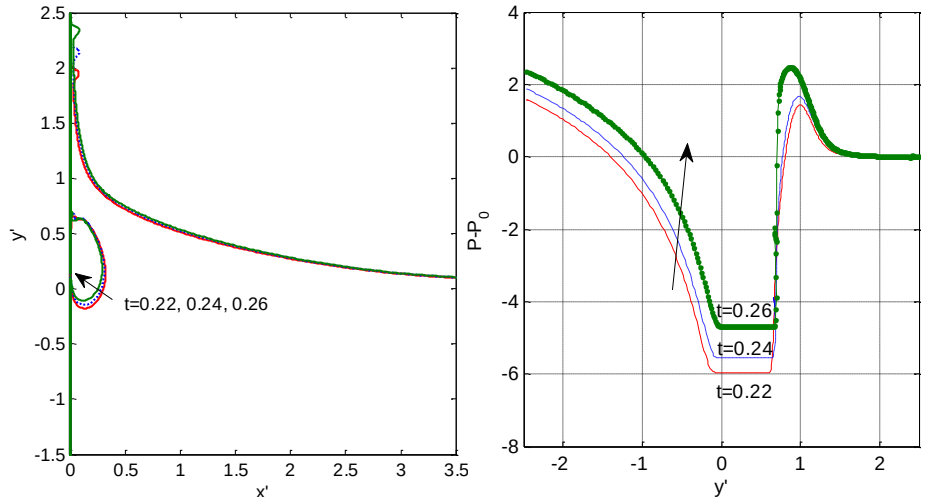

(c) 2nd contraction stage until the inner jet touches the nearby surface ($0.2045<t<0.2649$)

Figure 5.19. Evolution of free surface profiles (left) and pressure distribution on the wall (right) during the wall/wave/air cavity interaction in stage 3 (case *b*-1: x_0=9, P_0=10.087)

b-2. P_0=100.87

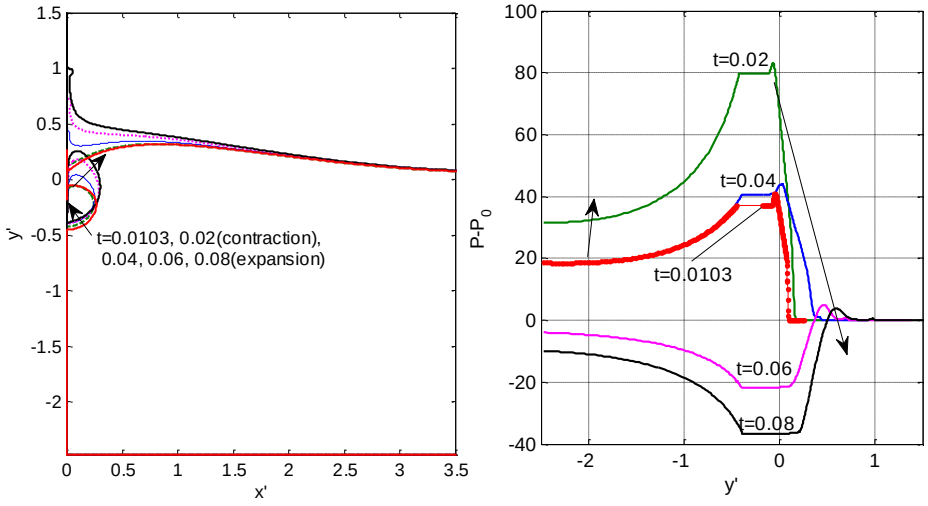

(a) 1st contraction (t<0.0255) and expansion (0.0255<t<0.0798) stages

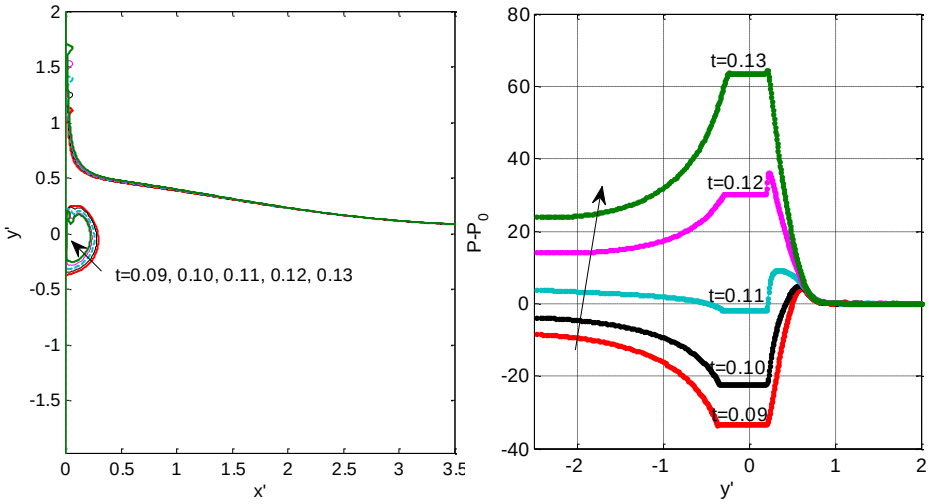

(b) 2nd contraction stage (0.0798<t<0.1362)

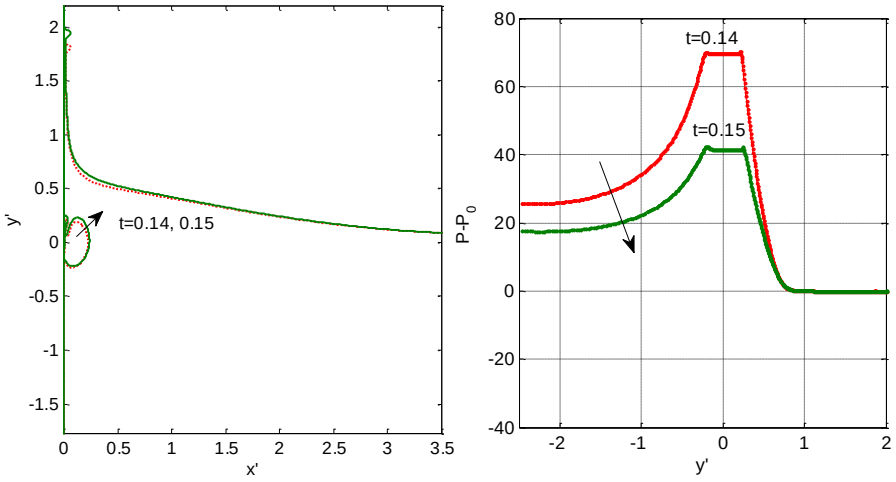

(c) 2nd expansion stage until the inner free jet touches the cavity surface (0.1362<t<0.1500)

Figure 5.20. Evolution of free surface profiles (left) and pressure distribution on the wall (right) during the wall/wave/air cavity interaction in stage 3 (case *b*-2: x_0=9, P_0=100.87)

b-3. P_0=2.0174

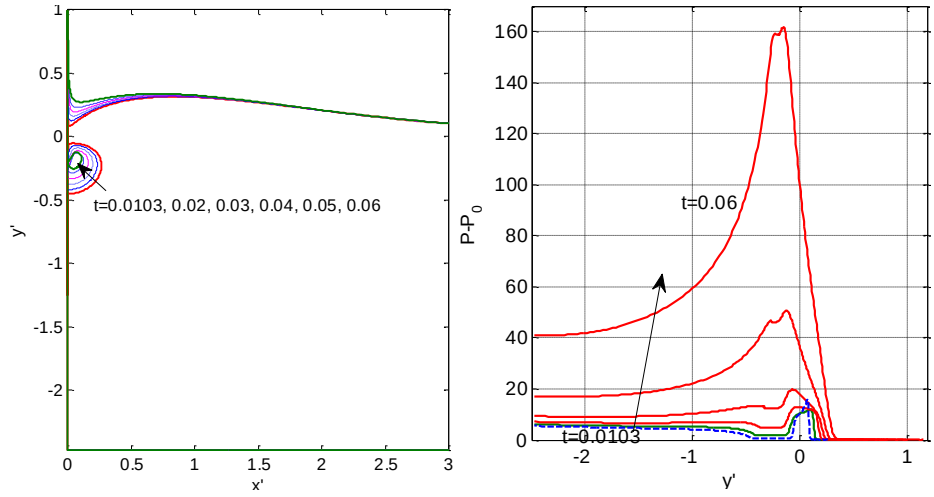

(a) 1st contraction stage (0.0103<t<0.0593)

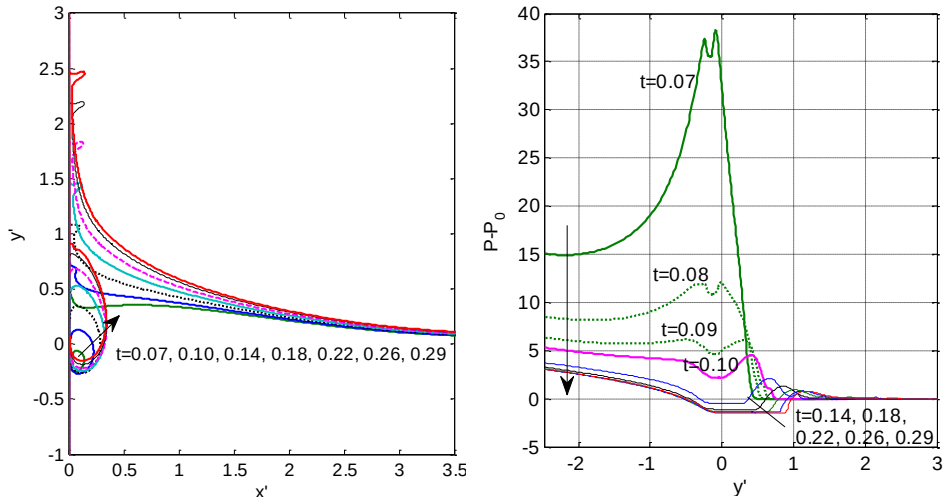

(b) 1st expansion stage (0.0593<t<0.2953)

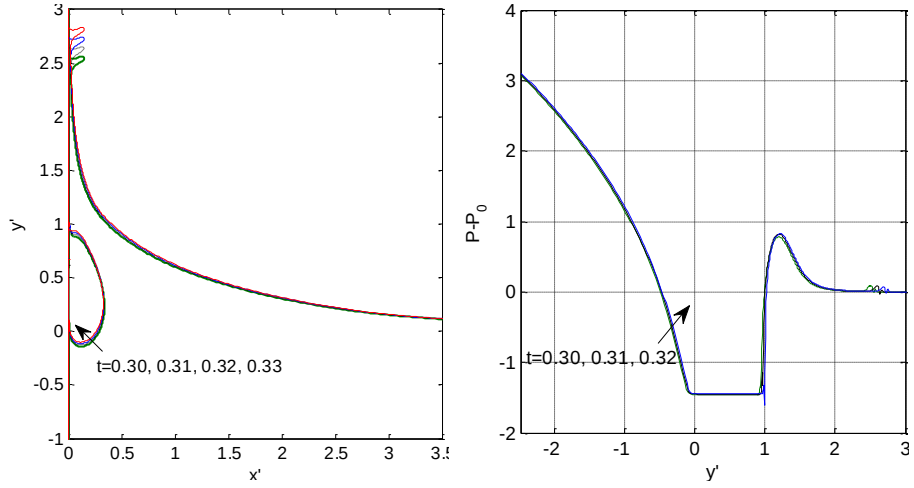

(c) 2nd contraction stage until the inner jet touches the nearby cavity surface(0.2953<t<0.33)

Figure 5.21. Evolution of free surface profiles (left) and pressure distribution on the wall (right) during the wall/wave/air cavity interaction in stage 3 (case *b*-3: x_0=9, P_0=2.0174)

Individually, the three initial air pressure values of P_0 with $x_0 = 9$ lead to different impact dynamics. Nevertheless, each of them follows the common features of wall/wave/cavity interactions during the post-direct impact process of stage 3, as discussed in the previous case of $x_0 = 10$. Proceeding with the initial compression stage, there is a significant wave surface elevation along the wall, pushed by a larger pressure, and therefore a larger pressure gradient in the top fluid region. A small free surface hump might be formed near the outer wave surface jet root (see Figure 5.19(a), Figure 5.20(b) & Figure 5.21(a)), caused by the extremely large pressure gradient from the pressure peak on the small wetted surface (located near the root of the incident wave crest surface jets). The cavity is elongated along the wall during its expansion, and its pressure drops below the atmospheric value. When the cavity is about to contract again, there is a 'fragile' area around the turning point of the upper cavity surface toward the wall. With a high local pressure gradient generated there from the nearby pressure peak on the wall, an inner jet with free surface on both sides is likely to be drawn there as the cavity contracts, which later impinges the nearby cavity surface forming multi-cavities. The outer wave surface only elevates slightly during the contraction stage, and so is the top cavity surface, while its lower surface could elevate significantly along the wall. Such process could repeat for several cycles. As a result, the cavity seems to climb along the wall in the water-air interaction process, with its top surface moving faster in the expansion stage while the lower surface faster during the contraction stage. The formation and evolution of such inner free jets, during the re-contraction of an expanded cavity along the wall, reveals the feature of cavity distortion as it interacts with the wall and the surrounding water wave. The subsequent impingement between the free jets and the nearby cavity surface could shed light on the mechanism of cavity fragmentation as observed frequently in experiments.

5.5 The scaling law related to the air cavity effect

- Energy transfer relation

In the current problem of plunging wave impact, the effect of gravity is important and included in the calculation. As mentioned during the case studies, the energy transfer relation discussed in section 4.3.5 needs to be updated to include the gravitational potential energy of the water flow, E_G. With the work done by the air

(both inside the cavity and from the surrounding atmosphere) to the moving liquid given in Eq. (4.7), it is equal to the increment in the mechanical energy of the water, including its kinetic energy K (Eq. (4.10)) and the gravitational potential energy E_G. With the potential energy of the cavity E_a defined in Eq. (4.9), we then have from the law of energy conservation

$$E_a + P_0V + E_G + K = E_{total} = \text{constant} \tag{5.24}$$

where P_0V is a term related to the work done by the surrounding atmosphere, and E_{total} is the total energy.

The variation of each term on the left hand side of Eq. (5.24), as well as as their sum, is plotted in Figure 5.22 corresponding to the wall/wave/air interaction process shown in Figures 5.10 & 5.11 for case a-1 ($x_0 = 10$, $P_0 = 10.087$). The gravitational potential energy E_G is given with respect to the reference line $y'=0$.

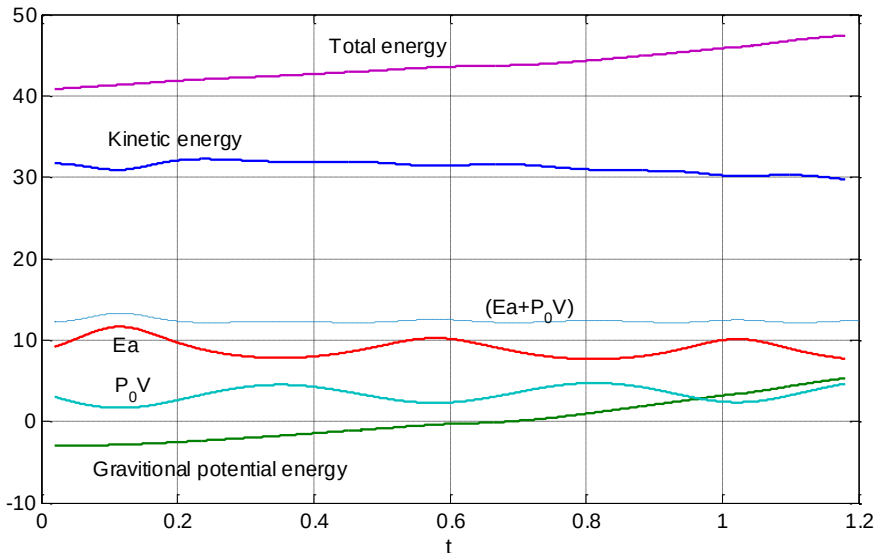

Figure 5.22. Energy transfer (see Eq. (5.24)) during wall/wave/air interaction of case a-1 (x_0=10, V_0=0.3438, P_0=10.087)

It can be seen that, the potential energy of the air cavity E_a grows to its biggest value at the end of the initial compression stage at around t=0.117. This is accompanied by a considerable decrement in the kinetic energy of the impacting wave. In spite of the variation in the individual energy terms in Eq. (5.24), the total energy stays approximately as a straight line which increases slowly. The deviation could be related to the neglect of the direct impingement by the cavity jet initially formed on the wall in the numerical simulation, which has been avoided by the numerical

treatment of the constant update of the jet tip before it meets the lower cavity surface. Although the liquid truncated away has been subtracted from the air volume, the associated possible loss in the kinetic energy caused by jet impingement and its influence on the fluid dynamics are not considered. Consequently, the numerical result of the total energy keeps increasing as the post-direct impact process continues. Even though, the deviation is within a rational range, with a relative increment of around 5% by the end of the second expansion stage at around t=0.8. The gravitational potential energy of the impacting flow has kept increasing, as the overall wave elevates along the wall during the oncoming process, as can be seen from the wave profiles shown in Figure 5.10. This could explain the attenuation in the energy transfer during the water-air interaction process, as well as the decrement in the pressure peak of the cavity during its secondary contraction stages, as the pressure history curve shown in Figure 5.11. Whereas for plunging wave overtopping a ship deck or a coastal structure, we can speculate that following the initial impact stage the gravitational potential energy of the overtopping wave E_G may decrease considerably as the fluid flows along the structure surface. This corresponds to an increment in the left energy terms in Eq. (5.24) (i.e. $E_a + P_0V + K$), while their individual variation demands further investigation.

- An investigation into the scaling law based on numerical results

The end of the first compression stage of the air cavity in the plunging wave impact could be found to correspond with the biggest potential energy of the cavity E_a (see Figure 5.22), as well as the largest cavity pressure as it contracts for more than once. Define the first maximum pressure inside the air cavity after the initial compression as $P_{\max}$. From the cases studied in sections 5.4.1 & 5.4.2 for the wall/wave/air intersection in stage 3, it has been found that, for the same wave impact model, the smaller the initial dimensionless air pressure P_0 is, the bigger $P_{\max}/P_0$ is generated for the air cavity, and the slower the oscillation is (in terms of dimensionless time). With the same initial air pressure value P_0, smaller initial air volume V_0 also leads to bigger $P_{\max}/P_0$ and faster oscillation process.

After including the variation of the gravitational potential energy of the water $\delta E_G = E_G - E_{G0}$ (E_{G0} the initial value upon impact) in the current case of plunging wave impact, Eq. (4.12) could be rewritten as

$$\left(\frac{P_{\max}}{P_0}\right)^{\frac{\gamma-1}{\gamma}}+(\gamma-1)\left(\frac{P_0}{P_{\max}}\right)^{\frac{1}{\gamma}}-\gamma=-\frac{\delta K+\delta E_G}{E_{a0}} \tag{5.25}$$

where $E_{a0}=P_0V_0/(\gamma-1)$ is the initial potential energy of the air cavity first defined Eq.(4.9). The minus sign on the right hand side of Eq. (5.25) indicates the transformation of the mechanical energy of the impacting liquid to the entrapped air during its initial compression stage, where $\delta K<0$ and $\delta E_G>0$ (see Figure 5.22). The relation between $P_{\max}/P_0$ (>1) and $-(\delta K+\delta E_G)/E_{a0}$ is the same as the curve plotted in Figure 4.14, where the value of $P_{\max}/P_0$ could be found to increase with that of $-(\delta K+\delta E_G)/E_{a0}$ in a nonlinear way. Thus the influence of initial P_0 and V_0 of the entrapped air cavity on the numerical results of $P_{\max}/P_0$ could be found to be in agreement with the expression in the above equation.

A further analysis is performed on the relation between the initial conditions of the air cavity and the $P_{\max}/P_0$ resulted in. The numerical results of $P_{\max}/P_0$ during the wall/wave/air interaction process (stage 3) of the six cases simulated in sections 5.4.1 & 5.4.2 (see Table 5.1), are summarized in Table 5.2. The corresponding values of $-(\delta K+\delta E_G)/E_{a0}$ are obtained from Eq. (5.25) (or Figure 4.14). We can then find for any two cases with the same initial air pressure P_0, $-(\delta K+\delta E_G)/E_{a0}$ is in an approximate reverse proportion to the initial cavity sizes ($V_0=0.3438$ in $x_0=10$, and $V_0=0.1052$ in $x_0=9$), or the initial potential energy of the cavity E_{a0}, as the two columns of bold numbers compared in Table 5.2.

Table 5.2 Relation of the first maximum pressure (numerical results), the energy transfer ratio (by Eq. (5.25)), and the initial potential energy of the cavity

P_0	$P_{\max}/P_0$ (numerical)		$-(\delta K+\delta E_G)/E_{a0}$ (by Eq. (5.25))			$E_{a0}=P_0V_0/(\gamma-1)$		
	(a) $x_0=10$	(b) $x_0=9$	(a) $x_0=10$	(b) $x_0=9$	$(b)/(a)$	(a) $x_0=10$	(b) $x_0=9$	$(a)/(b)$
(1) 10.087	2.803	7.045	0.1337	0.446	**3.336**	8.670	2.653	**3.268**
(2) 100.87	1.375	1.889	0.014	0.053	**3.786**	86.670	26.529	**3.268**
(3) 2.017	13.189	81.153	0.753	2.13	**2.829**	1.734	0.530	**3.268**

*(b)/(a) in row (1) denotes the ratio between the result of case b-1 ($x_0=9$, $P_0=10.087$) and that of case a-1 ($x_0=10$, $P_0=10.087$), and so forth.

To further confirm the result, for the impact situations developed from $x_0 = 10$ and $x_0 = 9$, ratios of $-(\delta K + \delta E_G)/E_{a0}$ between any two cases with different initial air pressure P_0 are summarized in Table 5.3, based on results given in Table 5.2. They are also found to correspond approximately with the reverse ratios of the initial potential energy of the cavity E_{a0} between the same two cases. The small discrepancy is related to the different magnitude of the loss in the mechanical energy (i.e. $\delta K + \delta E_G$) of the impacting flow by the end of the initial compression stage. It is in the nondimensional form, and thus varies only by a relatively small value for impact happening in different physical scales (of water depth or cavity size), compared with the variation of E_{a0}.

Table 5.3 Comparison between the ratios of $-(\delta K + \delta E_G)/E_{a0}$ and the corresponding reverse ratios of E_{a0} between any two cases with different P_0

Cases in comparison	$\frac{-\delta K - \delta E_G}{E_{a0}}$			E_{a0}		
	(1)/(2)	(3)/(1)	(3)/(2)	(2)/(1)	(1)/(3)	(2)/(3)
(a)-(a)	**9.550**	***5.632***	**53.786**	**10**	***5***	**50**
(b)-(b)	**8.415**	***4.776***	**40.189**	**10**	***5***	**50**
(b)-(a)	**31.857**	***15.931***	**152.143**	**32.681**	***16.344***	**163.435**
(a)-(b)	**2.523**	***1.688***	**14.208**	**3.060**	***1.530***	**15.303**

*(1)/(2) in (a)-(a) means the result of case a-1 ($x_0 = 10$, $P_0 = 10.087$) divided by that of case a-2 ($x_0 = 10$, $P_0 = 100.87$), and so forth.

From the comparisons in Tables 5.2 & 5.3, an important parameter is revealed which can largely influence the value of $P_{\max}/P_0$, or the compression degree of an entrapped air cavity during wall/wave/air interaction in breaking wave impact. The parameter is known prior to the impact process, which is the initial nondimensional potential energy of the air cavity E_{a0}. The finding in Tables 5.2 & 5.3 could be used to estimate the range of $P_{\max}/P_0$ in a piratical impact situation from a reference of laboratory experiment. Assume $P'_{\max}/P'_0$ is recorded in a laboratory experiment, the corresponding $-(\delta K' + \delta E'_G)/E'_{a0}$ could be gained from Eq. (5.25) (or Figure 4.14). Then the value of $-(\delta K + \delta E_G)/E_{a0}$ in the real impact situation could be approximated with the finding from Tables 5.2 & 5.3: by multiplying $-(\delta K' + \delta E'_G)/E'_{a0}$ with E'_{a0}/E_{a0}, which could be obtained through dimensional

analysis in the current work. The value of P_{max}/P_0 in the practical impact situation can then be estimated by solving Eq. (5.25) or checking against Figure 4.14 again.

5.6 Summary

To simulate the breaking wave impact on a wall with higher accuracy, a domain decomposition method, with different scales in each domain, is introduced in this chapter. The key technique is that the solution obtained with the stretched coordinate system method for the local impact zone is matched with that of the overall plunging wave in the normal Cartesian coordinate system. The effect of the trapped air cavity is examined in detail, including the scaling effect. A scaling law with regard to the air cavity effect is proposed, which could be used to estimate the range of the maximum pressure during breaking wave impact with air entrapment from a laboratory reference case. The obtained results give some deep insights into the entire impact dynamics, which can be summarised below:

1. When the direct impact on the wall occurs, smaller x_0 leads to a smaller initial air cavity volume V_0, which further leads to a larger maximum cavity pressure ratio relative to the ambient pressure P_0, or P_{max}/P_0, and a faster air pulsation motion. When other conditions are given, the smaller the nondimensionalised ambient pressure P_0 is, the larger P_{max}/P_0 and the slower the pulsation will be.

2. The direct impact by the wave crest generates local pressure peak or peaks on the wetted surface due to the sharp turn of the impinging free surface along the wall. The value of the peak is very much affected by the angle between the incident wave surface and the wall. As the wave further plunges and this angle increases, the value of the peak pressure will drop very rapidly.

3. When the air cavity is entrapped after the impact, pressure distribution on the wall, from top to bottom, is comprised of: (i) a local pressure peak region on the wetted surface, (ii) an approximately uniform pressure region next to the cavity and (iii) pressure with slower variation away from the cavity towards the bottom of the fluid. All the pressures in the three regions are very much affected by the variation of the internal pressure in the cavity.

4. After the entrapped air cavity is compressed to the minimum volume and starts to

expand, the water level is accelerated much faster upward along the wall than that in the compression stage, under the high internal pressure of the cavity. Small free surface hump is likely to be generated near the elevating outer wave surface jet root due to the large local acceleration (or pressure gradient). The air cavity will climb up along the wall as it contracts and expands for several cycles, with its upper surface elevating faster than the lower surface in the expansion stage, and its lower surface faster in the contraction stage. An inner free jet may be generated near the turning point of the upper cavity surface at the beginning of each re-contraction stage

5. Inner free jet impingement is observed. This may lead to multi-cavities or cavity fragmentation. This is in fact commonly observed in the laboratory and real impact situation. It is, however, beyond the scope of the current work and requires further research.

6. The ratio between the mechanic energy of the impacting liquid transferred to the air and the initial potential energy of the cavity, $-(\delta K + \delta E_G)/E_{a0}$, is found to decide the cavity pressure through a nonlinear relation. From the present numerical results, it is found to be in approximate reverse proportion to the nondimensional initial potential energy of the air cavity E_{a0}. The peak pressure on the wall in post-direct impact process is found to exceed the cavity pressure by a small value. The maximum pressure range in a real situation with entrapped air cavity could thus be estimated from a laboratory model test.

Chapter 6 Concluding remarks

6.1 Summary & conclusion

To acquire insight into the physics of the fluid/structure impact with air cavity effect in the context of marine engineering, two problems have been studied in this work: (i) impact by an axisymmetric cylinder water column on a rigid plate; (ii) plunging wave impact on a wall. The velocity potential theory and boundary element method for axisymmetric and 2D problems have been employed. The dynamics of both the direct water/structure impact and the subsequent body/water/air interaction process have been investigated. The main conclusions gained through the numerical study combined with analytical deductions are summarized below. For a more detailed description of the results obtained, refer to the summary sections at the end of each chapter.

(i) The direct impact between fluid/structure (without air cavity effect) can generate local pressure peak or peaks on the wetted surface due to the sharp turn of the impinging free surface along the wall. The value of the peak is closely related to the angle between the incident free surface and the wall. As the impact continues, it will drop very rapidly and then disappears. For the axisymmetric water column impact at constant velocity U with density ρ where the gravity effect can be ignored, the direct impact pressure is proportional to ρU^2 (below 1 above the atmospheric value).

(ii) There is an initial singularity in the radial velocity of the body/water/air intersection ($\phi_r \to \infty$) for perpendicular impact between an axisymmetric water column and a plate. It is caused by the initial incompatible conditions on the free surface and on the plate, and will be eliminated when a thin jet is formed on the plate soon after the initial impact stage. The feature of a longer thin jet in the numerical simulation is revealed, providing filed solution over a larger wetted surface without influencing the main impact dynamics. For the steady state, the radial velocity ϕ_r increases from 0 on the undisturbed free surface to nearly 1 outward along the jet region. The pressure (nondimensional) decreases from 0.5 at the impact centre to nearly 0 in the thin jet region.

(iii) An air cavity entrapped near the impact surface has significant effect on the impact dynamics. When an air cavity is entrapped on the impact surface by the water

column, the smaller the initial air radius in contact with the plate is, the larger the pressure gradient is next to cavity surface (approaching infinity when the air radius approaches zero); for air cavity trapped fully immersed in the water column, the initial impact pressure does not vary monotonically with the standoff distance. As the cavity is placed farther away from the plate, the pressure at the impact centre first increases from a small valley value to a peak value, and then gradually falls to a minimum value below that without air entrapment, and finally tends to the value as if no air were entrapped.

(iv) The entrapment of an air cavity can cause fast pressure oscillation with very large amplitude on the impact surface, owing to its deformation during the body/water/air interaction process and the adiabatic law. The nondimensional atmospheric pressure P_0 (or the initial air cavity pressure; $P_a/\rho U^2$ in Chapters 3 & 4, or $P_a/\rho gh$ in Chapter 5) and the initial air volume V_0 are found to largely influence the ratio between the first maximum cavity pressure and the atmospheric value ($P_{\max}/P_0$). Smaller V_0 or P_0 can lead to larger $P_{\max}/P_0$ .The mechanism underneath has been revealed through a deduction on the energy transfer relation during the body/water/air interaction process. For a given impact model, the initial potential energy of the air cavity, as E_a defined in this work, is found to largely influence the value of $P_{\max}/P_0$. An approximate scaling law is proposed based on the energy transfer relation and the numerical results. The range of the maximum impact pressure will thus be able to be estimated from laboratory results, with the dimensional analysis in this work.

(v) Some interesting characteristics are revealed for plunging wave impact on a wall entrapping an air cavity. Violent wave sprays (with free surface hump and spike observed) could be formed along the wall after the initial compression stage of the cavity, caused by the accumulated large pressure gradient in the top water area. On top of the pulsating motion, the air cavity would climb up along the wall gradually, with its upper surface elevating faster than the lower one in the expansion stage, and its lower surface faster in the contraction stage. At the beginning of each re-contraction stage, an inner free jet is found to be easily generated near the turning point of the upper cavity surface along the wall, owing to the local pressure peak on the wall (due to the reason in conclusion (i)) and the much smaller cavity pressure

nearby. Those inner jets can contribute to the distortion and fragmentation of the cavity, which constitutes an interesting feature yet to be investigated in future related experimental studies.

During the simulation on water impact with air cavity effect, some innovative numerical techniques and methods have been developed, tackling the numerical challenges involved:

(i) In the mathematical model and numerical procedure introduced in Chapter 2, two methods are proposed for computation of impact problem with long and thin jet (without cutting it off). One is based on a decoupled shallow water theory approximation; the other is a dipole distribution approximation. The former is successfully applied to the simulation of water column impact on a rigid plate in Chapter 3 and the local wave crest impact in the stretched coordinate system in Chapter 5.

(ii) In Chapter 3, the shallow water approximation for the thin jet region of a 2D case in previous work is extended to the axisymmetric case.

(iii) In the study of cylinder water column impact with entrapped air cavity on the rigid plate in Chapter 4, algorithms are proposed for the velocity calculation of the impinging point when the radial cavity jet meets at the impact centre, as well as for the possible immersion of fluid layers after the impingement.

(iv) In Chapter 5, for the more practical problem of plunging wave impact on a wall, a domain decomposition method based on the employment of a dual-system is developed, resolving the numerical difficulty caused by the large variation of scales involved in the local impact domain and the rest. Computation algorithms are developed, coupling the simultaneous simulation of local wave impact in the stretched coordinate system and the main wave plunging in the Cartesian system. This is the first time the stretched coordinate system is successfully applied for the exact free surface conditions during a plunging wave impact, also the first time that the plunging wave impact could be simulated by BEM without major approximations. It enables a simulation of higher accuracy for both the direct impact process and the subsequent wall/water/air interaction process. A paper entitled ‘Breaking wave impact on a wall with air entrapment’ has been submitted to Journal of Fluids and Structures based on some of the study in Chapter 5.

6.2 Future applications & perspectives

The numerical techniques and methods developed in this work could be applied to the study of general fluid/structure impact problems in the marine context, in which the jet formation and impingement is almost inevitable. In particular, the single contact point in plunging wave impact is a common feature in most practical engineering problems, such as green water on deck, slamming and sloshing, etc. The domain decomposition method with the employment of the dual-system developed in this work can thus be extended to the study of those problems, with which simulations on both the direct impact and the subsequent body/water/air interaction for cases with air entrapment could be carried out with improved accuracy. Two scenarios for the promising applications of the proposed domain decomposition method within BEM are shown as examples in Figure 6.1.

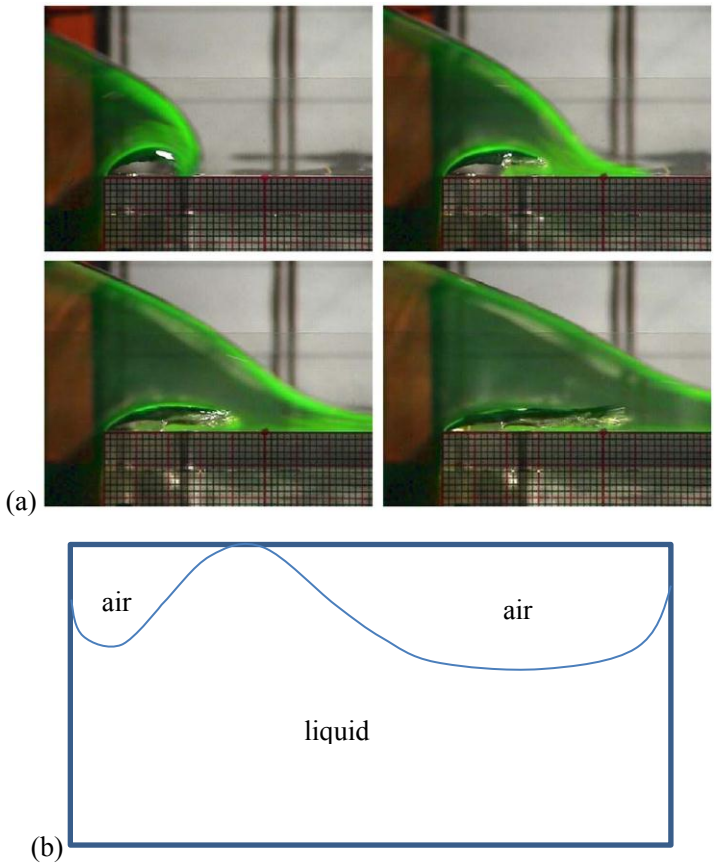

Figure 6.1 Promising applications of the domain decomposition method with BEM. (a) Snapshots of 2D laboratory experiment on overturning wave on deck (Greco et al. 2004); (b) sketch of a sloshing scenario in a tank

The investigation into the scaling law for plunging wave impact with air entrapment in this work could also be extended to other situations of fluid/structure impact

where an air cavity is enclosed with varying volume and pressure. However, there are still some problems to be solved before a more complete simulation of fluid/structure impact with air cavity effect can be achieved. Below we recapitulate some main problems emerged during the analytical and numerical studies in this thesis that require further work.

(i) The analytical solution of the initial impact pressure by the cylinder water column on the rigid plate, though has been deduced with the method of variables separation in Chapter 3, is found to fail to converge caused by the initial incompatible conditions near the three-phase intersection point and demands further analytical study.

(ii) The cavity jet impingement on the plate in the axisymmetric model is found to generate fast shooting vertical jet away from the impact surface. It will penetrate the cavity top surface and a toroidal cavity is expected to be formed after that. A dipole distribution might be applied on the penetration surface to carry on the simulation, but it is not included in the current simulation in Chapter 4 and demands future study.

(iii) The local jet impingement happening on the impact surface inside the cavity has been simulated for the axisymmetric water impact problem. It is, however, only applicable for axisymmetric or symmetric problems. The non-symmetric jet impingement in the air cavity during the plunging wave impact in Chapter 5 is not simulated, for which theoretical models need to be worked on.

(iv) For 2D plunging wave impact on the wall simulated in Chapter 5, inner free jet is found to be generated from the entrapped cavity surface near the wall. It will impinge with the nearby cavity surface, and thus multi-cavity can be formed. This could shed light on the mechanism of the cavity fragmentation observed in experiments, yet such process following the formation of the multi-cavity could not be simulated with the current model.

The current studies are based on axisymmetric and 2D models, which reveal some aspects of the mechanism of fluid/structure impact with air cavity effect. In terms of future perspectives, the numerical models and techniques developed in the present work provide foundation for the study of fully nonlinear 3D wave impact problems in practical engineering situations. Some of them could be extended directly to 3D

cases, for instance, the thin jet treatment schemes and the dual-system technique for impact starting from one point, though additional numerical difficulties might arise in the remeshing and smoothing of the 3D elements, due to the strong nonlinearity and large distortion of the free surface involved. In consideration of the effect of air cavity entrapped in 3D fluid/structure impact problems, however, it should be noted that there might be ventilation involved (e.g. for 3D plunging wave impact). It is not appropriate to apply the adiabatic law for a closed volume of gas any more, as that in the current work. The air flow entrapped then has to be modeled with theories related to aerodynamics, or combining experimental investigations, to provide the boundary condition at the water-air interface.

Appendix A. Water column impact with air cavity fully trapped inside (P_0=100)

Figure A.1 shows the temporal history of the volume and pressure change of fully entrapped cavity initially located at $z_0 = 0.22$ and 0.3, when the initial air pressure is bigger as $P_0 = 100$. The numerical results of the corresponding impact process until the internal jet penetrates the other side of the cavity are shown respectively in Figures A.2 & A.3. When the initial cavity is placed close to the plate at $z_0 = 0.22$, by the end of the first contraction stage at t=0.014, as shown in Figure A.2(a), the lower half of the cavity becomes slimmer in shape compared to its upper half, due to the pressure valley in the middle in the initial impact stages. A bulb shape is also formed at the end of the following expansion stage, as shown at t=0.046 in Figure A.2(b). After that the lower cavity bottom starts to move upward and form a vertical jet, in the second contraction stage shown in Figure A.2(c). During the short changing process of the cavity bottom shape, a local pressure peak can be also seen around t=0.050 and 0.055, until an upward jet is formed. The mechanism is also related to the acceleration of the cavity bottom at such moment prior to the formation of the shooting jet. A protruding jet has been well formed by the end of the second contraction stage at t=0.076. The cavity stars to expand again until the vertical jet reaches its top surface at t=0.1055, when it is about to reach the minimum volume. As a result, the air cavity experiences about 1.75 oscillation periods in total during the impact process before the penetration by the vertical jet.

When the cavity is placed farther away at $z_0 = 0.3$ at the beginning of the impact, it experiences much longer life period before the jet penetrates at t=0.158, which is nearly 2.75 oscillation circles according to Figure A.2. The cavity deforms with much smaller volume changing range compared with that of $P_0 = 10$ in Figure 4.16. The vertical jet formed in late the first expansion stage is much weaker, smaller in both curvature and its moving speed. It does not approach to the other side until nearly the end of the third expansion stage.

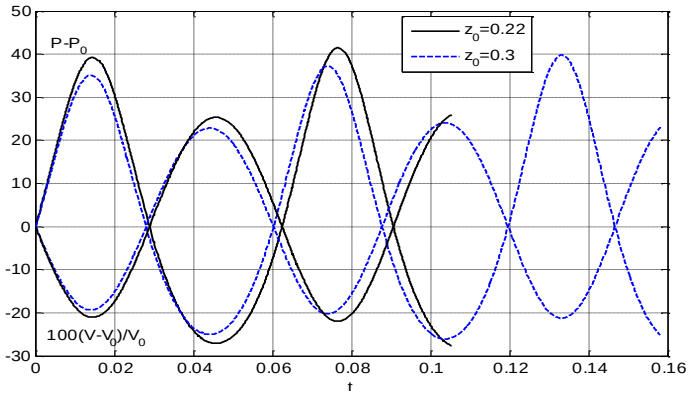

Figure A.1. Time history of cavity volume and its pressure inside with $z_0 = 0.22$ and 0.3 when $P_0 = 100$ ($R = 0.2$, $V_0 = 0.0335$)

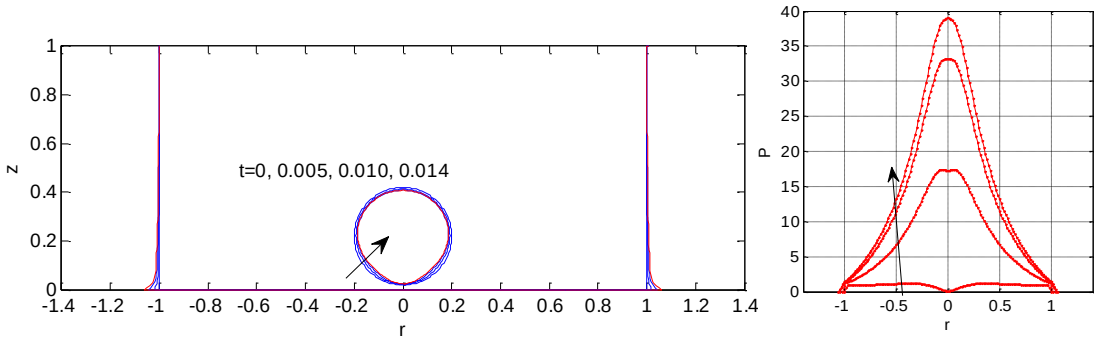

(a) 1st contraction stage ($t \le 0.0146$)

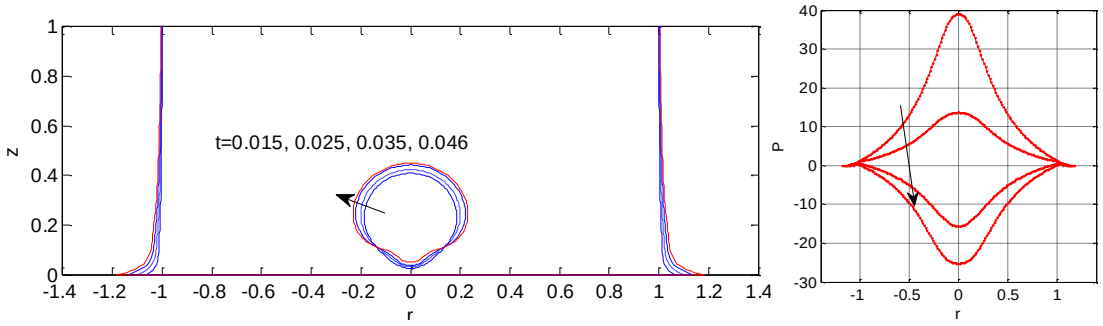

(b) 1st expansion stage ($0.0146 \le t \le 0.046$)

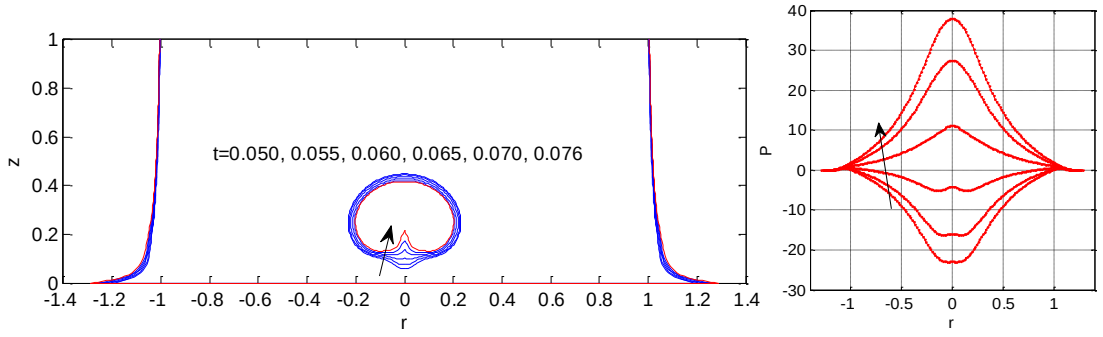

(c) 2nd contraction stage ($0.046 \le t \le 0.0765$)

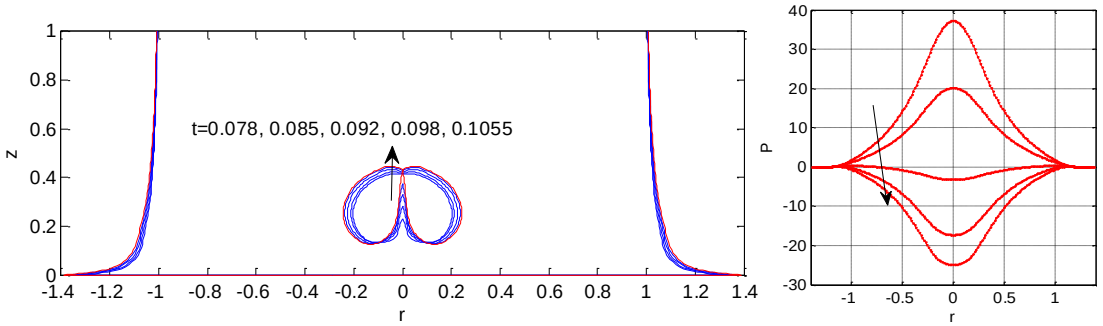

(d) 2nd expansion stage: before the penetration of the jet ($0.0765 \le t \le 0.1055$)

Figure A.2. Longitudinal sections of axisymmetric liquid column impact with spherical cavity trapped inside: deformation of the free surface near the rigid plate, and the corresponding impact pressure distribution. ($z_0 = 0.22$, $R = 0.2$, $P_0 = 100$)

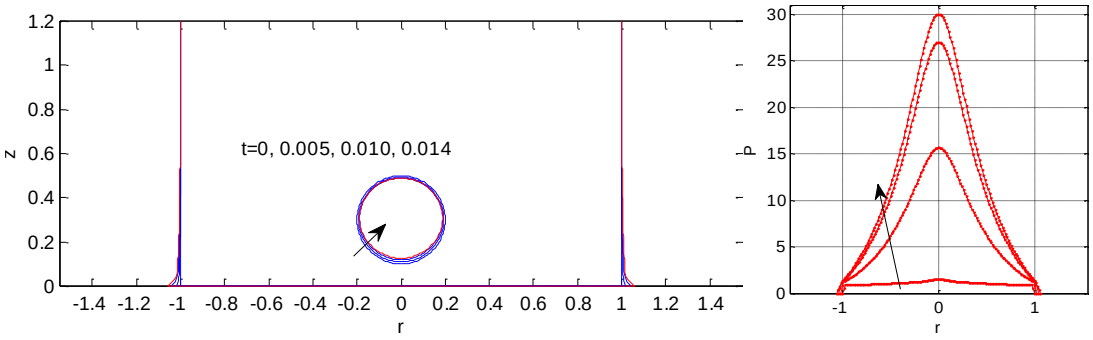

(a) 1st contraction stage ($t \le 0.014$)

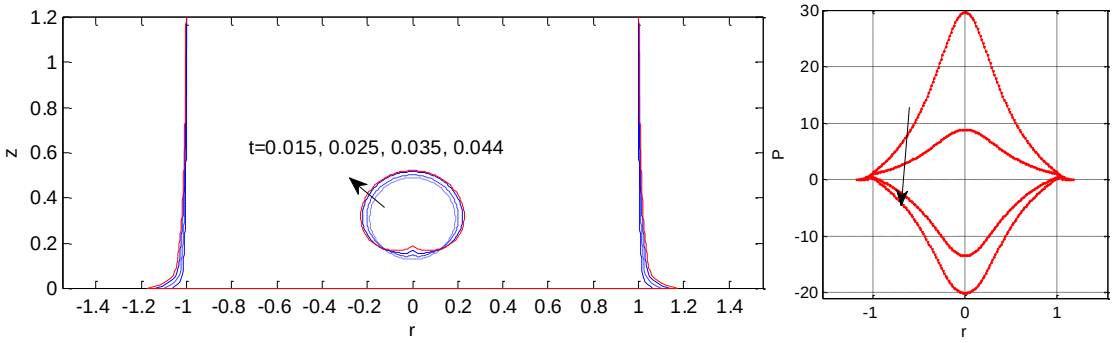

(b) 1st expansion stage ($0.014 \le t \le 0.044$)

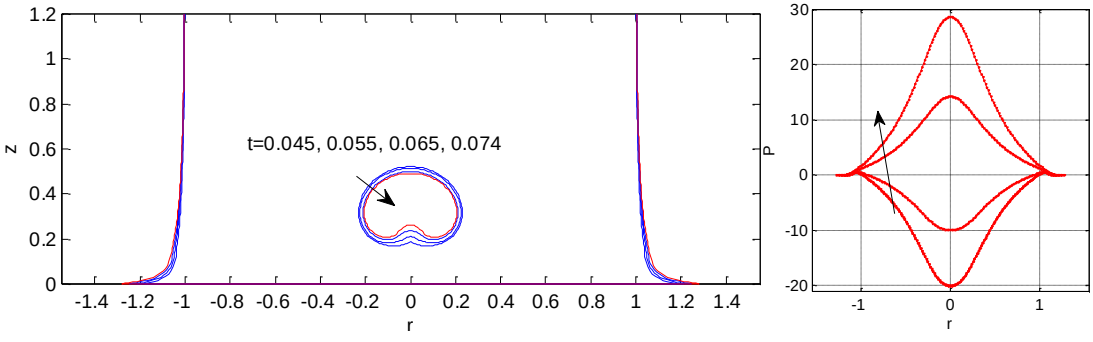

(c) 2nd contraction stage ($0.044 \le t \le 0.074$)

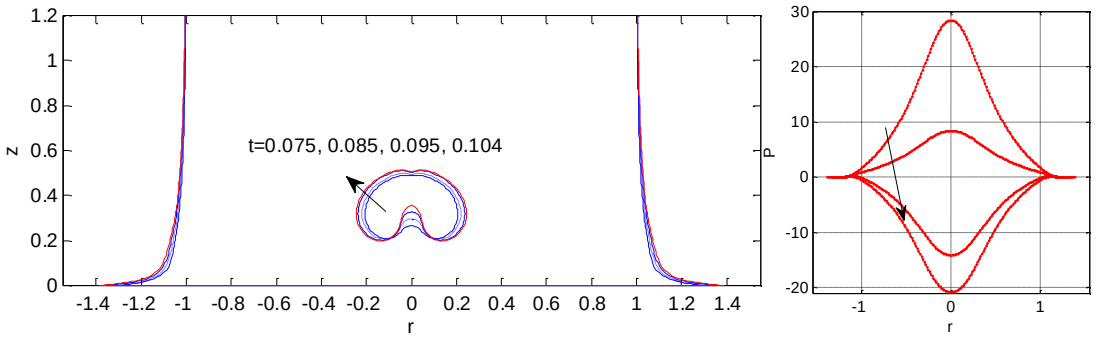

(d) 2nd expansion stage: before the penetration of the jet ($0.074 \le t \le 0.104$)

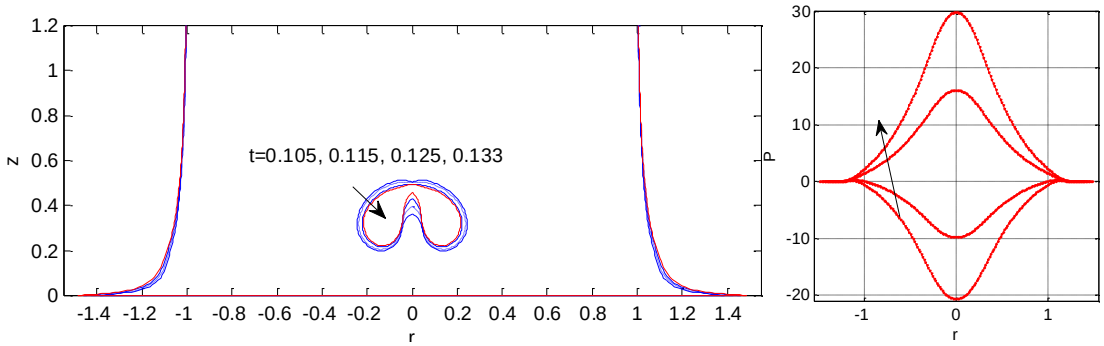

(e) 3rd contraction stage ($0.104 \le t \le 0.133$)

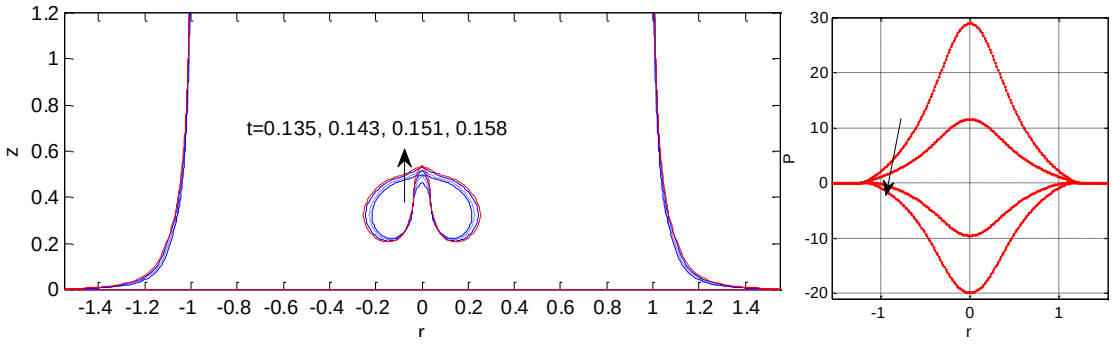

(f) 3rd expansion stage ($0.133 \le t \le 0.158$)

Figure A.3. Longitudinal sections of axisymmetric liquid column impact with spherical cavity trapped inside: deformation of the free surface near the rigid plate, and the corresponding impact pressure distribution. ($z_0 = 0.3$, $R = 0.2$, $P_0 = 100$)

References

Abramowitz, M., Stegun, I.A., 1972. Handbook of Mathematical Functions With Formulas, Graphs and Mathematical Tables. Washington, D.C.

Bagnold, R.A., 1939. Interim report on wave-pressure research. Journal of the Institude of Civil Engineers 12, 201-226.

Batchelor, G.K., 1967. An Introduction to Fluid Mechanics. Cambridge: Cambridge University Press.

Best, J.P., 1993. The formation of toroidal bubbles upon the collapse of transient cavities. Journal of Fluid Mechanics 251, 79-107.

Bredmose, H., Bullock, G.N., 2008. Scaling of wave-impact pressures in trapped air pockets. In Proc. 23rd Intl Workshop on Water Waves and Floating Bodies. Jeju, Korea

Bredmose, H., Peregrine, D.H., Bullock, G.N., 2009. Violent breaking wave impacts. Part 2: modelling the effect of air. J. Fluid Mech. 641, 389-430.

Cook, S.S., 1928. Erosion by Water-Hammer. Proc. R. Soc. London. Ser. A 119, 481–488.

Cooker, M.J., Peregrine, D.H., 1990a. A model for breaking wave impact pressures. Proceedings of 22nd Conference on Coastal Engineering, Delft, ASCE, 1473–1486.

Cooker, M.J., Peregrine, D.H., 1990b. A model of the shock pressure from breaking waves. 5th Int. Workshop on Water Waves and Floating Bodies, Manchester, England.

Cooker, M.J., Peregrine, D.H., 1990c. Violent water motion at breaking-wave impact. Coastal Engineering Proceedings 1, 22.

Cooker, M.J., Peregrine, D.H., 1992. Wave impact pressure and its effect upon bodies lying on the sea bed. Coastal Eng., 18, 205-229.

Cooker, M.J., Peregrine, D.H., 1995. Pressure-impulse theory for liquid impact problems. Journal of Fluid mechanics, 297, 193-214.

Cointe, R., Armand, J.L., 1987. Hydrodynamic Impact Analysis of a Cylinder. J.

Offshore Mechanics and Arctic Engineering 9, 237-243.

Cumberbatch, E., 1960. The impact of a water wedge on a wall. J. Fluid Mech. 7, 353–374.

Dobrovol'skaya, Z.N., 1969. On some problems of similarity flow of fluid with a free surface. J. Fluid Mech. 36, 805–829.

Dommermuth, D.G., Yue, D.K.P., Lin, W.M., Rapp, R.J., Chan, E.S., Melville, W.K., 1988. Deep-water plunging breakers: a comparison between potential theory and experiments. Journal of Fluid Mechanics 189, 423–442.

Duan, W.Y., Xu, G.D., Wu, G.X., 2009. Similarity solution of oblique impact of wedge-shaped water column on wedged coastal structures. Coastal Engineering 56, 400–407.

Eatock Taylor, R., Wu, G.X., Wei, B., Hu, Z.Z., 2008. Numerical wave tanks based on finite element and boundary element modeling. Journal of Offshore Mechanics and Arctic Engineering 130.

Faltinsen, O.M., Landrini, M., Greco, M., 2004. Slamming in marine applications. Journal of Engineering Mathematics 48, 187–217.

Fontaine, Tulin, M.P., 2001. On the prediction of nonlinear free-surface flows past slender hulls using 2d+t theory: The evolution of an idea. Ship Technology Research 48, 56–67.

Gibson, D.C., Blake, J.R., 1982. The growth and collapse of bubbles near deformable surfaces. Appl. Sci. Res. 38, 215.

Greco, M., Landrinia, M., Faltinsen, O.M., 2004. Impact flows and loads on ship-deck structures. Journal of Fluids and Structures, 19. 251–275.

Grilli, S., Subramanya, R., Svendsen, I., Veeramony, J., 1994. Shoaling of solitary waves on plane beaches. Journal of waterway, port, coastal, and ocean engineering 120, 609–628.

Grilli, S., Svendsen, I., Subramanya, R., 1997. Breaking criterion and characteristics for solitary waves on slopes. Journal of waterway, port, coastal, and ocean engineering 123, 102–112.

Grilli, S.T., Guyenne, P., Dias, F., 2001. A fully non-linear model for three-

dimensional overturning waves over an arbitrary bottom. Int. J. Numer. Methods Fluids 35, 829–67.

Hastings, C., 1955. Approximations for Digital Computers. Princeton University Press, Princeton.

Hattori, M., Arami, A., Yui, T., 1994. Wave impact pressure on vertical walls under breaking waves of various types. Coastal Engineering 22(1), 79–114.

Howison, S.D., Ockendon, J.R., Wilson, S.K., 1991. Incompressible water-entry problems at small deadrise angles. J. Fluid Mech. 222, 215-230.

Hull, P., Müller, G., 2002. An investigation of breaker heights, shapes and pressures. Ocean engineering 29, 59–79.

Judge, C., Troesch, A.W., Perlin, M., 2004. Initial water impact of a wedge at vertical and oblique angles. Journal of Engineering Mathematics 48, 279–303.

Khabakhpasheva, T. I., Korobkin, A. A., 2011. Fluid impact onto a corrugated panel with trapped gas cavity. In: Proc. 26th Intern. Workshop on Water waves and Floating Bodies, 2011, Athens, Greece.

Kihara, H., 2004. Numerical modelling of flow in water entry of a wedge. In: Proc. 19th International Workshop on Water Waves and Floating Bodies, Cortona, Italy, 28-31.

Korobkin, A.A., 1996. Entry problem for body with attached cavity. In: Proc. 11th Intern. Workshop on Water Waves and Floating Bodies, Hamburg, Germany, 4.

Korobkin, A.A., Pukhnach, V.V., 1988. Initial stage of water impact. Ann. Rev. Fluid Mech. 20, 159-185.

Lachaume, C., Biausser, B., Grilli, S.T., Fraunie, P., Guignard, S., 2003. Modeling of breaking and post-breaking waves on slopes by coupling of BEM and VOF methods. In Proc. 13th Intl Offshore and Polar Engng Conf., Honolulu, USA, 353–359. ISOPE.

Lamb, H., 1932. Hydrodynamics. Cambridge University Press.

Lin, W.M., 1984. Nonlinear motion of the free surface near a moving body. Ph.D. thesis, MIT, Dept. of Ocean Engineering.

Lin, W.M., Newman, J.N., Yue, D.K., 1985. Nonlinear forced motions of floating

bodies. In Proceedings 15th Symposium of Naval Hydrodynamics, ONR, Washington: National Academy Press.

Lu, C.H., He, Y.S., Wu, G.X., 2000. Coupled analysis of nonlinear interaction between fluid and structure during impact. Journal of fluids and structures 14, 127–146.

Lugni, C., Brocchini, M., Faltinsen, O.M., 2006. Wave loads: The role of flip-through. Phys. Fluids 18 (122101).

Lugni, C., Brocchini, M., Faltinsen, O.M., 2010. Evolution of the air cavity during a depressurized wave impact. II. The dynamic field. Physics of Fluids 22, 056102.

Longuet-Higgins, M.S., Cokelet, E.D., 1976. The deformation of steep surface waves on water, I. A numerical method of computations. Proceedings of the Royal Society of London, A 350, 1–26.

Maruo H., Song W., 1994. Nonlinear analysis of bow wave breaking and deck wetness of a high-speed ship by the parabolic approximation. In: Proc. 20th Symposium on Naval Hydrodynamics, University of California, Santa Barbara, California.

Maceie, A.G., 1962. A linearized theory of the water entry problem. Quart. J. Mech. and Appl. Math. 15, 137-151.

Mei, C.C., 1983. The Applied Dynamics of Ocean Surface Waves. Wiley-Interscience, New York.

Moore, M.R., Howison, S.D., Ockendon, J.R., Oliver, J.M., 2013. A note on oblique water entry. Journal of Engineering Maths 81, 67-74.

Nagai, S., 1960. Shock pressures exerted by breaking waves on breakwaters. J. Waterways, Harbors Div. ASCE 86, 1-38.

Newman, J.N., 1977. Marine Hydrodynamics. MIT Press.

Oertel, H., 2004. Prandtl's Essentials of Fluid Mechanics. New York.

Oumeraci, H., Klammer, P., Partenscky, H.W., 1993. Classification of breaking wave loads on vertical structures. ASCE J. Waterway, Port, Coastal Ocean Engng 119, 381–397.

Peregrine, D.H., Kalliadasis, S., 1996. Filling flows, cliff erosion and cleaning flows. J. Fluid Mech. 310, 365-374.

Peregrine, D.H., Thais, L., 1996. The effect of entrained air in violent water wave impacts. J. Fluid Mech. 325, 317.

Rafiee, A., Dutykh, D., Dias, F., 2013. Numerical simulation of wave impact on a rigid wall using a two-phase compressible SPH method. In Proceedings of IUTAM symposium of Particle Methods in Fluid Mechanics.

Salvesen, N., Tuck, E.O., Faltinsen, O.M., 1970. Ships motions and Sea Loads. SNAME Trans 78, 250-287.

Schiffman, M., Spencer, D.C., 1951. The force of impact on a cone striking a water surface (vertical entry). Communications on pure and applied mathematics 4, 379-417.

Scolan, Y.M., 2010. Some aspects of the flip-through phenomenon: A numerical study based on the desingularized technique. Journal of fluids and structures 26, 918–953.

Semenov, Y.A., Iafrati, A., 2006. On the nonlinear water entry problem of asymmetric wedges. Journal of Fluid Mechanics 547, 231–256.

Sun, H., 2007. A boundary element method applied to strong nonlinear wave-body interaction problems, Doctoral Thesis at NTNU, Trondheim, Norway.

Sun, H., Faltinsen, O.M., 2007. The influence of gravity on the performance of planing vessels in calm water. Journal of Engineering Mathematics 58(1-4), 91–107.

Sun, S.L., Wu, G.X., 2013. Oblique water entry of a cone by a fully three-dimensional nonlinear method. Journal of Fluids and Structures 42, 313–332.

Takemoto, H., 1984. Some considerations on water impact pressure. J. Soc. Naval Arch Japan 156, 314-322.

Tanizawa, K., Yue, D.K., 1992. Numerical computation of plunging wave impact loads on a vertical wall. Part 2. The air pocket. In Proc. 7th International Workshop on Water Waves and Floating Bodies.

Topliss, M.E., Cooker, M.J., Peregrine, D.H., 1992. Pressure oscillations during

wave impact on vertical walls, in Proceedings of the 23rd Inter- national Conference on Coastal Engineering. ASCE, Venice 2, 1639–1650.

Toyama,Y., 1993. Two-dimensional water impact of unsymmetrical bodies. J Soc Naval Arch Japan. 173, 285.

Von Karman, T.H., 1929. The impact on Seaplane Floats during Landing, NACA TN 321, Washington.

Wagner, H., 1932. ¨Uber Stoss- und Gleitverg¨ange an der Oberfl¨ache von Fl¨ussigkeiten. Z. Angew. Mach. Mech. 12, 193-235. (English transl: Phenomena associated with impacts and sliding on liquid surfaces. NACA Translation 1366.)

Wang, C.Z., Wu, G.X., 2006. An unstructured-mesh-based finite element simulation of wave interactions with non-wall-sided bodies. Journal of Fluids and Structures 22, 441–461.

Wood, D.J., Peregrine, D.H., Bruce, T., 2000. Wave impact on a wall using pressure-impulse theory. I: Trapped air. J. Waterway, Port, Coastal, Ocean Eng. 126, 182-190.

Wu, G.X., 1991. Hydrodynamic impact of the water wave. 6th Int. Workshop on Water Waves and Floating Bodies. Woods Hole, MA, USA.

Wu, G.X., 1998. Hydrodynamic force on a rigid body during impact with liquid. Journal of Fluids and Structures 12, 549-559.

Wu, G.X., 2001. Initial pressure distribution due to jet impact on a rigid body. Journal of fluids and structures 15, 365–370.

Wu, G.X., 2006. Numerical simulation of water entry of twin wedges. Journal of Fluids and Structures, 22, 99–108.

Wu, G.X., 2007a. Fluid impact on a solid boundary. Journal of Fluids and Structures 23, 755–765.

Wu, G.X., 2007b. Two dimensional liquid column and liquid droplet impact on a solid wedge. Quarterly Jnl. of Mechanics & App. Maths 60, 497-511.

Wu, G.X., Eatock Taylor, R., 1996. Transient motion of a floating body in steep waves. In: 11th Int Workshop on Water Waves and Floating Bodies, Hamburg.

Wu, G.X., Eatock Taylor, R., 2003. The coupled finite element and boundary element analysis of nonlinear interactions between waves and bodies. Ocean Engineering 30, 387–400.

Wu, G.X., Sun H, He, Y.S., 2004. Numerical simulation and experimental study of water entry of a wedge in free fall motion. Journal of Fluids and Structures,19, 277-289.

Wu, G.X., Hu, Z.Z., 2004. Simulation of nonlinear interactions between waves and floating bodies through a finite-element-based numerical tank. Proceeding of royal society, A, 460, 2797–2817.

Xu, G.D., Duan, W.Y., Wu, G.X., 2008. Numerical simulation of oblique water entry of an asymmetrical wedge. Ocean Engineering 35, 1597-1603.

Zhang, S., Dick, K.P., Yue, Tanizawa, K.,1996. Simulation of plunging wave impact on a vertical wall. Journal of Fluid Mechanics 327, 221-254.

Zhao, R., Faltinsen, O., 1993. Water entry of two-dimensional bodies. Ibid 246, 593–612.

Zhu, X.X., 2000. Modelling of Free-Formed Curves and Surfaces (in Chinese). Science Press, Beijing.